

**Dissertation**  
**submitted to the**  
**Combined Faculties for the Natural Sciences and for Mathematics**  
**of the Ruperto–Carola University of Heidelberg, Germany**  
**for the degree of**  
**Doctor of Natural Sciences**

presented by  
Dipl. Phys. Christoph Graf vom Hagen  
born in: Darmstadt (Germany)

Oral examination: 23.04.2008



# Towards a low-dimensional degenerate Fermi–Fermi–Bose mixture

Referees:

Prof. Dr. Jörg Schmiedmayer  
Prof. Dr. Jian–Wei Pan



# Zusammenfassung

## Auf dem Weg zu einer niederdimensionalen, quantenentarteten Fermi–Fermi–Bose Mischung

Diese Arbeit beschreibt ein Pilot–Experiment zur Erzeugung einer quantenentarteten Mischung aus zwei Fermi Gasen. Aus Messungen an  ${}^6\text{Li}$  (Fermion) und  ${}^{87}\text{Rb}$  (Boson) wurde der unelastische Verlustratenkoeffizient in einer Magneto–Optischen Falle (MOT) bestimmt. Der Wert dieser Koeffizienten wurde auf  $\beta_{\text{LiRb}} = (1.5 \pm 0.5) \times 10^{-10} \text{cm}^3 \text{s}^{-1}$  bestimmt. Das gemeinsame Speichern dieser Mischung in einer magnetischen Falle wurde demonstriert. Die Ergebnisse dieser Arbeit, in Kombination mit Ergebnissen aus anderen Forschungsgruppen, führten zum Aufbau eines zukunftsweisenden Experiments. Das Design und der anschließende Aufbau dieser Apparatur werden im Detail beschrieben. Im Ergebnis steht nun eine ideale Apparatur zur Untersuchung von entarteten Quantengasen in niedrigen Dimensionen zur Verfügung. Derzeit erlaubt die Mischung aus  ${}^{40}\text{K}$  und  ${}^{87}\text{Rb}$  Experimente mit Bose–Fermi Mischungen auf Atom Chips. Mit der geplanten Erweiterung der Anlage auf  ${}^6\text{Li}$  werden Experimente mit zwei verschiedenen Fermionen in niederdimensionalen Fällen erstmals möglich werden. Die Wechselwirkung von leichten und schweren Fermionen, sowie die unterschiedliche Wechselwirkung zwischen Bosonen und Fermionen mit anziehendem (KRb) und abstoßendem (LiRb) Potential können hier ebenso untersucht werden. Diese Art der Wechselwirkung kann sonst nur in der Umgebung einer Feshbach Resonanz untersucht werden.

## Abstract

### Towards a low–dimensional degenerate Fermi–Fermi–Bose mixture

This work introduces a pilot experiment towards the creation of a degenerate two–species Fermi gas. Experiments with a dual–species MOT of  ${}^6\text{Li}$  (fermion) and  ${}^{87}\text{Rb}$  (boson) led to the measurement of the inelastic loss rate coefficient  $\beta_{\text{LiRb}} = (1.5 \pm 0.5) \times 10^{-10} \text{cm}^3 \text{s}^{-1}$ . Furthermore, both species were trapped in a common magnetic microtrap. The results from this pilot experiment with  ${}^6\text{Li}$  and  ${}^{87}\text{Rb}$  and the development of  ${}^{40}\text{K}$  and  ${}^{87}\text{Rb}$  mixtures by other research groups were analysed. From this data set and the experience of three generations of atom chip experiments on hand, a truly next–generation experiment was designed. The design process and the construction of this experiment as well as the technological developments required are discussed in detail in this work.

The effort led to an ideal starting point for future experiments: a K–Rb machine. The study of low–dimensional pure and mixed quantum gases will already be possible. With the extension towards Li, the study of the interaction between heavy and light fermions will be possible. Furthermore, the interaction of bosons and fermions with attractive and repulsive interactions can be studied without the need of a Feshbach resonance, as the interaction between Rb and Li is repulsive and the interaction between Rb and K is attractive.



# **Part I**

## **Introduction**





# Introduction

During the past decade, a new field of atomic physics has emerged. This new and rapidly growing research area saw its starting point with the creation of a Bose Einstein condensate (BEC) [1, 2]. The subsequent realisation of a quantum degenerate Fermi gas [3] extended the possibilities even further. The unique level of control over important parameters in modern atomic physics experiments, such as temperature, interaction strength and even disorder, is fascinating. Particularly for experiments with degenerate Fermi gases, this is an big advantage over the solid-state environment. In the vicinity of a Feshbach resonance [4], the formation and condensation of quasi-bosons, composed of two opposite spin states could be demonstrated for  ${}^6\text{Li}$  and  ${}^{40}\text{K}$  [5, 6, 7]. Theory groups developed the methods to map problems, such as the BEC-BCS crossover, superfluid phases, Bose glasses and spin-charge separation from solid-state quantum systems to the pure world of degenerate quantum gases [8, 9, 10]. Meanwhile, a growing community developed the technique of atom chips. With these chips, single-atom detection with optical elements, electric and magnetic traps, and interferometers in time-dependent traps have already been realised.

This work discusses a piloting experiment towards the creation of a degenerate two-species Fermi gas.

Experiments with a dual-species MOT of  ${}^6\text{Li}$ (fermion) and  ${}^{87}\text{Rb}$ (boson) led to the measurement of the inelastic loss rate coefficient  $\beta_{\text{LiRb}} = (1.5 \pm 0.5) \times 10^{-10} \text{cm}^3 \text{s}^{-1}$ . Furthermore, both species were trapped in a common magnetic microtrap. The build up of this experiment and all methods used are described in detail. The results from this piloting experiment with  ${}^6\text{Li}$  and  ${}^{87}\text{Rb}$  and the development of  ${}^{40}\text{K}$  and  ${}^{87}\text{Rb}$  mixtures by other research groups were analysed. From this dataset and the experience of three generations of atom chip experiments on hand, a truly next-generation experiment was designed. The design process and the construction of this experiment are discussed in detail in this work. All methods and techniques developed within this work are also discussed and an overview of the current status given.

The experiment described here is an ideal starting point for future experiments. The study of low-dimensional pure and mixed quantum gases is already possible. With the extension towards Li, the study of the interaction between heavy and light fermions will be possible. Furthermore, the interaction of bosons and fermions with attractive and repulsive interactions can be studied without the need of a Feshbach resonance, as the interaction between Rb and Li is repulsive and the interaction between Rb and K is attractive.



# Contents

<b>Abstract</b>	<b>v</b>
<b>I Introduction</b>	<b>vii</b>
Introduction	ix
<b>II Theory</b>	<b>1</b>
<b>1 Foundations</b>	<b>3</b>
1.1 Magnetic Traps . . . . .	4
1.2 Magnetic Microtraps . . . . .	5
1.3 Mirror MOT . . . . .	7
1.4 Evaporative and Sympathetic Cooling . . . . .	8
1.5 Quantum Gases in Low Dimensions . . . . .	10
<b>2 Cold Collisions</b>	<b>13</b>
2.1 A Simple Collision Model . . . . .	13
2.2 Inelastic Collisions . . . . .	14
2.3 Elastic Collisions . . . . .	17
2.4 The MOT . . . . .	18
<b>III The Laser Systems</b>	<b>21</b>
<b>3 Locking Techniques</b>	<b>25</b>
3.1 Lock-In Method . . . . .	25
3.2 Frequency-Modulation Lock . . . . .	26
3.3 Frequency-Offset Lock . . . . .	27
<b>4 Li Laser System</b>	<b>29</b>
<b>5 Rb Laser System</b>	<b>33</b>
<b>6 K Laser System</b>	<b>35</b>
6.1 Repumper FM-Lock . . . . .	37
6.2 Cooler FO Lock . . . . .	39

6.3	Local Oscillator . . . . .	42
<b>IV Lithium - Rubidium Experiments</b>		<b>45</b>
<b>7</b>	<b><math>^6\text{Li}</math> - <math>^{87}\text{Rb}</math> Experiments</b>	<b>47</b>
7.1	Vacuum-Chamber and Coils . . . . .	47
7.2	Method of Detection . . . . .	49
7.2.1	Number of Atoms . . . . .	49
7.2.2	CCD Camera System . . . . .	50
7.3	The ADWin System . . . . .	50
7.4	The Dual-MOT Experiment . . . . .	51
7.5	Results . . . . .	52
7.6	Magnetic-Quadrupole-Trap Lifetime . . . . .	63
7.7	An Atom Chip for the Lithium-Rubidium Experiment . . . . .	64
7.8	Magnetic trap . . . . .	64
<b>V The <math>^6\text{Li}</math>-<math>^{40}\text{K}</math>-<math>^{87}\text{Rb}</math> Experiment</b>		<b>67</b>
<b>8</b>	<b>Design Goals</b>	<b>69</b>
8.1	Long Lifetime in the Magnetic Atom Chip Trap . . . . .	70
8.2	Stable, Robust and Short Experimental Cycle . . . . .	71
8.3	1D traps . . . . .	72
8.4	RF Wires . . . . .	73
8.5	High Performance Transversal Imaging . . . . .	73
8.6	Good Optical Access . . . . .	73
8.7	The Fermions: Potassium and/or Lithium . . . . .	74
<b>9</b>	<b>Final Design</b>	<b>77</b>
9.1	Glass Cell Or Not A Glass Cell? . . . . .	77
9.2	The Science Chamber . . . . .	80
9.3	Double-MOT Layout . . . . .	84
9.4	Construction . . . . .	87
9.5	Imaging . . . . .	88
9.6	Mounting and atom chip . . . . .	93
9.7	Technological Details . . . . .	94
9.8	Bias Field Coils . . . . .	95
9.9	Feedback . . . . .	97
9.9.1	Current-Feedback . . . . .	97
9.9.2	Laser Light . . . . .	98
9.10	Lithium . . . . .	98
<b>10</b>	<b>First Result the K-Rb MOT</b>	<b>101</b>
10.1	Isotope Enriched K-dispensers . . . . .	101
10.2	Assembly of the whole Vacuum System . . . . .	102

10.3 K-Rb MOTs . . . . .	102
<b>VI Conclusion &amp; Outlook</b>	<b>105</b>
11 Conclusion	107
12 Outlook	109
<b>VII Appendices</b>	<b>111</b>
<b>A Science Chamber CAD drawings</b>	<b>115</b>
<b>B Problems</b>	<b>133</b>
<b>C Other CAD files</b>	<b>135</b>
C.1 Optics Boards . . . . .	135
<b>D Level Schemes</b>	<b>143</b>
D.1 Potassium . . . . .	143
D.2 Rubidium . . . . .	143
<b>E Imaging</b>	<b>147</b>
<b>F Electronics</b>	<b>151</b>
F.1 Laser Electronics . . . . .	151
F.2 Charge Pump . . . . .	151
F.3 H-Bridge High Current Switch . . . . .	151
F.4 Current-Feedback . . . . .	154
<b>Acknowledgements</b>	<b>173</b>



# List of Figures

1.1	Current carrying wires and superimposed homogeneous magnetic fields cause (a) a sideguide, (b) a U-trap and (c) a Z-trap. The U-trap is an elongated quadrupole trap and can be used to operate a MOT and the Z-trap serves as a Ioffe-trap with a finite trap bottom. The top row shows a sketch of the traps and field geometries, whereas the bottom row shows the field along and orthogonal to the wires. . . . .	6
1.2	Working principle of a mirror-MOT. The light is reflected off the surface of the atom chip and changes its helicity. At the position of the MOT, this reflected light appears to come from behind the surface and so a "virtual" six-beam MOT is realised. . . . .	8
1.3	(a) Bosons: Plot of $\mu/\hbar\omega_{\perp}$ against $\omega_{\perp}$ . For values of $\mu/\hbar\omega_{\perp} > 1$ the system is 3D, below that it becomes effectively 1D. (b) Fermions, in this case $^{40}\text{K}$ : The plot shows $E_F/\hbar\omega_{\perp}$ against $\omega_{\perp}$ . For values of $E_F/\hbar\omega_{\perp} > 1$ the system is 3D, below that it becomes effectively 1D. Figures are reproduced from [11]. . . . .	11
2.1	The two main loss channels during light assisted collisions. The fine-structure changing collision (a) and the radiative escape (b). During a fine-structure changing collision two ground state atoms approach until they reach $R_0$ , where one of them absorbs a photon (1). On the attractive molecular potential the atoms are accelerated towards each other (2). At the crossing of the $S + P_{3/2}$ and $S + P_{1/2}$ molecular state a fine-structure change is possible. The colliding pair leaves in the $S + P_{1/2}$ state (3) with an excess energy of a fine-structure splitting. In case of radiative escape (RE) the colliding atoms also reach $R_0$ where they absorb a photon $\hbar\omega$ and are subsequently transferred to $S + P_{3/2}$ state (1). During the collision the excited atom can decay back into its ground state $S$ , hereby emitting a photon $\hbar\omega'$ (2). As $\hbar\omega' < \hbar\omega$ the pair of ground state atoms shares this excess energy (3). . . . .	15
4.1	The Li laser system, taken from [12]. The telescopes for the Rb light are also shown in the lower right hand side. . . . .	30
4.2	Spectroscopy layout for the Li laser lock. The AOM is used to shift the laser with respect to the spectroscopy line. Taken from [12]. Details of the spectroscopy cell may be found in [13] . . . . .	31
4.3	(a) Lithium spectroscopy showing the $^7\text{Li}$ D2 line. (b) Lithium spectroscopy showing the $^7\text{Li}$ D1 . Both plots taken from [12]. See table 4.1 for the corresponding transitions. . . . .	31

4.4	The Laser lock scheme for the ${}^6\text{Li}$ experiments. The laser is locked to the (K) line. As the spectroscopy –AOM shifts the spectroscopy by 105MHz, the main laser emission is at the (laser) line. Cooler and repumper are shifted by -161MHz and +70MHz, respectively. For the slowing beam both lines are shifted by an additional -96MHz. . . . .	31
5.1	Layout of the Rb cooler. The glass plate in this spectroscopy is 4mm–thick. This results in two parallel beams of which one is used for the spectroscopy signal and the other one for the APD and error signal . . .	34
5.2	Master-Slave layout for the rubidium repumper. The master is stabilised to a Rb spectroscopy and used to seed the slave laser. . . . .	34
6.1	Optical Layout of the potassium laser system. The fiber is used as the beatline between cooler and repumper. . . . .	36
6.2	Picture of the front part of the heated potassium spectroscopy cell. The heating ribbon, thermal insulation and cold spot are shown. . . . .	37
6.3	Error signal amplitude versus temperature of the potassium vapour cell. The peak was found at $42^\circ\text{C}$ . . . . .	37
6.4	Potassium Spectroscopy and lock scheme. The repumper is locked to the ${}^{39}\text{K}$ $F = 2 \rightarrow F'$ transition. Arrows indicate atomic transitions and fractional numbers refer to transitions of ${}^{40}\text{K}$ . Frequencies are either atomic values or according to an detuning $\Delta\nu$ of 30MHz. . . . .	38
6.5	Spectroscopy and error signal from the potassium repumper. Y-scale is in mV and for the error signal x-scale are freq in MHz and the spectroscopy is scaled by a factor of 20 in y direction. . . . .	39
6.6	The beatnote from the cooler and repumper. The sidebands of the repumper laser are visible at a distance of $\pm 21.4\text{MHz}$ from the carrier. There is a quadratic fit (red/dashed) to the central line which gives a FWHM of 1.15 MHz; this gives an individual linewidth of 812 kHz for each laser. . . . .	40
6.7	Potassium spectroscopy and error signal for the cooler. . . . .	41
6.8	The region around the lock point for the cooler. The spectroscopy signal(green/dashed) and the error signal are shown. The rising edge around the zero-crossing at $\sim 950\text{MHz}$ is currently the the lock-point for the cooler. . . . .	41
6.9	Functional block diagram of all components for the FO–lock. The signal from the APD is mixed down with the local oscillator. The FO–card generates an errorsignal which is used for feedback onto the laser via the PI–card. . . . .	42
6.10	Functional block diagram of all components within the local oscillator. .	43
6.11	Local oscillator trace pattern. According to this pattern the counters are expecting a larger or smaller frequency as a next point on the sweep. . . . .	43
6.12	VCO user interface. <i>Fixed</i> mode in the top figure and <i>Ramped</i> mode below. . . . .	44
7.1	Vacuum-chamber front view, not to scale [12]. . . . .	47



7.2	Vacuum-chamber top view, not to scale [12]. . . . .	48
7.3	(a) A typical single-shot trace from the number detection of Rb atoms. The amplitude $\delta V$ is extracted and converted into the actual photocurrent, which can in turn be converted into the number of atoms. (b) A typical fluorescence image of the Rb MOT, where the background is subtracted. These images are used to determine the width of the MOT through Gaussian fits to the cloud, (red) in the side panel plots. . . . .	51
7.4	Picture of the real experiment with MOT beams indicated, Rb beams <i>red</i> and Li light <i>yellow</i> . On the right hand side the Li oven and its electromechanical shutter is visible. The current feedthroughs from below are connected to the Rb dispenser sources. Around the central window the black heatschrink insulated MOT coil is also visible. . . . .	52
7.5	Experiment timing sequence for the dual-MOT experiment [12]. The experiments starts by loading the Rb atoms until a steady-state atom number is reached $\sim 20$ s. At this point, the fluorescence of the Rb MOT is recorded with the CCD cameras. This is followed by the loading of the Li MOT until, a steady-state atom number is also reached ( $\sim 40$ sec). At this point the number of trapped atoms is recorded for each species. After the total decay of fluorescence, background pictures for Li and Rb are taken before the Li is allowed to form a MOT again. At $\sim 65$ s, the Li-MOT has reached a steady-state and the fluorescence of the MOT is recorded with the CCD cameras. . . . .	53
7.6	A single shot Li loading curve, recorded with a photo diode. (red/dashed) The fit to the loading signal and the residuals (below) are shown. The high frequency noise does not harm the fit, as it is on a different timescale, see text. . . . .	54
7.7	Long-range molecular potentials, according to [14], for ${}^6\text{Li}$ - ${}^{87}\text{Rb}$ . The two asymptotic levels corresponding to $2^2P_{1/2} - 5^2S_{1/2}$ and $2^2P_{3/2} - 5^2S_{1/2}$ are repulsive and the two lower asymptotes, corresponding to $5^2P_{1/2} - 2^2S_{1/2}$ and $5^2P_{3/2} - 2^2S_{1/2}$ lead to attractive potentials. . . . .	54
7.8	The $\beta'_{LiRb}$ coefficient depending on the Rb laser power at a detuning of -12MHz, upper right hand graph. Also Li loading time with ( $\circ$ ) and without Rb atoms in the trap and Rb and Li densities are shown. . . . .	57
7.9	The $\beta'_{LiRb}$ coefficient depending on the Rb laser power at a detuning of -21MHz, upper right hand graph. Also Li loading time with ( $\diamond$ ) and without ( $\circ$ ) Rb atoms in the trap and Rb and Li densities are shown. . . . .	58
7.10	Supplement to figure 7.8. For a detuning of -12MHz these graphs show the number of atoms for Li and Rb and sizes and positions from the data analysis, where sizes and positions are measured in mm. The errorbars visualise the size of the clouds. . . . .	60
7.11	Supplement to figure 7.9. For a detuning of -21MHz these graphs show the number of atoms for Li and Rb and the sizes and positions from the data analysis, where sizes and positions are measured in mm. The errorbars visualise the size of the clouds. . . . .	61

7.12	Dependence of the loadingtime for Li and Rb on the Rb cooler detuning. Densities and the inelastic loss rate coefficient $\beta'_{LiRb}$ are shown. . . . .	62
7.13	Supplement to figure 7.12. Atom-numbers, sizes and positions from the data analysis, dimensions in mm. The errorbars visualise the size of the clouds. . . . .	65
7.14	Head of the atom chip holder. The marks "U" and "Z" depict the ports used for the U-MOT and Z-trap respectively. Dimensions are given in mm. . . . .	66
8.1	(blue) A cloud of atoms inside a Focus with waist $\omega_0$ . (red) A cloud extending out of the focus will blur the image, as the part not within the depth of field is defocused. . . . .	74
9.1	The atom chip and mirror-MOT beams, the starting point of all design considerations. The MOT is operated below the centre of the atom chip and the size of the MOT-beams is $1''$ . This leads to an atom chip with the dimensions of $29\text{mm} \times 32.5\text{mm}$ . The distance of the MOT to the edge of the atom chip is $14.5\text{mm}$ and $13.25\text{mm}$ , respectively. . . . .	78
9.2	First layout of the science chamber. The deformation is scaled by a factor of 1200. The colour map indicates increasing von Mises stress from blue to red. The whole upper half arc of the sealing surface is giving way due to the high load. . . . .	80
9.3	Stress distribution in the test piece. The piece is clamped at the back face and loaded at the front face with a force of $1000\text{N}$ perpendicular to the x-z-plane. The upper half of the pice experiences tension, whereas the bottom half experiences compression forces. This results in a central part where neither tension nor compression occurs. The colour map indicates increasing stress blue to red. . . . .	81
9.4	The whole vacuum assembly. Lower-MOT, science chamber, pump chamber and chip mounting. . . . .	81
9.5	The whole experiment setup including vacuum, mounting, bias and compensation coils, table and optics boards. Optics and light beams have been omitted for clarity. . . . .	82
9.6	Final version of the science chamber (a) and the deformation and von Mises stress distribution (b). assembly in the clean-room environment. . . . .	83
9.7	Science chamber after assembly in the clean-room environment. . . . .	84
9.8	The lower MOT cell during initial assembly. The CF-40 and CF-16 Viewports and the bellow to the ion pump are clearly visible. Also the threaded rods for the mirror mounts can be seen. The all-metal valve is now replaced by a viewport. . . . .	86
9.9	Optics layout of the two six-beam MOTs in the lower chamber. The cooling and repumping light for both species is superimposed at the other end of the fiber. It should be kept in mind that the beams are mutually perpendicular. All steering mirrors are summarised in the <i>beamlift</i> . . . . .	87

9.10	Chip layout and imaging light. Imaging light enters from the left hand side at an angle of $2^\circ$ (light-gray). The atoms (red) cast shadows from the direct and the reflected (dashed) light. No etchings in the gold are along the direct path of the incoming light to the atoms and on the path of the shadows. . . . .	88
9.11	Calculated rms spot size vs. tilt angle $\phi$ of the vacuum window. . . . .	89
9.12	The effect of a tilted 10mm thick glass window on the spot size of the imaging system is studied for different angles of tilt $\phi$ , (a)-(h). (top) Layout of the current lens system. (below) Zemax calculations of the spot size for different angles of tilt. For this calculation a plane wavefront enters the lens system from the left and the size of the focus is calculated. Scalebars in $\mu\text{m}$ . See [15] . . . . .	91
9.13	Optics-layout for the mirror MOT and the longitudinal absorption imaging. Mirrors and additional beam steering are omitted for clarity. Note that the imaging light will be circular polarised in this layout. This has to be taken into account in the image analysis, as the Clebsch-Gordan coefficients are different compared to the usually used linear polarisation.	92
9.14	(a) Assembled and mounted copper and Shapal parts and (b) before assembly. (c) The mounting head before bonding. The different layer are labelled: atom chip, Kapton foil and Cu structure. Note: the three elements of the copper structure are electrically disconnected. . . . .	93
9.15	(a) Overview of the current chip design and (b) close up of the central region. Note, that (b) is rotated by $90^\circ$ . The size of the whole chip (a) is $29\text{mm} \times 32.5\text{mm}$ and the width of the large wires (yellow) in (b) is $100\mu\text{m}$ .	94
9.16	First oval coil directly after the mould was removed. The Kapton insulated wire and the white epoxy are clearly visible. At this coil the wire enters the inside of the coil at "9 o'clock". in contrast, the wire enters the inside of the the X-bias coils at "12 o'clock". . . . .	96
9.17	Coils mounted to the chamber. The green epoxy-parts of the coil mounts are clearly visible. . . . .	96
9.18	Vacuum setup with bias-field coils. Connections for power and cooling to the coils are omitted for clarity. . . . .	97
9.19	Amplitude and phase dependence on the frequency for the coil, power supply and feedback loop. . . . .	98
9.20	Layout of the feedback loop used for stabilising the intensity after the optical fibers. The light (red) enters the AOM from the right and is afterwards fibercoupled. At a glass plate a fraction of 5% is taken out and detected with a photodiode. The deviation from the set point is inverted and the PI regulator used for feedback onto the AM input of the AOM driver. . . . .	99
9.21	An Artist's impression on the Li slower design. Solwer (large cone) and oven (box) are shown. The length of the slower is 400mm. . . . .	100
10.1	Two mounted NiCr boats as K dispenser. The white ceramic separator assure that the dispensers are not touching the vacuum chamber. . . .	102

10.2	The number of $^{40}\text{K}$ atoms in the MOT depending on the current through the dispenser source [16]. . . . .	103
12.1	Illustrated potentials for the proposed experiment; (red) corresponds to the potential for the fermions, (black) to the potential for the bosons. (a) static 1D traps for bosons and fermions. (b) asymmetric splitting for the Fermi cloud (c) symmetric splitting for the bosons. (blue-dot) a pictorial representation of the Bose gas and (red-dot) a representation of the Fermi gas. . . . .	110
A.1	Flange for the two large viewports at the science chamber. . . . .	116
A.2	Flange for the small viewport below the atom chip. . . . .	117
A.3	Flange for the two viewports on the thin side of the science chamber. The four holes for the 60mm-cage system are also visible. . . . .	118
A.4	Overview of the outside of the science chamber from all orthogonal projections. . . . .	119
A.5	Section through the science chamber parallel to the wide side and through the centre. . . . .	120
A.6	Section through the science chamber parallel to the thin side and through the centre. Also a detailed design of the groove for the HNV200 seal is shown. . . . .	121
A.7	Section through the science chamber orthogonal to the wide side and through a point above the large window. . . . .	122
A.8	Section through the science chamber parallel to the thin side and through the centre. Dimensions for the large windows are shown. . . . .	123
A.9	Overview of the science chamber and angles indicated for the DN 16 CF connections. . . . .	124
A.10	Section through the science chamber orthogonal to the wide side and through a point at the top, where the rim for the welding is shown. . . . .	125
A.11	Dimensions for the bolts for the large and small windows. . . . .	126
A.12	The CF 200 flange where the science chamber is welded in. This flange assures a tight connection to the pumping chamber. . . . .	128
A.13	Holder for lower-MOT precision mount. Angle and height is freely adjustable. The figure shows the clamp, which is attached to the CF-40 Ports of the lower-MOT. . . . .	130
A.14	Holder for lower-MOT precision mount. This Al-piece connects the two long bars, to which the two clamps are connected. . . . .	131
A.15	Holder for lower-MOT precision mount. These bars are vertically upwards and hold the clamps in place. The angle of the clamp is adjustable due to the circular-elongated-holes. . . . .	132
B.1	A broken window after a bakeout at $125^\circ\text{C}$ . The crack along the top-half of the window is clearly visible. . . . .	133
C.1	optics board L1 no1 . . . . .	136
C.2	optics board L1 no2 . . . . .	137

C.3	optics board L1 no3 . . . . .	138
C.4	optics board L2 no4 . . . . .	139
C.5	optics board L2 no5 . . . . .	140
C.6	optics board L2 no6 . . . . .	141
D.1	Atomic Level Scheme for $^{39}\text{K}$ and $^{40}\text{K}$ . . . . .	144
D.2	Atomic level scheme for $^{87}\text{Rb}$ . The transitions used are indicated. . . . .	145
E.1	The dependance of the signal-to-noise ratio on the number of atoms in the detection volume, for $\alpha = 1/10$ and $t = 35\mu\text{s}$ . . . . .	149
F.1	Changes to the FO-lock card from Heidelberg. Parts within the grey area are removed. The input is connected to the front plane plug, which is labelled <i>Photo Diode</i> . . . . .	152
F.2	Changes to the FO-lock board in detail. . . . .	153
F.3	The switch-on behaviour of the x-coils (red) and the z-coil (blue) with the charge pump. The difference in the switch on time for x and z is due to the difference in inductance. . . . .	154
F.4	The circuit diagram for the charge pump. . . . .	155
F.5	Diagram of the functional principle of the H-bridge circuit. A,B,C,D denote independent addressable switches. Current path AB and CD are used to reverse the current flow in the coil. . . . .	156
F.6	The circuit diagram for the H-bridge switch is shown. The four IGBT switches and the emptying circuits are clearly visible. . . . .	157
F.7	The circuit diagram for the driving circuits for the four IGBT gates are shown. . . . .	158
F.8	Bottom layout of the printed circuit board for the feedback circuit. . . . .	159
F.9	Top layer of the printed circuit board for the feedback circuit. . . . .	159
F.10	(a) the sensing resistor and (b) the assembled board. . . . .	160



# List of Tables

1.1	Scattering length for $^{87}\text{Rb}$ and the interspecies scattering length for the combinations $^6\text{Li}$ - $^{87}\text{Rb}$ and $^{40}\text{K}$ - $^{87}\text{Rb}$ . Where a negative sign denotes an attractive interaction. . . . .	9
2.1	Element Transition Lifetime Linewidth Reference . . . . .	24
4.1	Relative Frequencies of Transitions in $^6\text{Li}$ and $^7\text{Li}$ . . . . .	32
7.1	A summary of the values that enter equation 7.1. $\Omega$ is the solid angle, covered by the photodiode, $\alpha$ the overall detector efficiency. . . . .	49
7.2	Overview of the relevant energies for the cold collision between $^6\text{Li}$ and $^{87}\text{Rb}$ . The values for $E_{crit}$ are the maximal total energy release during a collision allowed. . . . .	55
9.1	Results of the deformation studies with the simple steel slab, see figure 9.3. All three methods agree well, at least within the order of magnitude.	81
9.2	Relevant parameters for the bias coils. . . . .	97





# **Part II**

# **Theory**



# 1 Foundations

The intention of this chapter is to remind the reader of some fundamentals which are needed later on in this work and also to represent the foundations in a way that is consistent with the formulation used in the experiment chapters. However, for detailed discussion of the underlying principles, the reader should refer to the given references.

Metcalf and van der Straten [17] give a good overview of atom-light interactions and the required techniques for trapping atoms. As the aim of this work is towards magnetic traps and atom chips in particular, this section will focus on magnetic traps and assume the reader to be familiar with the principle of a magneto-optical trap (MOT) [18]. Please note that this field earned the 1997 Nobel Prize in physics, which was shared by Steven Chu, Claude N. Cohen-Tannoudji, and William D. Phillips. A collection of the Nobel lectures may be found at: [http://nobelprize.org/nobel\\_prizes/](http://nobelprize.org/nobel_prizes/). Very briefly, a MOT uses spatially dependent resonant and near resonant scattering to cool and confine atoms. The spatial dependence is established with an inhomogeneous magnetic field, for example a quadrupole field, which causes a spatially dependent shift in the atomic resonance due to Zeeman splitting. The scattered light is typically supplied from a narrow laser source, see part III.

The MOT was a big step towards the achievement of ultracold quantum gases, either fermionic or bosonic. However, the typical phase-space density reachable in a MOT is  $\approx 10^{-8}$ , which is still lower than the desired

$$n\lambda_{deBroglie}^3 \approx 1, \quad (1.1)$$

where quantum degeneracy starts to occur. For a given number of atoms in a trap, the phase space density can be increased by reducing the temperature. A fundamental limit to this temperature is the scattering of near resonant light by the atoms in the trap. The recoil of an atom from scattered photons causes a brownian motion, which results in a finite temperature. This temperature is the Doppler temperature

$$T_D = \frac{\hbar\gamma}{2k_B}, \quad (1.2)$$

where  $\gamma$  is the linewidth of the transition used. Advanced methods, such as optical molasses (sub-dopplercooling) [19], lead to temperatures as low as  $\approx 2\mu\text{K}$  in Rb

[20], but not all the way to degeneracy. The key technology to the first Bose condensates [1, 2] was the method of evaporative cooling, see section 1.4. This method relies on the sequential removal of the hottest atoms from the trap. How atoms are removed from the trap, depends on the way atoms are trapped, i.e. how the trap is experimentally realised. In an optical trap, the intensity of the trap is lowered such that the hottest atoms can leave the trap. In the case of a magnetic trap, atoms are removed with radio-frequency (rf) or microwave (mw) fields, where trapped and untrapped states are coupled. The frequency of either rf or mw photons is tuned such that atoms with higher energies are removed from the trap.

## 1.1 Magnetic Traps

The previous section described how atoms could be cooled to the low microkelvin range with optical cooling techniques. However, in order to reach temperatures where the atomic gases enter the quantum-degenerate regime, other cooling techniques are needed, as these temperatures are approximately 100nK under typical experimental conditions. A solution to this problem is a magnetic trap for neutral atoms [21], which can trap atoms in total darkness. Advanced cooling methods (see section 1.4) allow a further cooling inside a magnetic trap deep into the quantum degenerate regime. In this section, the principle of the main work-horse in this research group will be discussed – the wire trap. In almost all experiments discussed in the upcoming sections wire-traps of some kind are employed<sup>1</sup>. Even though different technologies of wires are employed, the working principle is always the same and will be discussed below.

A neutral atom in a weak magnetic field  $B$  experiences the potential [22]

$$V_{mag} = -\boldsymbol{\mu} \cdot \mathbf{B} = g_F m_F \mu_B B \quad (1.3)$$

where  $g_F$  is the Landé factor of the atomic hyperfine state,  $m_F$  is the magnetic quantum number, and the Bohr magneton. This includes already the adiabatic approximation, which assumes that the atomic spin can follow any change of the magnetic field adiabatically. Hence, only the magnitude of the magnetic field  $B$  is important. Depending on the sign of  $m_F g_F$ , atoms are either attracted or repelled from a minimum in the potential. As magnetic minima are considerably easy to create, atoms are usually trapped in *low-field-seeking* states<sup>2</sup>.

---

<sup>1</sup>The only exception to this are the experiments described in section 7.4, which were done in a quadrupole field generated by external coils.

<sup>2</sup>High-field-seeking-state traps are experimentally hard to realise in free space, as magnetic field maxima do not exist in a source free field, hence some kind of matter is required at the position of the trap, see [23, 24].

A challenge in the design of such a trapping potential is the magnetic minimum, which should be small, but finite. If, as in a quadrupole trap, the minimum is a zero, atoms can flip into untrapped states and causes loss from the trap, these losses are called Majorana losses [25]. This is an increasing problem as the trapped atoms become colder. The colder the gas, the longer the trapped atoms spend in the region of low field; hence the probability of changing into untrapped states increases. Among other magnetic traps [26, 27], a magnetic microtrap is a solution to this problem. The principle of a magnetic microtrap is discussed in the following section.

## 1.2 Magnetic Microtraps

Here, the field generated by the a current-carrying wire and a perpendicular homogenous (bias)–field will be discussed. It is formulated in a cylindrical coordinate system, where the wire is located at the origin and oriented along the  $\hat{e}_z$  direction. The current in the wire is denoted by  $I_w$  and generates a magnetic field as:

$$\mathbf{B}_w = \frac{\mu_0 I_w}{2\pi r} \hat{e}_\varphi, \quad (1.4)$$

whereas the bias field is denoted by  $\mathbf{B}_b$ . At the distance  $r_0$ , the bias field will cancel the field generated by the wire, i.e.

$$r_0 = \frac{\mu_0 I_w}{2\pi B_b}. \quad (1.5)$$

The field around this zero point is, in a plane orthogonal to the wire, a two-dimensional quadrupole field. In three dimensions, this looks like a tube parallel to the wire at the distance  $r_0$ . The depth of such a trap is determined by the magnitude bias–field  $B_b$ , as the barrier to the wire is infinitely high, due to the  $1/r$  behaviour of the wire field. The magnetic field gradient around the minimum of the guide, is given by:

$$\left. \frac{dB}{dr} \right|_{r_0} = \frac{2\pi B_b^2}{\mu_0 I_w} = \frac{B_b}{r_0}. \quad (1.6)$$

A homogeneous field, parallel to the wire, added, a so-called Ioffe–Pritchard field, results in a closed trap, which has a curvature and trap frequency of:

$$\left. \frac{d^2 B}{dr^2} \right|_{r_0} = \frac{4\pi^2 B_b^4}{\mu_0^2 B_{IP} I_w^2} = \frac{B_b^2}{r_0^2 B_{IP}} \quad \text{and} \quad (1.7)$$

$$\omega = \sqrt{\frac{\mu_B g_F m_F}{m} \frac{d^2 B}{dr^2}} \quad (1.8)$$

$$\omega \propto \frac{B_b}{r_0} \sqrt{\frac{1}{m B_{IP}}} \quad (1.9)$$

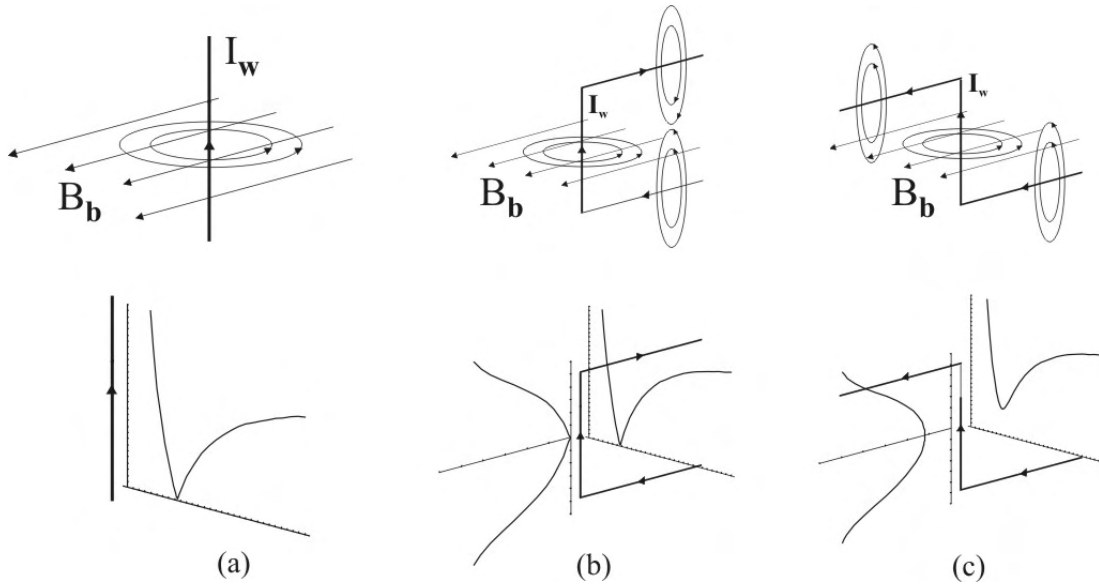


Figure 1.1: Current carrying wires and superimposed homogeneous magnetic fields cause (a) a sideguide, (b) a U-trap and (c) a Z-trap. The U-trap is an elongated quadrupole trap and can be used to operate a MOT and the Z-trap serves as a Ioffe-trap with a finite trap bottom. The top row shows a sketch of the traps and field geometries, whereas the bottom row shows the field along and orthogonal to the wires.

This particular shape of elongated trap with a finite trap bottom is called a Ioffe-Pritchard trap, following experimental results with a large scale magnetic trap of similar shape [26]. There is a way to design a wire trap that it needs one wire with a certain current and a bias-field to generate a trapping potential with a finite minimum. Within this work, two types of wire trap are used:

- The *Z-trap* is a wire configuration where the current carrying wire is bent in a planar Z shape (see figure 1.1 (c)). Parallel to the central bar of the Z, one finds a quadrupole guide, as in the side-guide situation discussed above. Due to the field generated by the top and bottom of the Z, one gets an additional field along the central bar of the Z, which is of the IP-type.
- The *U-trap* is created by bending the side guide in a planar U (see figure 1.1 (b)). The fields from the current carrying sides of the U point in opposite directions, which leads to a three dimensional quadrupole type field. The field configuration of such a trap is not ideal with a thin wire, but can be improved by enlarging the central bar of the U wire [28].

All statements about magnetic traps hold for any size of the trapping geometry, whether the wire dimensions are of the order of centimetres or as small as some 100 nanometers. Due to the  $1/r$  scaling of the wire-field, the wire traps are

ideally suited for miniaturisation. To illustrate the power of miniaturised wires, the scaling laws for these traps are summarised:

$$\diamond \text{ depth of the potential } B_b \propto \frac{I}{r_0} \quad (1.10)$$

$$\diamond \text{ gradient } \frac{\partial B}{\partial r} \propto \frac{I}{r_0^2} \quad (1.11)$$

$$\diamond \text{ trap frequency } \omega_{\text{trap}} \propto \sqrt{\frac{\partial^2 B}{\partial r^2}} \propto \frac{I}{r_0^2} \quad (1.12)$$

It should be noted that above discussion assumes infinitely thin wires. In a real wire, a current density according to the geometry of the wire will form the magnetic field. Usually, the field will not diverge as  $1/r$  towards the wire, but will deviate from the  $1/r$  behaviour at distances smaller than half the wire width. This will limit the maximal trap frequency and barrier towards the wire.

## 1.3 Mirror MOT

The scaling-laws of wire traps were introduced earlier, see section 1.2. To be able to fully exploit these scaling-laws, it is desired to bring the atoms close to, possibly thin, wires. As such wires are usually<sup>3</sup> opaque to light, an intrinsic incompatibility with a standard six-beam MOT occurs. As a solution to this problem a so-called mirror-MOT has been introduced [30, 31]. The advantage of a mirror-MOT is that the mirror reduces the required solid angle for optical access to the trap volume from  $4\pi$  to  $2\pi$ , which can be seen in figure 9.1. The important point is the fact that the helicity of circularly polarised light changes its sign upon reflection from a gold-surface. As can be seen in figure 1.2, at the centre of the trap it appears as though light would arrive from three mutually perpendicular directions towards the trap center. As a horizontal orientation of the atom chip is desired for reasons of symmetry with regard to the direction of gravity, the orientation of the quadrupole field has to be rotated by  $45^\circ$ . This can be done by rotating the quadrupole field coils by  $45^\circ$  or by employing a U-MOT [28]. The atom chip is usually facing down, as this allows for time-of-flight diagnostics. This method uses the free expansion of trapped atoms to map momentum distributions into spatial distributions, which then can be imaged [32].

---

<sup>3</sup>It is interesting to note that atoms have been successfully trapped with transparent atom chips [29]. This is possible due to permanent-magnetic substrates which are transparent.

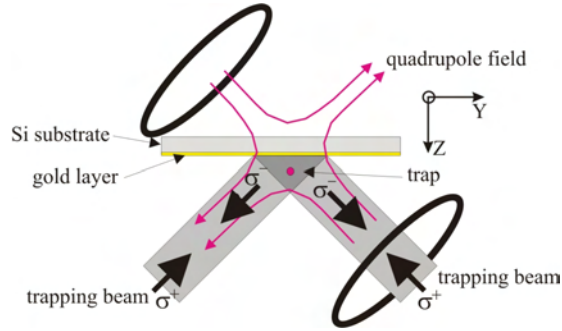


Figure 1.2: Working principle of a mirror-MOT. The light is reflected off the surface of the atom chip and changes its helicity. At the position of the MOT, this reflected light appears to come from behind the surface and so a "virtual" six-beam MOT is realised.

## 1.4 Evaporative and Sympathetic Cooling

Phase space densities that are reachable in MOTs are not high enough to enter the degenerate regime. The path to quantum degenerate gases was finally opened by the technique of evaporative cooling [33, 34, 35]. From the thermal distribution<sup>4</sup> of the trapped gas, a high-energy fraction is removed. Following this removal, the remaining gas is allowed to rethermalise due to elastic collisions. On average the gas needs  $\sim 2.7$  elastic collisions per atom to redistribute the energy [36]. Only elastic collisions assure this rethermalisation, as inelastic collisions lead to a loss from the trap, as discussed in section 2. The cross section for such an elastic collision is in the case of identical bosons in the limit of pure s-wave scattering

$$\sigma = 8\pi a^2 \quad (1.13)$$

where  $a$  is the scattering length. In the case of non identical particles the cross section is

$$\sigma = 4\pi a^2 . \quad (1.14)$$

A detailed derivation of these two cross sections can be found in [37]. The scattering length is effectively only the s-wave scattering length, as the higher partial waves have no significant contribution at these temperatures [38]. Table 1.1 is a list of scattering lengths, relevant to this work.

It should be noted that the s-wave scattering between fermions in the same state is not allowed. This scattering can only occur for two atoms in the same state, as this is forbidden for fermions due to the Pauli principle, s-wave scattering does not occur, see further below for details.

Due to inelastic collisions and collisions with the thermal background gas in

<sup>4</sup>It is safe to assume a Maxwell-Boltzmann distribution [34].



Atom(s)	a[ $a_0$ ]	Ref.
$^{87}\text{Rb}$	98.98	[39]
$^6\text{Li}-^{87}\text{Rb}$	20	[40]
$^{40}\text{K}-^{87}\text{Rb}$	-215	[41]

Table 1.1: Scattering length for  $^{87}\text{Rb}$  and the interspecies scattering length for the combinations  $^6\text{Li}-^{87}\text{Rb}$  and  $^{40}\text{K}-^{87}\text{Rb}$ . Where a negative sign denotes an attractive interaction.

the trap region atoms can leave the trap. These atoms do not contribute to the cooling as they are not selectively removed. For evaporative cooling it is therefore necessary to cool faster than the loss processes. However, the evaporation speed is limited as the gas needs to rethermalise before the high-energy tail can be removed again. If atoms are removed before the energy is redistributed within the gas, they do not contribute to the cooling. It is convenient to define  $\mathfrak{R}$  as the ratio between good and bad collisions

$$\mathfrak{R} = \frac{\Gamma_{elastic}}{\Gamma_{loss}} . \quad (1.15)$$

The average elastic scattering rate  $\Gamma_{elastic}$  depends on the relative velocity of the atoms [17],

$$\Gamma_{elastic} = \frac{4n\sigma\bar{v}}{\sqrt{3\pi}} \quad (1.16)$$

with  $\bar{v} = \sqrt{\frac{8k_B T}{m\pi}}$  the average velocity at a given temperature and  $n$  the density of the atoms. The inelastic rate is composed of three components; collisions with the background gas, inelastic two-body collisions and three-body recombinations. The collisions with the background gas scale with the absolute number of atoms  $N$ . Inelastic collisions scale generally with the density  $n$  and three-body recombinations scale with density squared  $n^2$ . For efficient cooling where the number of atoms in the degenerate regime should be maximized, a compromise between a fast cooling ramp and good thermalisation has to be found. To reduce the number of inelastic collisions and three-body recombinations it is possible to vary the confinement, which essentially tunes the density, of the atoms during the cooling process. Collisions with the background gas can only be reduced by improving the vacuum. The loss rate for collisions with the background gas  $\Gamma_{back}$  is

$$\Gamma_{back} = n_{back}\sigma_{back}\bar{v}_{back} . \quad (1.17)$$

From the ideal gas equation, the scaling of the density of the background gas can be found to be linear with the pressure,  $n_{back} = N/V = 1/(kT) \times p$ .

As mentioned before, s-wave scattering in a single-component polarised Fermi gas is forbidden due to the Pauli exclusion principle. Therefore, if it is necessary to cool a polarised Fermi gas to quantum degeneracy, direct evaporation does not work. However, a two-component Fermi gas can be cooled to quantum degeneracy using evaporative cooling [3]. To overcome this problem, Fermi gases are cooled sympathetically [42, 43]. The Fermi gas is brought into thermal equilibrium with a bath that can be cooled. This picture is true in the case of a Bose-Fermi mixture, but it should be noted, that Fermi gases have been successfully cooled in a spin mixture configuration [3]. The method of sympathetic cooling is, in principle, loss free.

## 1.5 Quantum Gases in Low Dimensions

One goal of the experiment, described below, is the study of one-dimensional degenerate quantum gases. The dimensionality of a trapped gas is important, as almost all interaction properties of the gas will change with its dimensionality. The Tonks gas is an extreme case of such a dependence, where bosons interact effectively as fermions. A collection of theory and experimental papers can be found in [44].

A Bose gas is classed as being effectively 1D when as its chemical potential ( $\mu$ ) and temperature ( $k_B T$ ) are below the transversal trap energy  $\hbar\omega_\perp$ . Figure 1.3 (a) shows the transition of a Bose gas from 3D [37] to effectively 1D [45] for different numbers of atoms in the trap and different longitudinal trap frequencies, i.e. different aspect ratios of the trap, where the aspect ratio is defined as  $\lambda = \omega_\perp/\omega_\parallel$ .

For a Fermi gas, the condition of being classified as effectively 1D is  $E_F \ll \hbar\omega_\perp$ , where  $E_F$  is the Fermi energy [45]:

$$E_F = \frac{\hbar^2(6\pi^2 n_{f(3D)})^{2/3}}{2m_f} \quad (1.18)$$

Figure 1.3 shows the transition of a Fermi gas from 3D to the effectively 1D regime in this case  $^{40}\text{K}$ . The number of fermions in the trap and the longitudinal trap frequencies are plotted. Whenever trap frequencies are mentioned, the value is given for  $^{87}\text{Rb}$ . The corresponding values for  $\text{Li}$  and  $\text{K}$  are by a factor of  $\sqrt{\frac{m_{\text{Rb}}}{m_{\text{Li}}}} \approx 3.81$  and  $\sqrt{\frac{m_{\text{Rb}}}{m_{\text{K}}}} \approx 1.47$  higher, respectively.

With the current generation of atom chips, trap frequencies in the 50kHz range and longitudinal trap frequencies  $\sim 1\text{Hz}$  are feasible, hence they are the ideal playground for experiments with 1D quantum gases.

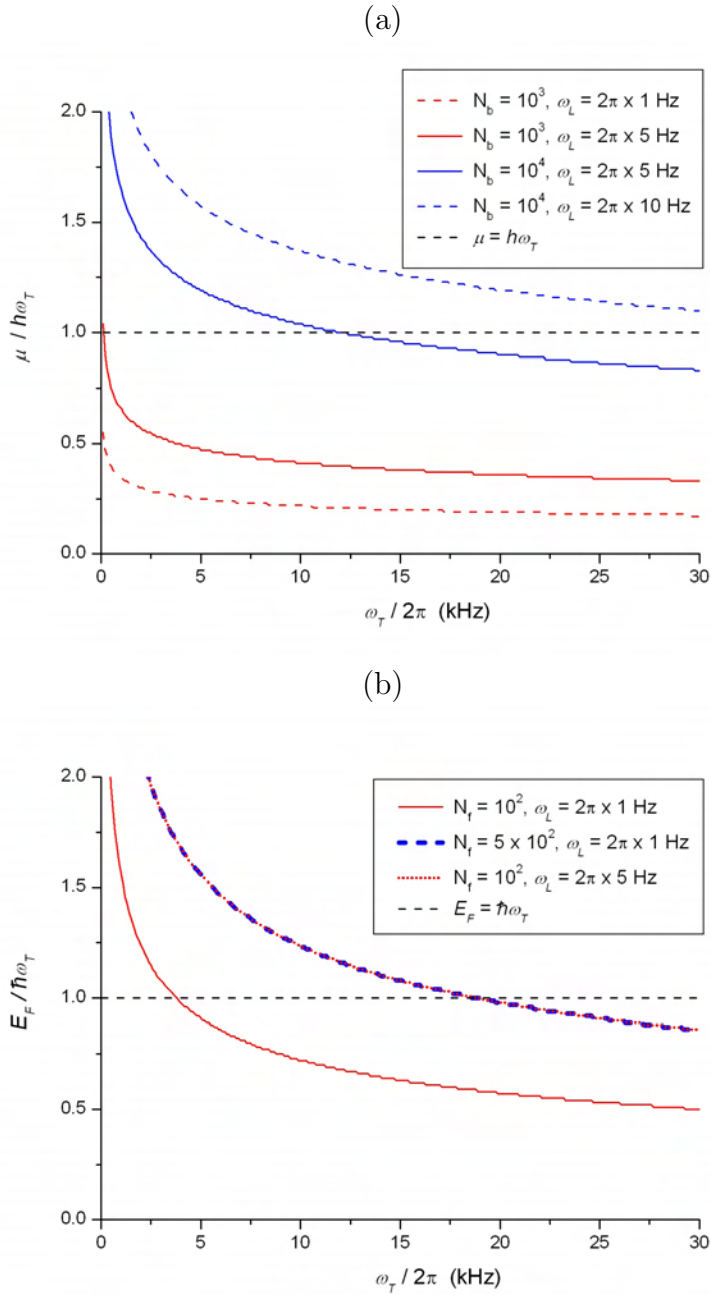


Figure 1.3: (a) Bosons: Plot of  $\mu/\hbar\omega_{\perp}$  against  $\omega_{\perp}$ . For values of  $\mu/\hbar\omega_{\perp} > 1$  the system is 3D, below that it becomes effectively 1D. (b) Fermions, in this case  $^{40}\text{K}$ : The plot shows  $E_F/\hbar\omega_{\perp}$  against  $\omega_{\perp}$ . For values of  $E_F/\hbar\omega_{\perp} > 1$  the system is 3D, below that it becomes effectively 1D. Figures are reproduced from [11].



## 2 Cold Collisions

In this section, the basic framework of cold collisions will be given. It is a discussion of low-energy collisions of neutral atoms and specifically in magneto-optical-traps (MOTs). In such a case, alkali-metal atoms usually have a temperature on the order of  $100\mu\text{K}$ . The exact temperature depends on various parameters, such as the atomic mass and the laser detuning from the atomic resonance. In this temperature regime, the atom's mean kinetic energy is on the same scale as the energy that is relevant for the cold collisions. As only low-energy collisions occur in such a cold atomic gas, it is possible to introduce some simplifications to the scattering problem. Generally, it is important to distinguish two types of scattering: elastic scattering, where energy and momentum are conserved during a scattering event, and inelastic scattering, where internal atomic energy is converted into kinetic energy of the colliding atoms. If this gain in kinetic energy is larger than the trap depth (equation 2.9), atoms can escape from the trap. In contrast, the elastic scattering preserves the atoms in the trap and is of great importance for the thermalisation of the gas, as energy is redistributed within the gas through these collisions. In the beginning of this chapter, a simple collisional model will be introduced. The second and third sections deal with inelastic and elastic scattering, respectively.

### 2.1 A Simple Collision Model

Due to the low-energy regime in which this scattering takes place, it is possible to simplify significantly the generally very complex description of two scattering atoms. The entire collision can be considered as an adiabatic one. This means that the nuclei of the colliding atoms are treated as quasi-fixed and the electron cloud adapts immediately to any change in the nucleus position. This is the Born–Oppenheimer approximation, where the electronic and nuclear motion can be treated independently, sometimes this approximation is also called the adiabatic approximation. This leads to the formation of a diatomic quasi-molecule, where the nuclei follow a molecular Born–Oppenheimer potential. Furthermore, due to the large extent of the molecule, the electron clouds do not overlap. This assumption is valid, as long as the nuclear separation is larger than the LeRoy radius [46], which is typically in the order of  $10a_0$ .

In the simplest case, the interaction potential between two colliding atoms is

given by

$$U_{eff}(R) = U(R) + \frac{\hbar^2 l(l+1)}{2\mu R^2}, \quad (2.1)$$

where the interaction potential is composed from a long range interaction potential and a centrifugal term. The interatomic separation is  $R$  and  $\mu$  is the reduced mass of the binary system. For the low energy scattering the interaction potential  $U(R)$  can be approximated by

$$U(R) = D - \sum_n \frac{C_n}{R^n}, \quad (2.2)$$

where  $D$  is the dissociation energy of the system and the series expansion  $C_n/R^n$  describes the multipole interaction<sup>1</sup> of the colliding atoms. The dispersion coefficients  $C_n$  are accessible via perturbation theory [14]. The interaction between identical atoms in two different states is governed by the resonant dipole interaction, described by a  $C_3/R^3$  potential, higher orders being neglected. In the case of different atoms the collision interaction is governed by the induced-dipole moment  $C_6/R^6$ , which is, in fact, the van-der-Waals interaction. The dispersion coefficients used in this work are taken from [14] and represent calculations for the Hund's case "c", which means that the spin-orbit interaction within each atom is taken into account for the calculation of the coefficients. An extended discussion on collisions of cold atoms may be found in [47, 17].

## 2.2 Inelastic Collisions

In the presence of resonant or near resonant light used in a MOT, atoms can collide not only in the ground state  $S + S$ , but also in excited states. A ground state atom can be combined with either the  $P_{1/2}$  or  $P_{3/2}$  fine structure level of the excited state atom. During such a collision, a photon from the MOT light can be absorbed by a colliding atom pair at a distance of  $R_0$ , which results, for example, in



The distance  $R_0$  is called the Condon Point, see [47]. The two main processes, which lead to trap loss can now be identified: the fine-structure-changing collision (FCC) and radiative escape (RE) [48]. The FCC is illustrated in figure 2.1 (a). Two atoms in the ground state approach each other (1) until one of the two

---

<sup>1</sup>For neutral atoms, static multipole moments do not usually exist. An exception is the resonant dipole interaction, which occurs in the scattering of two identical atoms in different states.

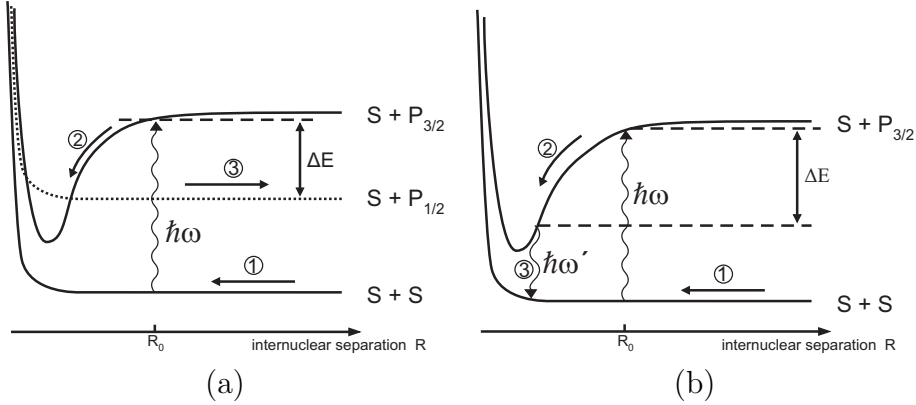
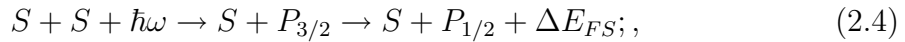


Figure 2.1: The two main loss channels during light assisted collisions. The fine-structure changing collision (a) and the radiative escape (b). During a fine-structure changing collision two ground state atoms approach until they reach  $R_0$ , where one of them absorbs a photon (1). On the attractive molecular potential the atoms are accelerated towards each other (2). At the crossing of the  $S + P_{3/2}$  and  $S + P_{1/2}$  molecular state a fine-structure change is possible. The colliding pair leaves in the  $S + P_{1/2}$  state (3) with an excess energy of a fine-structure splitting. In case of radiative escape (RE) the colliding atoms also reach  $R_0$  where they absorb a photon  $\hbar\omega$  and are subsequently transferred to  $S + P_{3/2}$  state (1). During the collision the excited atom can decay back into its ground state  $S$ , hereby emitting a photon  $\hbar\omega'$  (2). As  $\hbar\omega' < \hbar\omega$  the pair of ground state atoms shares this excess energy (3).

absorbs a photon  $\hbar\omega$  at  $R_0$  from the MOT light. The two atoms are transferred to an attractive molecular potential and, hence, accelerated towards each other (2). At a point with a shorter distance  $R < R_0$  between the atoms, the molecular potential may cross the potential (dotted) of the  $S + P_{1/2}$  long range molecule. At this point, a fine-structure change is allowed and the molecule can dissociate into  $S + P_{1/2}$  and the excess energy of the fine structure splitting. The whole process is described by



where  $\Delta E_{FS}$  is the energy of the fine-structure splitting. The excess energy is transferred to both collision partners. In the case of atoms of the same species, the energy is equally shared  $\Delta E/2$ , whereas, in the case of two different atoms, the energy is distributed according to the difference in mass,

$$E_B = \frac{m_A}{m_A + m_B} \Delta E_{FS} \quad (2.5)$$

with  $E_X$  and  $m_X$  being the energy acquired and the mass of the atom  $A$  or  $B$  respectively. For the energy of atom  $A$ , the indices  $A$  and  $B$  have to be

interchanged. In the case of  ${}^6\text{Li}$  and  ${}^{87}\text{Rb}$ , the amount of energy gained by the Rb atom is  $\sim 7\%$  of the total energy released.

The second loss process is RE, which is illustrated in figure 2.1 (b). Again, the two atoms are promoted from the ground state to an attractive long-range potential by a photon  $\hbar\omega$  from the trapping light (1). During the subsequent approach, the excited atom can decay back into the ground state by emitting a photon  $\hbar\omega'$  (3). The energy released is just the difference between the two photons and observed as kinetic energy shared by the two atoms according to equation 2.5. The RE process can be written as,

$$S + S + \hbar\omega \rightarrow S + P_{3/2} \rightarrow S + S + \hbar\omega' + \Delta E . \quad (2.6)$$

where the energy difference  $\Delta E = \hbar(\omega - \omega')$ .

After the first cold collisions were observed in a Na experiment, Gallagher and Pritchard introduced a model [49], the GP-model. The aim of this model is to quantify the two main loss processes from a MOT, the FCC and the RE, by a semi-classical model. There will be a summary of the main aspects of this model for this work, whereas a detailed discussion and more advanced models may be found in [47]. The GP-model starts with two atoms in the ground state at an internuclear distance of  $R_0$ . This pair can now absorb a photon  $\omega_L$  from the trapping laser light. The rate of molecular excitations is given by

$$R = \left[ \frac{(\Gamma_M/2)^2}{(\Delta_M)^2 + (\Gamma_M/2)^2} \right] \frac{I\lambda^2}{\hbar\omega_L 2\pi} , \quad (2.7)$$

where  $\Delta_M = \omega_L - \omega(R_0)$ ,  $\omega(R_0) = \omega_A - C_3/\hbar R_0^3$  is the resonance frequency at  $R_0$  and  $\omega_A$  is the atomic resonance frequency. The term  $\lambda^2/2\pi$  is the photoabsorption cross section, and  $I$  and  $\omega_L$  are the intensity and wavelength of the trapping laser respectively. In the particular case of two identical atoms the interaction potential will be dominated by an induced dipole interaction, hence, here the  $C_3/R^3$  dependence; for the general case there is a  $C_n/R^n$  term and, for the heteronuclear case,  $C_6/R^6$  is the leading coefficient. The term  $C_n/(\hbar R_0^n)$  represents the energy of the molecular potential at the Condon point  $R_0$ .

Afterwards the atoms are accelerated due to the attractive nature of this potential. The collision time can be approximated by the time the atoms need to reach  $R = 0$ , even though the atoms will never reach this point,

$$t = \left(\frac{m}{4}\right)^{1/2} \int_0^{R_0} \left[ \frac{C_n}{R^n} - \frac{C_n}{R_0^n} \right]^{-1/2} dR = \alpha \left( \frac{MR_0^{n+2}}{4C_n} \right)^{1/2} , \quad (2.8)$$

where  $m$  is the atomic mass and  $\alpha$  is a numeric constant which is 0.747 for the case of  $C_3/R^3$  and 0.431 for the case of  $C_6/R^6$ . This is essentially the time for a molecular pair of atoms ( $A^* + B$ ) to reach the short-range zone of the molecular



potential where FCC can take place. If the pair does not decay back into the ground state, this pair will cross the range where FCC can take place twice, on the way in and back, in a short time interval. This increases the total probability of a FCC. For the case of sodium atoms in a MOT the authors of [49] find an enhanced probability for FCC over RE by a factor of 20.

If two atoms collide and both atoms remain in the ground state during the entire collision, only elastic or hyperfine-structure changing collision (HCC) can take place. As the maximal energy released from such a collision is  $\Delta E_{HFS}$ , which is the energy of this hyperfine-structure splitting, it can usually be neglected for a MOT. However, in the absence of light, this can be a significant heating and loss mechanism.

So far, the amount of energy needed to leave the trap has not been specified. This energy is connected to the dissipative force from the MOT light that an atom experiences, as it tries to escape from the MOT region [50, 51]. Therefore, the depth of a MOT is given by

$$E = \frac{3}{2}mv_c^2, \quad (2.9)$$

where  $m$  is the mass of the atom. The capture velocity  $v_c$  is defined as

$$v_c = \sqrt{\frac{\hbar k \Gamma}{4m}} d, \quad (2.10)$$

where  $k$  is the wavenumber of the trapping light, and  $\Gamma$  and  $m$  are the natural linewidth of the atom and its mass respectively. The diameter of the MOT beam is introduced with  $d$ . The capture velocity is the maximal velocity an atom can have to be still captured and trapped by the MOT. Under typical conditions in the experiment,  $v_c = 37\text{m/s}$  for Rb and  $v_c = 151\text{m/s}$  for Li can be found.

## 2.3 Elastic Collisions

At the temperatures and densities in a cold atomic sample, the contribution of higher partial waves in a scattering event is lower the lower the temperature [38]. The main process is the s-wave scattering between identical or distinguishable atoms. In the case of identical bosons, this elastic scattering assures the thermalisation of the sample during evaporative cooling, which turned out to be the key to realisation of an atomic BEC [2]. In the case of nonidentical collision partners, such as two different spin states of the same atom or two different species, elastic scattering can be employed for sympathetic cooling [42]. On route to a DFG, sympathetic cooling is used to cool the Fermi gas with a cooling agent. In the proposed experiment, this cooling agent is a gas of bosonic rubidium atoms.

Sympathetic cooling with two different spin states of a fermionic atom has also been successfully demonstrated [3].

## 2.4 The MOT

The temporal evolution of the atom number in a MOT can be described by

$$\frac{dN}{dt} = L - \alpha N - \beta \int_V n^2 d^3r, \quad (2.11)$$

with

- $L$  the loading rate of the MOT
- $\alpha$  is the loss-rate coefficient for scattering with background gas, which consists of hot atomic vapour of untrapped atoms and other vacuum contaminants. As discussed in section 8.1, trapped atoms are lost from the trap after such a collision. This rate depends on the density of the background gas  $n_0$ , the scattering-crosssection  $\sigma$  and the mean velocity  $\bar{v}$  of the background atoms

$$\alpha = n_0 \sigma \bar{v}. \quad (2.12)$$

- $N$  the number of atoms in the MOT
- $\beta$  is the loss-rate coefficient due to inelastic collisions among the trapped atoms. The main loss channels are radiative escape, fine-structure changing collisions and hyperfine-structure changing collisions, see section 2.2.
- $n$  is the density of the trapped atoms

To take the effects of a second atomic species into account, equation 2.11 has to be extended to

$$\frac{dN_A}{dt} = L_A - \alpha_A N_A - \beta_A \int_V n_A^2 d^3r - \beta'_{AB} \int_V n_A n_B d^3r. \quad (2.13)$$

The subscripts  $A$  and  $B$  denote the different species. As equation 2.13 describes the temporal evolution of species A in the presence of species B,  $\beta_{AB}$  is the loss rate due to inelastic collisions between atoms from species A and atoms from species B. The inter species loss rate coefficient is the figure of interest.

The density distribution of trapped atoms in a MOT can be described by a Gaussian distribution function. For example, for the atoms of species A it reads

$$n_A = n_{0,A} e^{-2(r/w_A)^2} \quad (2.14)$$

Inserting this distribution into equation 2.13 gives

$$\frac{dN_A}{dt} = L_A - \left( \alpha_A + \beta'_{AB} N_B \left[ \frac{2(w_A^2 + w_B^2)}{\pi(w_A w_B)^2} \right]^{3/2} \right) N_A - \beta_A \left( \frac{4}{\pi w_A^2} \right)^{3/2} N_A^2, \quad (2.15)$$

where terms proportional to  $N_A$  and  $N_A^2$  have been collected. However, there is a difficulty with this equation. From a fit to a single-species loading transient, see figure 7.6, it is not possible to determine  $\alpha_A$  and  $\beta_A$  independently. This can only be achieved if different steady-state situations can be compared.

Fortunately, in the case of simultaneously trapped Li and Rb, there is a valid approximation, which allows the extraction of the interspecies loss coefficient from the transient loading data. As the Li MOT is entirely surrounded by the Rb cloud and  $w_{Rb} \gg w_{Li}$ , it is valid to assume that the density  $n_{Rb}$  does not change over the extend of the Li-cloud. Equation 2.13 can then be written as

$$\begin{aligned} \frac{dN_A}{dt} &= L_A - \alpha_A N_A - \beta_A f(N_A) n_A N_A - \beta'_{AB} n_B N_A \\ &= L_A - (\alpha_A - \beta_A f(N_A) n_A - \beta'_{AB} n_B) N_A \\ &= L_A - \Gamma N_A. \end{aligned} \quad (2.16)$$

Here,  $\Gamma$  is the inverse time constant of the trap loading and  $f(N_A)$  a measure of the reduced collision rate owing to the nonuniform density distribution and nonzero temperature, see [52, 53]. From a fit to the measured loading curves  $\Gamma_A$  and  $\Gamma_{AB}$ , which are defined as

$$\Gamma_A = (\alpha_A - \beta_A f(N_A) n_A) \quad (2.17)$$

$$\Gamma_{AB} = (\alpha_A - \beta_A f(N_A) n_A - \beta'_{AB} n_B), \quad (2.18)$$

$\beta'_{AB}$  can be calculated according to

$$\beta'_{AB} = \frac{\Gamma_A - \Gamma_{AB}}{n_B}. \quad (2.19)$$

It should be noted that the exact knowledge of  $f(N_A)$  is not required, as it drops out of the equation at this point. Furthermore,  $\beta'_{AB}$  depends only on quantities which are measurable in the existing experiment. Refer to section 7.2 for details on the method of detection.



# **Part III**

## **The Laser Systems**



The key demand on a laser system for an ultra-cold-atom experiment will be discussed in the beginning of this section. As the use of optical traps<sup>2</sup> is not intended, this work will focus on the requirements of cooling and detecting. A brief list of such requirements is given here:

- **Narrow linewidth:** For efficient cooling, a laser linewidth below the natural linewidth of the driven transition is sufficient - in the case of Potassium the linewidth of the  $D_2$  transition is  $2\pi \times 6.02\text{MHz}$  [55]. Refer to Table 2.1 for an overview of the employed transitions and their properties for all elements used in this work.
- Apart from the narrow linewidth, a **long-term stability** is also required. The laser system needs to stay reproducibly at a specific frequency for the time an experiment-run lasts - effectively over many hours. The frequency drift has to be much smaller than the natural linewidth of the transition. Along term stability of a fraction of the laserlinewidth is typically sufficient.
- **Sufficient power** is needed as for efficient cooling the number of scattered photons is important [17]. At resonance an atom can scatter on average  $N$

$$N \approx \frac{\Gamma}{2} \times t, \quad (2.20)$$

number of photons in a time interval  $t$ . With each scattered photon the atom gets a momentum  $\hbar k$  transferred, which is the reason for the cooling. Therefore is this intensity the minimum intensity required at the MOT region. The output of a stabilised laser also needs additional stages for preparation, such as acousto-optical modulators and optical fibers. All these stages will cause losses to the initial power. Therefore, intensities which are much larger than the saturation intensity are necessary. A detailed discussion of the intensities used will be given at the individual chapters.

- **Tuneability:** At certain points in the experiment cycle<sup>3</sup> a change in the laser frequency by several linewidths is required. Therefore, it is required that any laser system is capable of performing a frequency sweep and that it returns afterwards reproducibly to its lock point.
- **Ease of operation:** As the laser system is *only* a means to an end, it should, once it has been set up, require the least amount of attention.

Within this section a detailed discussion of the laser systems, which were built within this work, will be given. All relevant optical systems as well as electronics required will be documented in detail. If not otherwise stated, the electronics used

---

<sup>2</sup>A comprehensive review on optical dipole traps can be found in [54]

<sup>3</sup>Such a point could be a molasses cooling stage, see [17].

Element	Transition	Lifetime	Linewidth	Reference
Li	2s <sub>1/2</sub> - 2p <sub>3/2</sub>	27.10 ns	$2\pi \cdot 5.87$ MHz	[57]
Rb	5s <sub>1/2</sub> - 5p <sub>3/2</sub>	26.24 ns	$2\pi \cdot 6.07$ MHz	[58]
K	4s <sub>1/2</sub> - 4p <sub>3/2</sub>	26.45 ns	$2\pi \cdot 6.02$ MHz	[55]

Table 2.1: Element Transition Lifetime Linewidth Reference

are from the electronics workshop in Heidelberg. The design for these electronics was a joint effort between the workshop and members of this research group. The circuit diagrams in section F.1 are taken from [56] and changes to it are indicated. This chapter is organised in four parts:

- Locking Techniques
- Li Laser System
- Rb Laser System
- K Laser System



## 3 Locking Techniques

In order to achieve the above requirements it is not sufficient to have the lasers free-running, as they usually offer a free-running linewidth around 100 MHz and are very sensitive to thermal fluctuations. In the following sections the schemes employed for stabilizing the lasers to atomic transitions whilst maintaining excellent tuning properties will be explained. It is not intended to give a reference manual on different laser locking techniques; however, all the different locking techniques used in this work and a collection of references, will be given.

For any method of stabilisation an error signal is required. Suppose, a signal  $U_{act}$  is required to have a value of  $U_{set}$ . An error signal is proportional to the difference of the signal from a set point, i.e.  $U_{act} - U_{set}$ . A feedback loop, containing PI or PID regulators, is used to stabilise the system around the set point. In the following sections various methods of generating such an error signals is discussed. The error signal should be approximately linear around the lock point so that it can be used with standard feedback electronics.

### 3.1 Lock-In Method

It is desired to stabilize a laser to an atomic transition, which, for example, shows up as a peak/dip in a doppler-free saturation spectrum<sup>1</sup>, such as in figure 6.5. A derivative of such an atomic spectrum can serve as an error signal for locking, as it features a linear section around the lock point. This derivative can be obtained with a lock-in amplifier [60]. A lock-in amplifier is a device for measuring very small AC amplitudes, even in the presence of large noise amplitudes. A lock-in uses a phase sensitive detector to measure a signal at a very specific reference frequency and phase. The noise around this point is rejected. An example should illustrate the power of such a device: suppose a signal with an amplitude of 10nV should be measured. A typical amplifier with a bandwidth of 100kHz and gain 1000 can be used to amplify the signal to a measurable 10 $\mu$ V. The input noise of such an amplifier is typically  $5\text{nV}/\sqrt{\text{Hz}}$ ; in the above example this sums up to 1.6mV broadband noise ( $5\text{nV}/\sqrt{\text{Hz}} \times \sqrt{100 \times 10^3 \text{Hz}} \times 1000$ ). Hence, the signal will be obscured by noise. If the bandwidth is reduced to 10mHz, the noise contribution is 0.5 $\mu$ V, which is a factor of 20 less than the signal. Such a reduction in

---

<sup>1</sup>An overview of various spectroscopic methods can be found in [59]

bandwidth can be achieved with a lock-in amplifier<sup>2</sup>, due to the phase sensitive detector.

Usually the frequency of the laser source is modulated with a small amplitude. This can be done either directly or, as is described in chapter 4, on parts of the laser. As it is intended to work with very small modulation amplitudes, noise is a considerable factor. The bandwidth of most lock-in amplifiers is limited, hence, the modulation frequency is usually below 100 kHz. Considering just  $1/f$ -noise one can see that a modulation at some 10MHz is less likely to be noise dominated than the same modulation amplitude at 10kHz. However, the power of the lock-in method is that the signal can still be retrieved; unfortunately lock-in amplifiers are not exactly cheap.

### 3.2 Frequency-Modulation Lock

In the previous section the application of a lock-in amplifier in laser locking applications was discussed. To avoid the  $1/f$ -noise problem and the high costs of a lock-in amplifier other locking methods can be used. The lock technique commonly used throughout this research group is the FM-lock technique, which will be discussed in the following. The FM-lock technique relies on a beating signal from sidebands to the carrier frequency with the carrier frequency. This carrier frequency is the laser line<sup>3</sup> onto which sidebands are modulated. There are various ways of creating sidebands to a laser; however, throughout this work only two methods are employed: modulation of the laser current for diode lasers and through the electro-optical effect [62] for the Ti:Sa laser, see section 5. The modulated laser field can be written as

$$E(t) = E_0 e^{i(\omega_0 t + M \sin(\omega_m t))} . \quad (3.1)$$

This can be expanded using Bessel-functions,

$$E(t) = E_0 e^{i\omega_0 t} \sum_{n=-\infty}^{n=\infty} J_n(M) e^{in\omega_m t} \quad (3.2)$$

where  $J_n$  is the  $n$ -th order Bessel-function. If the modulation amplitude is small  $M < 1$ , sidebands with  $n > 1$  can be neglected. This results in  $n \in \{-1, 0, 1\}$  and hence, the carrier and two sidebands at  $\omega_o \pm \omega_m$ . If there is no absorber, such as an atomic-vapour cell, in the laser beam, the detector output will be a

---

<sup>2</sup>A detailed discussion on lock-in amplifiers is beyond the scope of this section and may be found in an application note [61] by Stanford Research Systems, Inc.

<sup>3</sup>It is assumed that the laser is operated with single frequency. Furthermore it is assumed that the linewidth of this frequency is much smaller than the distance from the central line to the sidebands.

DC signal according to the intensity of the carrier and the two sidebands. The beat signal between the sidebands is small and filtered and will not be considered in the following discussion. However, the beat signal between the carrier and its sidebands matters. In the case of no absorber there will be a beat signal from the carrier and the lower sideband at a frequency  $\omega_m$ , and at the same frequency a signal from the upper sideband and the carrier. As Bessel-functions have a point symmetry, like

$$J_{-n}(M) = n(-1)J_{+n} , \quad (3.3)$$

the beatnote of the lower and upper sidebands with the carrier are of the same frequency and amplitude, but exactly out of phase and hence, cancel. If there is an absorber in the optical path the situation changes and a beat signal will be detected. In the case of an atomic-vapour cell in the optical path, the beat signal contains all information about the absorption and dispersion of the light within this cell. This information may be retrieved from the beat signal with a phase detector. With the assumption that  $|\delta_n - \delta_{n+1}| \ll 1$ ,  $|\phi_n - \phi_{n+1}| \ll 1$ ,  $M \ll 1$  and  $J_0(M) \approx 1$ , as well as  $J_1(M) \approx M/2$ ; equation 3.2 becomes [63]

$$\begin{aligned} |E^2(t)| = E_0^2 \exp(-2\delta_0) [1 + M(\delta_{-1} - \delta_1) \cos(\omega_m t) \\ + M(\phi_{-1} + \phi_1 - 2\phi_0) \sin(\omega_m t)] . \end{aligned} \quad (3.4)$$

Here  $\delta_m$  denotes field amplitude attenuation and  $\phi_m$  the phase shift at the frequency  $\omega_m$ . Equation 3.4 contains a DC and two time-varying parts. The absorption component is  $\propto \cos(\omega_m t)$ , whereas the dispersion component is  $\propto \sin(\omega_m t)$ . With the help of a phase detector the two components can be separately recorded. The dispersive part is of particular interest, as it vanishes at resonance and has opposing signs for positive or negative deviations from the resonance frequency  $\omega_0$ . The dispersive part of the signal in equation 3.4 is used for generating the error signal. A detailed discussion of FM lock techniques can be found in [64, 65] as well as in [66, 67, 56].

### 3.3 Frequency–Offset Lock

The frequency-offset lock uses the beatnote between two lasers to fix the frequency, and optionally the phase, between the two sources. Depending on the application, the beatnote may be between some 10 MHz and several GHz. In the case of high beat frequencies, it is convenient to transfer them down into a frequency domain below 100MHz. The advantage of this strategy is that in this frequency domain reliable and comparably cheap electronic components are available. Such a transfer can be done with a mixer. A mixer shifts the input frequency to  $\nu_{in} \pm \nu_{LO}$ , where  $\nu_{LO}$  is the frequency of the local oscillator. With a low-pass filter the  $\nu_{in} - \nu_{LO}$  component is selected. In the current design,

the beatsignal  $\Delta\nu$  is mixed with a local oscillator  $\nu_{local}$  and the  $|\Delta\nu - \nu_{local}|$  component is selected with a low-pass filter. The signal is subsequently split in two equal parts and one part is delayed with a  $\sim 4\text{m}$  long coaxial cable, which results in a delay  $\tau$  of 20ns. Afterwards, the two components are compared at a phase detector, where the output is  $\cos(2\pi(\Delta\nu - \nu_{local})\tau)$ . The output of this phase detector is used as the error signal for locking. As the zero-crossings are  $1/\tau$  spaced, the laser can be locked at any frequencies corresponding to one of those crossings. By varying the time<sup>4</sup>  $\tau$  the error signal can be optimised for a large capture range<sup>5</sup> or a frequency resolution, which is determined by the steepness of the slope around the zero-crossing. By varying the frequency  $\nu_{local}$  of the local oscillator the zero-crossings can be placed on the frequency axis at will. A typical spectral plot of such a beatnote can be seen in figure 6.6. The envelope of the error signal is due to the limited bandwidth of the phase detector. The long-term frequency stability of such a lock is determined by the quality of the local oscillator. Further discussion on FO-locks and their stability may be found in [68, 69, 66, 56] and references therein.

---

<sup>4</sup>In practice, this is done by altering the length of the delay line.

<sup>5</sup>The capture range describes the maximal frequency deviation of the laser from the set point where it can still be regulated back to the set point. The steepness of the "linear" slope of the error signal around the set point defines if this capture range is broad (slowly rising error signal) or narrow (rapidly rising error signal).

## 4 Li Laser System

For the lithium experiments, laser light at 670nm was required. As a source, a ring-dye laser<sup>1</sup> was used, as it was already available in this research group. In the beginning, the dye laser was pumped by a individual DPSS-laser<sup>2</sup>, but was later pumped by the same DPSS-laser as that for the Ti:Sa used for the rubidium experiments, see section 5. For stability reasons, the laser system was kept under a flow box installed above the optical table. The dye laser provided up to 700mW with fresh dye and 5W of pumping power and degraded to  $\sim 400\text{mW}$  within 8 months of daily operation.

Due to the low abundance of  ${}^6\text{Li}$  in a Li sample of natural abundance the laser was locked to the  ${}^7\text{Li}$  transition, labelled (k) in table 4.1. The AOM in the spectroscopy layout, see figure 4.2, shifts the actual emission of the laser by 105MHz. From this point all other necessary frequencies are generated with AOMs, as can be seen in figures 4.1 and 4.4. The layout on the optical table may be found in figure 4.1. As only a single laser source was available the hyperfine splitting in the  ${}^6\text{Li}$   $\sim 800\text{MHz}$  needed to be bridged with AOMs. The large detuning of the slower light is discussed in section 7. The AOM in the spectroscopy setup is modulated with a small sinusoidal frequency of 95kHz. This modulation results in a small frequency modulation that is used to generate the error signal for locking. In this case a lock-in amplifier was used and the error signal generated as described in section 3.1.

Spectroscopic traces shown in figures 4.3 (a) and (b) and labelled according to spectroscopy data are taken from [70]. A full list of the labeled transitions may be found in table 4.1.

---

<sup>1</sup>It is a 899-21 ring-dye laser from Coherent, Inc. The used dye (product number: LD688) was obtained from Radiant Dyes. The powder was bought and mixed with the solvent EPH according to a secret recipe.

<sup>2</sup>Verdi V-10, Coherent, Inc.

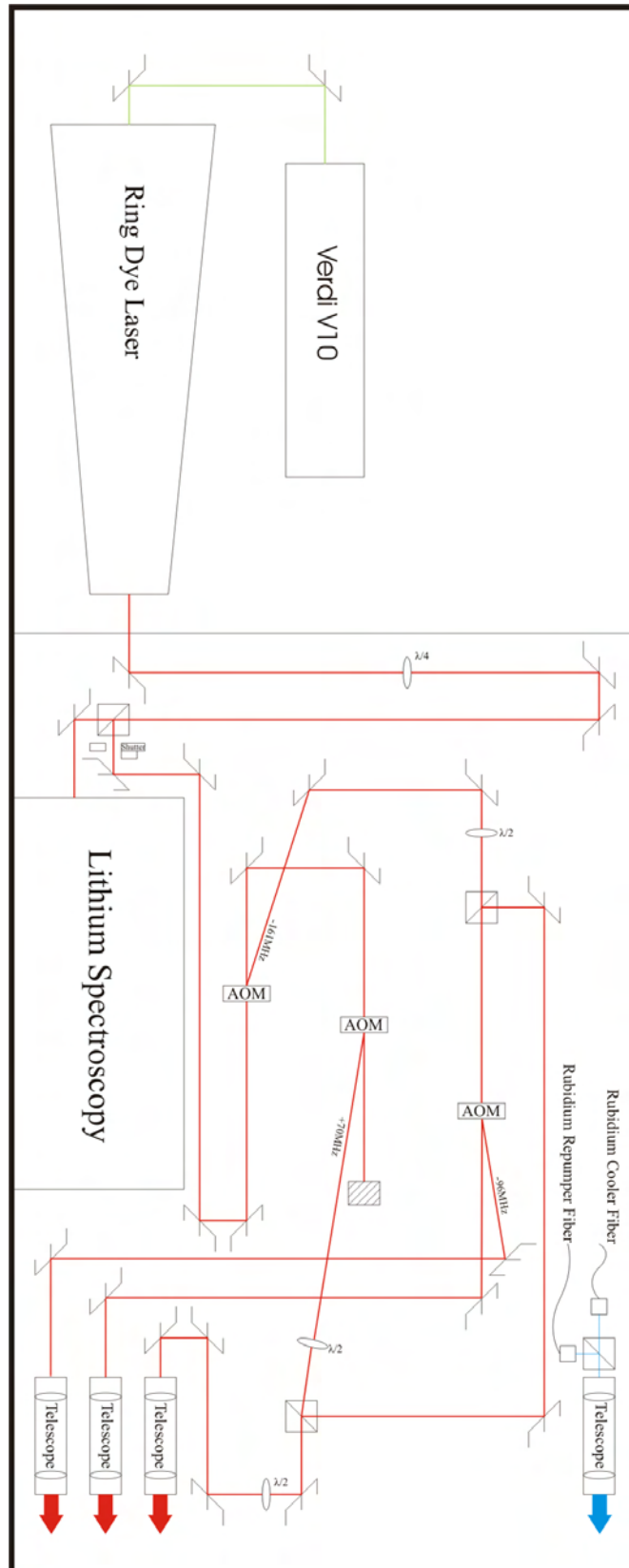


Figure 4.1: The Li laser system, taken from [12]. The telescopes for the Rb light are also shown in the lower right hand side.

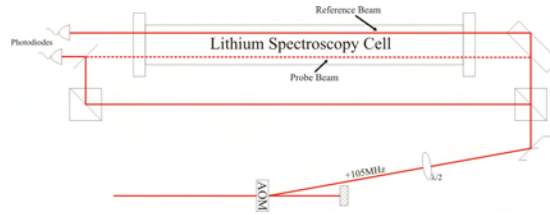


Figure 4.2: Spectroscopy layout for the Li laser lock. The AOM is used to shift the laser with respect to the spectroscopy line. Taken from [12]. Details of the spectroscopy cell may be found in [13]

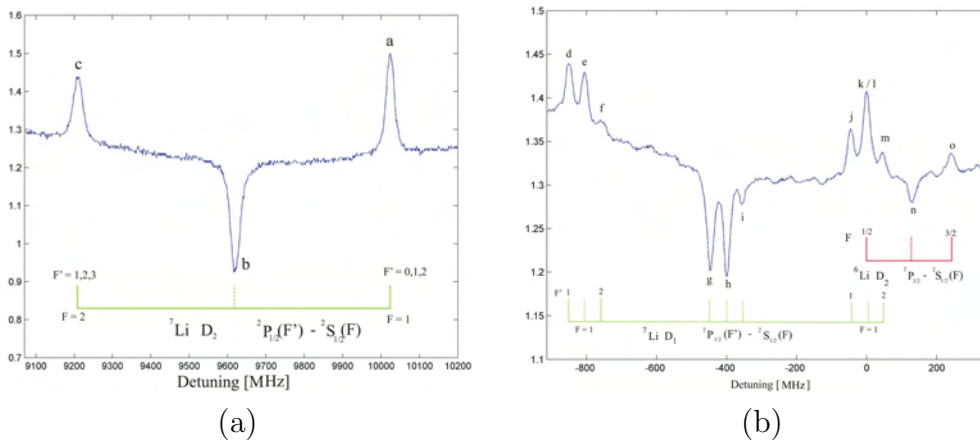


Figure 4.3: (a) Lithium spectroscopy showing the  ${}^7\text{Li } D_2$  line. (b) Lithium spectroscopy showing the  ${}^7\text{Li } D_1$  . Both plots taken from [12]. See table 4.1 for the corresponding transitions.

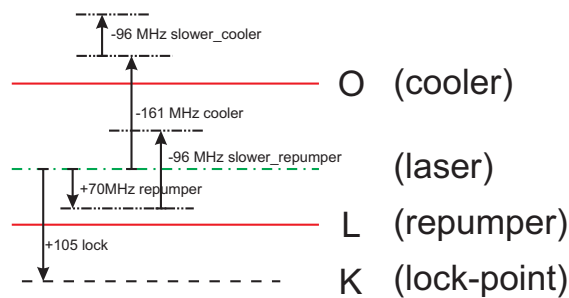


Figure 4.4: The Laser lock scheme for the  ${}^6\text{Li}$  experiments. The laser is locked to the (K) line. As the spectroscopy –AOM shifts the spectroscopy by 105MHz, the main laser emission is at the (laser) line. Cooler and repumper are shifted by -161MHz and +70MHz, respectively. For the slowing beam both lines are shifted by an additional -96MHz.

ID	Line	Transition	$F_L$	$F_U$	Rel.Freq [MHz]
a	${}^7\text{Li } D_2$	$2s^2S_{1/2} - 2p^2P_{3/2}$	1	0,1,2	10873.1
b	${}^7\text{Li } D_2$	crossover(a/c)			10468.2
c	${}^7\text{Li } D_2$	$2s^2S_{1/2} - 2p^2P_{3/2}$	2	1,2,3	10064.8
d	${}^7\text{Li } D_1$	$2s^2S_{1/2} - 2p^2P_{3/2}$	1	2	849.5
e	${}^7\text{Li } D_1$	crossover(d/f)			803.3
f	${}^7\text{Li } D_1$	$2s^2S_{1/2} - 2p^2P_{1/2}$	1	1	757.5
g	${}^7\text{Li } D_1$	crossover(d/j)			447.9
h	${}^7\text{Li } D_1$	crossover(d/m & f/j )			401.8
i	${}^7\text{Li } D_1$	crossover(f/m)			356.0
j	${}^7\text{Li } D_1$	$2s^2S_{1/2} - 2p^2P_{1/2}$	2	2	46.0
k	${}^7\text{Li } D_1$	crossover(j/m)			0.0
l	${}^6\text{Li } D_2$	$2s^2S_{1/2} - 2p^2P_{3/2}$	1/2	1/2,3/2	-15.0
m	${}^7\text{Li } D_1$	$2s^2S_{1/2} - 2p^2P_{1/2}$	2	1	-46.0
n	${}^6\text{Li } D_2$	crossover(l/o)			-129.2
o	${}^6\text{Li } D_2$	$2s^2S_{1/2} - 2p^2P_{3/2}$	3/2	1/2,3/2,5/2	-243.3

Table 4.1: Relative Frequencies of Transitions in  ${}^6\text{Li}$  and  ${}^7\text{Li}$



## 5 Rb Laser System

The purpose of this chapter is twofold. As the Rb laser system has had only minor changes during the move from Heidelberg to Vienna, the discussion given here holds for both experiments. After initial tries with an existing laser system [71, 72] and 30m-long single-mode polarisation-maintaining fibers, see figure 4.1, a dedicated laser system for this experiment was set up. This will be described in the following.

The cooling light at 780nm is generated in a Ti:Sa ring laser<sup>1</sup>. This laser is pumped with 10W from a DPSS laser<sup>2</sup> at a wavelength of 532nm. The output of the Ti:Sa is  $\sim 1.6$  W at 780.24nm and has a specified linewidth of 100kHz<sup>3</sup>. As can be seen in figure 5.1 a fraction of 5mW is passed through an EOM, before it enters the spectroscopy. Due to the phase modulation the EOM creates sidebands [62] to the light at a distance of  $\pm 21.4$ MHz, which are used for the FM-lock, as described in section 3.2. It turned out to improve the quality of the error signal, if a polariser was placed directly after the EOM.

The laser is stabilised to the  $F = 2 \rightarrow F' = 3$  crossover on the rubidium  $D_2$  line. The remaining frequency shift is achieved with AOMs, which are operated in a double-pass scheme following [73] to improve the efficiency and compactness of the setup.

The repumper used in the Heidelberg setup was a single diode laser with an output of 50mW. This extended-cavity diode laser<sup>4</sup> was built according to [71]. As in the Vienna setup more power is needed, this laser is now seeding a slave laser. In contrast to the master-slave layout described in [71], a 40dB optical isolator with a side-port was used to seed the slave laser, see figure 5.2.

---

<sup>1</sup>MBR 110, Coherent, Inc.

<sup>2</sup>Verdi V-18, Coherent, Inc.

<sup>3</sup>Judging from the spectroscopy signal, the linewidth is below 1 MHz and therefore sufficient for cooling and detection. The exact linewidth has not been measured due to the lack of a narrow reference.

<sup>4</sup>Foundations on ECDLs may be found in [74] and references therein.

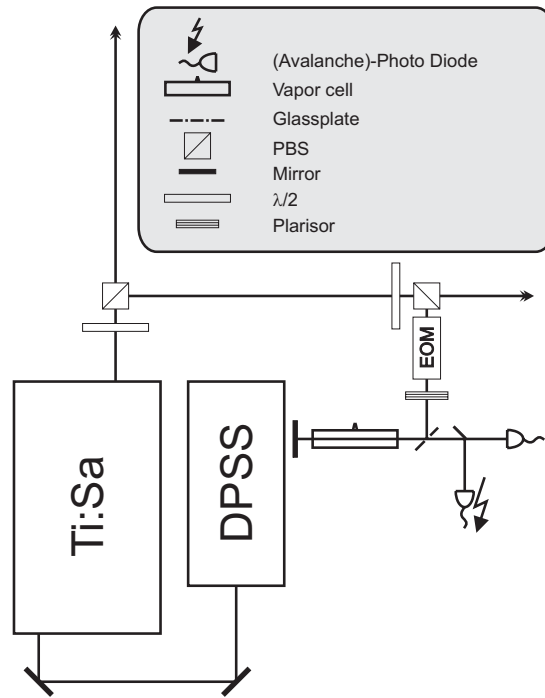


Figure 5.1: Layout of the Rb cooler. The glass plate in this spectroscopy is 4mm-thick. This results in two parallel beams of which one is used for the spectroscopy signal and the other one for the APD and error signal

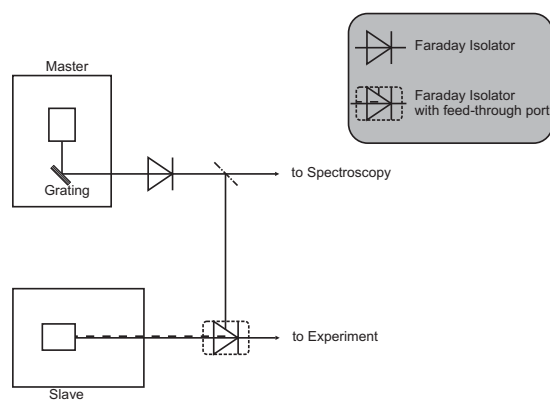


Figure 5.2: Master-Slave layout for the rubidium repumper. The master is stabilised to a Rb spectroscopy and used to seed the slave laser.

## 6 K Laser System

A schematic overview of the Potassium laser system can be found in figure 6.1. Briefly, the repump-laser<sup>1</sup> is locked to an atomic transition on the  $^{39}\text{K}$   $D2$  line and the cooling laser<sup>2</sup> is locked to the repumper via a frequency-offset lock.

As single high-power laser diodes for the 767nm transition are not available on the market, a commercial laser system was bought. The DLX110 laser [75] consists of a tapered amplifier diode, which is anti-reflection coated on the back facet. Feedback is established with a diffraction grating, where the first order is fed back into the back facet. This results in a higher power than a single laser-diode, in our case  $\sim 450\text{mW}$ , and the tuning capabilities are comparable to those of a grating stabilized laser, see, for example, [76, 71]. The atomic-vapour cells were manufactured in the glass-blowing workshop in Heidelberg. They are evacuated to  $\sim 10^{-2}\text{mbar}$  and filled with rubidium or potassium in natural abundance. Due to the difference in vapour pressure for potassium and rubidium [77, 58], the vapour cells for potassium need to be heated. In figure 6.3 the peak-to-peak amplitude of the error signal of the potassium  $F = 2 \rightarrow F'$  is plotted against the temperature of the vapour cell. An increase in the temperature, by  $20^\circ\text{C}$  results in an increase in error signal amplitude by a factor of  $\sim 4$ . Currently, the vapour cells are kept at  $42^\circ\text{C}$ . At this temperature, the error signal is sufficiently large for a stable lock and any air turbulence around the heated cell is negligibly small. With further increase in the cell temperature the cell becomes optically opaque; hence, the amplitude of the error signal decreases again. To avoid any coating of the windows of the vapour cells with potassium, a cold spot needs to be established. In the current design the cold spot is at the point where the vapour cells were filled, see figure 6.2 for a picture of a heated vapour cell.

Before the individual locks will be described in detail, it is convenient to become familiar with the overall lock scheme. In figure 6.4, a spectroscopy trace of the potassium and the resulting error signal are depicted. In fact, this trace has been taken with the repumper. The frequency scale is set to zero at the lock point of the repumper, which is the  $F = 2 \rightarrow F'$  transition in the  $^{39}\text{K}$   $D2$  line. Due to the low abundance of  $^{41}\text{K}$ , the transitions are less pronounced and only visible in the error signal. For the same reason there is no signal resolvable for  $^{40}\text{K}$ , which is naturally even less abundant. The positions of the atomic transitions

---

<sup>1</sup>This will be referred to as the repumper.

<sup>2</sup>This will be referred to as the cooler.

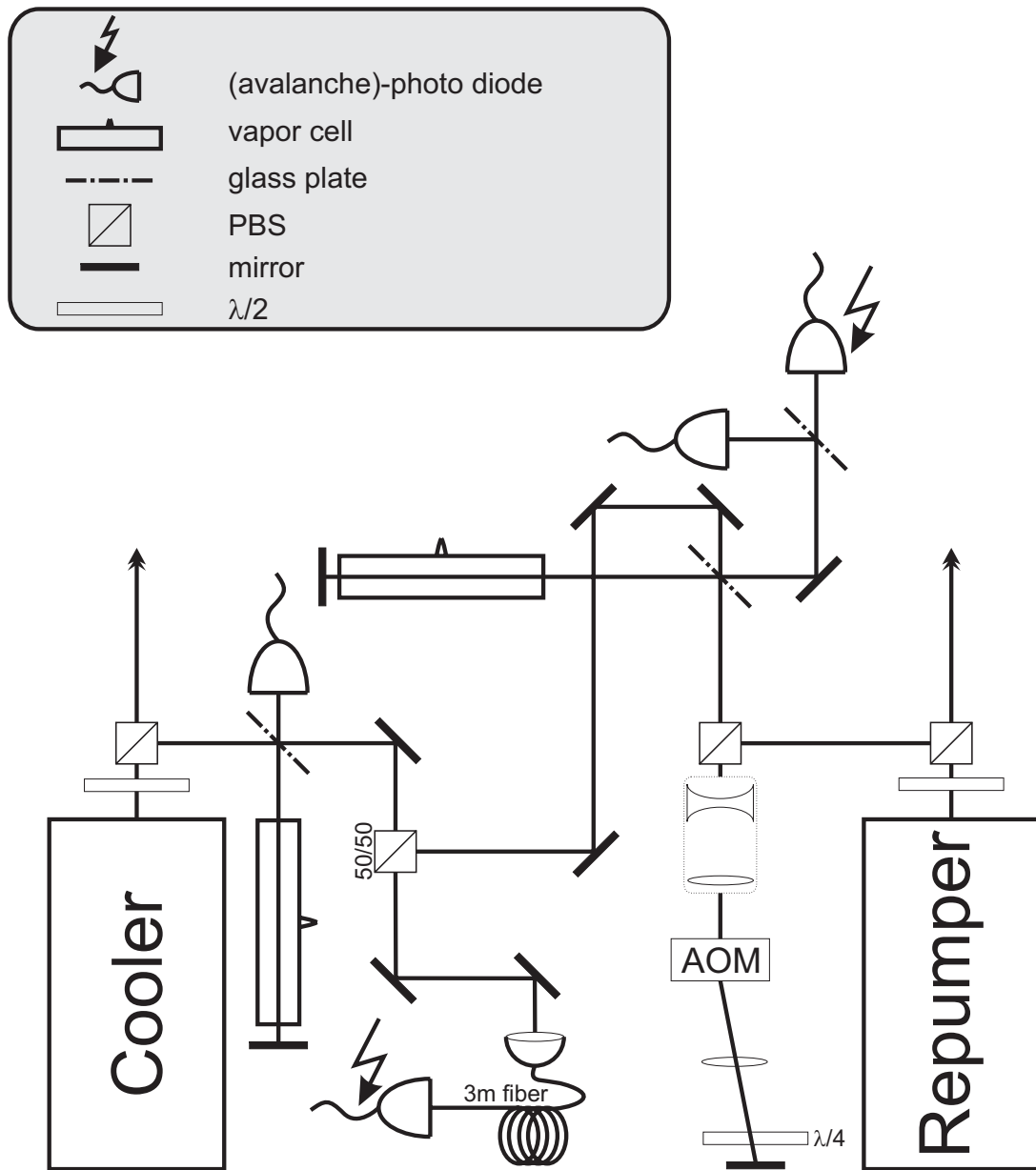


Figure 6.1: Optical Layout of the potassium laser system. The fiber is used as the beatline between cooler and repumper.

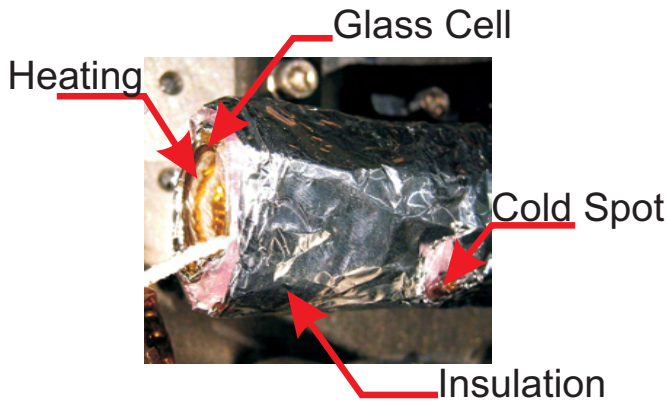


Figure 6.2: Picture of the front part of the heated potassium spectroscopy cell. The heating ribbon, thermal insulation and cold spot are shown.

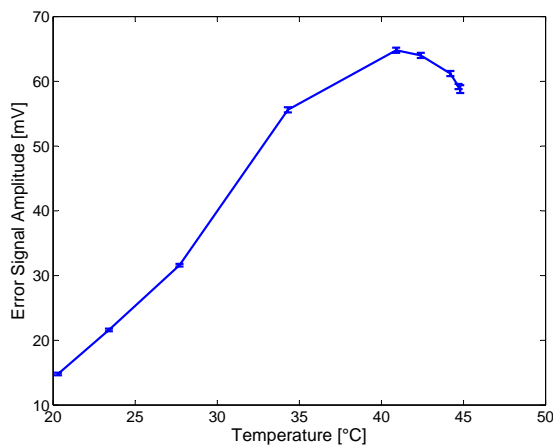


Figure 6.3: Error signal amplitude versus temperature of the potassium vapour cell. The peak was found at 42 °C

are marked with arrows in figure 6.4 and a MOT detuning  $\Delta\nu$  of 30MHz to the red side of the transition is assumed in this example. The cooler and repumper transitions are 870.2MHz and -335.6MHz, respectively, away from the lock point. The -110MHz take the AOM into account that is needed for switching the light for the lower- and science MOTs. As described below, the -335.6MHz is bridged by the AOM in the repumper spectroscopy, whereas the large 950MHz distance is covered by the FO-lock.

## 6.1 Repumper FM-Lock

It was decided to lock the repumper to an atomic transition, as less power in this beam is needed and hence, enough power for spectroscopy, double-pass AOM and FO-lock is available, see figure 6.1. As one may see in figure 6.1, some light of the repumper is taken out at the first PBS behind the laser. This light is shifted  $2 \times (-156)$  MHz by a double pass AOM setup and then used for a doppler-free saturation spectroscopy. With this method it is possible to shift the repumper within  $\pm 50$ MHz with respect to its lock point, here an atomic line of  $^{39}\text{K}$ . Furthermore, it was decided to employ the FM-lock technique, see section

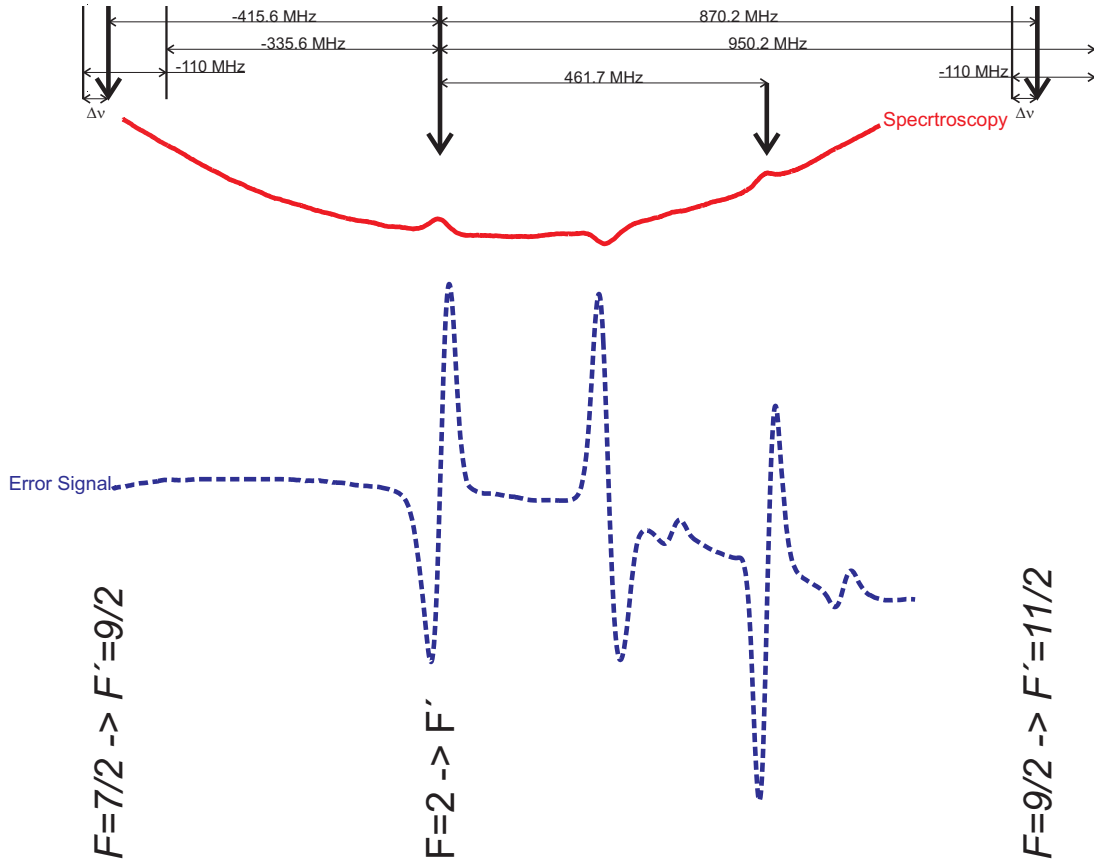


Figure 6.4: Potassium Spectroscopy and lock scheme. The repumper is locked to the  $^{39}\text{K}$   $F = 2 \rightarrow F'$  transition. Arrows indicate atomic transitions and fractional numbers refer to transitions of  $^{40}\text{K}$ . Frequencies are either atomic values or according to an detuning  $\Delta\nu$  of 30MHz.

3.2, mainly because it was found to be very stable in current and past experiments [78, 72, 56]. The sidebands<sup>3</sup> for the lock are modulated electronically via a bias-tee<sup>4</sup> at a frequency of 21.4 MHz onto the laser current. A typical spectroscopy trace can be found in figure 6.5. The error signal is fed to a PI regulator, which acts on the grating and current<sup>5</sup> of the laser diode.

<sup>3</sup>Typically there is less than 1% of the total carrier power in the sidebands.

<sup>4</sup> (Optional Bias Tee)[75]

<sup>5</sup>The signal is connected to the scan offset at the laser controller. As the scan unit employs also a feed-forward on the laser current, implicitly we also feed back to the current. The bandwidth of this input is 10kHz according to [79]

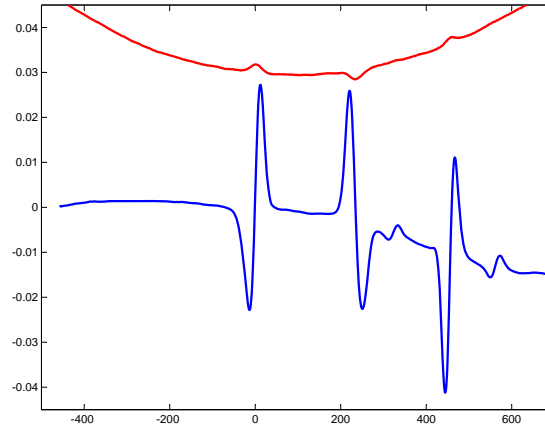


Figure 6.5: Spectroscopy and error signal from the potassium repumper. Y-scale is in mV and for the error signal x-scale are freq in MHz and the spectroscopy is scaled by a factor of 20 in y direction.

## 6.2 Cooler FO Lock

The  $^{40}\text{K}$  hyperfine splitting is 1.3 GHz. In principle, it would be possible to lock also the cooling laser directly to an atomic line as in case of the repumper. However, the loss of light for a double-pass AOM setup is not favourable. Due to the low intensities needed for a FO-lock, see section 3.3, and the easy and wide tuning possibilities, the decision was made to employ an FO-lock for the potassium cooler. Figure 6.1 shows the optical layout of this lock scheme. A block diagram showing the main electronic components of this lock setup can be found in figure 6.9. At the glass plate 5% of the light is used to perform a doppler-free saturation spectroscopy at a dedicated vapour cell, see figure 6.7. However, this spectroscopy is only used as a reference for the user and not of any use for locking. The ambient field from the optical isolator in the cooler laser, which is not more than 5cm away from the vapour cell, causes a shift of the spectroscopy by several linewidths. Therefore, this stray field is shielded with soft-iron layers next to the laser housing. The remaining fraction of the light is overlapped at a 50/50 beamsplitter cube with the repumper light. At this cube the position and the polarisations of the cooler and repumper are exactly matched and the light is afterwards coupled into a 3m-long polarisation-maintaining single-mode fiber. By doing so, the fiber turns into a 3m-long beat-line for the two lasers. As spatial overlap and polarisation are well matched, a large beatnote can be observed after the fiber, even with intensities of  $\sim 300\mu\text{W}$  after the fiber for each beam. As a beatnote around 1GHz can be expected and the beat-line is inside a fiber, also a fiber coupled photo diode<sup>6</sup> is used for detection. As the existing FO-lock cards could not handle such high frequencies, the board was slightly modified

<sup>6</sup>Thorlabs, Model SV2-FC, bandwidth >2GHz

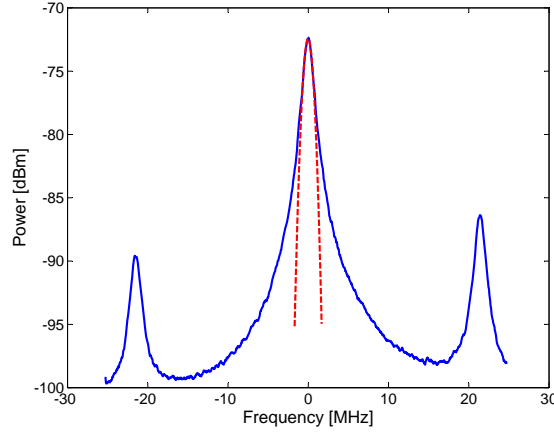


Figure 6.6: The beatnote from the cooler and repumper. The sidebands of the repumper laser are visible at a distance of  $\pm 21.4$  MHz from the carrier. There is a quadratic fit (red/dashed) to the central line which gives a FWHM of 1.15 MHz; this gives an individual linewidth of 812 kHz for each laser.

to generate the error signal. After the detector, the beat signal is amplified and mixed with a local-oscillator. This is done with independent electronics. The mixed-down beat-signal is then fed into the modified FO-lock card, see appendix F.1 for changes in the circuit. The local-oscillator design is described in detail in section 6.3. A zoomed-in view of the cooler spectroscopy and error signal can be found in figure 6.8. Following the example in figure 6.4 the lock point is at the rising edge of the error signal at  $\sim 950$  MHz. Figure 6.6 shows the beatnote of the cooler and repumper after mixing. This spectrum was taken with both lasers locked. This is possible as a directional coupler was used to couple out a -20 dB part of the mixed signal before it entered the FO-lock card. The central beatnote and the two sidebands from the repumper can be seen. The increase in amplitude with higher frequencies can be explained by the increasing gain curve of the amplifier after the photodiode. Furthermore, the quadratic fit (red/dashed) to the central peak is used to derive the width of this peak, which is, at the -3 dB point 1.15 MHz wide. Fitting a quadratic function to the line is justified as it is a Gaussian-distribution in non-log space. Assuming that the noise of the laser lines is only flicker noise, a Gaussian-distribution is a good approximation [68]. With this ansatz, the common linewidth of the two lasers is:

$$\sigma_{total}^2 = \sigma_{repumper}^2 + \sigma_{cooler}^2 . \quad (6.1)$$

Assuming that the cooler and repumper feature the same linewidth and therefore  $\sigma_{repumper} = \sigma_{cooler}$ , the individual linewidth can be derived from the measured beatnote to be 812 kHz.

As a side remark, it is interesting to note that the scan of the diode laser is not linear over a wide ( $\geq 2$  GHz) scan, as seen in figure 6.7. The scan was taken with



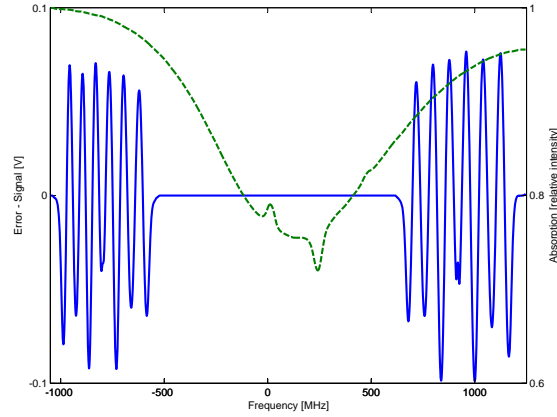


Figure 6.7: Potassium spectroscopy and error signal for the cooler.

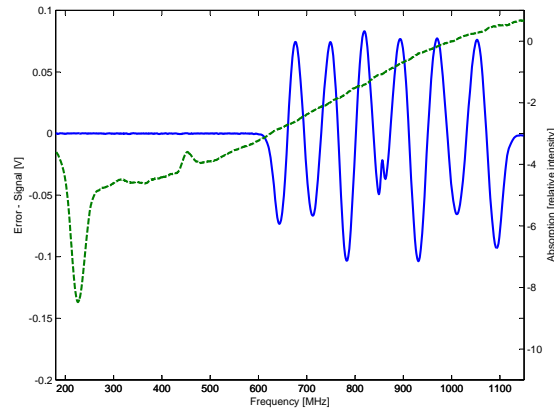


Figure 6.8: The region around the lock point for the cooler. The spectroscopy signal (green/dashed) and the error signal are shown. The rising edge around the zero-crossing at  $\sim 950$  MHz is currently the lock-point for the cooler.

a reference oscillator frequency of 856 MHz. The beatnote shows this feature at +856 MHz where the difference of cooler and repumper is 856 MHz and the mixer puts out a DC signal, which causes the signal to deviate from the expected cosine shape after the phase detector. This point should be also visible at -856 MHz, however, as can be seen in figure 6.7, it is not. This non-linearity can be accounted for by the behaviour of the piezo used inside the laser and the fact that the scan units also perform a feed-forward onto the laser current. For the experiment, this non-linearity is of no concern, as the laser is only operated in a  $\pm 100$  MHz region around the lock-point and the feedback tracks the relative frequency and not the driving signal.

As a result of this scheme, we are able to sweep the cooler laser with respect to repumper by several MHz per millisecond. This is of particular use for our atom number sweeps, as discussed in section 10.

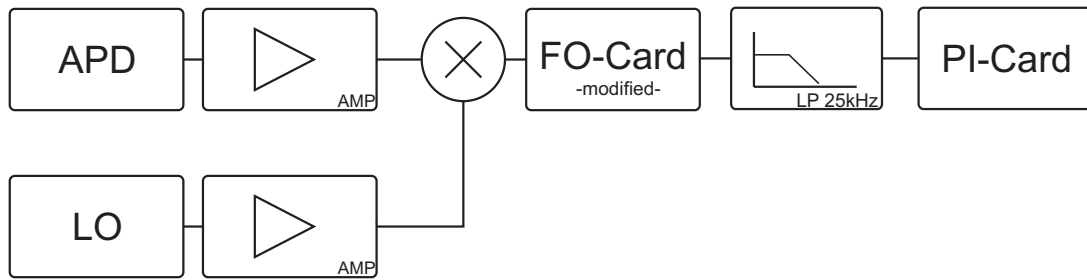


Figure 6.9: Functional block diagram of all components for the FO-lock. The signal from the APD is mixed down with the local oscillator. The FO-card generates an errorsignal which is used for feedback onto the laser via the PI-card.

### 6.3 Local Oscillator

The purpose of this section is to document the development of a local oscillator module for high frequency<sup>7</sup> laser offset locking. As commercially available frequency sources are rather expensive and in most cases lack the possibility to perform wide frequency sweeps, a dedicated device was designed, based on a PLL circuit<sup>8</sup>. With this PLL circuit, a built-in VCO is tuned such that it maintains a fixed phase relation between a reference and the output signal. In the particular case, the reference is a highly stable TCXO oscillator, which, if needed, could be replaced with an external frequency standard from an atomic clock or GPS<sup>9</sup> receiver. For a detailed description of a PLL circuit one should refer to [81, 60]. However one should be aware of the fact that one usually compares fractions of the input and output respectively at the phase detector, which makes it possible to generate a wide range of frequencies.

All components, except the reference oscillator, are incorporated in a single chip device, which can be programmed via the SPI<sup>10</sup> bus. For reasons of convenience, the starting point is the appropriate evaluation board from AD. The programming was carried out using a micro controller ( $\mu\text{C}$ )<sup>11</sup>.

After power up, the microcontroller waits for the MATLAB GUI to send data via the USB Port. As soon as this transfer is successfully terminated and all data are written to the microcontroller, the PLL is programmed to its steady state frequency, the first value in figure 6.12 for *ramped* and *fixed* mode. Furthermore, the TTL interrupt is enabled and the port set to high impedance, resulting in

<sup>7</sup>There is basically no limitation for the frequencies generated, see Analog Devices, Inc. for a list of currently available PLL circuits. Currently, frequencies from a few hundred MHz up to several GHz are available.

<sup>8</sup>ADF4360 Family from Analog Devices, Inc. [80]

<sup>9</sup>Global Positioning System. For example Hopf system

<sup>10</sup>Serial Peripheral Interface, Motorola

<sup>11</sup>Currently Atmega128 controller from Atmel are used.

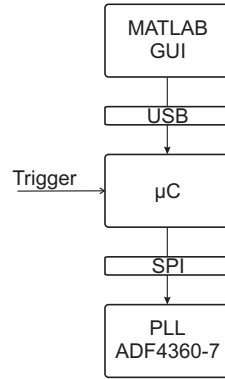


Figure 6.10: Functional block diagram of all components within the local oscillator.

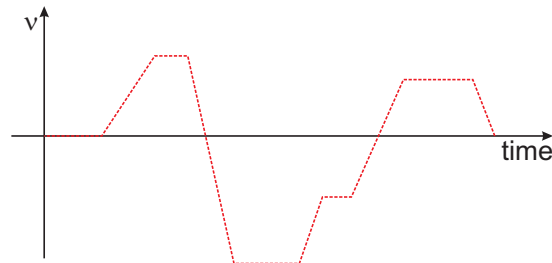


Figure 6.11: Local oscillator trace pattern. According to this pattern the counters are expecting a larger or smaller frequency as a next point on the sweep.

an input resistance of  $\sim 1\text{M}\Omega$ . As soon as the  $\mu\text{C}$  receives a TTL from the experiment control, see section 7.3, it begins with a frequency sweep according to the pattern in figure 6.11. This pattern can easily be modified but is adapted to our needs. In figure 6.12 an example for such a trace can be found. After a trigger is received the LO stays at  $856\text{MHz}$ <sup>12</sup> for 10ms and sweeps then to  $900\text{MHz}$  in 1ms. It remains at this point for 20ms before it sweeps to  $830\text{MHz}$  and so on. Therefore, the pattern specifies only if  $\nu_n > \nu_{n+1}$  or  $\nu_n < \nu_{n+1}$ . The last time in figure 6.12, here 5ms, defines the time in which the LO sweeps back to the first frequency value, here  $856\text{MHz}$ , which is then also the steady state frequency. In the *fixed* mode the LO does not sweep at all and the microcontrollers interrupt is disabled.

Ending this section, it should be noted that by simply exchanging the PLL to a different type from this family and some small changes to the C-code one can change to a different frequency domain with the least possible effort. Furthermore, the low costs of approximately  $\text{€}200$  per unit should be pointed out. A commercially available microwave generator with the sweeping capabilities is not available below several  $\text{k€}$ . Due to the use of a standard USB port, a system is

<sup>12</sup>Values are taken from the figure 6.12 for clarity and may be changed at will.

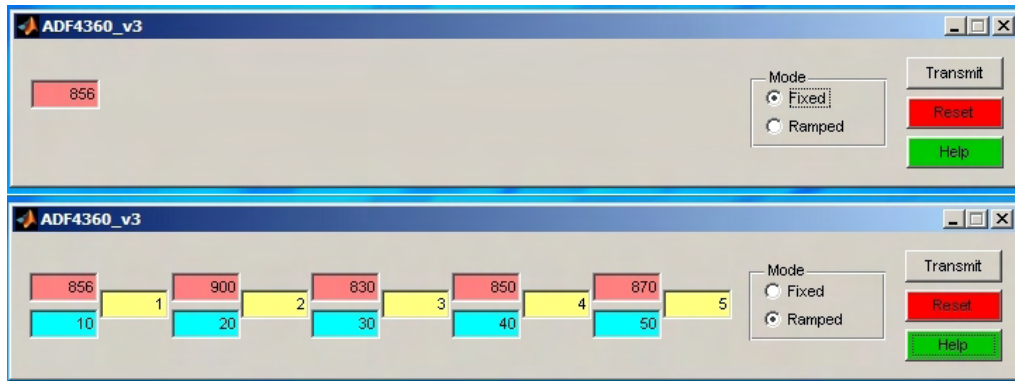


Figure 6.12: VCO user interface. *Fixed* mode in the top figure and *Ramped* mode below.

easily expanded to further sources and, as a side note, it should be mentioned that the whole system is powered via the USB bus.

## **Part IV**

# **Lithium - Rubidium Experiments**



# 7 $^6\text{Li}$ - $^{87}\text{Rb}$ Experiments

The documentation of all changes made to the previously-existing  $^7\text{Li}$  setup [13] is the purpose of this chapter. It should be kept in mind that all changes were made in the light of a temporary solution, as the move from Heidelberg to Vienna was always immanent. When the decision to test the combination of  $^6\text{Li}$  and  $^{87}\text{Rb}$  was made there was no published work on this mixture. A loss of atoms can be observed if atoms of different species are magneto-optically trapped in a combined trap. Such loss rates had been observed in all other mixtures. Large loss rates [82] do not allow the operation of a common MOT, the two traps have to be spatially or temporarily separated, whereas small losses can be accepted. Therefore, a trial experiment was set up to check if the loss rates are of any significance for the selected mixture. Results on these studies can be found in section 7.4.

## 7.1 Vacuum-Chamber and Coils

The vacuum chamber consists of a DN 63 CF six-way cross where four additional DN 40 CF ports are welded on to it, see figures 7.1 and 7.2 .

This chamber is pumped by a turbo molecular pump<sup>1</sup> during bake-out and, once sealed off with the mechanical valve, it is pumped with a ion-pump<sup>2</sup> and

---

<sup>1</sup>Varian, Turbo-V250

<sup>2</sup>Varian, VacIon Triode, 60l/s

Front View

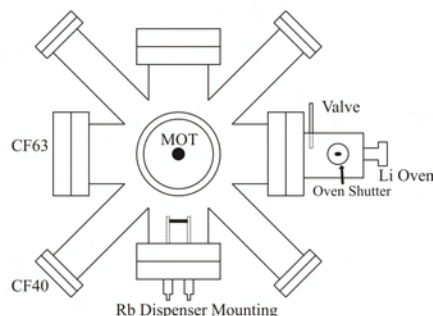


Figure 7.1: Vacuum-chamber front view, not to scale [12].

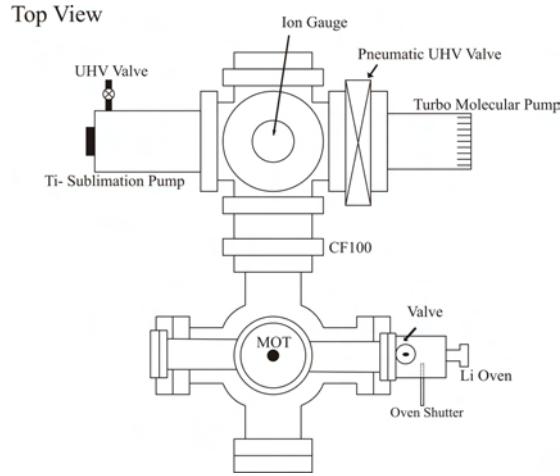


Figure 7.2: Vacuum-chamber top view, not to scale [12].

a TSP cartridge<sup>3</sup> in a DN 63 CF tube. With this combination, an ultimate pressure of  $\sim 10^{-11}$  mbar was reachable. There is a Li-oven connected to the chamber via a DN 63 CF port. Details of this oven may be found in [12, 83]. It is interesting to note that in this setup there is no Zeeman-slower [84] used for slowing the Li atoms from the oven. Therefore the large detuning ( $-96\text{MHz}$ ) for the slower light is required. Initially the oven was loaded with a Li mixture of natural abundance<sup>4</sup> and later, see section 7.7, replaced by an enriched sample to remove the unwanted flux of  ${}^7\text{Li}$  atoms. Note, the Li-spiral-atom chip [85] was removed from the vacuum-chamber and replaced by two Rb-dispensers<sup>5</sup>.

The  $45^\circ$ -mirror-MOT coils were removed and new coils were directly wound onto the vacuum chamber, as indicated in figure 7.4. Each of the two coils in anti-Helmholtz configuration, consists of 65 turns of insulated copper tubing<sup>6</sup> and has an approximate radius of 50mm. The two coils are 150mm apart and are usually operated at 16A, resulting in a gradient of 22G/cm. The coils were tested up to 50A with water cooling. Additionally, three Helmholtz coil pairs are attached to the chamber and are used for compensating the ambient field.

<sup>3</sup>Varian, Ti-sublimation-cartridge 916-0061

<sup>4</sup>The natural isotopic mixture (3% ${}^6\text{Li}$  and 97% ${}^7\text{Li}$ ) was replaced by an enriched sample (95.56% ${}^6\text{Li}$  and 4.44% ${}^7\text{Li}$ ) from Sigma Aldrich

<sup>5</sup>Dispensers are obtained from SAES-Getters (RB/NF/7/25 FT 10+10).

<sup>6</sup>The copper tube has an inner diameter of 2mm and an outer diameter of 3mm. The insulation is assured by heat-shrink.



	<sup>6</sup> Li	<sup>87</sup> Rb
$\Gamma$ [MHz]	$2\pi$ 5.87	$2\pi$ 6.065
$\Omega$	0.014	0.0027
$\alpha$	0.43	0.52
$E = hc/\lambda$ [eV]	1.84	1.58

Table 7.1: A summary of the values that enter equation 7.1.  $\Omega$  is the solid angle, covered by the photodiode,  $\alpha$  the overall detector efficiency.

## 7.2 Method of Detection

For the experiments discussed below, it is necessary to detect the number, position and shape of the trapped atoms. For experiments with two atomic species it is necessary to have a species-selective method of detection. Within this section, all methods of detection will be described. The number of trapped atoms was detected with photodiodes, equipped with optical filters to select the specific wavelength. CCD cameras were used for the detection of the position and shape of the trapped cloud.

### 7.2.1 Number of Atoms

To determine the number of trapped atoms, the light scattered by the trapped atoms is detected. In the limit where  $I/I_s \gg 1$  and on resonance, where  $I_s$  is the saturation intensity of the atomic transition, the scattering rate is  $\Gamma/2$  [17]. These photons are scattered over the whole solid angle of  $4\pi$ , of which only a fraction  $\Omega$  is detected with an efficiency of  $\alpha$ . In order to obtain this signal, the trapping light is swept rapidly  $\sim 1$ ms across resonance. Figure 7.3 (a) shows a typical trace, which is recorded with a photodiode during such a sweep. Before the sweep starts the steady state fluorescence from the MOT is observed. During the sweep the fluorescence increases to a maximum value and drops off rapidly at resonance, as the trap is destroyed at this point. The difference in photocurrent between peak intensity and background after the sweep is used to determine the atom number. The number of atoms can be calculated from this signal according to

$$N = \frac{2}{\Gamma} I \frac{4\pi}{\Omega} \frac{1}{\alpha \hbar \omega_{atom}} \quad (7.1)$$

Here  $\Gamma$  is the linewidth of the atomic transition,  $\Omega$  the solid angle of the detector,  $\alpha$  the detection efficiency and  $\hbar \omega_{atom}$  the energy of a resonant photon. In table 7.1 all relevant parameters are collected, which are used for analysis.

The atomic clouds were imaged onto photodiodes<sup>7</sup> with standard lenses. The magnification/demagnification was selected such that the detector area is filled,

<sup>7</sup>Photodiodes (Model DET110) where obtained from Thorlabs.

depending on the size of the cloud. Where necessary, optical narrow-band filters were used to distinguish between light from different species. The photo current was amplified with a low-noise current amplifier<sup>8</sup>. The long term signal, such as shown in figure 7.5, is recorded with the analog-in channels of the experiment control system<sup>9</sup>. The transient signal from the atom number detection is recorded with an oscilloscope<sup>10</sup>, from which data are transferred to the experiment computer via a serial bus. In principle the transients are also available in the trace recorded with the ADWin control system, see section 7.3, however with the oscilloscope method a higher temporal resolution is assured for the measurement of the transient signal.

### 7.2.2 CCD Camera System

Two CCD-cameras<sup>11</sup> from two orthogonal directions were used for the detection of size and position of the trapped clouds. The self-written C++/MFC application, called *Phototrap*, acquires the images from the cameras, optionally subtracts a saved background picture, displays the pictures and finally saves the images for later analysis with a MATLAB program. This program is capable of simultaneously operating up to three cameras.

The MATLAB code subtracts, if required, a background picture and is capable of fitting a function to the density distribution. The fit functions can be selected as either Gaussian, parabolic or bimodal distributions. The Gaussian fit function is used for the analysis of the MOT pictures to determine the width of the cloud. With the measured width, the atomic density can be calculated according to

$$n = \frac{N}{V_{eff}} = \frac{N}{(2\pi)^{3/2} \sigma_x \sigma_y \sigma_z}, \quad (7.2)$$

where the width of the clouds  $\sigma_A$  (A denotes a direction x,y,z) is introduced.

## 7.3 The ADWin System

Once the previous <sup>7</sup>Li experiment had been upgraded to a two-species experiment, the experiment control system needed to be changed. The number of analog and digital channels as well as the flexibility of the NI cards and the LabView Software was not sufficient for the new requirements. Following initial efforts [86] an experiment control system based on an ADWin System was implemented. The ADWin System contains a dedicated CPU, which can exchange

<sup>8</sup>Amplifiers from Stanford Research Inc., Model SR345, where used.

<sup>9</sup>Refer to 7.3, for a detailed description of the experiment control system.

<sup>10</sup>Standard Tektronics TDS220 with a serial port extension.

<sup>11</sup>The cameras are from Pulnix, model number TM-6AS. The images were acquired with a framegrabber from Inspecta.

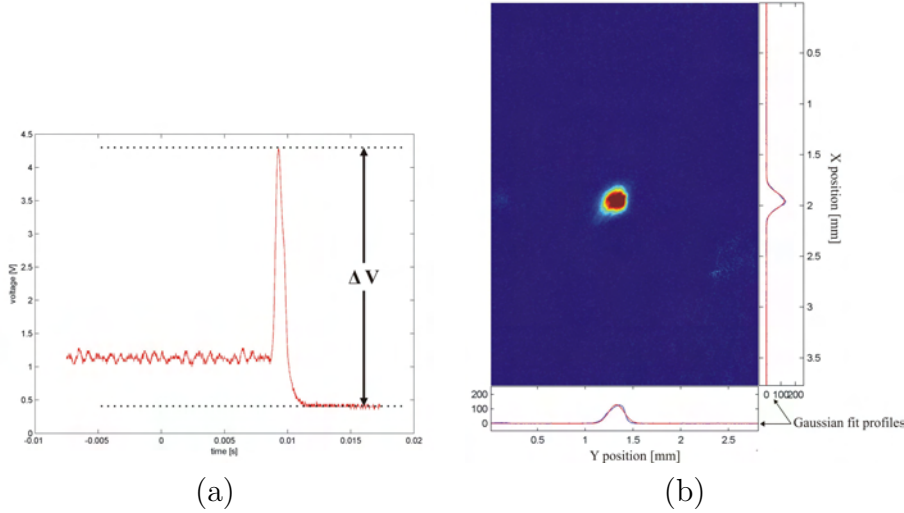


Figure 7.3: (a) A typical single-shot trace from the number detection of Rb atoms. The amplitude  $\delta V$  is extracted and converted into the actual photocurrent, which can in turn be converted into the number of atoms. (b) A typical fluorescence image of the Rb MOT, where the background is subtracted. These images are used to determine the width of the MOT through Gaussian fits to the cloud, (red) in the side panel plots.

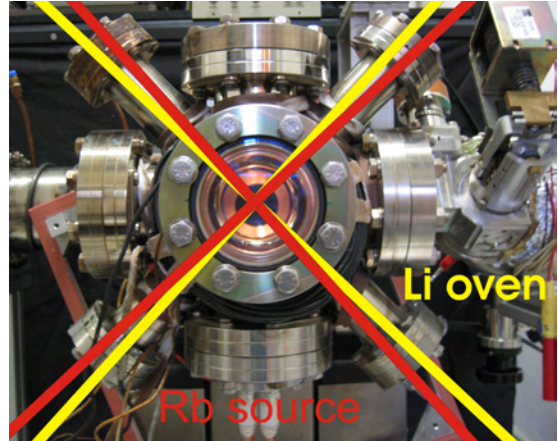
data to a control PC via the local area network (LAN). Such a system allows for a better time resolution over a longer time, as not only data vectors from the memory are clocked out, but the CPU is capable of computing intermediate data points. The employed system is equipped with 16 analog-out, 64 digital-in/out and eight 16-bit analog-in channels. A standard PC runs a MATLAB code which generates a global data vector and transmits this to the ADWin system. A detailed description of this MATLAB code may be found in [72, 86, 87]. To protect the digital channels and to avoid ground loops, all are opto-coupled before they are used in the experiment. Analog channels are decoupled with instrumentation amplifiers<sup>12</sup>.

## 7.4 The Dual-MOT Experiment

After the changes to the vacuum vessel were made, see section 7, there was enough space to operate a six-beam MOT. After initial attempts with six independent beams for each direction turned out to be very sensitive to air turbulences, the setup was changed to a retro-reflected beam layout. Four of the six beams are depicted in figure 7.4, whereas the two remaining beams are into and out of the plane respectively. It should be noted that there is an angle between

<sup>12</sup>The used amplifiers are from TI/BB; model number INA114.

Figure 7.4: Picture of the real experiment with MOT beams indicated, Rb beams *red* and Li light *yellow*. On the right hand side the Li oven and its electromechanical shutter is visible. The current feedthroughs from below are connected to the Rb dispenser sources. Around the central window the black heatshrink insulated MOT coil is also visible.



the two colours, i.e. frequencies, where red denotes the Rb light and yellow the Li light. This angle results from the fact that independent optics for Li and Rb were used. This angle is approximately  $2^\circ$  and given due to the size of the two 1-inch retro-reflectors<sup>13</sup>, which were placed as close to the vacuum windows as possible. The experiment-sequence can be seen in figure 7.5.

## 7.5 Results

In section 2, the theory of cold collisions was summarised. This section will combine the ideas developed in the theory section with the results from the measurements on the  ${}^6\text{Li}$ - ${}^{87}\text{Rb}$  dual-MOT. From all possible long-range molecular states, only the attractive states play a role in the loss rate. If two atoms are approaching each other and are promoted to a repulsive potential, no long-range molecule is formed and the atoms are repelled from each other. Therefore, out of the sixteen long range Hund's case" c" potentials calculated by [14] and plotted in figure 7.7,

only the two lower asymptotes are attractive. These lower levels represent the  $5^2P_{1/2} - 2^2S_{1/2}$  and  $5^2P_{3/2} - 2^2S_{1/2}$  configuration. All other potentials are repulsive. This leads to the following result for the  ${}^6\text{Li}$ - ${}^{87}\text{Rb}$  dual-MOT. Only the  ${}^6\text{Li}$ - ${}^{87}\text{Rb}^*$  molecules contribute to the loss, as only those feature an attractive potential and, hence, reach the short distances needed for FCC to occur. This theoretical prediction from the semi-classical GP-model [49] is in good agreement with the experimental observations. A loss of Li atoms is observed in the presence of Rb atoms, however; no loss of Rb atoms in the presence of a Li MOT can be detected.

All relevant energies are summarised in table 7.2. Equation 2.9 is used to

<sup>13</sup>The retro- reflectors consist of a mirror holder for a 1-inch mirror and a 1-inch quarter wave plate.

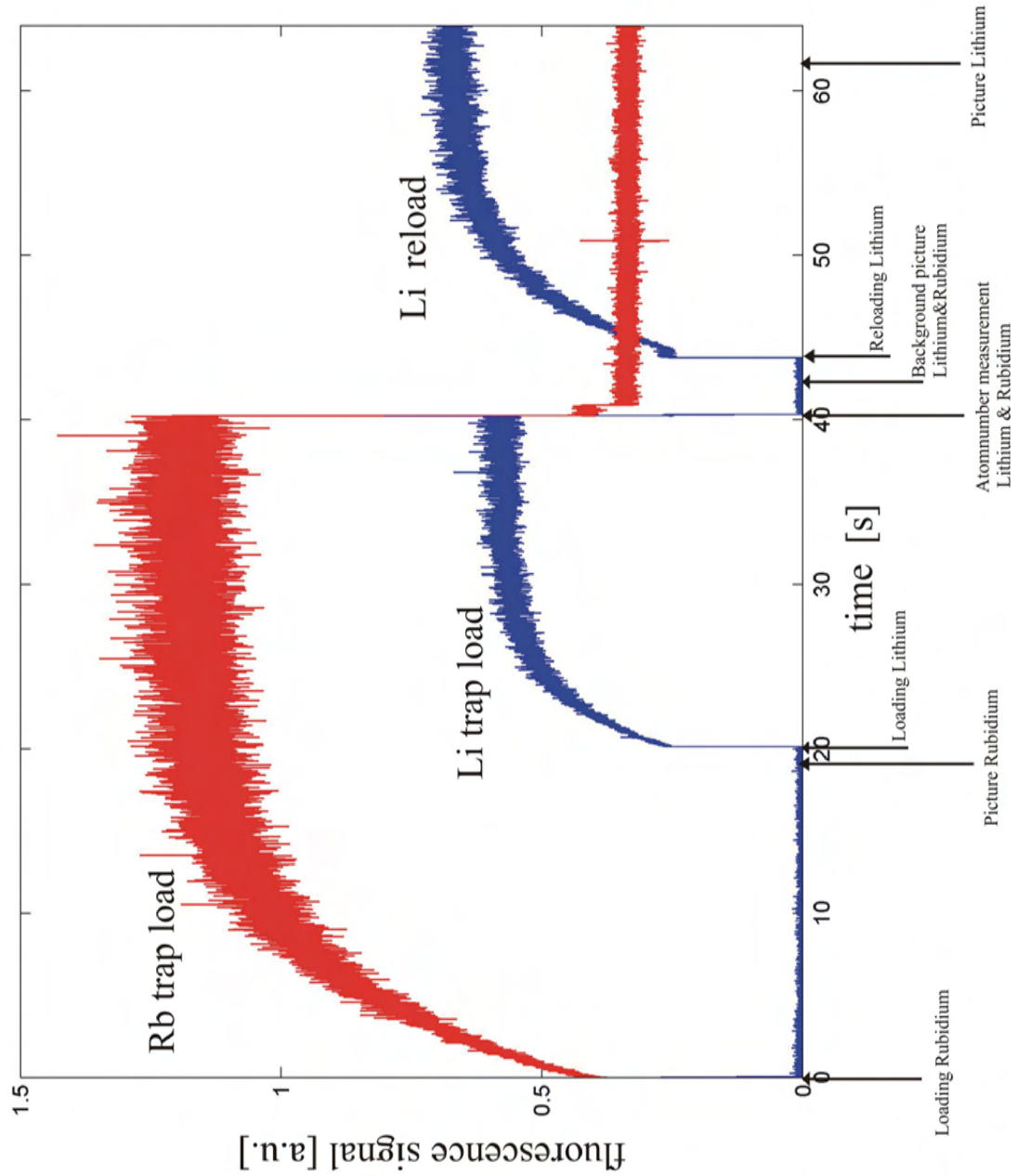


Figure 7.5: Experiment timing sequence for the dual-MOT experiment [12]. The experiment starts by loading the Rb atoms until a steady-state atom number is reached  $\sim 20$  s. At this point, the fluorescence of the Rb MOT is recorded with the CCD cameras. This is followed by the loading of the Li MOT until a steady-state atom number is also reached ( $\sim 40$  sec). At this point the number of trapped atoms is recorded for each species. After the total decay of fluorescence, background pictures for Li and Rb are taken before the Li is allowed to form a MOT again. At  $\sim 65$  s, the Li-MOT has reached a steady-state and the fluorescence of the MOT is recorded with the CCD cameras.

Figure 7.6: A single shot Li loading curve, recorded with a photo diode. (red/dashed) The fit to the loading signal and the residuals (below) are shown. The high frequency noise does not harm the fit, as it is on a different timescale, see text.

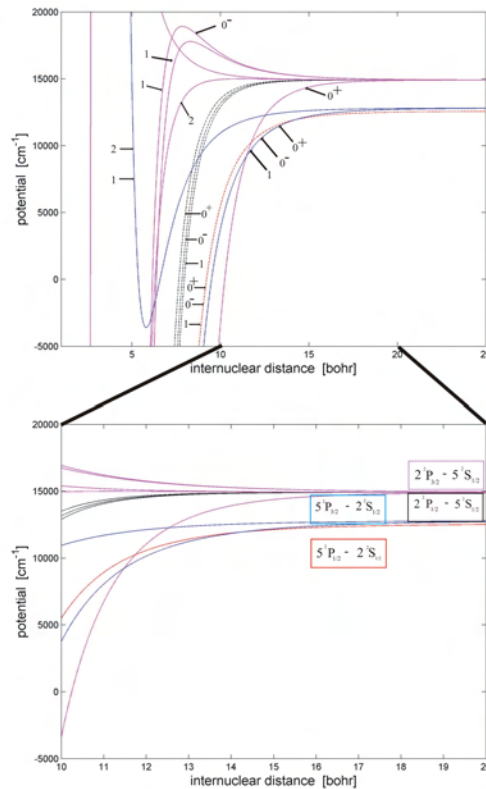
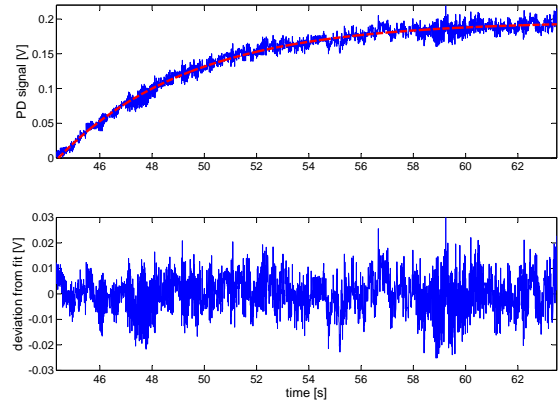


Figure 7.7: Long-range molecular potentials, according to [14], for  ${}^6\text{Li}-{}^{87}\text{Rb}$ . The two asymptotic levels corresponding to  $2^2P_{1/2} - 5^2S_{1/2}$  and  $2^2P_{3/2} - 5^2S_{1/2}$  are repulsive and the two lower asymptotes, corresponding to  $5^2P_{1/2} - 2^2S_{1/2}$  and  $5^2P_{3/2} - 2^2S_{1/2}$  lead to attractive potentials.

	<sup>6</sup> Li	<sup>87</sup> Rb
trap depth [GHz]	516	458
$E_{crit}/h$ [GHz]	552	7100
$E_{FS}/h$ [GHz]	10	7120
$E_{HFS}/h$ [GHz]	0.8	6.8

Table 7.2: Overview of the relevant energies for the cold collision between <sup>6</sup>Li and <sup>87</sup>Rb. The values for  $E_{crit}$  are the maximal total energy release during a collision allowed.

calculate the depth of a MOT with 1-inch laser beams for Li and Rb. With the help of equation 2.5,  $E_{crit}$  can be calculated. As the energy of an inelastic collision is shared between the two atoms according to their masses, a critical energy  $E_{crit}$  can be defined as the maximal total energy, which can be released during a collision and does not lead to trap loss. Any energy release with  $E > E_{crit}$  will result in a trap loss of the specific species.

From table 7.2 it can be seen, that the energy release of a HCC is not sufficient to remove either an Li or Rb atom from the MOT. Therefore, HCCs will lead to a heating of the MOT, but can be neglected for the analysis of the loss processes. The energy,  $E_{FS(Li)}$ , released from an inelastic Li\*-Rb collision is not sufficient to remove a Rb atom from the trap.

All above points show that the relevant loss channel in the Li-Rb dual-MOT is the Li-Rb\* collision, as it has an attractive molecular potential and the energy release is large enough to remove Li atoms from the trap. It should be noted that such a collision can also remove Rb atoms from the trap, as  $E_{FS(Rb)} \sim E_{crit(Rb)}$  however this is not observable in the experiment. This can be explained by the fact that  $E_{FS(Rb)}$  and  $E_{crit(Rb)}$  are of same order of magnitude and the trap depth is not an exact value, as the dissipative force for an individual atom depends on the exact path of the atom. Secondly, the number of atoms lost is small compared to the total number of trapped Rb atoms.

Before the results from the MOT loading curves, as shown in figure 7.5, are discussed in detail, the method of analysis is described. In order to obtain the interspecies inelastic loss rate coefficient  $\beta'_{LiRb}$  loading curves of a <sup>6</sup>Li MOT are measured; with and without the presence of the <sup>87</sup>Rb. The sequence is as follows:

- the <sup>87</sup>Rb MOT is allowed to form
- fluorescence pictures of the Rb-MOT are taken with the two CCD cameras; at the time  $\sim 20$ s in figure 7.5
- the <sup>6</sup>Li MOT is allowed to form until a steady-state atom number is reached

- the number of atoms is measured for both species, hereby destroying both MOTs
- background pictures with just the MOT light present are taken
- finally the  ${}^6\text{Li}$  MOT is allowed to form again, this time without the presence of Rb atoms. After a steady-state atom number is reached fluorescence pictures of the Li MOT are taken.

The analyses of the pictures taken with the CCD cameras and atom number measurements are discussed in section 7.2.2 and section 7.2.1, respectively.

In section 2.4, the loading behaviour of a MOT in the presence of losses is discussed. The general description of such a loading, see equation 2.13, can be simplified under the assumption that one of the MOTs is fully immersed in the other one. This results in a constant density assumption, which simplifies equation 2.13 significantly. From the result, see equation 2.16, two measurable quantities can be derived for the Li–Rb dual MOT,

$$\Gamma_{Li} = (\alpha_{Li} - \beta_{Li}f(N_{Li})n_{Li}) \quad (7.3)$$

$$\Gamma_{LiRb} = (\alpha_{Li} - \beta_{Li}f(N_{Li})n_{Li} - \beta'_{LiRb}n_{Rb}), \quad (7.4)$$

and  $\beta'_{LiRb}$  can be calculated according to

$$\beta'_{LiRb} = \frac{\Gamma_{Li} - \Gamma_{LiRb}}{n_{Rb}}. \quad (7.5)$$

The experiment setup is designed such that it allows for the independent alignment of the Li MOT and the Rb MOT laser beams. This is important for the exact positioning of the two clouds to a common center and, hence, assures a good overlap. Figures 7.11, 7.10, 7.13 show the position and size of the Li and Rb MOTs from the two orthogonal directions, labelled *I* and *II*. The errorbars in the plots labelled with *posX I/II* and *posY I/II* represent the size of the clouds from the Gaussian fits. With the help of these graphs, the overlap of the two MOTs can easily be checked.

The loading curves are extracted from the recorded photodiode signal and solutions to equation 2.16 are fitted to them with a least-squares algorithm. The quality of the fit is judged by the analysis of the residuals. See figure 7.6 for such a plot. The high-frequency noise on the signal shown in figure 7.5 does not harm the quality of the fit, as the relevant timescale for the fit is of the order of 10s.

The dependence of  $\beta'_{LiRb}$  on the Rb-cooler intensity is analysed for two values of Rb-cooler detuning, -12MHz and -21MHz respectively. The result can be found in figure ?? and figure ??, respectively. Each of the figures is accompanied by a supplement figure, which show additional relevant data, such as the overlap of the two clouds. Furthermore, the dependence of  $\beta'_{LiRb}$  on the Rb-cooler detuning



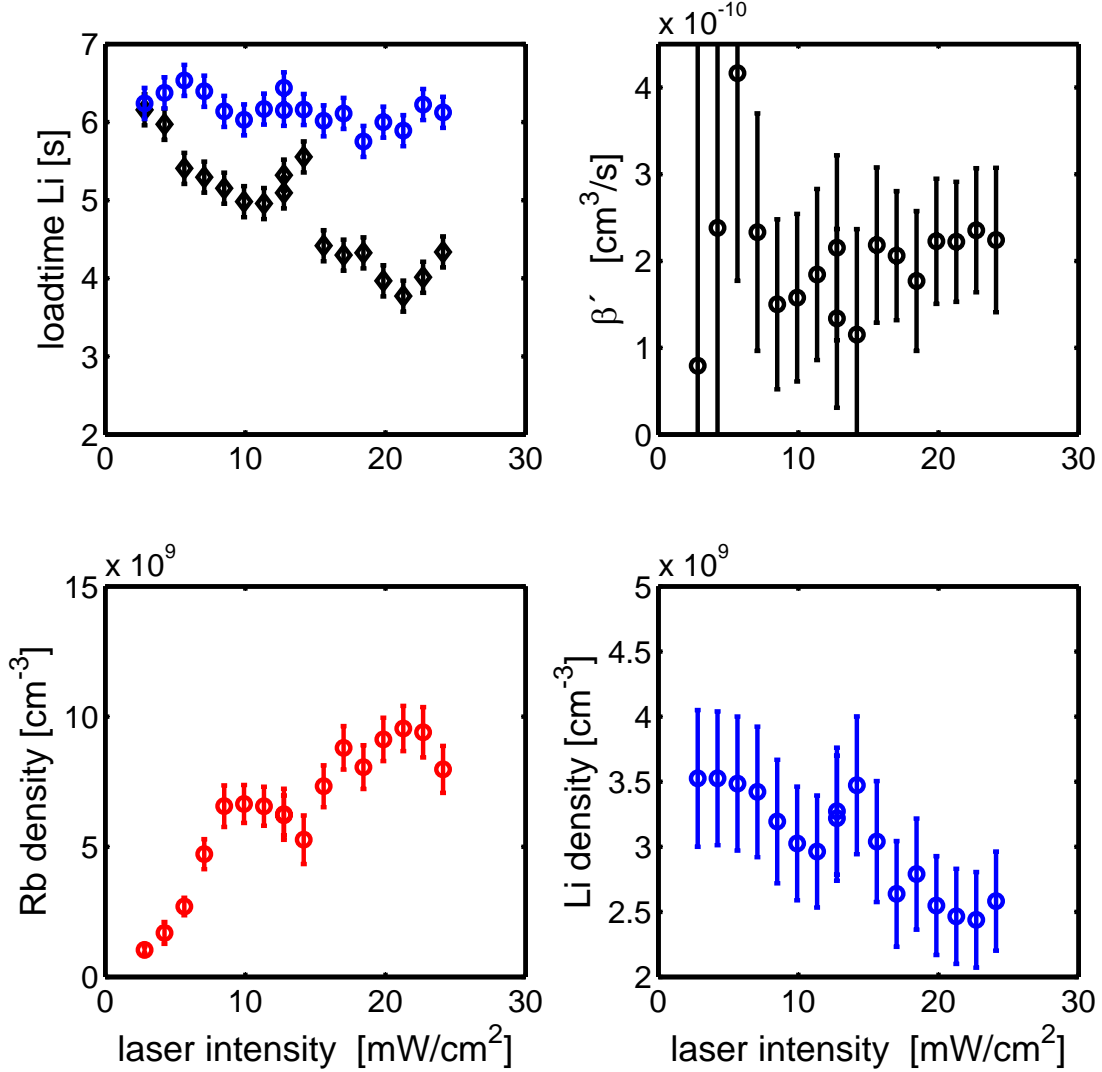


Figure 7.8: The  $\beta'_{LiRb}$  coefficient depending on the Rb laser power at a detuning of  $-12\text{MHz}$ , upper right hand graph. Also Li loading time with (o) and without Rb atoms in the trap and Rb and Li densities are shown.

is analysed for a fixed Rb-cooler intensity. The measurements for the intensity variation are performed at a field gradient of  $18.2 \text{ G}/\text{cm}$ , whereas the measurements for the detuning variation are done in a slightly stiffer trap, at a gradient of  $22.4 \text{ G}/\text{cm}$ . The slightly larger gradient is needed to assure the good spatial overlap.

For both measurements of the  $\beta'_{LiRb}$  dependence on the Rb-cooler intensity an increase in  $\beta'_{LiRb}$  with higher intensities can be observed. This increase is, for both values of Rb-cooler detuning, in the order of  $1 \times 10^{10} \text{ cm}^3 \text{ s}^{-1}$ . This increase

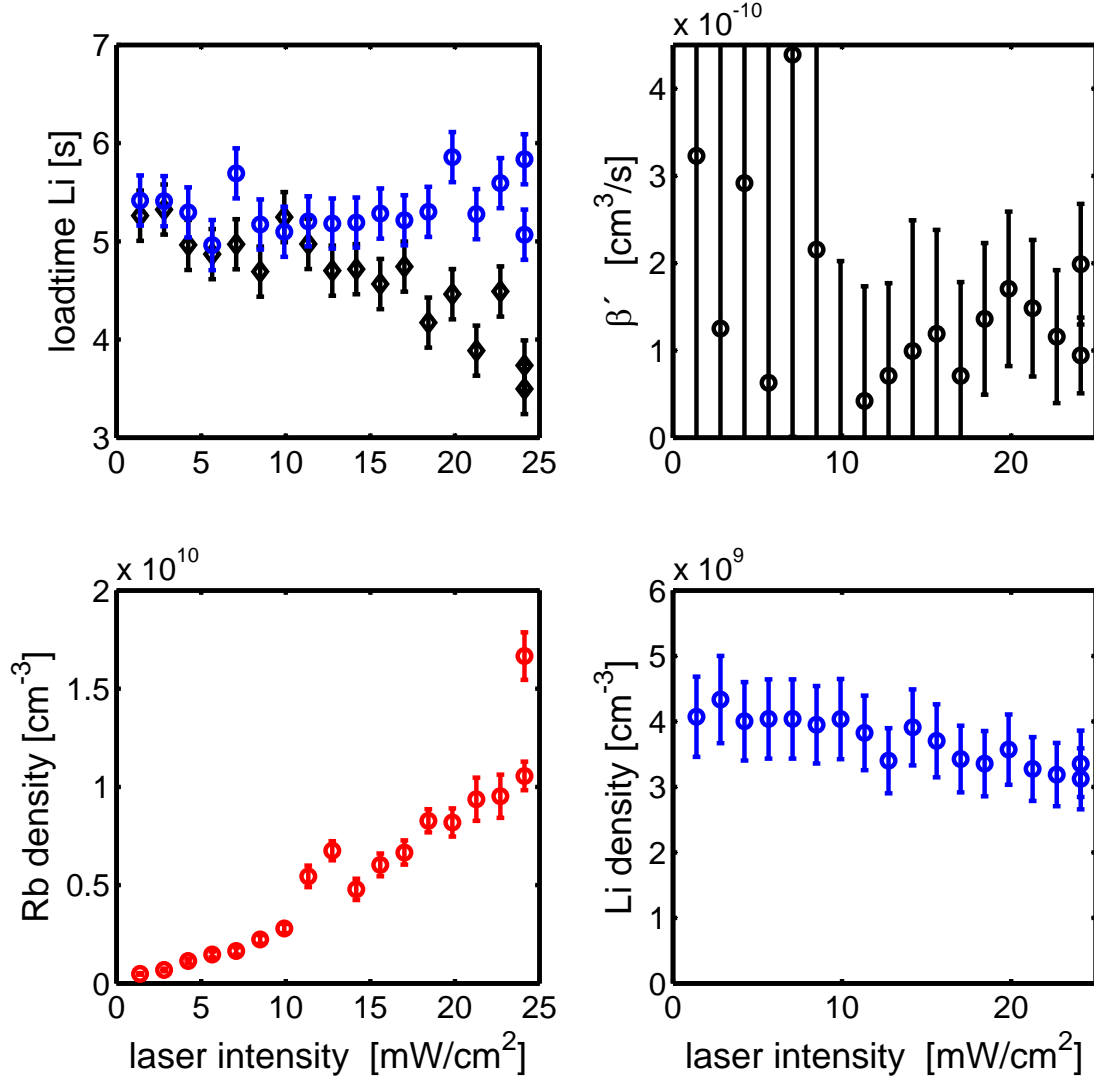


Figure 7.9: The  $\beta'_{\text{LiRb}}$  coefficient depending on the Rb laser power at a detuning of  $-21\text{MHz}$ , upper right hand graph. Also Li loading time with ( $\diamond$ ) and without ( $\circ$ ) Rb atoms in the trap and Rb and Li densities are shown.

can be understood in the following way. From a two-level atom model [17] it can be expected that the population distribution of the excited ( $5P_{3/2}$ ) and the ground state ( $5S_{1/2}$ ) of the Rb atoms to be 1/2 in each state. This assumption is true for the limit of  $I/I_{\text{satt}} \rightarrow \infty$ , where  $I_{\text{satt}}$  is the saturation intensity of the transition. As long as this relation is not fulfilled, a larger population of the ground state can be expected. Hence, as the LiRb\* collision could be singled out as the dominant contribution channel,  $\beta'_{\text{LiRb}}$  is expected to rise with increasing population of the  $5P_{3/2}$  state.

The large fluctuations, especially at low intensities, can be attributed to the density fluctuations of the Rb cloud. Equation 2.16 shows that the density of Rb contributes linearly to the Li loss rate. It should also be kept in mind that equation 2.16 assumes a constant density over the whole extend of the Li MOT. Therefore, the density of the Rb cloud is constantly underestimated, which leads to a larger  $\beta'_{LiRb}$  than expected. In figures 7.9, 7.8, 7.12 a good correlation between the density and the loading time of the Li MOT is found. This correlation between the Li loss and the presence of Rb is also evident in the supplement plots, see figures 7.11,7.10,7.13. Especially for low intensities  $I_{Rb} < 10mW/cm^2$  of the Rb cooler the results for  $\beta'_{LiRb}$  are not reliable, as the large errorbars indicate. However, as these points give an indication to where the validity of the model starts, they are not excluded from the plots.

Furthermore, despite the identical shape of the two  $\beta'_{LiRb}$  vs. intensity curves, an offset between the two curves is visible. This offset can be expected, as, for smaller detunings, the population of the excited state is higher for the same intensity. This result is well reproduced by the experimental data. The factor between the two loss rate coefficients  $\beta'_{LiRb}$  for the two detuning values is  $\sim 1.5$ . This value is in good agreement with the different values for  $\beta'_{LiRb}$ , which are obtained from detuning measurement, this factor is 1.6, therefore slightly larger. However, within the error, both values are in good agreement.

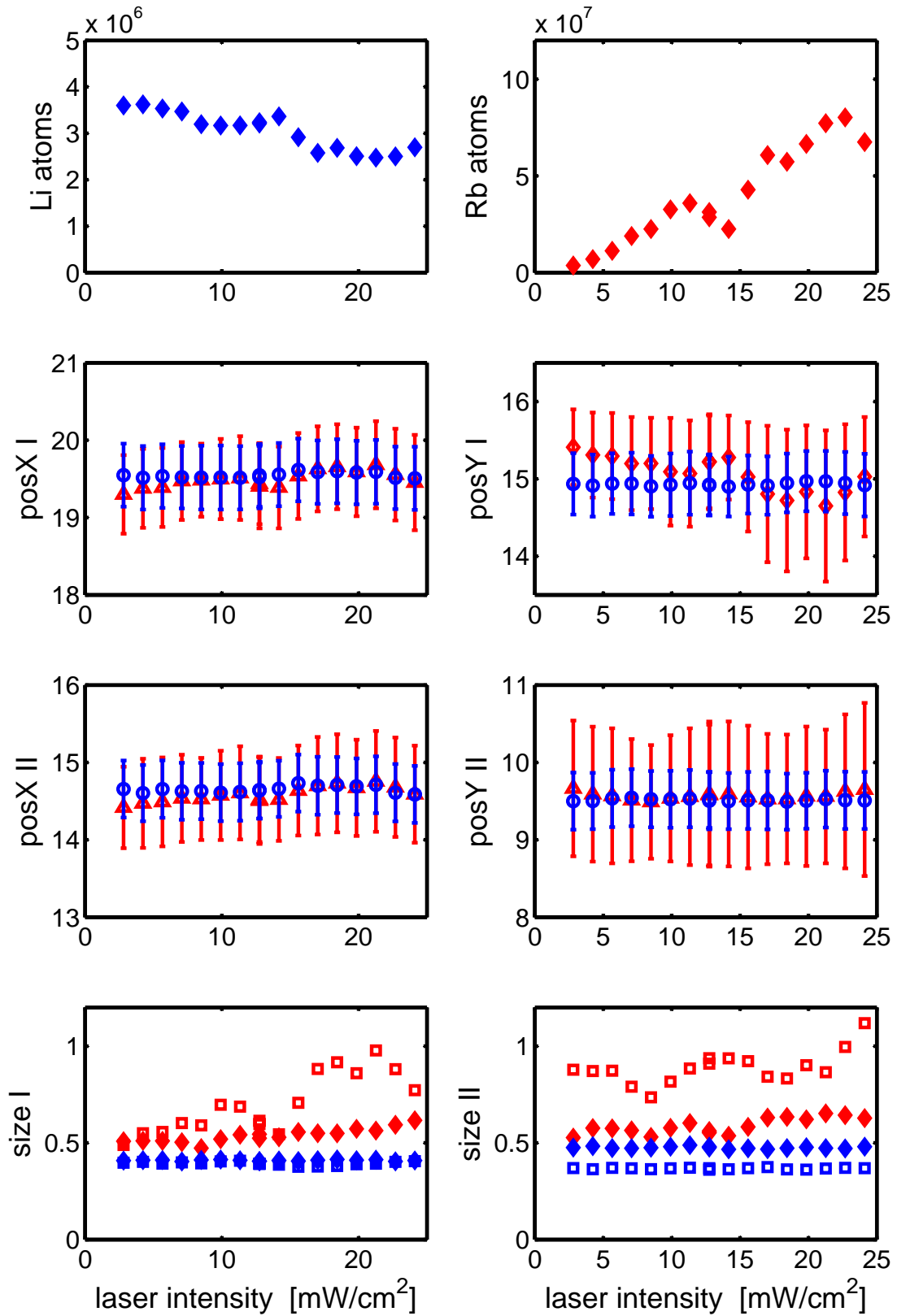


Figure 7.10: Supplement to figure 7.8. For a detuning of  $-12\text{MHz}$  these graphs show the number of atoms for Li and Rb and sizes and positions from the data analysis, where sizes and positions are measured in mm. The errorbars visualise the size of the clouds.

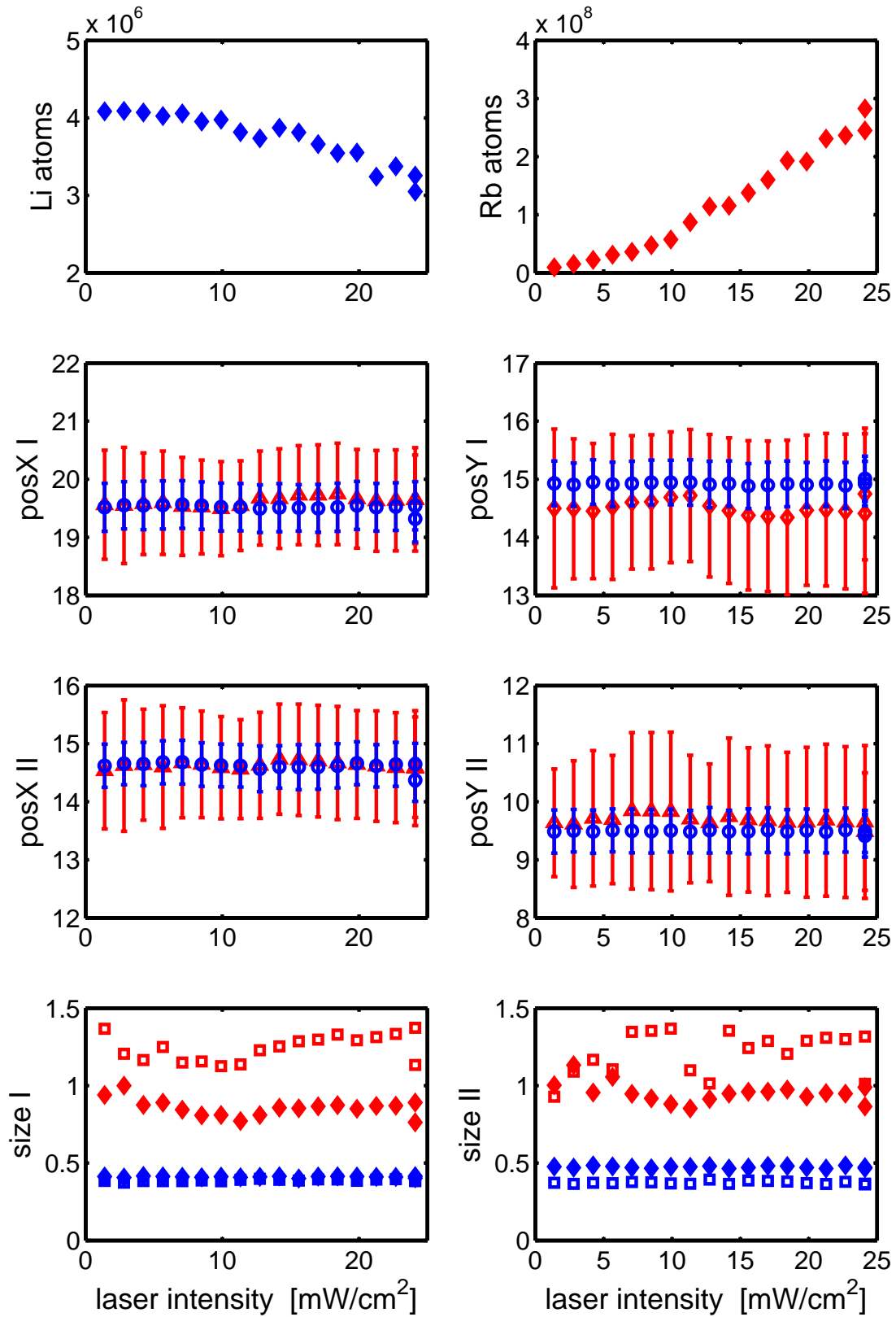


Figure 7.11: Supplement to figure 7.9. For a detuning of -21MHz these graphs show the number of atoms for Li and Rb and the sizes and positions from the data analysis, where sizes and positions are measured in mm. The errorbars visualise the size of the clouds.

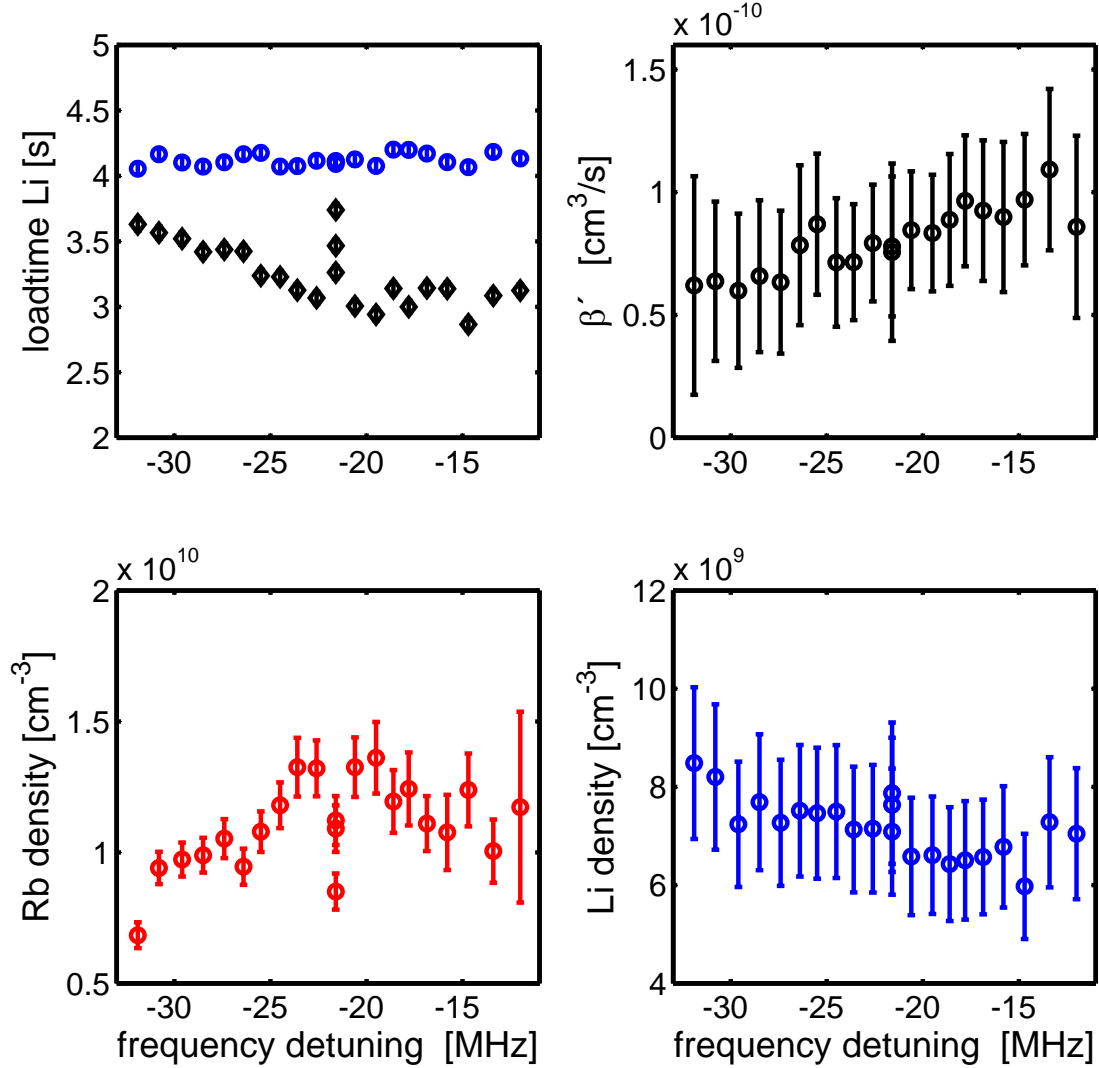


Figure 7.12: Dependence of the loadingtime for Li and Rb on the Rb cooler detuning. Densities and the inelastic loss rate coefficient  $\beta'_{LiRb}$  are shown.

The dependence of  $\beta'_{LiRb}$  on the Rb-cooler detuning is plotted in figure 7.12 and the supplemental data can be found in figure 7.13. The increase in  $\beta'_{LiRb}$  from  $0.6 \times 10^{-10} \text{cm}^3/\text{s}^{-1}$  at a detuning of -32 MHz to  $1.2 \times 10^{-10} \text{cm}^3/\text{s}^{-1}$  at a detuning of -12 MHz can be seen. This change in the interspecies scattering rate can be explained by the decreasing amount of Rb atoms in the excited state with increasing detuning from resonance.

In conclusion, the light-assisted loss rate for a  ${}^6\text{Li}$  MOT in the presence of a  ${}^{87}\text{Rb}$  MOT is measured for the first time<sup>14</sup>. The intensity dependence of

<sup>14</sup>Note that the data was taken in November 2004.

the inelastic loss rate coefficient  $\beta'_{LiRb}$  for two fixed detunings as well as the dependence of  $\beta'_{LiRb}$  on the detuning for a fixed intensity is measured. From all these measurements,  $\beta'_{LiRb}$  could consistently<sup>15</sup> be determined to be  $\beta_{LiRb} = (1.5 \pm 0.5) \times 10^{-10} \text{cm}^3 \text{s}^{-1}$ .

This value is of the same order of magnitude as values for experiments with other species. Unfortunately, there are no data for the  $\beta'_{LiRb}$  from [40] published. The only published result for  $\beta'_{LiRb} = 8 \times 10^{-12} \text{cm}^3/\text{s}^{-1}$  from [88], which deviates significantly from this result. However, it is not published how the authors of [88] obtained this value.

## 7.6 Magnetic-Quadrupole-Trap Lifetime

The results discussed in the previous section are very encouraging for further studies of the  $^6\text{Li}$  and  $^{87}\text{Rb}$  mixture. The possibility of operating two MOTs simultaneously in time and space reduces the experimental complexity significantly and establishes a solid starting point for a common magnetic trap. Furthermore, the prospect of reaching the lowest temperatures of a DFG with this particular combination [89] of a Bose–Fermi gas was a driving factor to continue with this mixture. The desire to reach temperatures well below the Fermi temperature results from theoretical predictions, where finite temperatures are usually difficult to include.

With the existing experiment setup, it was simple to extend the research to a magnetically trapped mixture of  $^6\text{Li}$  and  $^{87}\text{Rb}$ . Once both MOTs are loaded to a steady–state atom number, the light is switched off and the magnetic quadrupole–field gradient is, in 15ms, increased from the MOT field of 8.4G/cm to a field of 70G/cm. After a time  $t$  in the magnetic trap, the light is switched on and swept from far red detuned across the resonance in  $\sim 2\text{ms}$ . The fluorescence of the trapped atoms is recorded using a CCD camera. The lifetime was found to be  $\tau = 28 \pm 2\text{s}$  at a background pressure of  $\sim 1 \times 10^{-11}\text{mbar}$ .

These results proved that a simultaneous magnetic trap for this combination is possible; however the experiment setup was not suitable for further studies. As a quadrupole trap has a zero in the magnetic field at the centre of the trap, atoms can transfer into untrapped states and leave the trap, see section 1.1. Therefore, it was decided to change the experimental setup in several points, these changes are documented in the next section.

---

<sup>15</sup>The value was derived from the five highest intensities in figure 7.8 and the five highest intensities in figure 7.9.

## 7.7 An Atom Chip for the Lithium-Rubidium Experiment

An atom chip mounting, adapted from [71, 90] was manufactured in the mechanical workshop in Heidelberg and inserted into the vacuum chamber. Briefly, the mounting consists of a large-scale copper structure for macroscopic traps and an atom chip for microscopic traps. Figure 7.14 shows a picture of the actual mounting head (a) where the connections used for U and Z traps are labelled. Figure 7.14 (b) shows the dimensions of the copper structure and (c) an illustration of the atom chip and the copper structure below.

Due to the presence of the atom chip, the optical setup was changed to a mirror-MOT configuration, see 1.3 for details. The concept of independent beams for Li and Rb was remained. The change on the vacuum system also included a change of the used Li sample in the oven to an enriched one. The  $45^\circ$ -mirror-MOT coils were put back on to allow for operating a mirror MOT. Note, that in contrast to [13], the chip is upside down and facing towards the table.

## 7.8 Magnetic trap

After the mounting was inserted into the chamber, a magnetic Z-trap was established for Rb and Li. Both species were pumped into their maximal stretched spin states. Optical pumping resulted in an increase of the trapped atoms of Rb by a factor of  $2.5 \pm 0.2$ . It was possible to trap  $(2 \pm 1) \times 10^4$   ${}^6\text{Li}$  atoms and  $(1.4 \pm 0.3) \times 10^6$   ${}^{87}\text{Rb}$  atoms simultaneously. The numbers were taken after the atoms were 1s in the trap.

In the subsequent step the lifetime of the magnetic  ${}^{87}\text{Rb}$  trap was determined. The lifetime was found to be  $3.5 \pm 0.1$  seconds. This short lifetime could be tracked back to bad vacuum conditions and a defect ion pump. During the experiment cycle the vacuum went up to  $9.8 \times 10^{-10}$  mbar. Unfortunately the trap frequencies were not high enough to allow for a rapid cooling to degeneracy with the low number of trapped bosons. At this point the long thermalisation times for Li and Rb were reported [40] and the final decision made for the groups move from Heidelberg to Vienna. Therefore, all efforts were directed towards the new setup which is described in section 8.



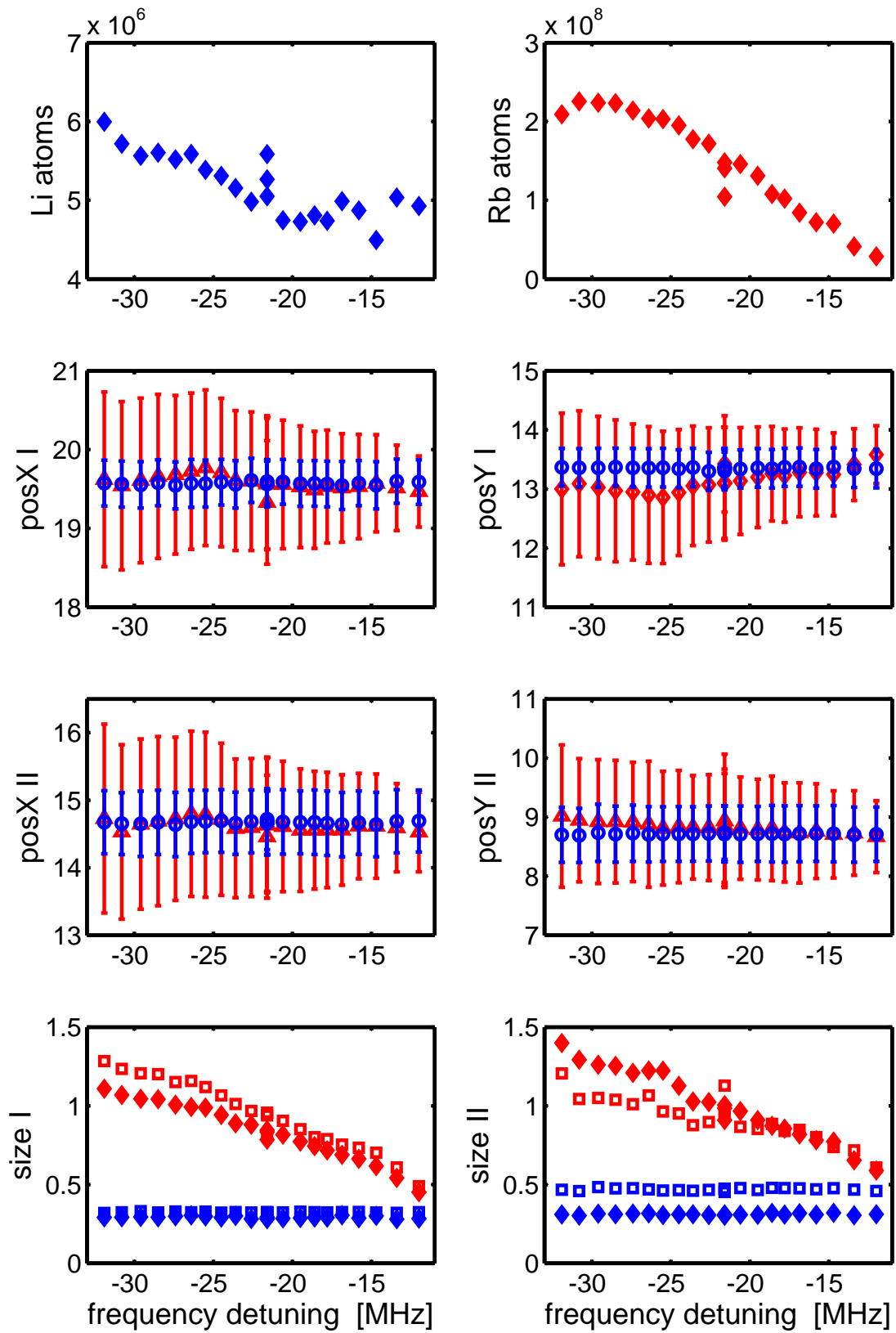


Figure 7.13: Supplement to figure 7.12. Atom-numbers, sizes and positions from the data analysis, dimensions in mm. The errorbars visualise the size of the clouds.

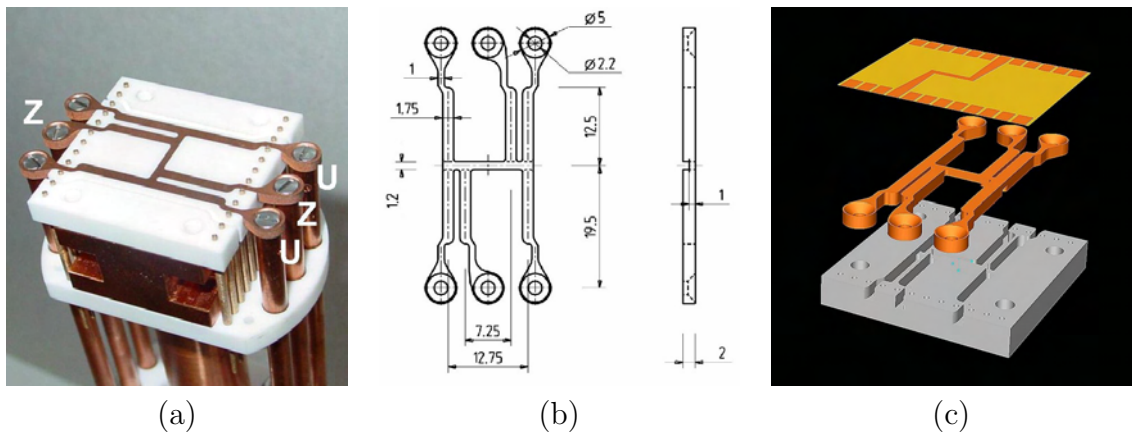


Figure 7.14: Head of the atom chip holder. The marks "U" and "Z" depict the ports used for the U-MOT and Z-trap respectively. Dimensions are given in mm.

## Part V

# The ${}^6\text{Li}$ - ${}^{40}\text{K}$ - ${}^{87}\text{Rb}$ Experiment



## 8 Design Goals

This chapter will summarise all design constraints that led to the current design of the Vienna experiment. As mentioned above, there was the unique opportunity to redesign the whole experimental setup due the move from Heidelberg to Vienna. After the piloting tests with Li and Rb, see section 7, a long list of possible changes was assembled. At this time, several experiments with mixtures [91, 92] and pure fermionic systems [93, 94, 95, 96] were already set up, as well as the first experiments creating homonuclear molecules of fermionic Lithium [4, 97] and Potassium [98, 6]. These developments opened the door to new and exiting physics, such as the study of the BEC-BCS crossover with condensed molecules [99]. An overview of experiments including degenerate Fermi gases can be found in a comprehensive review article [100]. All experiments employ combinations of large-scale magnetic traps and optical dipole traps or just optical traps. The Toronto experiment [101] was the first experiment to use microtraps for the study of a mixture of bosons and fermions. After the decision was made to focus on experiments towards single low dimensional systems, it was decided to employ the atom chip technology for this purpose. The advantage of the atom chip technology [102] is its capability of creating single low-dimensional traps of unsurpassed purity. In contrast to the multiple one-dimensional traps in a two-dimensional optical lattice [103], on an atom chip it is possible to realize a single one-dimensional gas. This can be an big advantage, as effects are not washed out due to the interference from many lattice sites [104], but also an experimental challenge, as detection is considerably more difficult due to the low line densities. Furthermore, the prospect of comparing results from pure quantum systems on the atom chip to the world of solid-state quantum systems is challenging and exciting.

All these constraints led to a set of design goals for the new experiment in Vienna. After an overview of these goals, the remaining part of this section will discuss these goals in detail and their implications and importance.

- Long lifetime in the magnetic atom chip trap
- Fast loading
- Stable, robust and short experimental cycle
- Single 1D traps

- RF wires
- High-performance transversal<sup>1</sup> imaging
- Good optical access from all other directions for imaging and optical traps.
- Lithium

## 8.1 Long Lifetime in the Magnetic Atom Chip Trap

The lifetime of a magnetic trap describes the time until one half of the initially trapped atoms have left the trap. Trap losses can have different origins; one of them is the collision between trapped atoms and molecules from the thermal background gas. As atom traps are usually of rather small depth, typically of the order of  $\mu\text{K}$ , the energy needed to remove one atom from such a trap can easily be gained from a collision with a thermal background gas molecule. Such collisions can be avoided by removing any thermal background gas, which is done by evacuating the experiment region. The lifetime of a magnetic trap due to limited vacuum is  $t_{1/2} \propto 10^{-8}/p$ , with  $t_{1/2}$  in seconds and  $p$  in torr [17].

A good measure for the vacuum requirements is the ratio between good and bad collisions,  $\mathfrak{R}$  as defined in equation 1.15. Considering the scaling of this ratio

$$\mathfrak{R} \propto \frac{1}{p} \quad (8.1)$$

$$\mathfrak{R} \propto a^2 \quad (8.2)$$

where  $p$  is the pressure in the experiment volume and  $a$  is the s-wave scattering length, see table 1.1 for all relevant scattering lengths. Experiments [105] have shown that it is possible to create a BEC of  $^{87}\text{Rb}$  atoms within a few seconds. And, as can be expected from table 1.1, for the mixture of  $^{40}\text{K}$  and  $^{87}\text{Rb}$ , rapid cooling to degeneracy has been reported [101]. A mixture of  $^6\text{Li}$  and  $^{87}\text{Rb}$  has a scattering length, which is a factor five smaller than the pure  $^{87}\text{Rb}$  scattering length, hence a long cooling time is reported [40, 106]. It should be noted, that there is a factor of almost 14.2 between the elastic inter species scattering length of  $^6\text{Li}$ - $^{87}\text{Rb}$  and  $^{40}\text{K}$  and  $^{87}\text{Rb}$ . This means that, given the same atomic densities and vacuum conditions, the elastic scattering rate is a factor of 201 larger. However, this high scattering rate shows only, that both gases are in thermal equilibrium, but the cooling rate is dominated by the shorter bosonic scattering rate. Cooling times for both species are reported to be a factor of 2 larger for Li-Rb, compared to K-Rb [106].

As mentioned before, the incorporation of all of the above-mentioned species in the Vienna experiment is intended. Having a short lifetime does not harm if

---

<sup>1</sup>Transverse denotes the direction perpendicular to the longest extend of the cloud.

rapid cooling is possible; however, harsh vacuum conditions would make certain experiments impossible. Therefore, it was decided that a long lifetime is a major design goal.

## 8.2 Stable, Robust and Short Experimental Cycle

*Stability* was a key demand throughout the whole building process. A challenge of a single 1D trap is the difficulty in detecting the atoms composing it. Due to low line densities, absorption in the transversal detection is weak. Therefore, it is advantageous if the experiment can operate over many cycles without significant fluctuations. An estimate illustrates the demand on stability: A typical trap on an atom chip has a transversal trap frequency of  $\omega_{\perp} = 2\pi \times 5\text{kHz}$  and a longitudinal frequency of  $\omega_{\parallel} = 2\pi \times 5\text{Hz}$ . Such a trap can be composed with a current through the trapping wire of 1A, which would form the trap at distance  $r_0$  of  $50\mu\text{m}$  with a 40G bias field. For low dimensional gases the energy of the lowest transverse state in the trap  $\hbar\omega_{\perp}$  is an important energy scale. For example, trapped gas is considered to be quasi-1D if  $\mu \ll \hbar\omega_{\perp}$ . Therefore, it is a good assumption that a long term stability of  $\frac{1}{10}\hbar\omega_{\perp}$  will assure a reproducible trap. This demand can be translated into a stability requirements for the fields composing the trap and rf-sources for cooling or time dependent traps. The energy can be related to a magnetic field as

$$\Delta B = \frac{\hbar\omega_{\perp}}{10\mu_B} \quad (8.3)$$

where  $\mu_B$  is Bohr's magneton. For the numbers given above, this results in  $\Delta B = 3.6 \times 10^{-4}\text{G}$ . For comparison, during the experimental realisation of a cw-atom-laser the fields were stable to 0.1mG [107]. From  $\Delta B$  the stability requirements for the current through the wire and the coils can be calculated. Equation (1.5) gives for  $\Delta I$

$$\Delta I = \frac{2\pi r_0 \Delta B}{\mu_0} = \frac{2\pi r_0}{\mu_0} \times \frac{\hbar\omega_{\perp}}{10\mu_B} \quad (8.4)$$

with the above value  $\Delta I = 9 \times 10^{-6}\text{A}$ . Using the values from table 9.2 deviations for the current through the coils can be calculated to:  $\Delta I_X = 1 \times 10^{-4}\text{A}$ ,  $\Delta I_Y = 3 \times 10^{-4}\text{A}$  and  $\Delta I_Z = 2.1 \times 10^{-4}\text{A}$ . Effectively, all values for the relative stability are in the high  $10^{-6}$  range. This is a long term requirement, i.e. a day to day reproducibility, higher short-term stabilities could be required for certain experiments [108].

*Robustness* means two things in this context: firstly that the experiment should be able to produce a BEC with a fluctuation of  $< 10\%$  in the number of condensed atoms. Comparable numbers are expected for the DFG. Secondly, the

experiment should be inert to perturbations from the lab environment, such as change in temperature and humidity.

*Short Cycle:* Potassium turned out to be very suitable to be cooled by rubidium, due to the fact that the Rb-K interspecies s-wave scattering length is  $a_{FB} = -284a_0$  [109]. This is nearly a factor of three larger than the Rb s-wave scattering length, which is 98.98 Bohr-radii [39]. The large K-Rb interspecies scattering length compared to the one of Li and Rb makes sympathetic cooling for a K-Rb mixture efficient and fast, see above. As discussed in section 1.4 it can be assumed that the K-Rb mixture is in thermal equilibrium at all times. Therefore, the speed of evaporation is dominated by the time the Rb gas needs to thermalise. Such a short experimental cycle will allow the averaging over many runs and hence improve the quality of the acquired data. Furthermore, if the experimental cycle is short, i.e in the order of 30s, it will be possible to take many runs in a reasonable time and hence result in good statistics for data analysis. It will also be possible to cover a larger fraction of the parameter space. A fast cycle will also ease the stability demands a little.

### 8.3 1D traps

The experiment should be capable of realising single one-dimensional<sup>2</sup> traps for cold bosons as well as cold fermions. A two-dimensional optical lattice would be an option, but with the added difficulty of emptying all except one lattice site. An atom chip is another option for such traps. It seems to be better suited as it can be structured in such a way that a single long and smooth trap can be formed, and can even be box-like<sup>3</sup>. Considering the groups expertise with atom chips, it was decided that the new experiment should be able to incorporate an atom chip. Furthermore, the chip design needs to be adapted to these demands and a suitable mounting had to be designed.

However, it should be kept in mind, that atom chip traps have been reported to show corrugation of the trapping potential [110, 111, 112, 113]. This effect has been employed to measure the magnetic and electric field of conductors with high accuracy [114] and furthermore, to measure long-range correlations in the electron transport [115, 78]. The potential roughness depends on parameters such as the distance of the cloud to the wire, the polycrystalline structure and fabrication method [116]. To reduce the potential corrugation two methods are reported, one incorporating a time orbiting potential (TOP) [117] and polishing

---

<sup>2</sup>Refer to section 1.5 for a definition.

<sup>3</sup>The trap enclosure from a single wire usually has a quadratic form. By using more than one wire, with the right current pattern, it is possible to reduce the harmonic components and reach a almost box-like enclosure.



the wires on the atom chip with a focused ion beam [118].

## 8.4 RF Wires

Lead by the first experiments on RF-induced potentials [119, 120], it was decided that the new experiment should also provide RF wires to realise double wells and other time-dependent trap geometries. Such a double well configuration is a good atom interferometer [119] and may also be used for quantum information processing. With the correct parameters, such a double well can be state and / or species selective, hence fulfilling one of the key demands of the Calarco proposal [121]. As mentioned above, there are also techniques [117] for removing, potentially, all corrugations of the trapping potential from the traps by employing a time-orbiting potential [117].

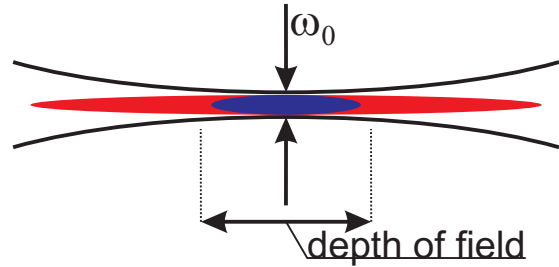
## 8.5 High Performance Transversal Imaging

Having the possibility of creating a single 1D trap is also challenging from an imaging point of view. Low line densities ( $\sim 1 \text{ atom}/\mu\text{m}$ ), which lead to very low absorption during an imaging pulse, can be expected. As an example, at 1/10th of the saturation Intensity and at resonance a single atom scatters 68 photons of the 1105 photons arriving in a circular area with radius of  $1 \mu\text{m}$  and an exposure time of  $50 \mu\text{s}$ . This area represents the size of the spatial resolution of the proposed imaging system. With a good imaging design, it will be possible to detect such low densities and maybe even fluctuations within the trapped gas. This is exactly what is only possible with a single realisation of a 1D gas and hence it is desired to have the maximum performance at this point. The current aim is a resolution of approximately  $2 \mu\text{m}$  over an area of  $500 \times 500 \mu\text{m}$ . Currently, a Diploma thesis is being carried out to design and build a lens for exactly this purpose [15]. A two-lens system as described in [122] will not be sufficient to reach the required resolution over the whole field of view. Therefore, a multi-element approach as discussed in [123] is pursued. Refer to section E for a numerical example for the achievable signal-to-noise ratio with the constructed imaging setup.

## 8.6 Good Optical Access

Apart from the transversal imaging optical access from the two other sides, i.e. along the longitudinal direction of the cloud and the second transversal axis, should not be neglected. In the longitudinal direction, demands are not as high as in the transversal direction; since the cloud in a 1D case extends over several hundred microns, absorption of the imaging light is larger compared to the imaging along the transversal direction. For the longitudinal imaging, it is interesting

Figure 8.1: (blue) A cloud of atoms inside a Focus with waist  $\omega_0$ . (red) A cloud extending out of the focus will blur the image, as the part not within the depth of field is defocused.



to discuss two regimes. If the whole cloud is of interest, it is important that the cloud is not extending out of the depth of field, i.e. extending over a larger volume compared to the Rayleigh volume of the imaging system, see figure 8.1.

This assured, a full absorption signal can be expected, as it is practically an integration over the whole cloud. However, the resolution will be moderate. If a detailed view of a cross-section somewhere along the cloud is of interest, it is not advantageous to just increase the resolution, as atoms out of focus will spoil the image quality. In such a situation it would be promising to follow the approach of the vortex experiments such as [124], where single slices of the cloud are pumped into particular states, where they can be imaged with high resolution. In this case, only a thin slice of the cloud will absorb the imaging light, the rest of the cloud is transparent to the imaging light. Also, superimposing a standing wave along this direction will allow the implementation of Bragg spectroscopy of the trapped atoms [72].

The second transversal axis is obscured by the planned atom chip and has therefore the lowest priority. The quality of images along this direction will strongly depend on the surface quality of the atom chip. It can surely be used for fluorescence detection and will be of some help during mode-matching between different stages of the experiment, for example during the initial loading of the magnetic Z-trap from the molasses.

## 8.7 The Fermions: Potassium and/or Lithium

It was mentioned above, that a K-Rb mixture is very suitable for fast sympathetic cooling. Once the low s-wave scattering length between Li and Rb had been established [40], either the coolant or the cooling agent could have been changed. A suitable cooling agent for Li is Na [92, 82]. Cooling of Na would have involved the construction of a long Zeemann-slower and operation of a second dye-laser and abandoning the essentially new Ti:Sa laser. However, there are more reasons for adding potassium to the setup.

For the attractive interaction between K and Rb the collapse of the system at high densities has been observed [109] and the formation of bright solitons has been predicted [45, 125].

Furthermore, the scattering length of the Na-K mixture is with  $\sim 50a_0$  considerably shorter than the K-Rb one with  $-215a_0$ . The decision was made towards potassium for the following reasons:

- Efficient thermalisation with Rb
- Cooling and detecting possible with diode-laser system
- Suitable for double-MOT layout
- K-Li possible

The last point is a far reaching extension to the planned experiment, but it will be briefly discussed here. Two fermions in different spin-states can form a composite boson. This has been observed in Li [4, 97] and K [98] experiments and the condensation of these stable dimers has also been observed [4, 126]. Furthermore, the creation of weakly bound dimers of two different fermionic atoms could be possible [5, 6, 7]. With both fermions in the experiment it will be possible to study the difference between attractive interaction between bosons and fermions as well as repulsive interaction; this will be possible without a Feshbach resonance. A study of a diatomic pair of a light and a heavy fermion is thinkable.



## 9 Final Design

In the previous section, a set of design goals was derived. Some of these goals are mutually exclusive, e.g. the shortest possible working distance for imaging and the size of vacuum chamber containing the atom chip; hence, a compromise between all design constraints had to be found. This section will introduce the final design, which is currently being set up in Vienna and also give reasons for weighting certain design constraints more heavily than others. This will serve two purposes: firstly, it is a documentation of the experiment actually being built, and, furthermore, a thorough motivation of why things were designed the way they are. A design is always a compromise between different design ideas and technological options. It is not a single experiment for which this machine is designed for, but certainly for a certain class of experiments. It is designed to have a long lifetime and high flexibility. However, with all decisions taken it was always tried to leave as many possibilities open for other ideas as possible. This discussion should help future generations of Ph.D students to understand and fully exploit the possibilities of this experiment.

### 9.1 Glass Cell Or Not A Glass Cell?

This remained the question to ask for a quite long time. The obvious advantage of good optical access and a low form factor are balanced by the incompatibility<sup>1</sup> with an atom chip and a double MOT layout. The atom chip was found to be a necessity in order to realise a single 1D trap. Also, as discussed in section 9.3, the double-MOT layout is regarded as being important.

Another drawback of a glass cell is the fact that it is not possible to obtain commercially glass cells with anti-reflection coating on the inside, which is a big drawback for high-performance imaging. The possibility of gluing a glass cell from AR coated glass pieces was rejected, because this had been tried in some groups with varying success[127, 128]. At the end of the day, it was clear that due to the many details in any of the glass cell designs, untested in this research group, and the time needed for testing them is too long.

From this point onwards, the focus was on the design of a steel chamber with high-quality AR-coated viewports. Starting from standard components, it was quickly realised that these would be incompatible with the high imaging demands.

---

<sup>1</sup>It is possible to operate a glass cuvette, which is open at both ends. However this approach had been rather unsuccessfully tried in past experiments in this group.

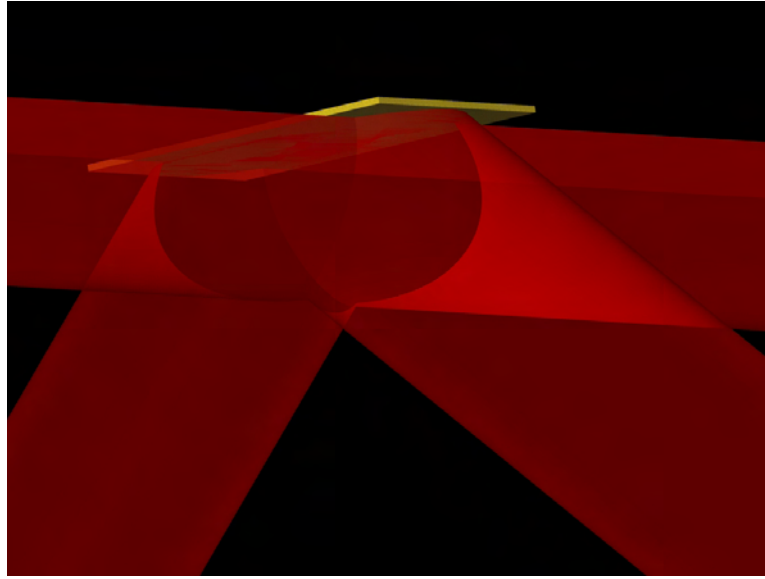


Figure 9.1: The atom chip and mirror-MOT beams, the starting point of all design considerations. The MOT is operated below the centre of the atom chip and the size of the MOT-beams is 1". This leads to an atom chip with the dimensions of 29mm×32.5mm. The distance of the MOT to the edge of the atom chip is 14.5mm and 13.25mm, respectively.

It could have been possible to have one good imaging direction, to the cost of two other rather poor ones. Furthermore, the quality of the available viewports<sup>2</sup> with the usual CF seals is rather low. Alternatively, it is an option to use standard optical quartz windows which can be AR-coated on both sides and to seal them with Helicoflex seals<sup>3</sup>. This type of sealing is also used in all other experiments in this research group.

The atom chip with the MOT beams, as depicted in figure 9.1, is the heart of the experiment and defines the least volume needed for operation. The entire design follows the narrow path between small size on one hand and structural integrity on the other. A step-by-step discussion of this path can be found in the remaining part of this section.

With respect to the other design goals and the constraint of keeping the design as versatile as possible, the intention was to realise as much optical access, i.e. window area, as possible. Using an atom chip made it necessary to build a mirror MOT. It is also possible to start with an ordinary six-beam MOT and then transfer atoms magnetically into a chip trap as described in[101]. However,

<sup>2</sup>Highest-quality viewports in CF technology can be obtained from Kurt J. Lesker Company ([www.lesker.com](http://www.lesker.com)).

<sup>3</sup>The Helicoflex seals are supplied by Garlock Helicoflex, and may be found here: [www.helicoflex.com](http://www.helicoflex.com).

the transfer efficiency of magnetically trapped atoms in a quadrupole trap into a IP-trap on the atom chip can be inefficient. With the technology on hand of a two-layer design [129, 90] of macroscopic copper wire structures and fine wires upon the atom chip it is possible to improve the transfer efficiency. A description of a mirror MOT can be found in section 1.3. From previous experience, and to keep the setup compact, it was decided to work with MOT beams of  $\varnothing$  25mm along the  $45^\circ$  direction and slightly larger beams along the horizontal direction, parallel to the atom chip. Starting with a chip of a slightly larger size compared to the experiments before [129] account for the beam size chosen. To be able to reflect the total beam under a  $45^\circ$  angle the chip had to be  $\sqrt{2}$  times 1", hence it was chosen to be 29mm  $\times$  32.5mm large. This immediately limits the closest possible distance of a window to the chips centre. The layout of the mounting and the atom chip was designed in such a way to overcome this limitation slightly. The details can be found in section 9.6. The size of the two large windows was chosen to be the smallest possible size to allow the 45 degree beams to pass unhindered into the science chamber. This size then limited the closest possible distance the three other viewports could be placed from the chips centre. All windows need some additional space for the seals and flanges, which was minimised. Section 9.2 gives an overview of the design.

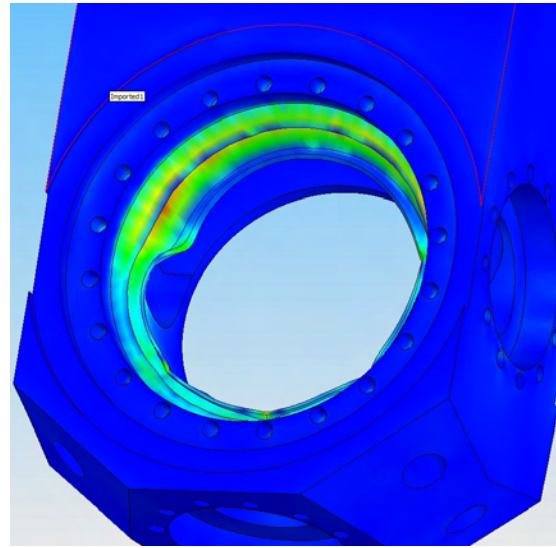
Still two problems remained: how to bring the atoms in and how to pump the science volume efficiently. For a push beam to work efficiently it is important to minimize the distance between the two MOTs. We subsequently optimised the distance of our second MOT with respect to the cost of limiting optical access to the science MOT. The result can be found in figure 9.4.

Consulting the Helicoflex catalogue suggested that basically all shapes of seals are possible. This led to the idea of reassembling a cuvette like chamber on a thin steel frame with a connection for the lower MOT. From previous experience and discussions with other groups it was decided that the risk of getting the tightening moments wrong or unevenly spread along the seal was too high. To avoid asymmetric tension in the glass windows it was agreed to stick with symmetric shapes, i.e. round windows. With today's experience, see appendix B, this turned out to be a very important decision. It was found that the load on the seals is the dominating load in the whole setup. The total tightening load<sup>4</sup> for one of the large window seals is  $\sim 63\text{kN}$  and  $\sim 21\text{kN}$  for the small windows. The clamping section in the design needs to be able to handle these loads. In section 9.2 one may find finite element calculations on the forces occurring in the final chamber design.

---

<sup>4</sup>The values are calculated from  $F = 2\pi D \times Y_2$ , where  $Y_2$  is the tightening load per unit-length in [N/mm] and 180 for the large and 140 for the small windows respectively.

Figure 9.2: First layout of the science chamber. The deformation is scaled by a factor of 1200. The colour map indicates increasing von Mises stress from blue to red. The whole upper half arc of the sealing surface is giving way due to the high load.



## 9.2 The Science Chamber

As the whole chamber had been designed without any outside support, a numerical analysis on the forces and subsequent deformations on the window seal clamps was performed. Initial attempts with the FEMLAB software packages were stopped, as the mesh generator could not handle the complexity of the final chamber design. Therefore, the finite element code within the Solidworks CAD software was used and the ring, which supports the seal, was loaded with 63kN. The results of our first design attempt were devastating, see figure 9.2. This design was not able to handle the load, large deformations and forces above the maximal ductile stress limit of the steel where found. Analysis with the finite-element code revealed deformations up to  $25\mu\text{m}$ .

To evaluate the reliability of the employed code the results of a very simplified model were compared to analytical solutions and the two finite-element codes. The model used for the test of methods is the bending of a steel slab, which is fixed at one surface and loaded at the opposing surface with a force of 1000N, see figure 9.3 for the deformed shape and stress distribution (color) from the SolidWorks output. The test sample is  $10\text{mm}\times 10\text{mm}\times 2\text{mm}$  in size. The displacement is well reproduced by all methods, the maximum von Mises stress differs slightly between the methods. The results are summarised in table 9.1. The deviation is acceptable, as in this analysis the order of magnitude is the relevant measure.

As the steel block had already its outer shape, the freedom for changes was therefore very limited. The resulting chamber layout can be found in section A. The windows were moved outwards by 3 mm and on the inside there was some material left in the corners, see figure A.7 for a cross section. Furthermore, all corners which were initially at a straight angle, were rounded to allow a smoother loading of these corners, see figure A.6 for a details. The results of these



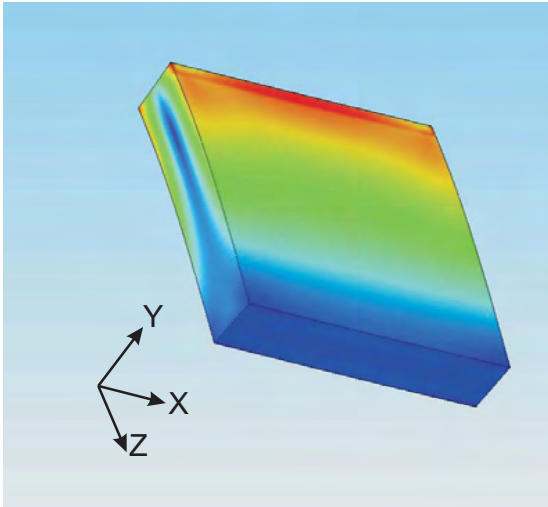


Figure 9.3: Stress distribution in the test piece. The piece is clamped at the back face and loaded at the front face with a force of 1000N perpendicular to the x-z-plane. The upper half of the piece experiences tension, whereas the bottom half experiences compression forces. This results in a central part where neither tension nor compression occurs. The colour map indicates increasing stress blue to red.

Method	max. deformation [m]	max. von Mises stress [N/m <sup>2</sup> ]
SolidWorks	$2.63 \times 10^{-4}$	$1.48 \times 10^9$
FEMLAB	$2.63 \times 10^{-4}$	$1.51 \times 10^9$
Analytical Model	$2.63 \times 10^{-4}$	$1.50 \times 10^9$

Table 9.1: Results of the deformation studies with the simple steel slab, see figur 9.3. All three methods agree well, at least within the order of magnitude.

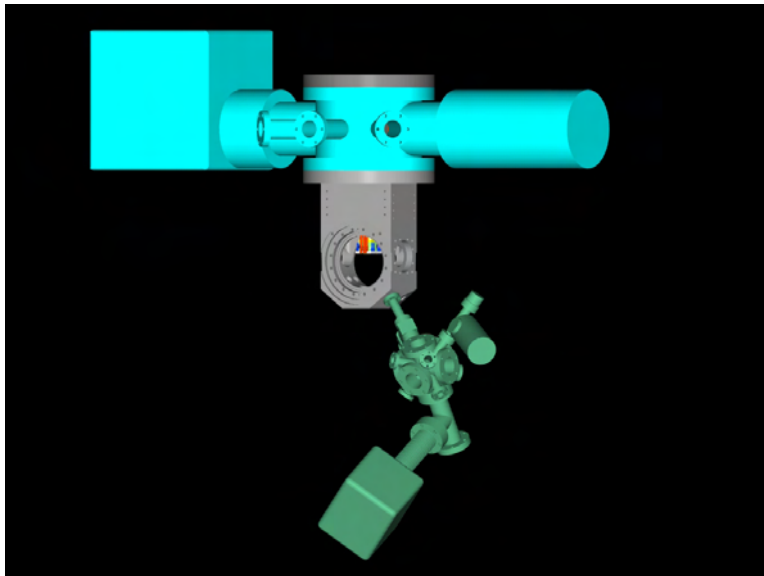


Figure 9.4: The whole vacuum assembly. Lower-MOT, science chamber, pump chamber and chip mounting.

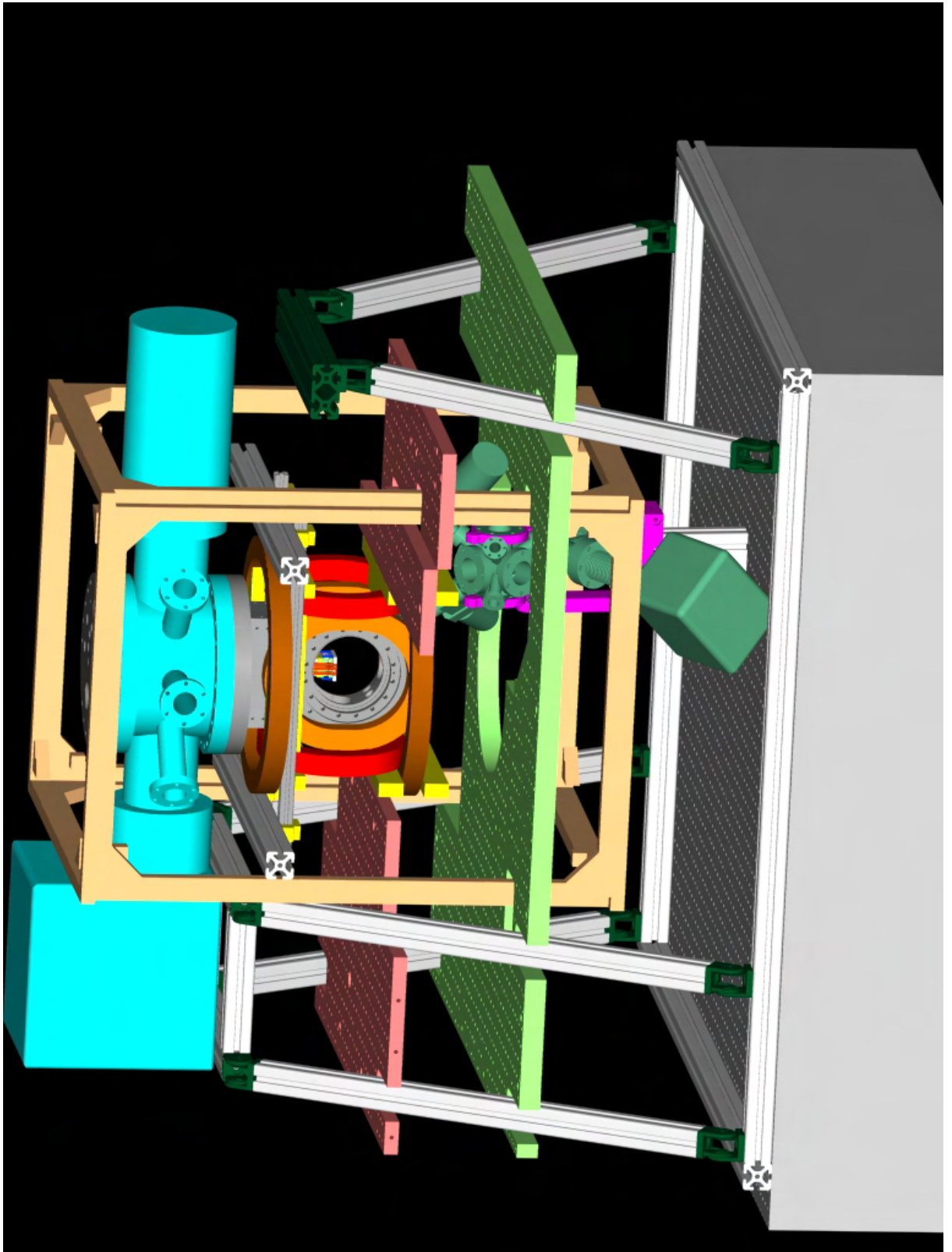


Figure 9.5: The whole experiment setup including vacuum, mounting, bias and compensation coils, table and optics boards. Optics and light beams have been omitted for clarity.

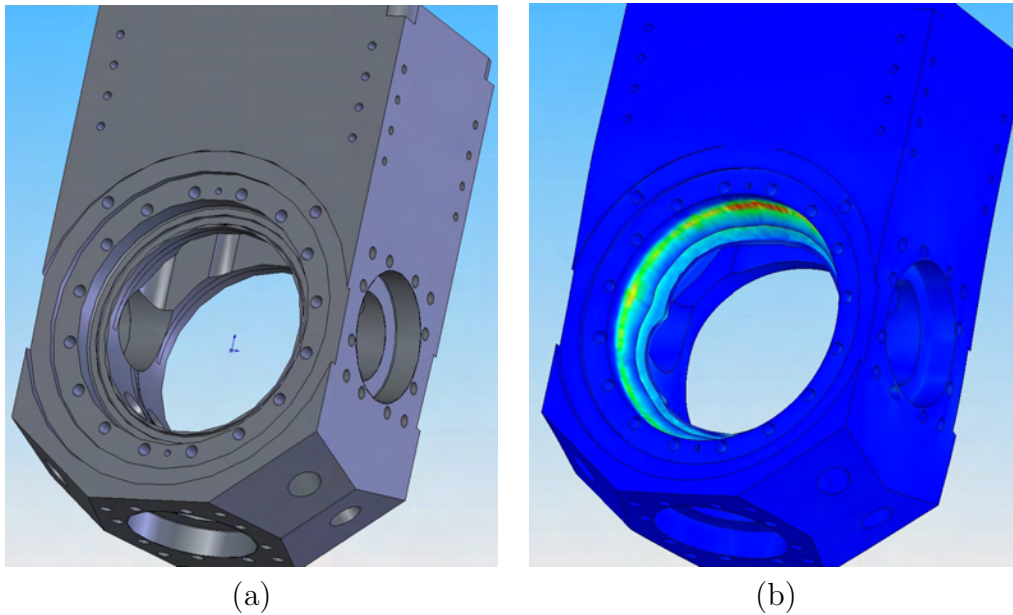


Figure 9.6: Final version of the science chamber (a) and the deformation and von Mises stress distribution (b). assembly in the clean-room environment.

changes can be seen in figure 9.6, it should be noted that the scale for the colour maps and deformations in figure 9.6 and figure 9.2 are different. This is due to the fact that the SolidWorks software chooses the scaling factors and colour scales automatically and there is no option to change these values by the user. The deformation is scaled by a factor of 4000 and a maximal deformation was found to be  $6\mu\text{m}$ . This is a reduction of a factor of over four.

Drawback of the changes made are the following. Moving the windows out increases the minimal working distance for the transversal imaging optics and therefore imaging quality and the material on the inside reduces the open cross-section for pumping by 20%. This reduction in cross-section reduces the achievable pump speed.

It was decided that the pumping would be done from the remaining side. This is the same side as from where the mounting and atom chip is brought into the science chamber, the vertical direction in figure 9.4. For this purpose the so-called pumping chamber, which can be seen in figure 9.4 was constructed off this chamber, a TSP<sup>5</sup> and an ion pump<sup>6</sup>. The TSP is inside the tube on the upper right-hand side and the ion pump is the big box in the upper left hand corner of the picture. There are also six CF 40 ports to this chamber. Currently three are in use: one for a UHV ion gauge, one for an all-metal valve to seal off the chamber and one for a standard viewport. The Mounting and science chamber

<sup>5</sup>Titanium Sublimation Pump

<sup>6</sup>Varian StarCell 150 l/sec

are attached via the two opposing CF 200 ports.

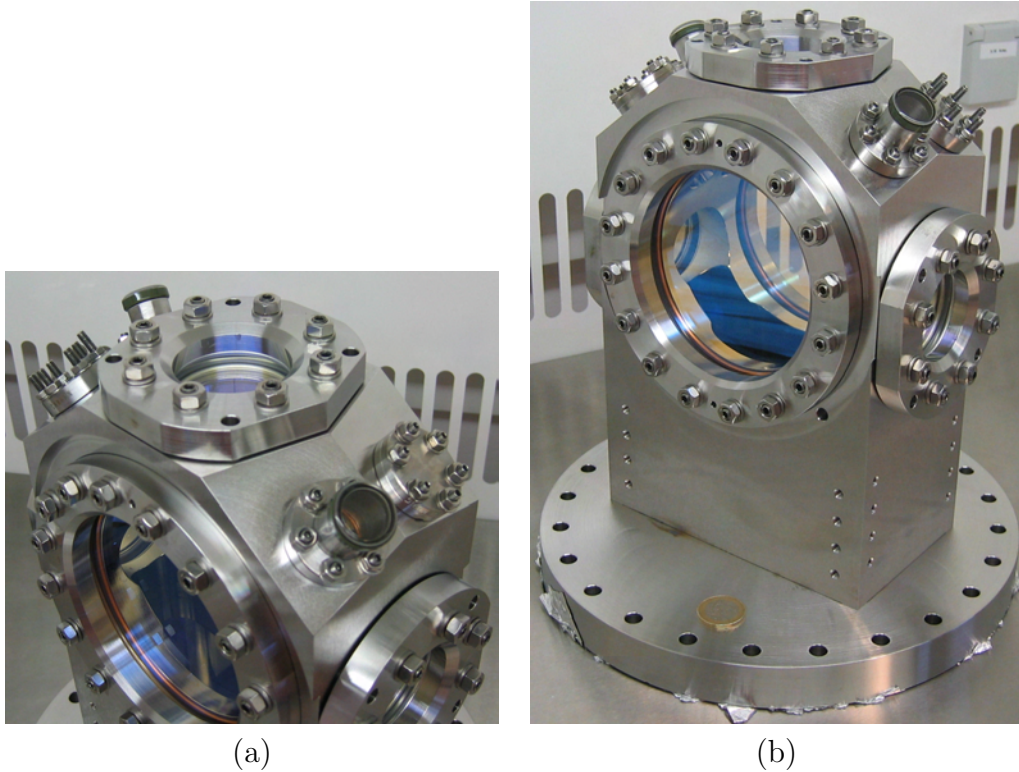


Figure 9.7: Science chamber after assembly in the clean-room environment.

### 9.3 Double-MOT Layout

The desire for a long lifetime in the magnetic trap lead to the development of a double-MOT layout. The necessary vacuum<sup>7</sup> conditions in a single-chamber setup can only be achieved with a very high pumping speed, as dispenser sources always spoil vacuum at this level. A discussion on vacuum conditions and dispenser operation in a single-chamber setup can be found in [130]. However, high pumping speed in the experimental region is usually connected to a large cross section for the connection to the pump<sup>8</sup>. This unfortunately collides with the constraint of good optical access from possibly all sides.

Apart from dispenser sources there are also other methods[131, 132, 133] for generating a large background pressure from which a sufficiently large<sup>9</sup> number of atoms can be trapped in a MOT. As these methods were not well established

<sup>7</sup> $p < 10^{-11}$  mbar

<sup>8</sup>Currently available Ion Pumps need a CF 100 flange for a pumping speed of 150 l/s and a CF 150 flange for a pumping speed of 300 l/s.

<sup>9</sup>Some  $10^9$   $^{87}\text{Rb}$  atoms should be expected in a such a MOT.

at this time and initial tries with Rb in one of the Heidelberg experiment did not give promising results, it was decided that the Vienna experiment should not depend on this method. Learning from the first BEC Experiment [134, 129] in Heidelberg, the idea of a double-MOT layout was adapted. Also other experiments [109, 3] employed similar techniques with good success. The possibility of connecting two separate vacuum chambers with very different pressures whilst maintaining this difference in pressure through a resistive connection is a huge advantage compared to a single-chamber setup. Through this resistive coupling it is possible to transfer atoms via a laser beam<sup>10</sup> and still maintain more than three orders of magnitude in pressure difference between the two volumes. Hence, the connection to the pumps from the science-chamber<sup>11</sup> can be of a smaller cross section and the whole science chamber becomes slimmer. With the current layout it is possible to maintain a high pumping speed and possibly excellent vacuum in the science chamber, as well as a very small footprint. The cost for this is the additional effort of operating two extra MOTs and a push beams.

The lower MOT consists of a CF 40 6-way-cross, where CF 16 ports are welded into all corners. This results in 6 Cf 40 ports and 8 CF 16 ports. An image of this chamber may be found in figure 9.8. An ion pump<sup>12</sup> is connected through a CF40 bellow to a CF 40 T-piece. All CF 40 Ports are sealed by standard uncoated windows. These six ports are used for the six-beam MOTs in this chamber. Two CF 16 flanges are connected to dispenser sources, one for Rb AMDs<sup>13</sup> and one for the home-built K dispensers. The dispenser sources are heated due to ohmic heating and current is brought into the vacuum chamber via 10A electric-feedthroughs. There are always two dispensers mounted in parallel on a Macor spacer to prevent electric contact to the chamber. Two other flanges are connected to CF 16 all-metal valves, where one is for the connection to the differential pumping stage towards the science chamber<sup>14</sup> and the other one is to seal the chamber off from the environment and to allow for pumping after the vacuum has been opened. The remaining CF 16 flanges are sealed with standard CF 16 Viewports. The opposing port to the differential pumping station is reserved for the push beam and the remaining ports are available for diagnostics. Such diagnostics could be a calibrated photodiode for the detection of fluorescence from the MOTs and simple cameras for aligning purposes. As the connection to the science chamber is very fragile and the tapped blind holes are quite fragile, a special mount was

---

<sup>10</sup>There are also other options for this transfer, such as moving coils or magnetic conveyor belts. As a laser is used in this setup there will be no further discussion on other methods, see for example [135, 106].

<sup>11</sup>From now on the chamber containing the atom chip at UHV will be termed science chamber. The chamber containing the atom sources will be referred to as the lower MOT.

<sup>12</sup>The pump is an Varian 20l/s Star-Cell ion pump.

<sup>13</sup>Commercially available dispensers from SEAS Getters Inc., model number ...

<sup>14</sup>One could argue that this valve is not necessary. But this allows to change the chip without braking the vacuum of the lower MOT and vice versa.

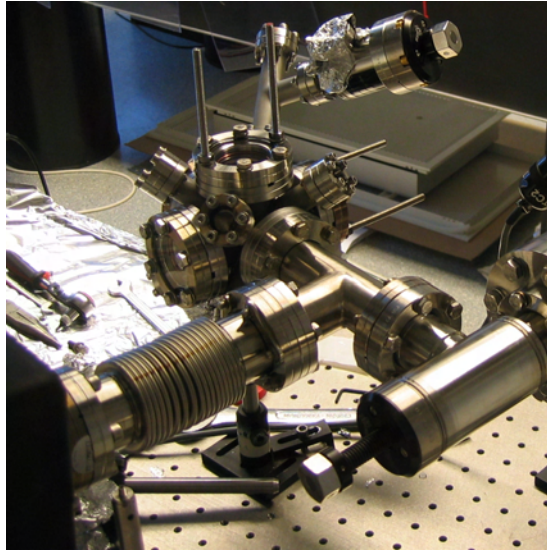


Figure 9.8: The lower MOT cell during initial assembly. The CF-40 and CF-16 Viewports and the bellow to the ion pump are clearly visible. Also the threaded rods for the mirror mounts can be seen. The all-metal valve is now replaced by a viewport.

designed to be able to position the lower MOT chamber precisely and take all weight from it. Drawings for this mount may be found in the section A, figures A.13, A.14 and A.15.

The quadrupole field for the lower MOT is generated by two coils<sup>15</sup> which are directly wound onto the chamber. Furthermore, there is a set of compensation coils for each direction attached to each flange. The cooling light for the lower MOT is retro-reflected for each direction. This reduces the amount and space taken by optics for a separate beam in each of the six directions. The mechanical mount for the retro-reflecting mirrors is quite simple. Two of the six M6 bolts in three of the CF 40 window flanges are threaded rods extending approximately 9 cm outwards. The mirrors are screwed to bars which are attached to those threaded rods. Quarter-wave-plates are glued to the mirror mounts. A picture of the complete lower MOT setup can be found in figure 9.8. Details of the optical layout for the lower MOT can be found in figure 9.9; however it should be kept in mind that the MOT beams for K and Rb are superimposed and brought to the experiment region via optical fibers.

Comparing the current layout to the previous one [134, 129], there is one striking difference - the angle between science chamber and lower MOT. Most ex-

<sup>15</sup>Two coils of insulated  $\varnothing$  1.5 mm copper wire with 90 turns each generate a calculated gradient of 4 G/cm/A.

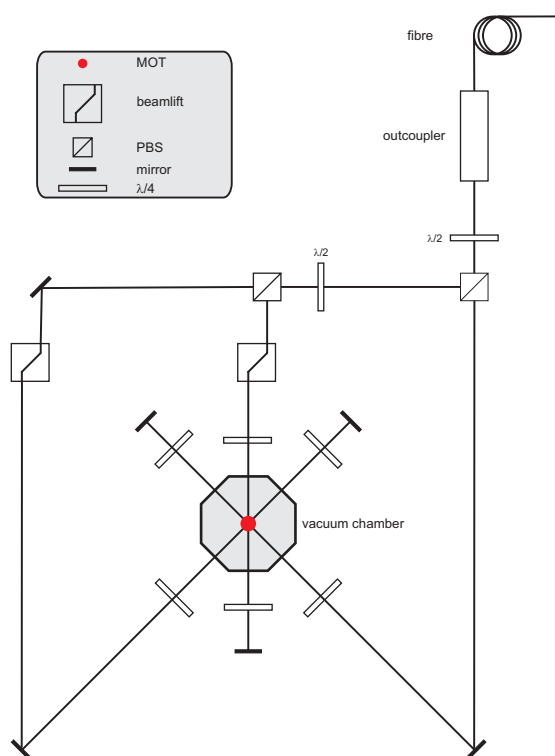


Figure 9.9: Optics layout of the two six-beam MOTs in the lower chamber. The cooling and repumping light for both species is superimposed at the other end of the fiber. It should be kept in mind that the beams are mutually perpendicular. All steering mirrors are summarised in the *beamlift*.

periments with push beams are orientated in such a way that the push beam is parallel to the the direction of gravity [109, 90]. It was decided to move away from the central axes to allow for an unobstructed viewport from below. Therefore, the current layout is a compromise between the parallel layout and the orthogonal layout, as described in [3]. Optical access from below the chip was not possible with the old setup [129] and could be of some interest, as mentioned in section 8.6. As the distance between the lower MOT and the science-MOT is shortened from 500mm to 255mm it can be expected to perform equally well; however this has to be proven. The axes of the push beam runs through the differential pumping stage and also through the chip's centre and the lower MOT centre.

## 9.4 Construction

The science chamber is supported by a ridged aluminium frame<sup>16</sup>, which rests on the optical table. The optics boards are connected to this frame and are contributing to the stiffness of the frame; hence, the chamber and the optics boards are a fixed compound. The coils are supported with a separate frame and are mechanically disconnected from the chamber and the optics boards. This assures that all mechanical vibrations from the coils are transferred away from

<sup>16</sup>Versatile aluminium profiles are obtained from item, see: [www.item.info](http://www.item.info)

the chamber. To avoid eddy currents, the mounting of the coils is made from insulating glass reinforced epoxy material.

## 9.5 Imaging

Transversal imaging was defined as a major design goal. Imaging close to the chip is best done in a slightly reflecting way [71, 78]. This way of imaging is advantageous for two reasons: firstly, it minimizes the amount of diffracted light from the edges and, secondly, it gives one the possibility of judging the distance between the trapped atoms and the surface of the atom chip, as a reflection of the cloud is visible in the gold mirror. Therefore, it is advantageous for imaging close to the chip to increase the angle well above a glazing incidence. It should be kept in mind that the imaging light will form a standing wave below the chip. The periodicity  $a$  of this standing wave increases with the angle  $\alpha$  of incidence according to  $a = \lambda/2 \sin(\alpha)$ , where  $\lambda$  is the wavelength of the light. This standing wave will cause a modulation in the absorption, as the intensity periodically varies between no light and 4 times the incident intensity [78, 72]. Knowing this, it was decided that the whole chamber should be optimised for transversal imaging under an angle of  $2^\circ$ . However, not only the chamber had to be designed to this angle, but also the chip layout is such that that the imaging beam will not be disturbed by structures in the chip, see also figure 9.10. The imaging light (light-gray) enters from the left hand side at an angle of  $2^\circ$ . The cloud of atoms (red) will absorb light from the imaging beam and cast a shadow (black) towards the right hand side. There is one shadow from the un-reflected imaging light and one from the reflected light, illustrated with the dashed lines in figure 9.10. The gold on the chip is placed in such a way that on the direct paths the imaging light before and after the cloud will not reflect of any etchings in the gold.

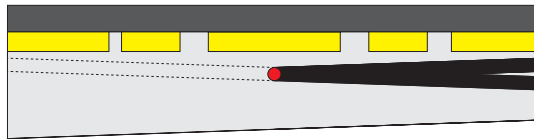


Figure 9.10: Chip layout and imaging light. Imaging light enters from the left hand side at an angle of  $2^\circ$  (light-gray). The atoms (red) cast shadows from the direct and the reflected (dashed) light. No etchings in the gold are along the direct path of the incoming light to the atoms and on the path of the shadows.

The properties of an imaging system will deviate from its free-space performance as soon as it is used for imaging through a thick glass plate, i.e. the vacuum



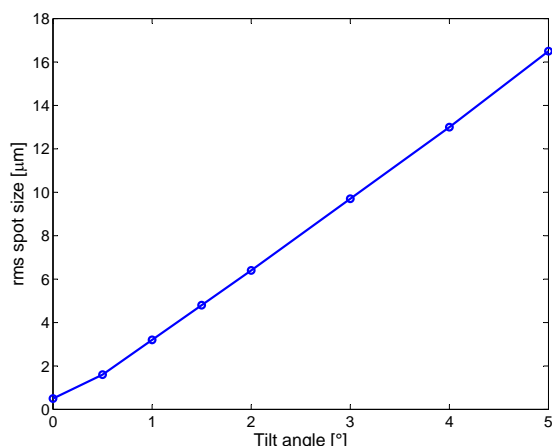


Figure 9.11: Calculated rms spot size vs. tilt angle  $\phi$  of the vacuum window.

window. A lens design aiming at high resolution has to take the glass plate into account. In the present layout all windows<sup>17</sup> are 10mm-thick AR-coated quartz windows<sup>18</sup>. As an aid during the design process of an optimised lens for this special imaging application, optical design software<sup>19</sup> was used. The effect of the thick glass plate can be taken into account as long as the window is perpendicular to the optical axis. As soon as the window is at an angle to the axis, things become increasingly difficult, as aberrations become asymmetric and in general, very difficult to compensate for, see figure 9.12 for details. The figure shows the actual design for the lens system used for imaging. The lens for selecting the required magnification has been omitted. Parallel light is entering the lens from the left hand side and is focused. Between the last optical element and the focus, a 10 mm-thick quartz glass plate is placed. In the lower half of figure 9.12, the spot sizes in the focal plane for various tilt-angles  $\phi$  are shown, (a)–(h). For comparison the Airy disk of the optical system and the rms spotsizes are also shown and plotted in figure 9.11. The size of the reference bars is given in  $\mu\text{m}$ . It is notable that even for small angles a strong asymmetry is visible and a spot size better than  $3\mu\text{m}$  cannot be achieved if the angle is  $1^\circ$  or more. To fully exploit the advantage of the tilted windows, the optics has to be carefully aligned orthogonal to it. The current chamber layout features holes for alignment rods, at the angle of  $2^\circ$ . This will allow for easy alignment of the imaging optics and, hence, high resolution imaging in a range of  $2^\circ \pm 0.5^\circ$ .

The distance from the window to the chip's centre should be as small as possi-

<sup>17</sup>Due to damage to one of the large windows, it was replaced by a standard uncoated 15 mm thick BK7 substrate. This will be used to bring the imaging light in, as it will harm the least at this point.

<sup>18</sup>The windows are made from Vitreosil IR, specifications can be obtained from Saint-Gobain Quartz PLC

<sup>19</sup>The software in use is developed and distributed by ZEMAX Development Corporation: [www.zemax.com](http://www.zemax.com)

ble, therefore, the point of rotation for the large windows was set exactly there, see figure A.8. As the lower parts of the window moved inwards with increasing angle the largest possible size for the window from below is reduced. The angle of two degrees is a compromise between large angle imaging and a reasonably large window from below. The current design allow to place the first optical element of the transversal imaging optics as close as 40mm to the chips centre. As the cloud will move 2mm away from the chips centre due to the trap geometry, see section 9.6, the closest working distance is 38mm. It should also be pointed out that the whole imaging optics assembly has to be mounted in such way that it can be precisely tilted by the same angle. This is is a non-trivial task, as it needs to be movable along the optical axis for focusing with a resolution in the order of the depth of field, which is the  $\sim 2\mu\text{m}$ . It needs to move along the vertical direction by 2mm to follow the cloud during time-of-flight and as mentioned before the angle needs to be adjustable. Furthermore, there is an option for an overview image in the transversal direction. This is realised with the help of a 1 inch flip mirror holder<sup>20</sup> and a pixelfly<sup>21</sup> camera.

In section E a calculation of the expected performance of the actual imaging setup can be found. It shows, that 2 atoms per resolution size  $(\pi(1e - 6)^2)$  can be detected with a signal to noise ratio of 2.

Along the longitudinal direction, imaging will be superimposed on the MOT beams, as depicted in figure 9.13. In principle, the first lens of the imaging system could be placed as close as 82mm from the chip's centre. However, it was decided not to do this in the first layout. As the MOT beam passes through the same optical path and should be a collimated beam, it would have to be focused beforehand to compensate for the imaging optics. This is of course possible in the current design; however, the additional effort in aligning such a system is avoided at this stage. Currently, the imaging optics is located just behind a polarising beam splitter cube, where the MOT and imaging light is separated. This results in a working distance of 150mm.

Due to the rigid construction of the optics boards, see section 9.4, around the science chamber, it will also be possible to employ interferometric non-destructive imaging methods [136]. This could be useful if the evolution of the cloud in situ is of interest and could be applied transversally as well as along the cloud.

Along the third direction, orthogonal to the atom chip, it will be possible to introduce a standing wave dipole trap, which would result in an array of 2D traps. Those traps would be stacked like a pile of pan cakes[137, 130]. Furthermore the imaging of a light-sheet-detector, as discussed in [138], can be realized along this direction. As the distance from the atom chip to the first possible optical element

---

<sup>20</sup>New Focus Model number 8892

<sup>21</sup>The pixelfly cameras are manufactured and sold by PCO AG, [www.pco.de](http://www.pco.de) is the current web address. Here the qe-double-shutter version is used.

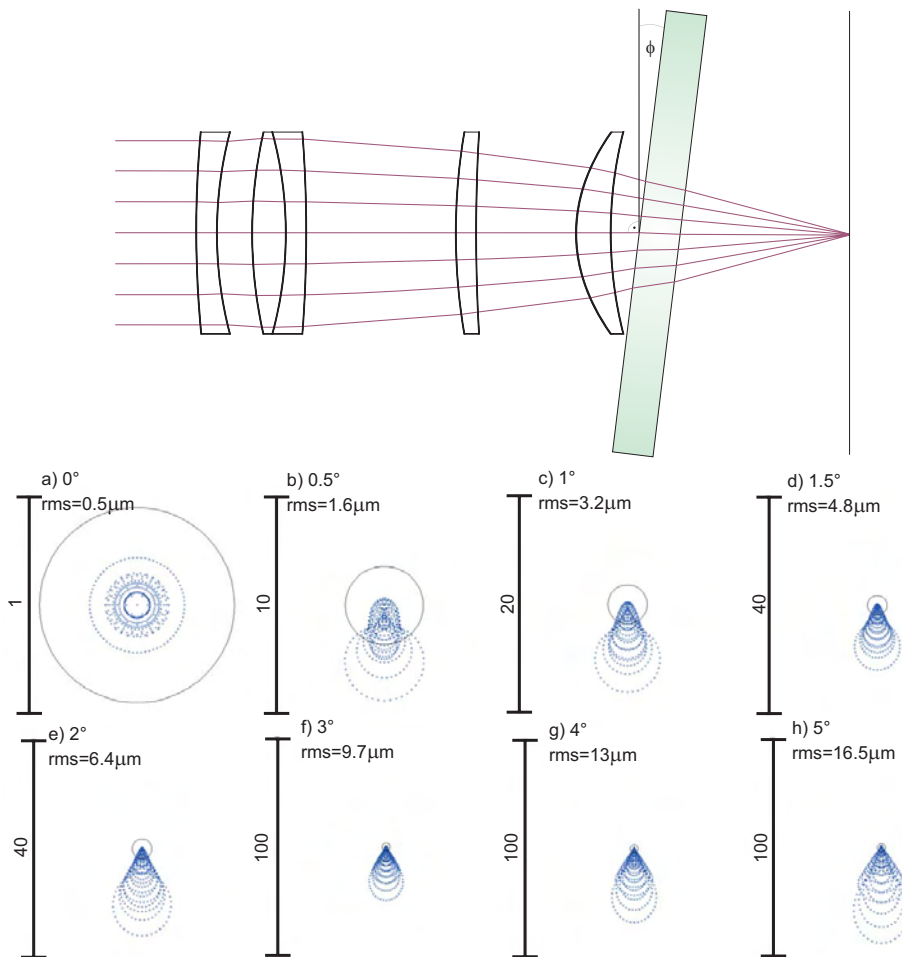


Figure 9.12: The effect of a tilted 10mm thick glass window on the spot size of the imaging system is studied for different angles of tilt  $\phi$ , (a)-(h). (top) Layout of the current lens system. (below) Zemax calculations of the spot size for different angles of tilt. For this calculation a plane wavefront enters the lens system from the left and the size of the focus is calculated. Scalebars in  $\mu\text{m}$ . See [15]

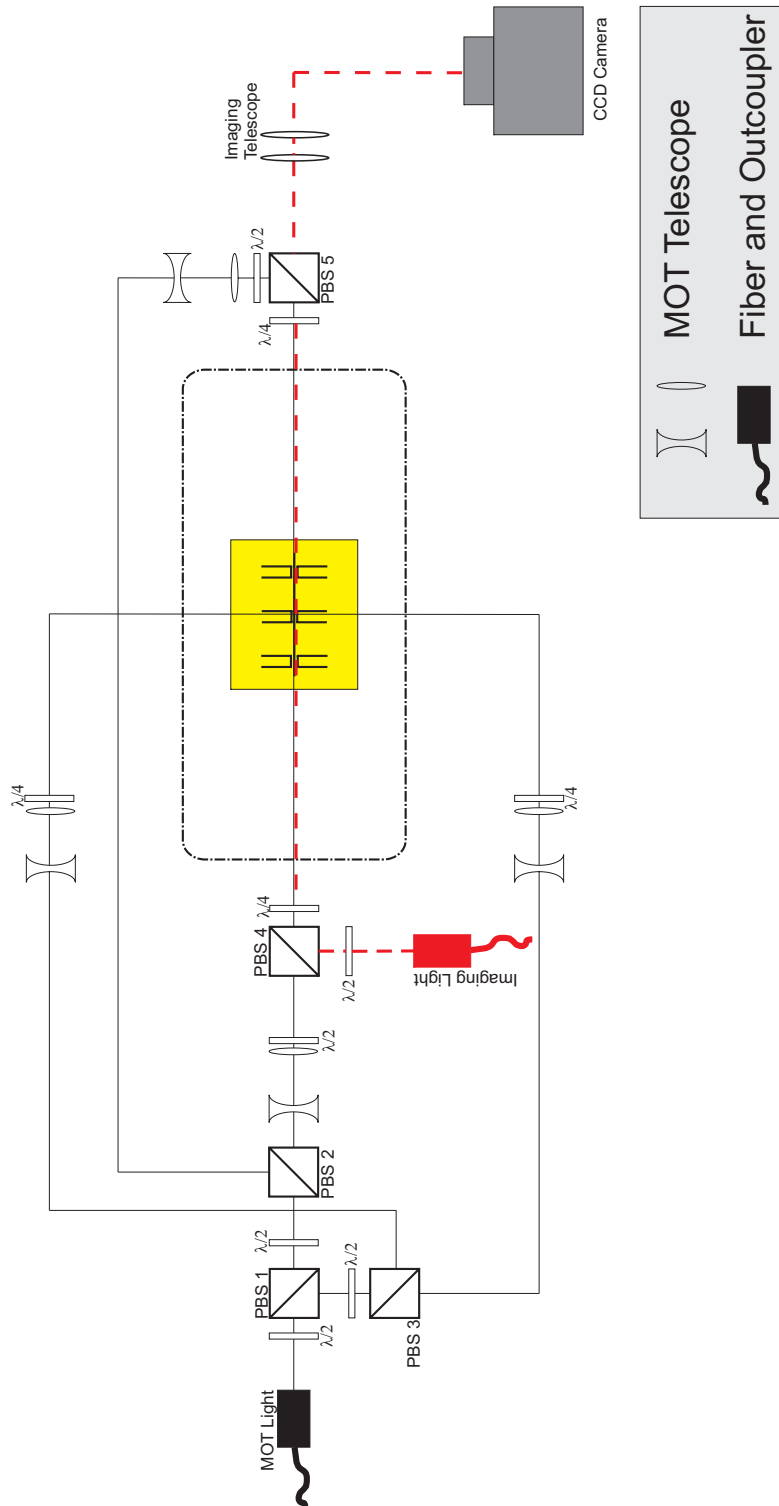


Figure 9.13: Optics-layout for the mirror MOT and the longitudinal absorption imaging. Mirrors and additional beam steering are omitted for clarity. Note that the imaging light will be circular polarised in this layout. This has to be taken into account in the image analysis, as the Clebsch-Gordan coefficients are different compared to the usually used linear polarisation.

is  $\sim 105\text{mm}$  at a free diameter of  $40\text{mm}$  a  $f/\# = 2.6$  is already feasible. With the help of a re-entrant window, this could be improved to a  $f/\# = 1.7$ .

## 9.6 Mounting and atom chip

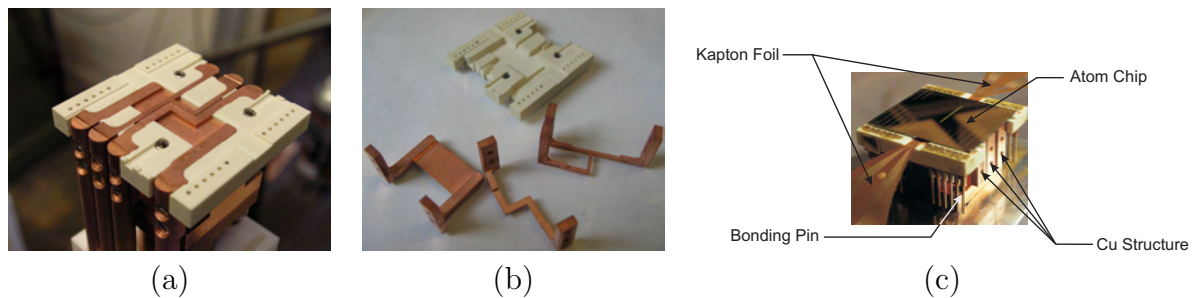


Figure 9.14: (a) Assembled and mounted copper and Shapal parts and (b) before assembly. (c) The mounting head before bonding. The different layer are labelled: atom chip, Kapton foil and Cu structure. Note: the three elements of the copper structure are electrically disconnected.

In this section there is only a short overview of the employed mounting and atom chip. A thorough discussion and all technical details can be found in [139]. In the current layout, the mounting head consists of four layers, see figure 9.14 (c). Layer one is the atom chip itself. Figure 9.15 shows an overview as well as a zoom in on the central region of the chip. Layer two consists of two Cu parts, see figure 9.14. The two Z-shaped wires can be operated independently of each other. This results in a large-volume trap at the initial loading of the magnetic trap. After this initial loading stage, the current in the big structure is ramped down and the trap is compressed towards the small structure. This moves the whole trap approximately 2 mm towards the imaging window. This asymmetry can also be found in the atom chip layout. The third layer is a large Cu wire in a flat U-shape [28] and is used for the mirror MOT. The fourth layer is a  $50\mu\text{m}$ -thick Kapton foil<sup>22</sup> with  $35\mu\text{m}$ -high and  $500\mu\text{m}$ -wide copper wires. These are intended to be used in time-dependent traps and are connected via coaxial cable<sup>23</sup> to the outside world.

<sup>22</sup>This foil is a flexible glue-less printed circuit board material. The readily patterned strips are obtained from Andus: [www.andus.de](http://www.andus.de)

<sup>23</sup>Cable and feedthroughs are obtained from a Berlin based company Allectra, <http://www.allectra.com/>.

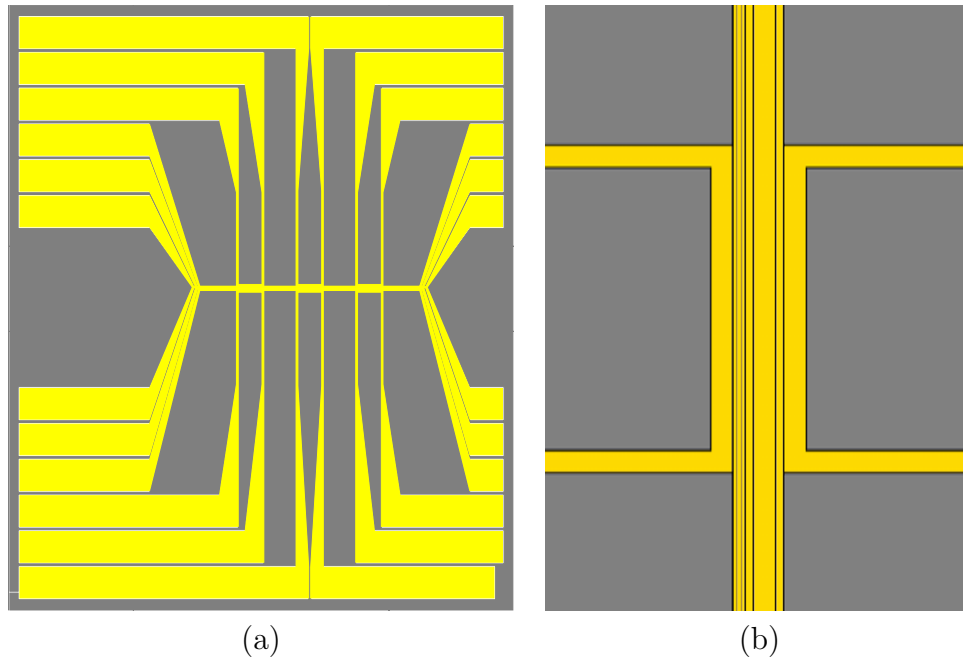


Figure 9.15: (a) Overview of the current chip design and (b) close up of the central region. Note, that (b) is rotated by  $90^\circ$ . The size of the whole chip (a) is  $29\text{mm} \times 32.5\text{mm}$  and the width of the large wires (yellow) in (b) is  $100\mu\text{m}$ .

## 9.7 Technological Details

Once the design was agreed on, all drawings were finished and sent the off to a mechanical workshop<sup>24</sup>. The body of the science chamber was milled out from a single block of steel, and afterwards the chamber was welded into a CF 200 flange, see details from figure A.12. The details of this welding may be found in figure A.10.

After all the mechanical work had been done, the chamber was sent off for electropolishing of the inside surface. From the remaining steel the three flanges for the Windows were machined according to figures A.1, A.2 and A.3. Apart from the screw holes for tightening the seal, four additional reamed holes were introduced, which are arranged at the corners of a  $60 \times 60$  mm square. These holes assure a precise alignment of the flange to the chamber. Furthermore, they are designed such that they are compatible with the 2" cage system from Thorlabs. This is particularly useful as it allows for precise and easy alignment of optical components with respect to the chamber. To tighten all flanges we use M6 threaded bolts and nuts. This is a safety feature of some sort, as it assures

<sup>24</sup>The workshop is located in Vienna and called Mitech([www.mitech.at](http://www.mitech.at)). This workshop can be warmly recommended to all our competitors, as this company is "fast" and "reliable".

that the flange can be removed even if the nut is baked<sup>25</sup> to the bolt. The drawings for the two large windows can be found in figure A.1. Note the difference between the the large and small windows with respect to the point where the seal is located. As HLV-290 seals with a little wing are used for the small windows, the alignment is achieved due to the rim of the 1.5 mm recess. For the large windows, Cu HNV-200 seals are used, which do not have the wings. All seals need to be well aligned to each other, as otherwise shear forces could destroy the quartz glass windows. Hence, the groove is designed for the Cu seals as specified by Helicoflex manufacturers. The alignment of the large flange with respect to the chamber is assured with the two  $\varnothing 3\text{mm}$  reamed holes. To avoid the steel touching the glass directly and to be able to judge the compression of the seal-window-seal system, two seals are used, one below and one above the window. As the outer flange does not touch the chamber, a dial gauge was used to determine the exact compression of the seals around the flange. For this purpose, a reference surface at the  $2^\circ$  angle is machined onto the chamber. The torque on the bolts can only serve as an indication as differences in lubrication can cause severe deviations from the expected value.

## 9.8 Bias Field Coils

The mirror MOT and all magnetic traps are designed in such a way that only homogeneous bias fields are needed. For the large scale Cu-wire traps, bias fields up to 120G are required. For the traps on the atom chip, fields up to 30G are needed. These demands could be met with two approaches, one coil for the whole range or dedicated sets of coils for improved performance. For reasons of space, it was decided to build only one set of coils for each direction, leaving the possibility of adding another set of coils if it turns out to be insufficiently stable after some time. Especially for the Y-direction, this could become useful, as a field of approximately 1 Gauss is required to maintain the trap bottom once the atoms are entirely in the chip traps. With the given constraints of the chamber, the coils are built as close to the Helmholtz configuration as possible. To speed up manufacturing, it was also decided to have four almost-identical coils and two different of a different shape. The four coils for X and Y directions are almost identical except for the location where the wire enters and exits the coil; this has been shifted by a quarter turn so that it will not obscure optical access, see figure 9.16. The coils were manufactured inhouse with the help of the mechanical workshop in Vienna. The wire in use is a hollow Cu wire with a quadratic cross-section which is cooled on the inside via a cooling liquid and insulated with a woven Kapton ribbon on the outside. To avoid any eddy currents, the coils are mounted such that the current paths in metal assembly parts are broken and

---

<sup>25</sup>To prevent this and also to prevent the bolts from getting stuck in the chamber lead based anti seas grease was used to the bolts and nuts.

Figure 9.16: First oval coil directly after the mould was removed. The Kapton insulated wire and the white epoxy are clearly visible. At this coil the wire enters the inside of the coil at "9 o'clock". in contrast, the wire enters the inside of the the X-bias coils at "12 o'clock".

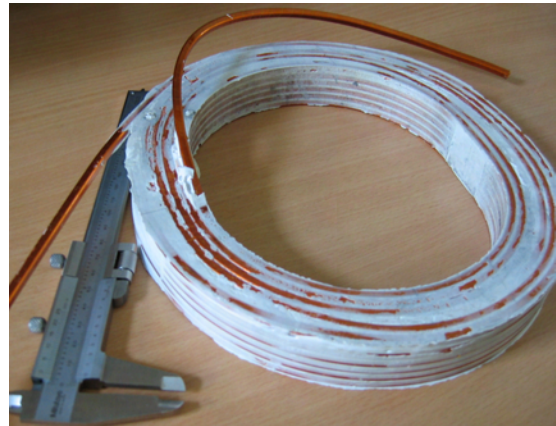
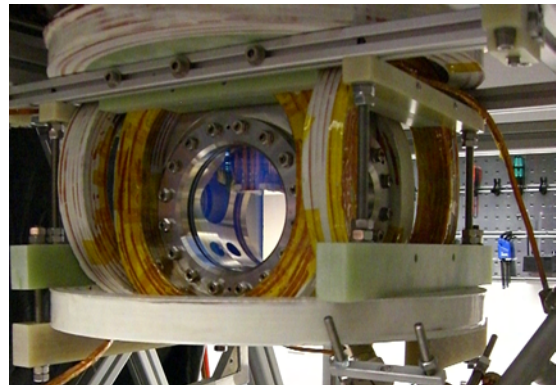


Figure 9.17: Coils mounted to the chamber. The green epoxy-parts of the coil mounts are clearly visible.



most mounting parts are manufactured from glass-reinforced epoxy material<sup>26</sup>. The entire coil and coil-mount package can safely be heated up to 150 °C. This reduces the time needed for a chip change significantly, as the coils do not need to be removed for vacuum bakeout.

The cooling liquid prevents the coils from heating, and reducing the amount of possible mechanical deformations and gives also additional stability, as the resistance<sup>27</sup> of the coils will not change much. In chapter 9.9, further means to avoid any drift or fluctuations within the bias fields will be discuss. Table 9.2 lists relevant parameters for the actual coils.

<sup>26</sup>The fiber-glass-reinforced epoxy is EPG-GC-201 and supplied and machined by Hippe, [www.hippe.de](http://www.hippe.de)

<sup>27</sup>As discussed in ?? the power supplies are operated in a constant voltage mode. In this mode the supplies are less noisy on the current they supply.



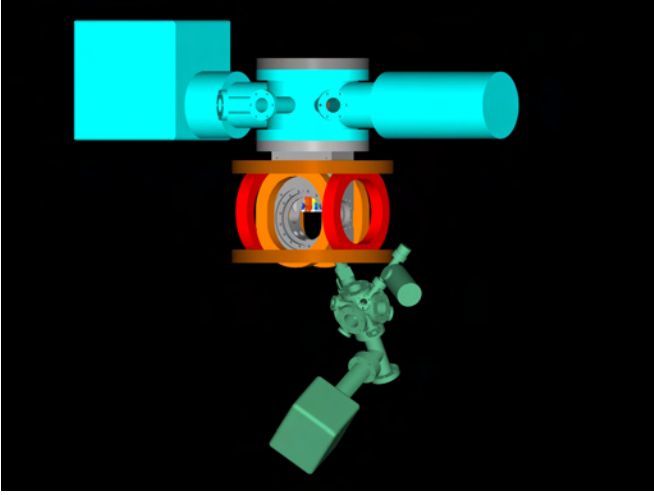


Figure 9.18: Vacuum setup with bias-field coils. Connections for power and cooling to the coils are omitted for clarity.

Direction	X	Y	Z
Turns	36	36	36
Field [G/A]	2.7	1.2	1.7
Inductance[mH]	0.28	0.28	0.7
Resistance[m $\Omega$ ]	100	99	XYZ
Shape	oval	oval	round

Table 9.2: Relevant parameters for the bias coils.

## 9.9 Feedback

### 9.9.1 Current–Feedback

As discussed in section 8.2, the stability of the currents through the wires and coils has to be stable, to produce stable traps. Following initial efforts of [72], a dedicated high-current feedback module was developed. In contrast to [72], where the current is sensed with a flux sensor, the current design employs a resistor for the current sensing. This is done to reduce the noise from the sensor signal. The resistor has to be picked as large as possible for the current range used. Limitations to the resistance are given due to the power dissipated at this point. The resistors in use are ultra stable high current resistors, see figure F.10. Details of the circuit can be found in F.4.

The combination of power supply has a bandwidth of  $\sim 200\text{Hz}$ . With the feedback loop installed the bandwidth could be increased to  $\sim 670\text{Hz}$ , see figure 9.19.

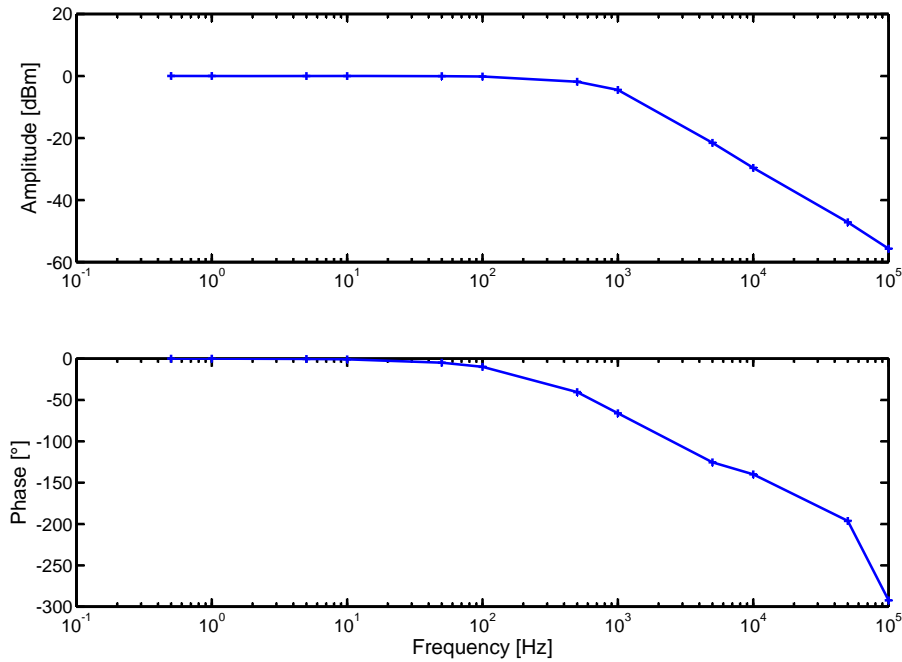


Figure 9.19: Amplitude and phase dependence on the frequency for the coil, power supply and feedback loop.

## 9.9.2 Laser Light

Optical single mode fibers are used to guide light from the laser table to the experiment table. Even after elaborate alignment small intensity fluctuations after the fiber can never be fully eliminated. To compensate for those a feedback circuit acting back to rf amplitude of the appropriate AOM was introduced such that those variations are strongly suppressed. Figure 9.20 shows a block diagram of an exemplary feedback loop. A detailed analysis of the performance can be found in [16].

## 9.10 Lithium

Even though is not currently under construction, an overview of the planned extensions to the current design will be given. Incorporating Lithium as the third species in the lower MOT would over-complicate the situation in at least two points. Firstly, the optical access to the MOT volume is not large enough to allow sufficiently large MOT beams for lithium and, secondly, it is not clear how efficiently the comparatively light lithium atoms could be transferred by a

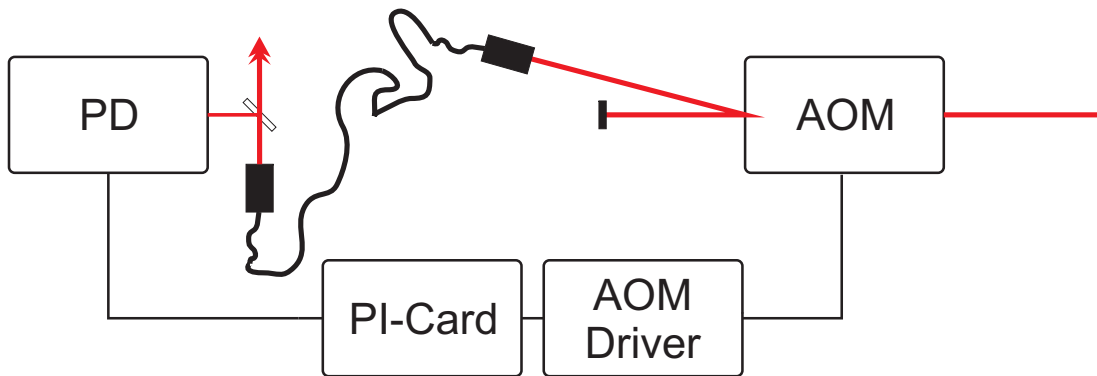


Figure 9.20: Layout of the feedback loop used for stabilising the intensity after the optical fibers. The light (red) enters the AOM from the right and is afterwards fibercoupled. At a glass plate a fraction of 5% is taken out and detected with a photodiode. The deviation from the set point is inverted and the PI regulator used for feedback onto the AM input of the AOM driver.

push beam. Therefore, the current plan is to connect an oven-slower combination to one of the CF 16 ports of the science chamber. This system can be pumped separately and a differential pumping stage can assure good vacuum within the science chamber. As an enriched oven can be used, see section 7.7 for details, and an efficient Li Zeemann slower can be comparably short [140] this should be a relatively compact setup, see figure 9.21. It is the intention to slow the Lithium atoms directly towards the MOT region in the science chamber. The current design allows for slowing via a slower beam reflected off the atom chip.

The theoretical interest in such a three-species atomic mixture is large, with the first results from a Li-K-Rb system just published [106]. The mixture is expected to be stable close to a Feshbach resonance, hence forming diatomic molecules. Due to the difference in mass, novel quantum states can be formed which are expected to show features similar to other many-body systems. As this is not within the scope of this thesis, the reader is left to the following references [5, 8, 9].

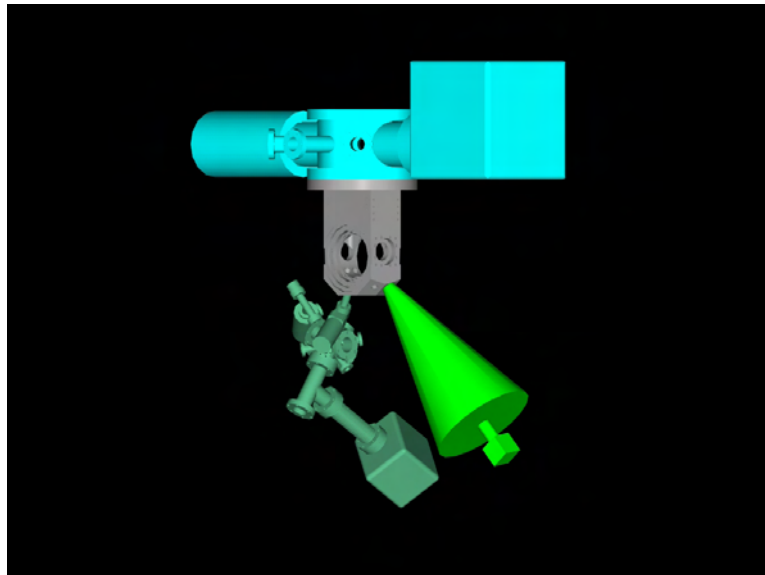


Figure 9.21: An Artist's impression on the Li slower design. Solwer (large cone) and oven (box) are shown. The length of the slower is 400mm.

# 10 First Result the K–Rb MOT

This chapter will document the current status of the experiment. Also, an overview of the first results will be given.

## 10.1 Isotope Enriched K–dispensers

As isotope enriched K dispensers were commercially not available the dispenser were manufactured inhouse. Following the method described [141], the enriched sources were produced. The dispenser works in the following way; the enriched KCl–Ca powder mixture is heated and the K is released, whereas the Ca captures the Cl and other contaminants. The heating is realised via ohmic heating of NiCr boats, see figure 10.1. In the following, the main points of the procedure are given:

- To purify the Ca, it was baked at 430°C for 6 days at a vacuum of  $\sim 10^{-6}$ mbar.
- The NiCr boats were degassed with a current of 13A each under a vacuum pressure of  $\sim 10^{-6}$ mbar for 30min.
- Using diamond files the Ca was ground into a fine powder and afterwards sieved with a titanium wire mesh(grid size 190  $\mu$ m).
- 12mg $\pm$ 1mg of KCl where mixed with 28mg $\pm$ 1mg of Ca powder.
- KCl and Ca were thoroughly mixed and subsequently filled into the NiCr boats.
- The boats are closed and mounted<sup>1</sup>, see figure 10.1.

The enriched KCl was obtained from Trace Science International. It has an isotope abundance of 5.5% of <sup>40</sup>K. The whole manufacturing process was done in a closed off workbench, where the humidity of the air could be reduced to 5%. Initial trials in a glove–box showed a contamination of the Ca and were therefore stopped.

---

<sup>1</sup>The installation in the vacuum chamber had to be done rapidly, as the time the dispensers should be exposed to normal atmosphere should be as small as possible.

Figure 10.1: Two mounted NiCr boats as K dispenser. The white ceramic separator assure that the dispensers are not touching the vacuum chamber.



## 10.2 Assembly of the whole Vacuum System

After the science chamber was finally sealed, the mounting was cleaned and assembled. Details of this assembly can be found in [139]. The mounting was tested in a test chamber, modified from [134], to meet our vacuum demands and brought down to  $p < 1 \times 10^{11}$  mbar. Following this test it was inserted into the science chamber and the whole setup, with the lower MOT attached, pumped down to  $2 \times 10^{-10}$  mbar. The pressure is higher than initially expected. This can be attributed to the fact, that the whole setup was only baked at a temperature of  $80^\circ\text{C}$  to avoid any trouble with the windows, see section B. At this level of vacuum, the differential pumping stage between the lower MOT and the science MOT works as expected, as there is no increase in pressure measurable in the science chamber while a  $^{40}\text{K}$  MOT is operated in the lower MOT.

## 10.3 K-Rb MOTs

The dispenser sources were tested in the lower MOT before science chamber and lower were joint. The optical layout can be found in 9.9. At a current of 2A in the quadrupole coils the Rb MOT was found to operate nicely. Subsequently a  $^{40}\text{K}$  MOT was established. The current through the K dispensers was varied and the number of trapped potassium atoms measured. The number of trapped atoms was determined due to a sweep of the cooling laser across resonance. The method is discussed in detail in section 7.2.1. In figure 10.2 the number of trapped  $^{40}\text{K}$  atoms depending on the current through the dispensers is plotted.

The slow increase in the number of trapped atoms up to a current of 6A, can

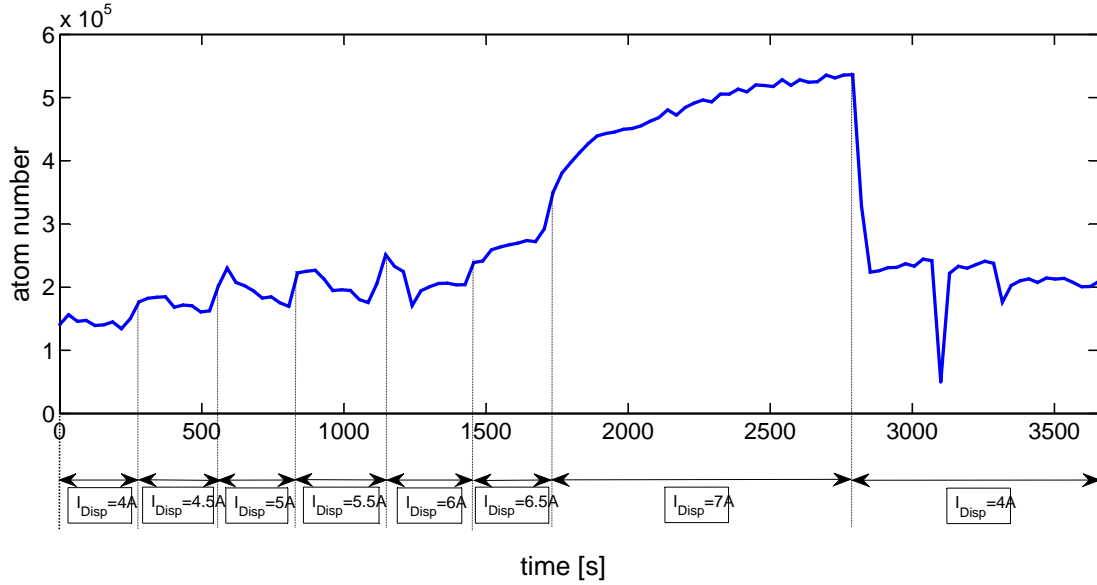


Figure 10.2: The number of  $^{40}\text{K}$  atoms in the MOT depending on the current through the dispenser source [16].

be explained by a heating and evaporation of K atoms which stuck to the surface of the dispenser from previous experiments. The step increase in the number of trapped atom at a current of 7A can be assumed to be the actual operation of the dispenser. This correlates well with the fact, that the number of trapped atoms settles back to the previous value at 4A on a short time scale after reducing the current from 7A to 4A.

Now, as the whole vacuum chamber is assembled, the optimal parameters for the lower MOT can be established. For the push beam the absolute size of the lower is of less importance compared to the loading rate. The real figure of merit is the number of atoms loaded in to the mirror MOT in the science chamber per second. The value to compare to is the value of the previously mentioned push beam experiment [129, 134, 72], where  $1 - 2 \times 10^8$  atoms are loaded in 10s into the science MOT.





# **Part VI**

## **Conclusion & Outlook**



# 11 Conclusion

This thesis represents the design and implementation of a next-generation atom chip experiment, with the aim of producing low-dimensional gases of bosons, fermions, and Bose–Fermi mixtures. Indeed, specifically, two major steps towards the creation of a degenerate mixture of two fermionic ( ${}^6\text{Li}$  and  ${}^{40}\text{K}$ ) and one bosonic ( ${}^{87}\text{Rb}$ ) species in low-dimensional traps are reported in this work.

In the first step a mixture of  ${}^6\text{Li}$  and  ${}^{87}\text{Rb}$  was prepared in a magneto-optical trap. With this it was possible to measure the inelastic loss rate coefficient between the two species for the first time. It was found to be  $\beta_{\text{LiRb}} = (1.5 \pm 0.5) \times 10^{-10} \text{cm}^3 \text{s}^{-1}$ . Furthermore, it was possible to trap both atoms simultaneously in a magnetic Z-trap. The lifetimes in the magnetic trap did not allow a cooling into the degenerate regime, showing the limitations of the Heidelberg setup. With this background, the design phase for the new setup in Vienna started. During this time the scattering length between  ${}^6\text{Li}$  and  ${}^{87}\text{Rb}$  and novel ideas for the combination of heavy and light fermions were published. In this light it was decided to design an experiment which could be used with two fermionic species, i.e.  ${}^6\text{Li}$  and  ${}^{40}\text{K}$ . The design process and the final design are described in detail in this work.

The second step was the construction of the  ${}^{40}\text{K}$ – ${}^{87}\text{Rb}$  experiment in Vienna. This experiment represents the latest generation in atom chip experiments. During the entire design and construction phase, strong and weak points of previously existing atom chip experiments were carefully analysed, where possible, improvements were made. Regarding  ${}^6\text{Li}$ , all provisions were made so that the incorporation of the third species is on the shortest possible time scale. The layout of the atom chip is specifically designed towards 1D traps. The realisation of atom chip traps with high aspect ratios is possible with the current design of the atom chip [139]. Aspect ratios of  $\omega_{\perp}/\omega_{\parallel} > 10^4$  are feasible.

To date, the experiment is fully set up. This includes the complete assembly of and evacuation of the science chamber and the lower MOT; the atom chip is in place and its functionality tested. A stable laser system for Rb and K is ready. Furthermore, the computer control system is adapted to the needs of the new experiment. Therefore, the current status of the experiment is an ideal starting point towards degeneracy and for the study of low dimensional quantum systems in a variety of combinations.



# 12 Outlook

As this experiment is in such an early stage, it is difficult to predict the future outcome of it. Considering the actually realised design of the experiment in Vienna, the realisation of a 1D trap for a Fermi gas seems reachable. Such 1D traps were created for bosons in this research group, see for example [142]. Consider a trap with  $\omega_{\perp}/\omega_{\parallel} = 10^4$  filled with DFG of 1000  $^{40}\text{K}$ -fermions. Furthermore, the temperature of this gas should be small enough that excitations in the first excited transversal states are unlikely. If the density distribution along the trap is of interest, it could be imaged directly with the method discussed in 9.5. However, detection of such low densities remains at the technical limit. Possibly, there is a novel method of detecting this distribution, which will be sketched in the following.

For a trapped Bose gas, a double-well interferometer was reported [142], where the longitudinal density fluctuations of trapped 1D quasi-condensates were studied. This experiment shows the relative phase between two 1D systems, which were coherently split with no tunnelling possible afterwards, for several hold times. The relative phase between the two 1D quasi-condensates is initially zero and evolves in time. The evolution of the relative phase depends on the experimental parameters, such as the local density and trap geometry. This interferometric method could be used to detect the density distribution of the above specified DFG in the following way. Initially, fermions and bosons are trapped in a static trap, see figure 12.1 (a). The fermions (red) are in a stronger confining potential compared to the potential for the bosons (black). With an imbalanced time dependant potential<sup>1</sup>, the fermions can be trapped in one side of the resulting asymmetric double well, see figure 12.1 (b). Subsequently the bosons are coherently split.

For the evolution of the relative phase of the two 1D quasi-condensates two cases have to be distinguished. The *undisturbed case*, where only bosons are present and the *disturbed case* where fermions are present at one side of the interferometer.

In the *disturbed* case, the interaction between the bosons and fermions will lo-

---

<sup>1</sup>The exact shape of the time-dependent potential will depend on parameters such as the fermion in use, the trap geometry, the phase, power and detuning of the rf field. Such a field can be calculated following [143] and exemplary potentials for a mixture of K and Rb can be found in [139].

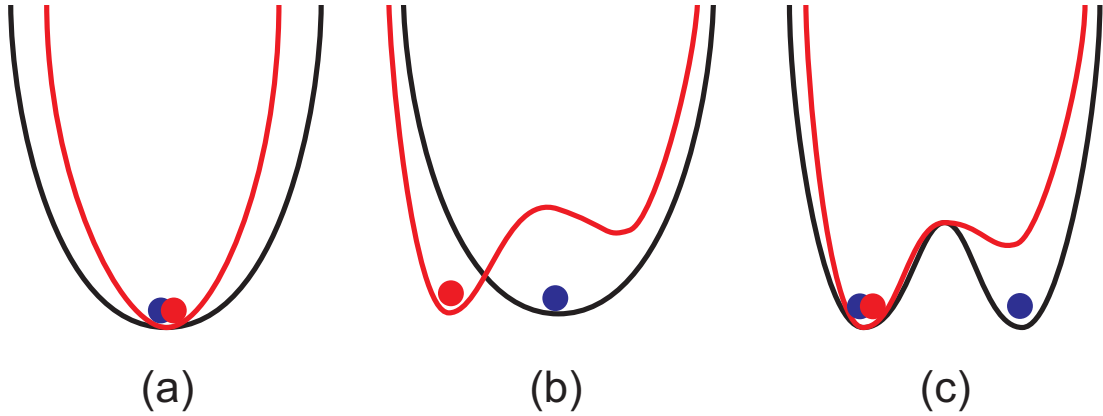


Figure 12.1: Illustrated potentials for the proposed experiment; (red) corresponds to the potential for the fermions, (black) to the potential for the bosons. (a) static 1D traps for bosons and fermions. (b) asymmetric splitting for the Fermi cloud (c) symmetric splitting for the bosons. (blue-dot) a pictorial representation of the Bose gas and (red-dot) a representation of the Fermi gas.

cally deform the trapping potential. For example, the interaction in a mixture of  $^{40}\text{K}$ - $^{87}\text{Rb}$  is attractive. In the limit of a low density of fermions, the potential, seen by the bosons, will be deeper around the fermion. Such an effect has been observed in an optical lattice, where the presence of impurities due to fermions shifts the transition parameter for the superfluid to Mott insulator transition significantly [144]. In the interferometer proposed here, this local deformation of the trapping potential will drive the relative phase of the bosons in the vicinity of this deformation. In an ideal case, the separation of the (low number) fermions is such, that they are further spaced than the average correlation length of the quasi 1D condensate. In this case, the bosons would map the density distribution of the fermions in a relative phase between the traps, compared to the *undisturbed* case. Hence, the phase contribution of the fermions can be measured with interferometric precision. If this method turns out to be stable enough, it can be extended and possibly be used to extract the correlation function [145] of a 1D Fermi gas.

# **Part VII**

## **Appendices**





# List of Abbreviations

AOM	Acousto-Optic Modulator
AR	Anti Reflection
BEC	Bose Einstein Condensate
CF	ConFlat
DFG	Degenerate Fermi Gas
DPSS	Diode Pumped Solid State
FCC	Fine-structure changing collision
GPS	Global Positioning System
HCC	Hyperfine-structure changing collision
IP	Ioffe–Pritchard
MOT	Magneto Optical Trap
PLL	Phase Locked Loop
RE	Radiative Escape
RF	Radio Frequency
Ti:Sa	Titanium–Sapphire Crystal
TOP	Time Orbiting Potential
TSP	Titanium Sublimation Pump
UHV	Ultra High Vacuum



# **A Science Chamber CAD drawings**

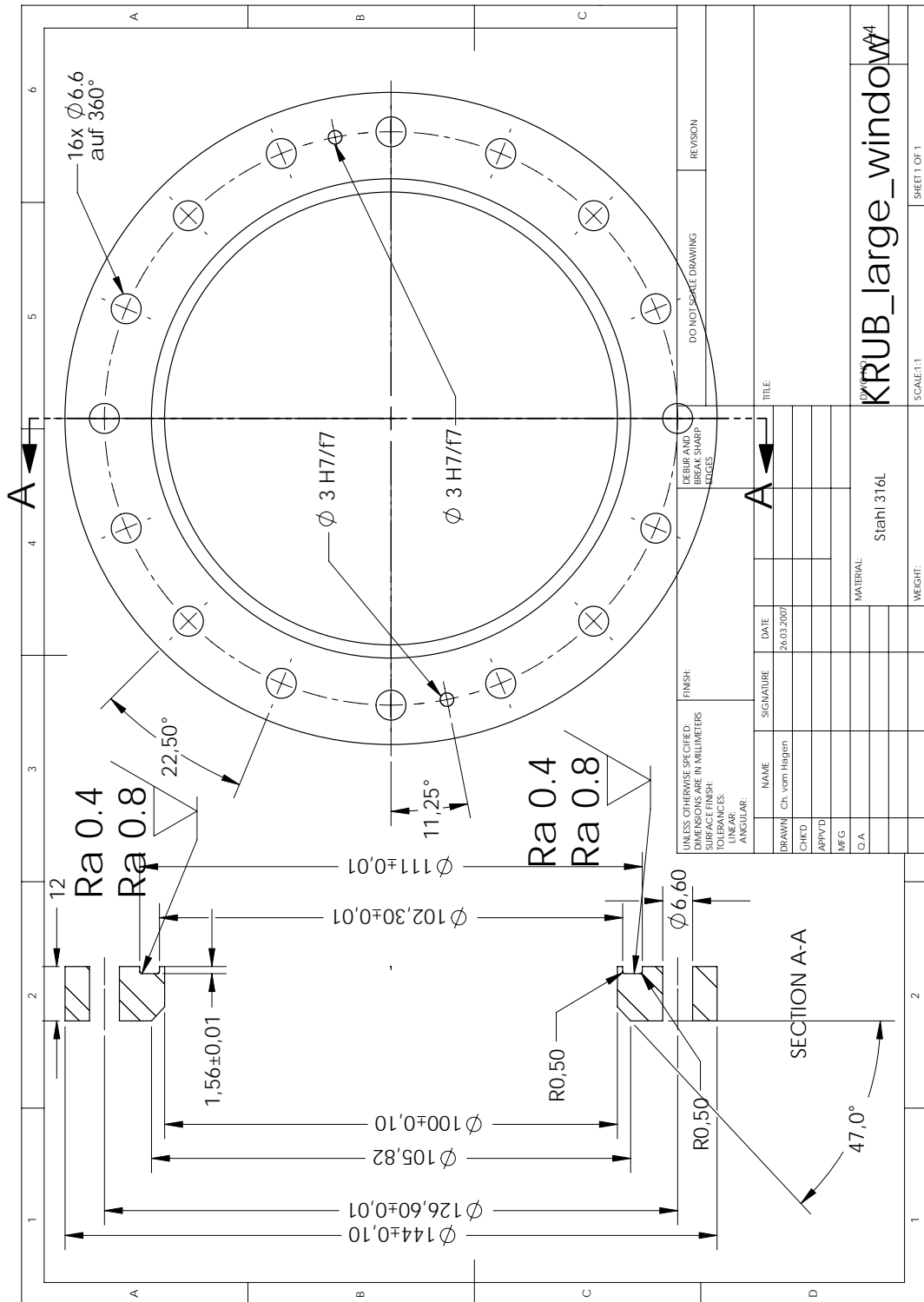


Figure A.1: Flange for the two large viewports at the science chamber.

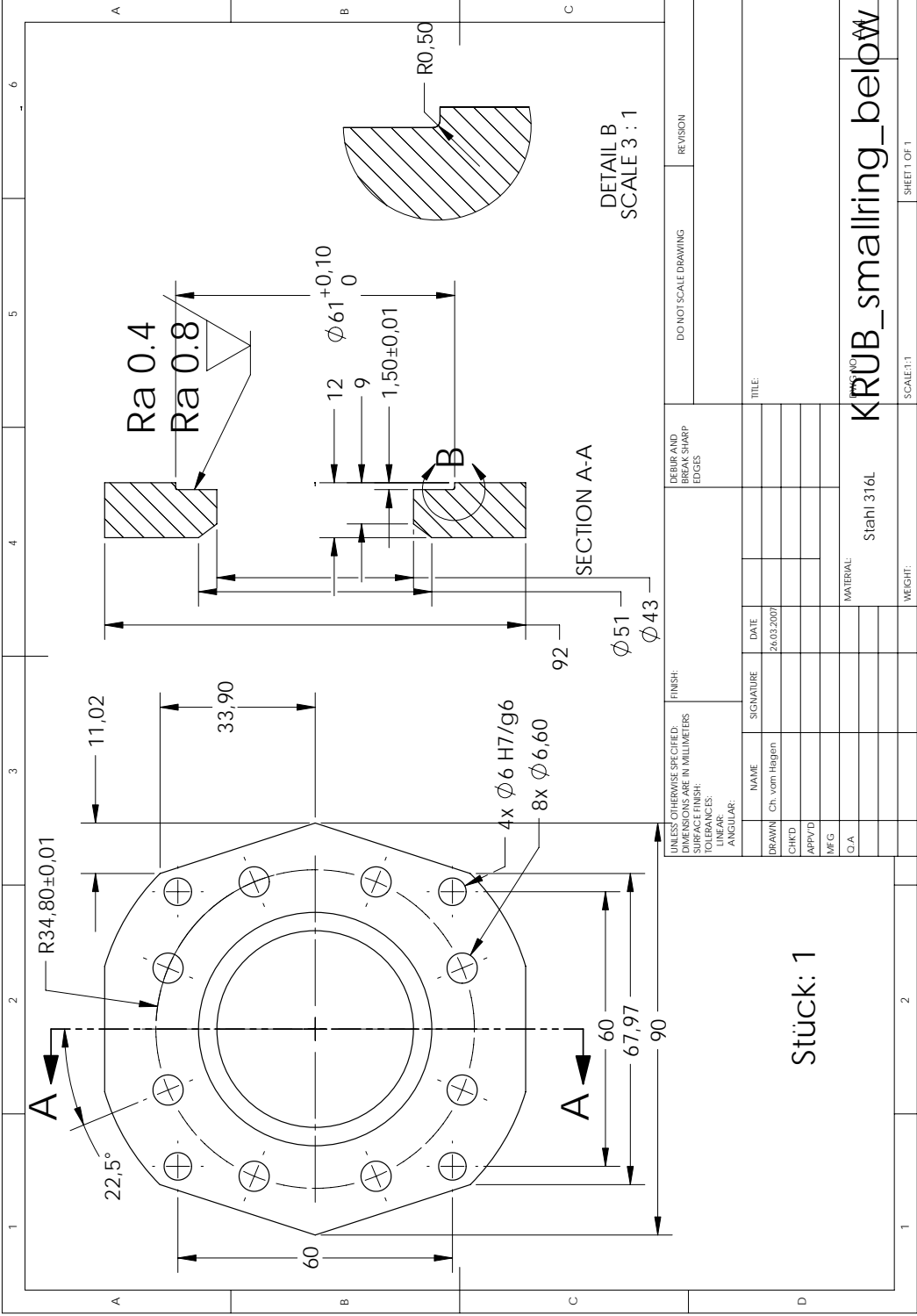


Figure A.2: Flange for the small viewport below the atom chip.

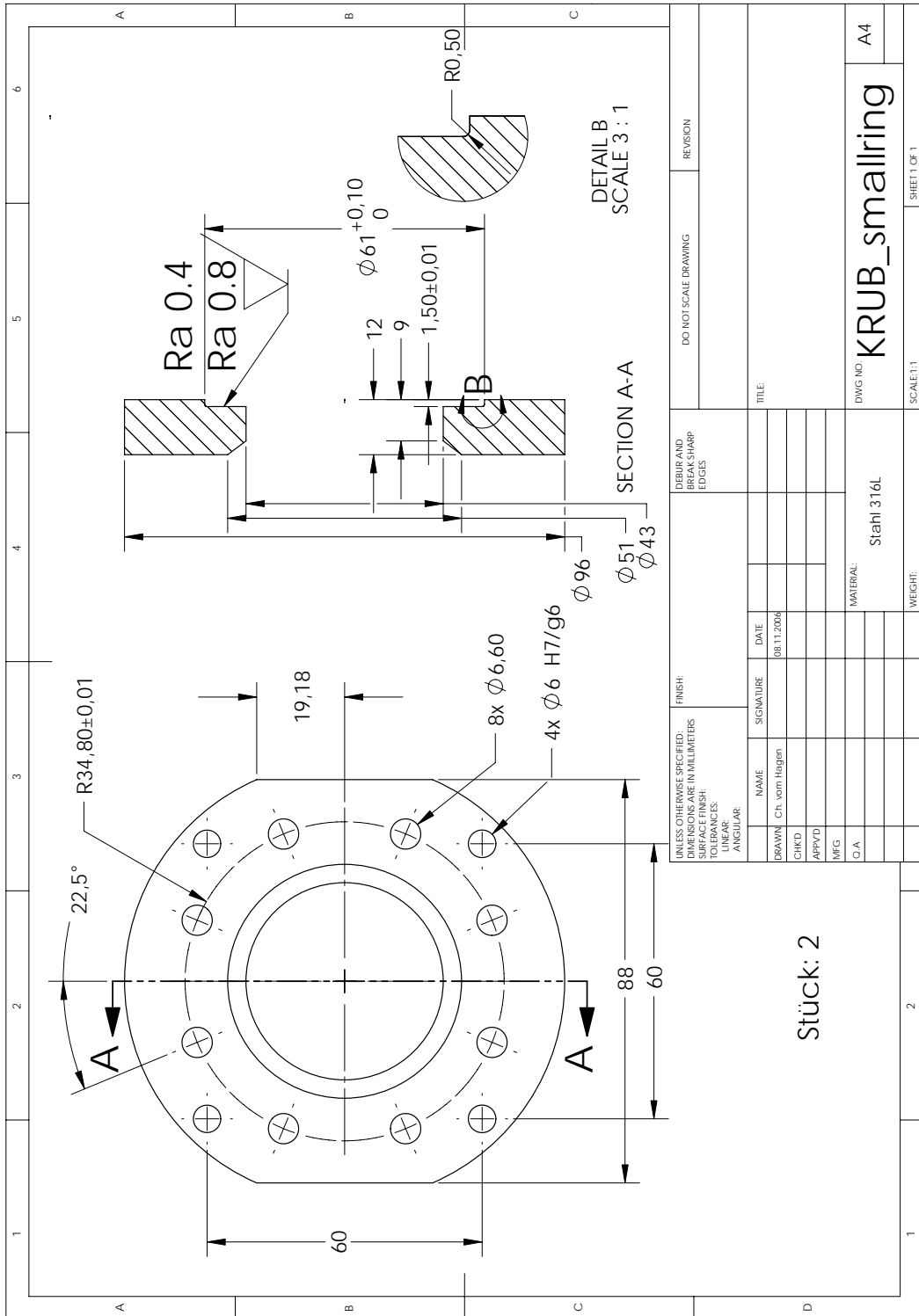


Figure A.3: Flange for the two viewports on the thin side of the science chamber. The four holes for the 60mm–cage system are also visible.

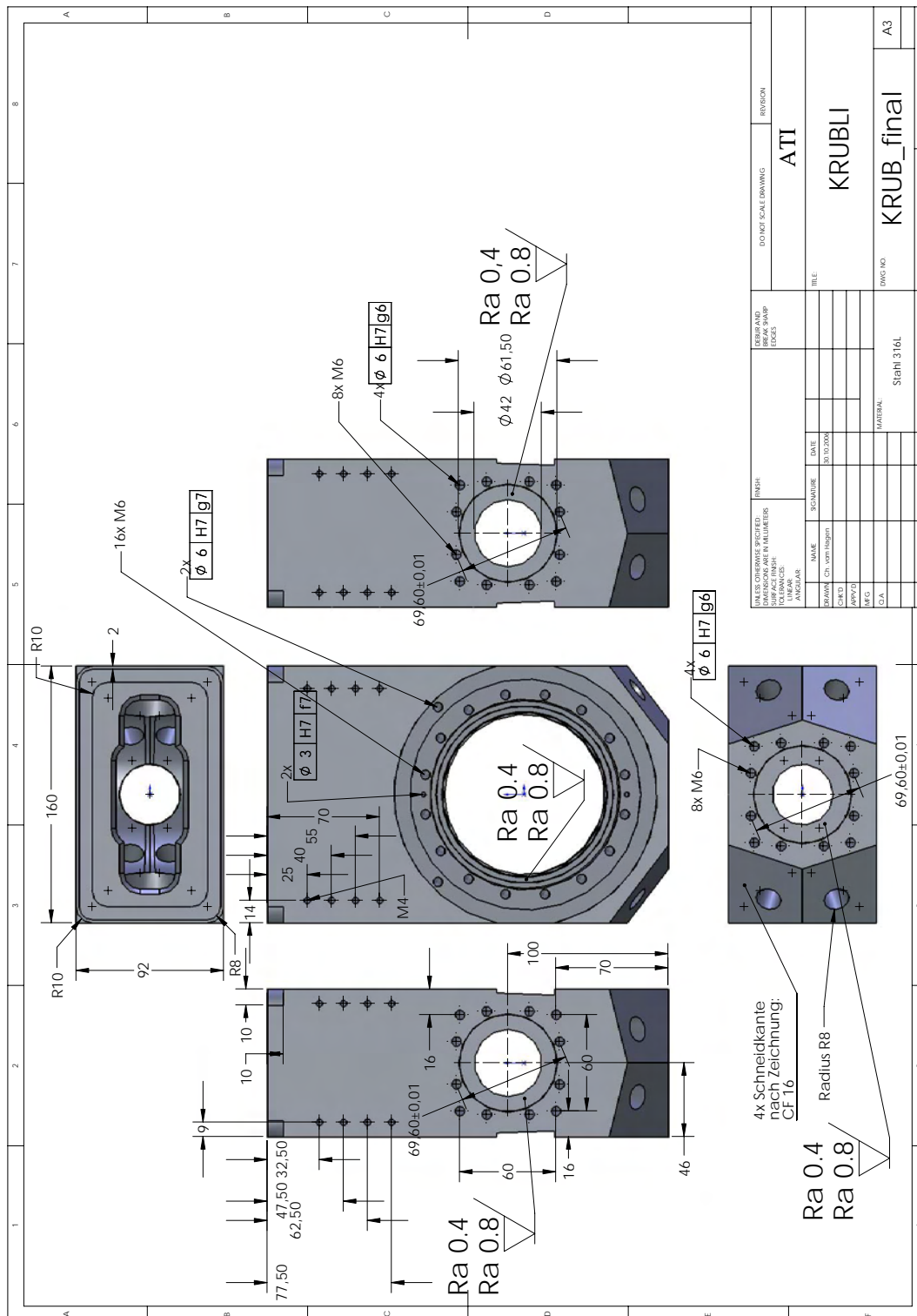


Figure A.4: Overview of the outside of the science chamber from all orthogonal projections.

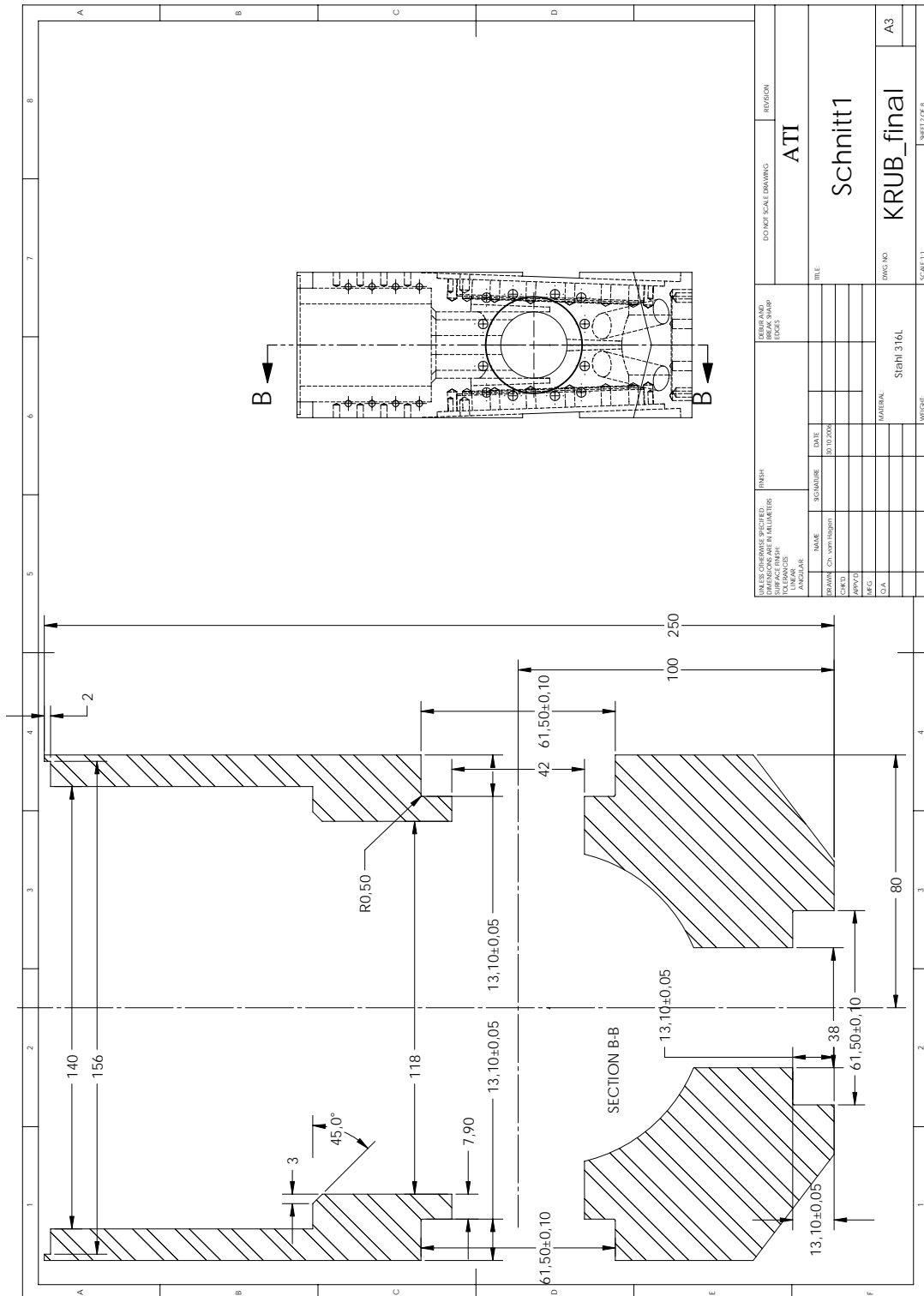


Figure A.5: Section through the science chamber parallel to the wide side and through the centre.



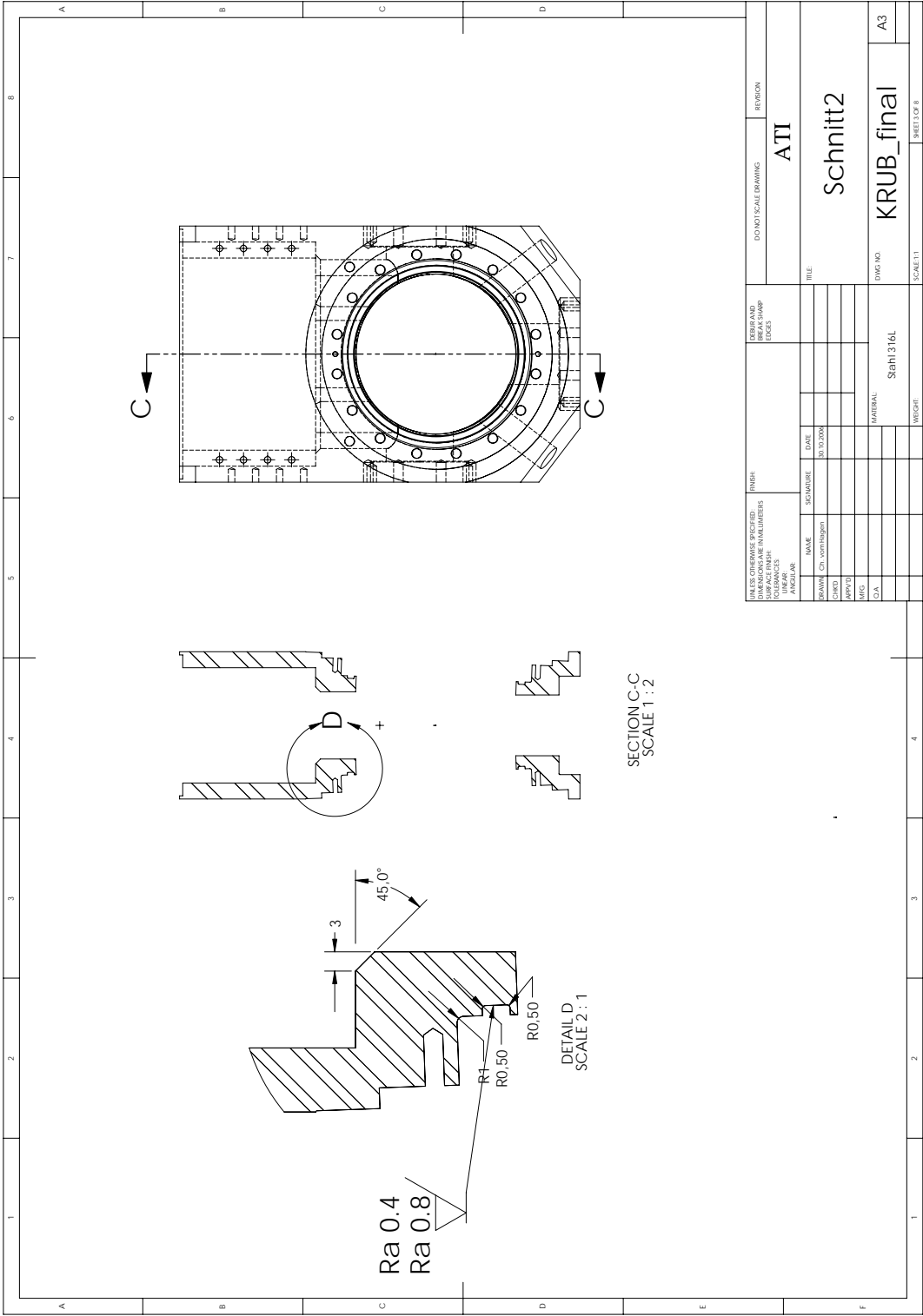


Figure A.6: Section through the science chamber parallel to the thin side and through the centre. Also a detailed design of the groove for the HNV200 seal is shown.

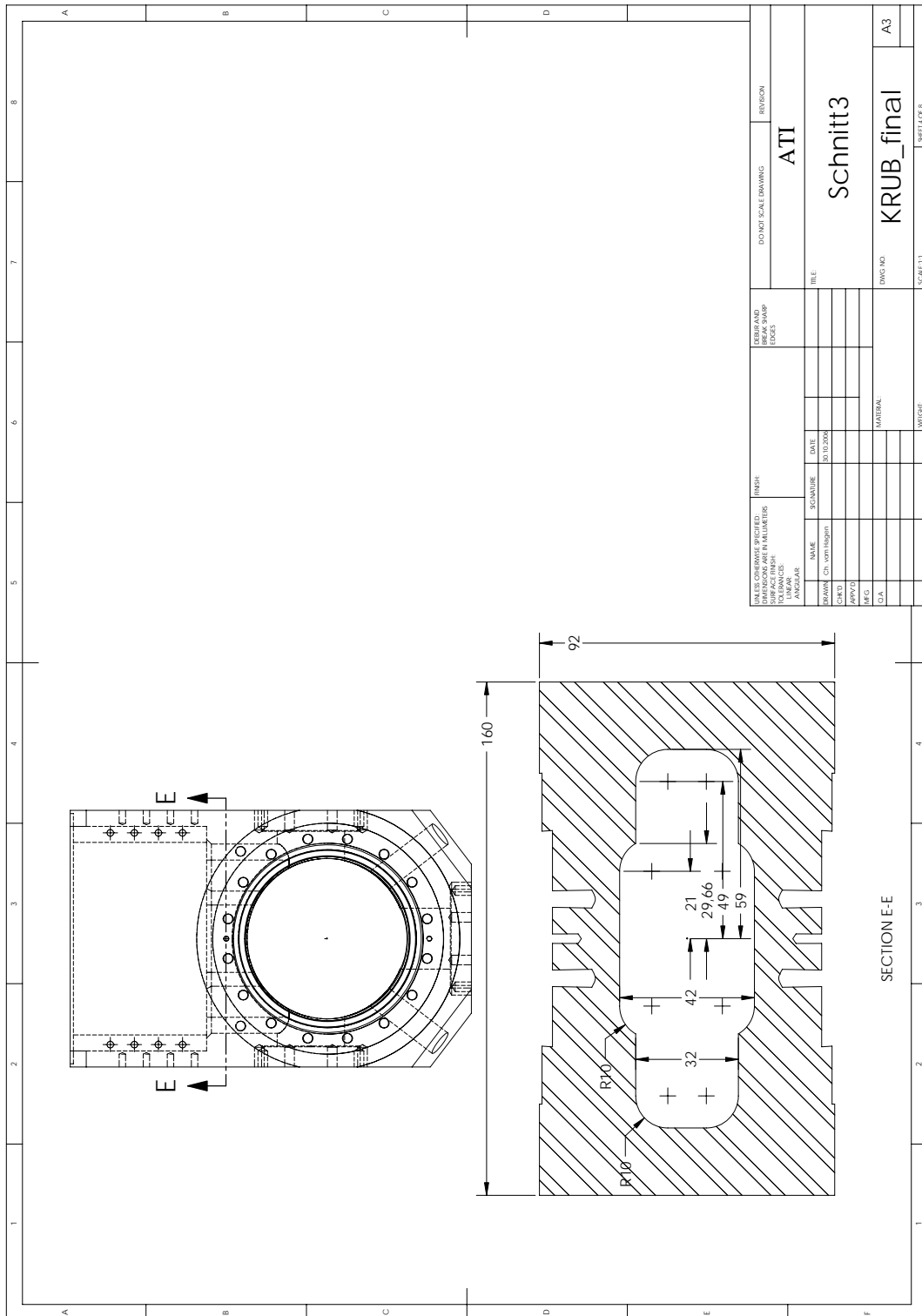


Figure A.7: Section through the science chamber orthogonal to the wide side and through a point above the large window.

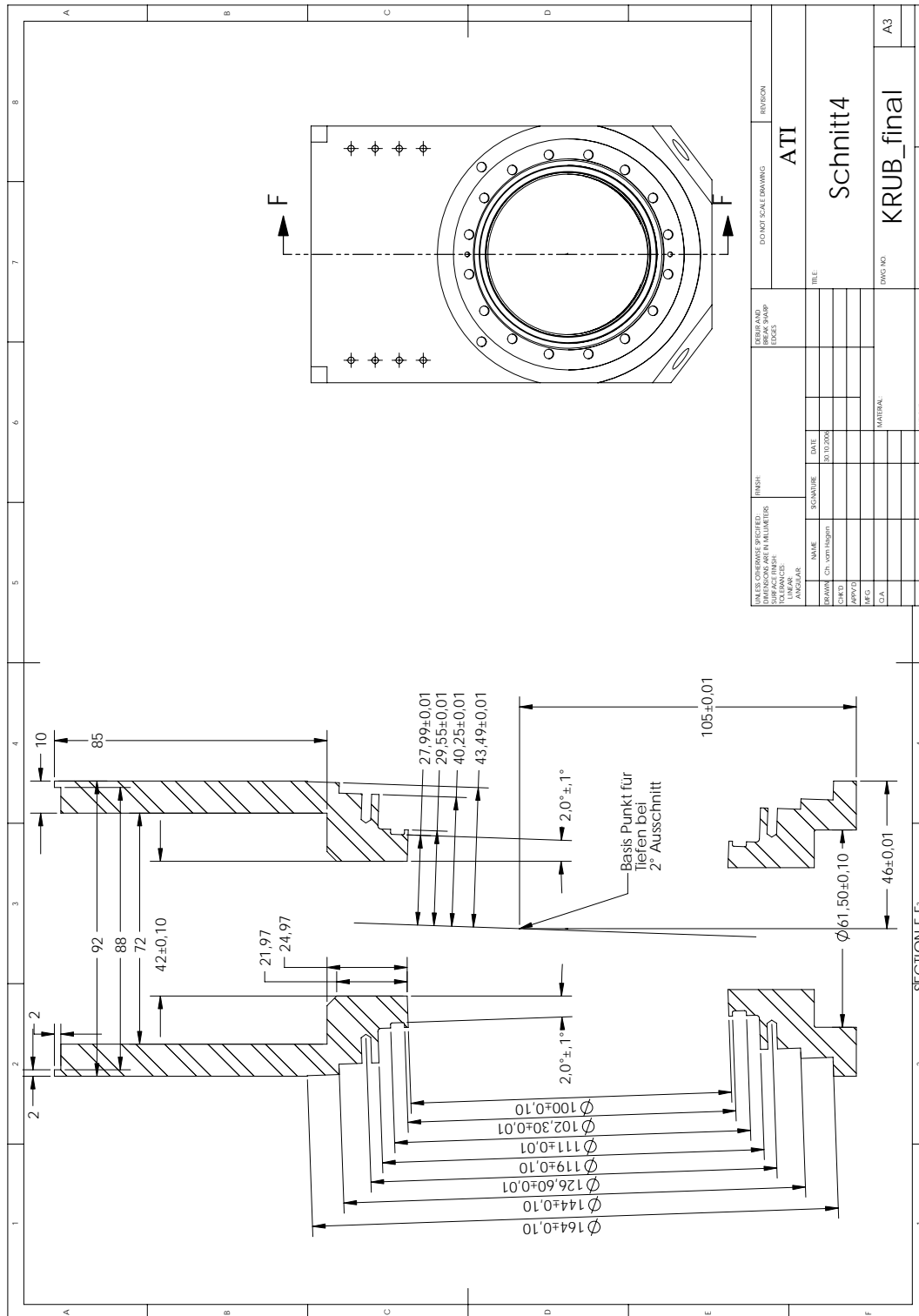


Figure A.8: Section through the science chamber parallel to the thin side and through the centre. Dimensions for the large windows are shown.

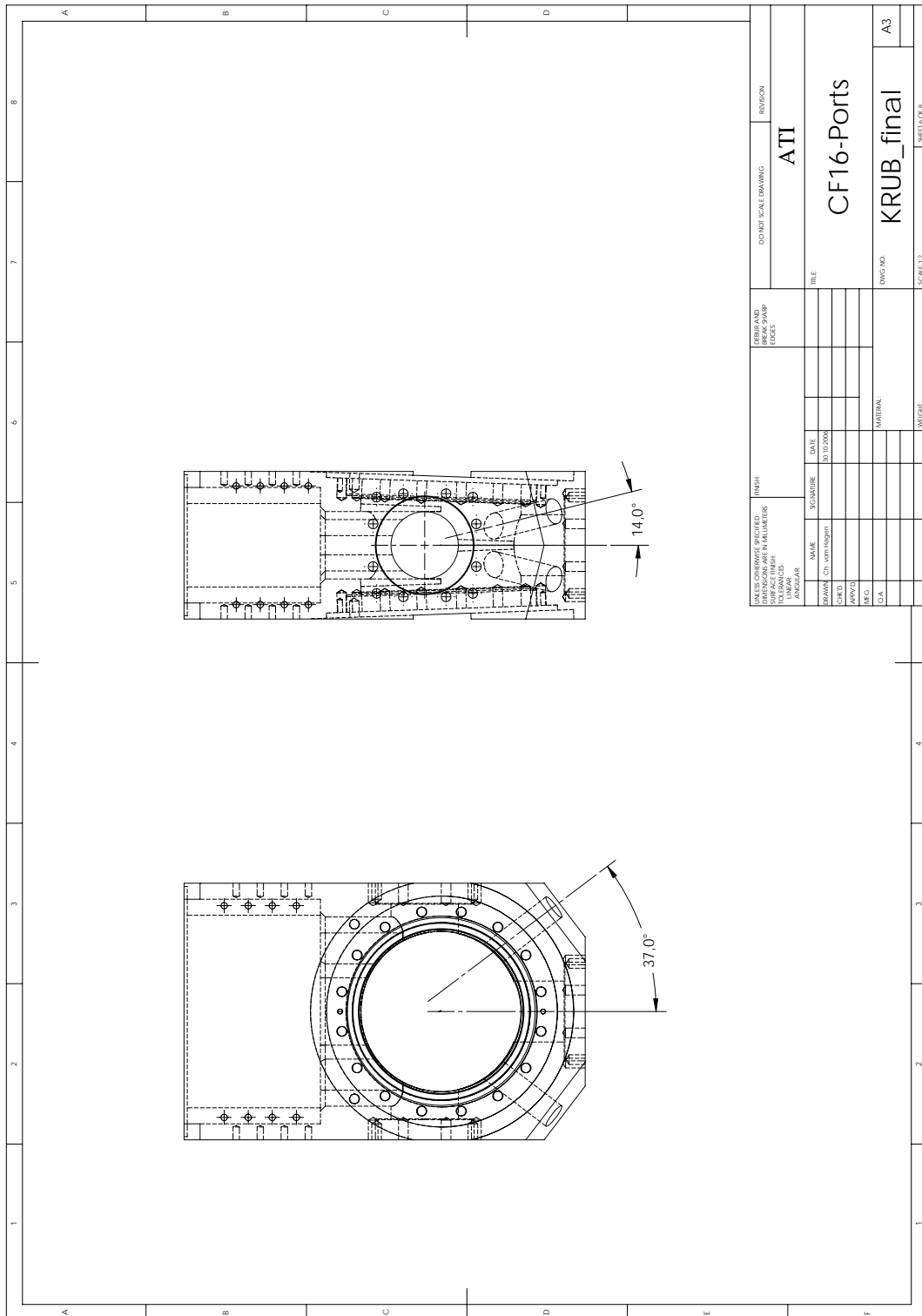


Figure A.9: Overview of the science chamber and angles indicated for the DN 16 CF connections.

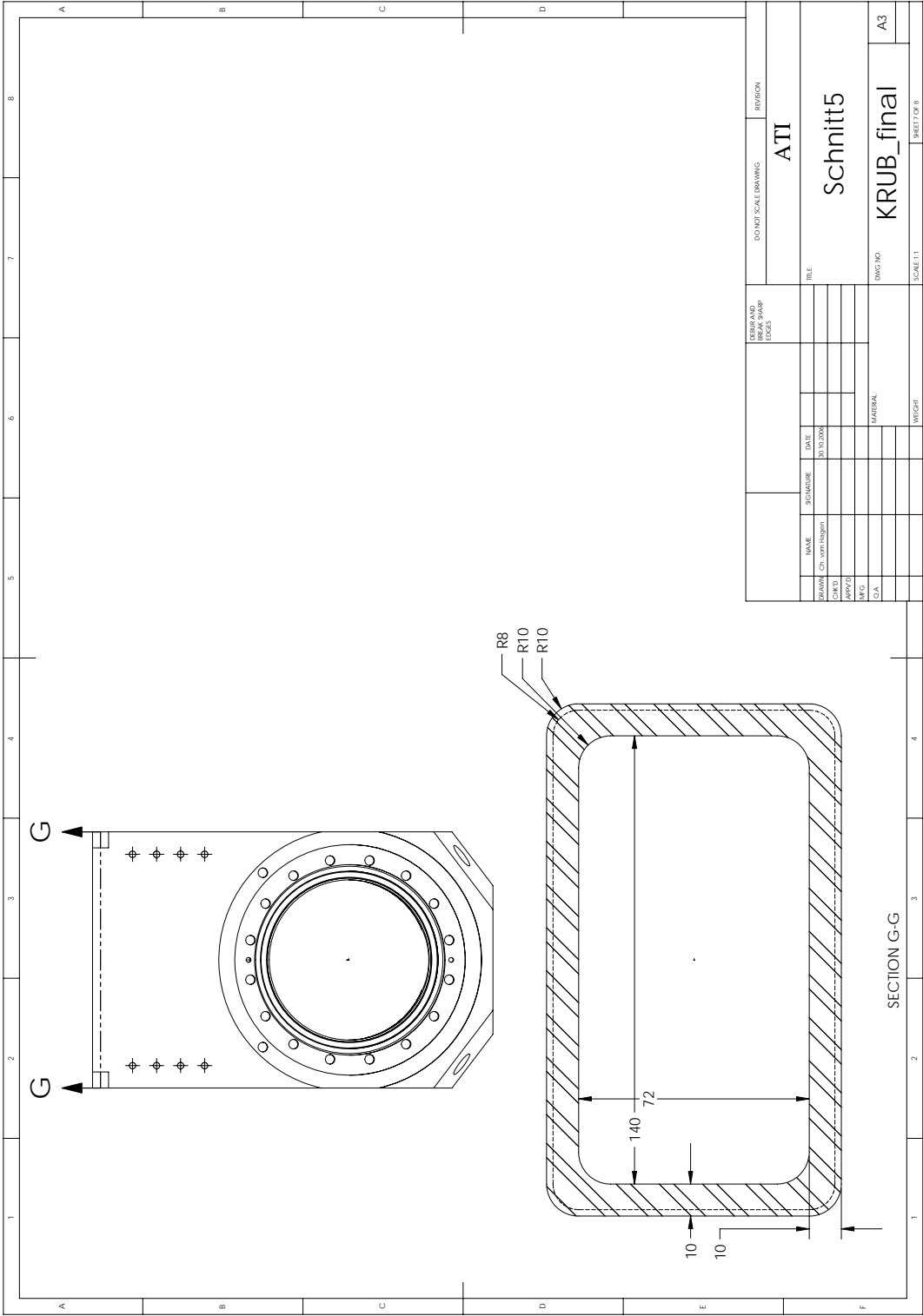


Figure A.10: Section through the science chamber orthogonal to the wide side and through a point at the top, where the rim for the welding is shown.

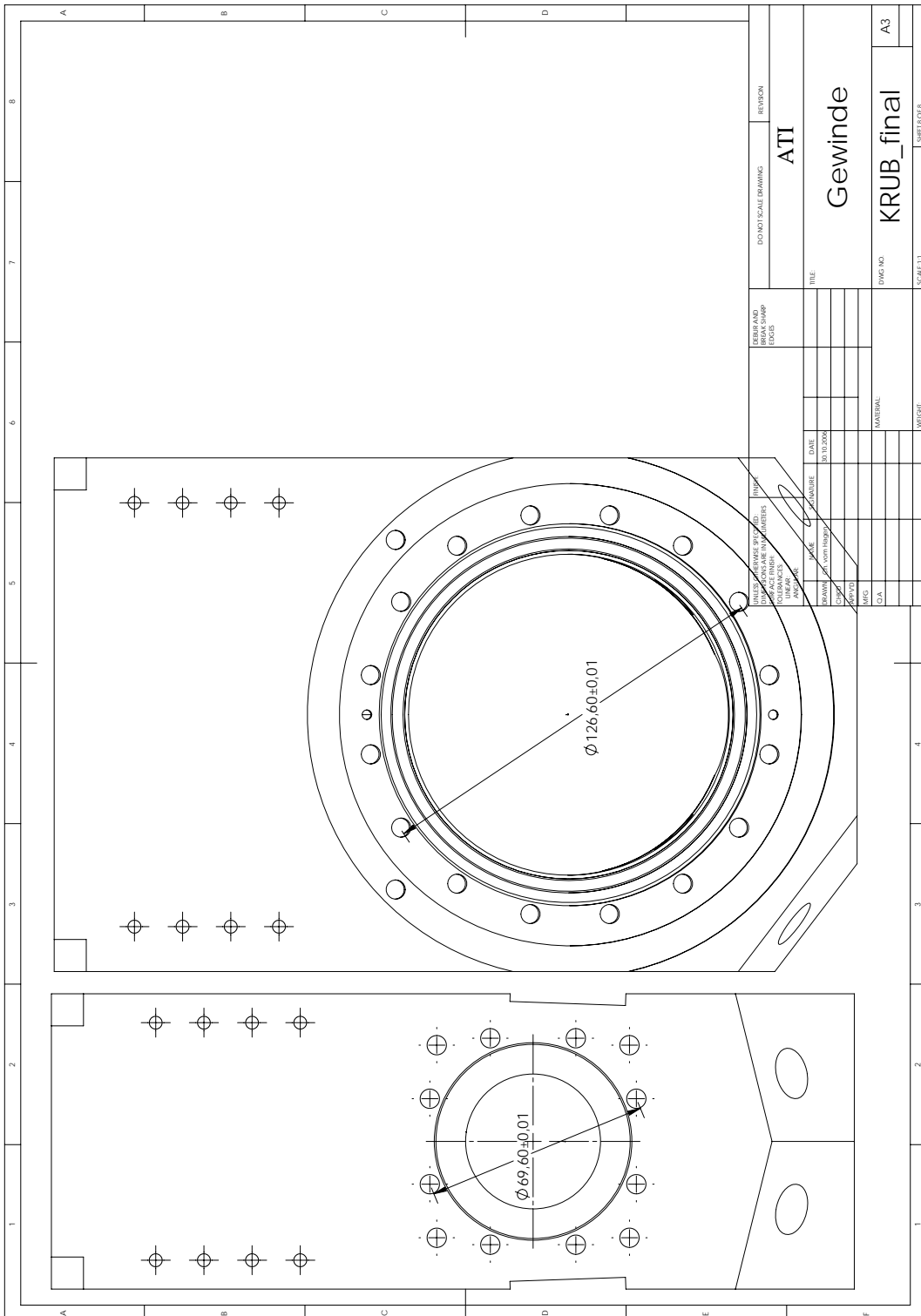
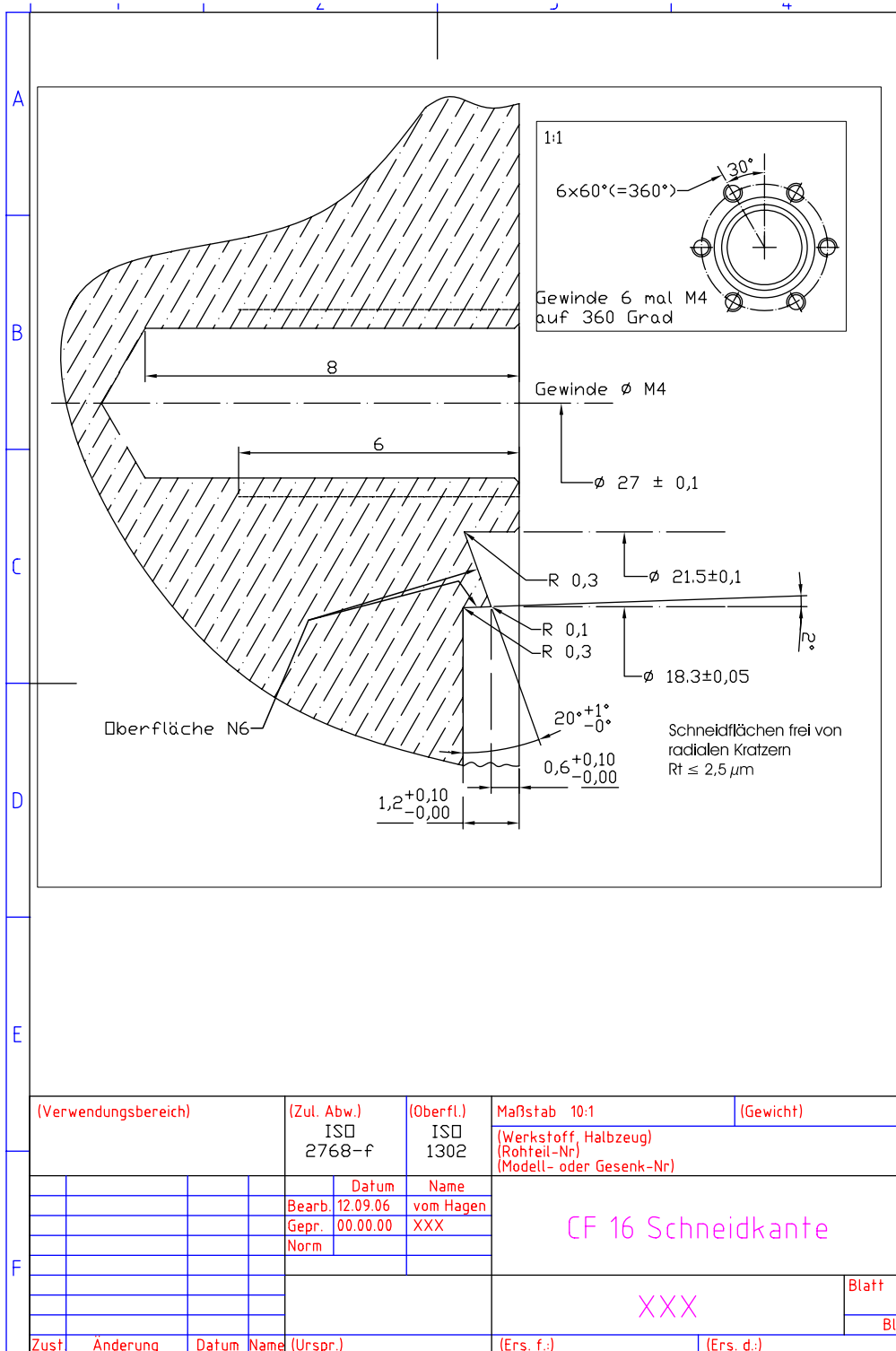


Figure A.11: Dimensions for the bolts for the large and small windows.



(Verwendungsbereich)		(Zul. Abw.) ISO 2768-f	(Oberfl.) ISO 1302	Maßstab 10:1	(Gewicht)
				(Werkstoff, Halbzeug) (Rohteil-Nr) (Modell- oder Gesenk-Nr)	
		Datum	Name	CF 16 Schneidkante	
		Bearb. 12.09.06	vom Hagen		
		Gep. 00.00.00	XXX		
		Norm			
				XXX	Blatt
					Bl.
Zust	Änderung	Datum	Name (Urspr.)	(Ers. f.)	(Ers. d.)

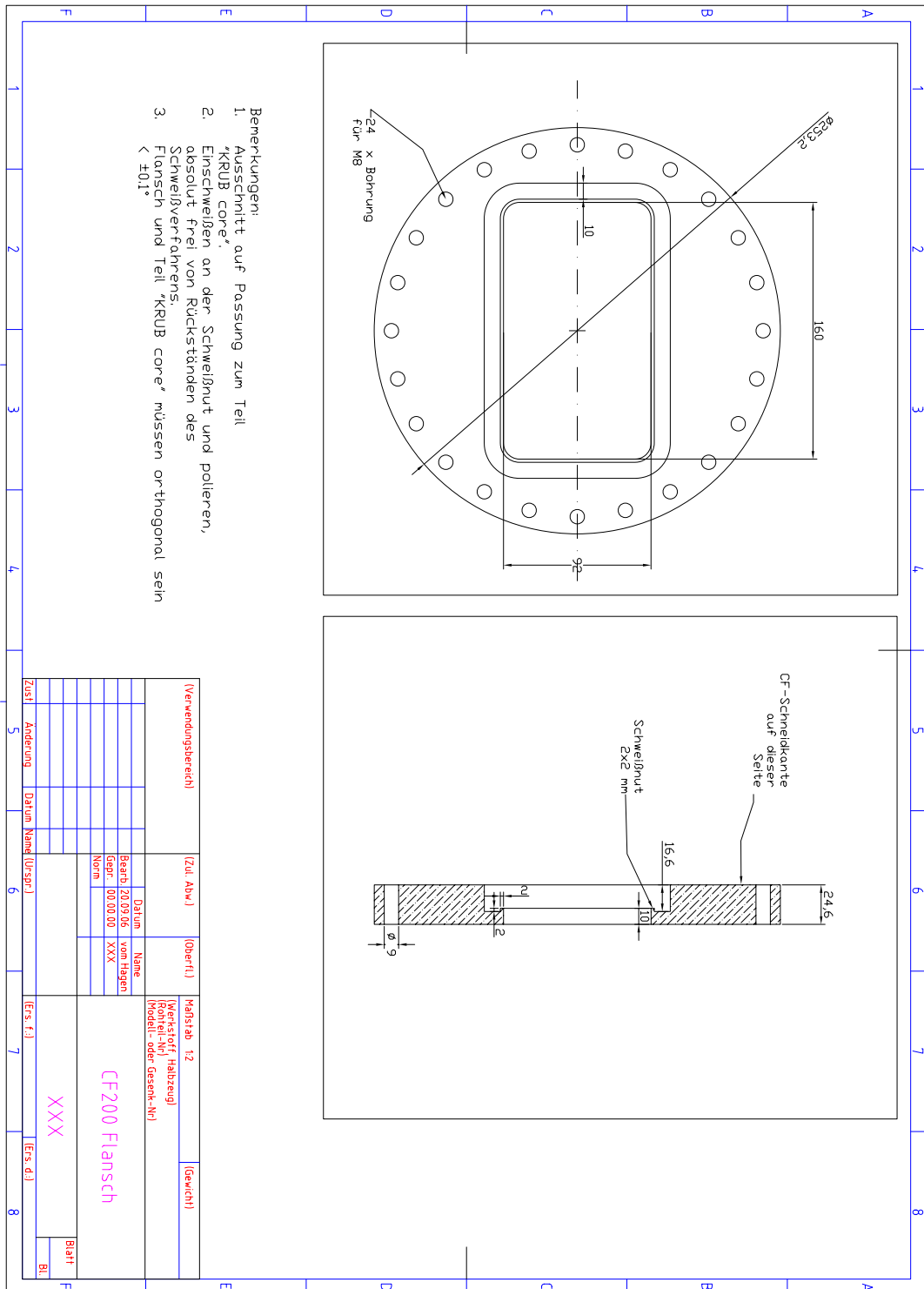
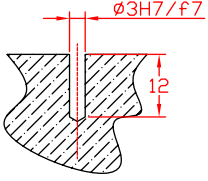
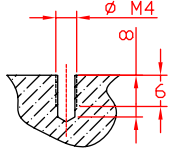
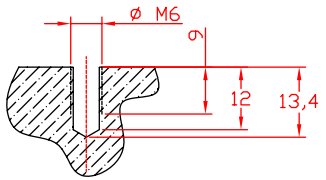


Figure A.12: The CF 200 flange where the science chamber is welded in. This flange assures a tight connection to the pumping chamber.



A	<div style="display: flex; justify-content: space-around; align-items: center;"> <div style="text-align: center;"> <p>∅ 3 mm Paßloch</p>  </div> <div style="text-align: center;"> <p>M4 Gewindeloch</p>  </div> </div>																																																									
B																																																										
C	<div style="text-align: center;"> <p>M6 Gewindeloch</p>  </div>																																																									
D																																																										
E																																																										
F	<table border="1" style="width: 100%; border-collapse: collapse;"> <tr> <td style="width: 30%;">(Verwendungsbereich)</td> <td style="width: 15%;">(Zul. Abw.)</td> <td style="width: 15%;">(Oberfl.)</td> <td style="width: 20%;">Maßstab 1:1</td> <td style="width: 20%;">(Gewicht)</td> </tr> <tr> <td colspan="3"></td> <td colspan="2">(Werkstoff, Halbzeug) (Rohteil-Nr) (Modell- oder Gesenk-Nr)</td> </tr> <tr> <td></td> <td></td> <td>Datum</td> <td colspan="2">Name</td> </tr> <tr> <td></td> <td></td> <td>Bearb. 24.09.06</td> <td colspan="2">vom Hagen</td> </tr> <tr> <td></td> <td></td> <td>Gepr. 00.00.00</td> <td colspan="2">XXX</td> </tr> <tr> <td></td> <td></td> <td>Norm</td> <td colspan="2"></td> </tr> <tr> <td colspan="3"></td> <td colspan="2" style="text-align: center; color: magenta; font-size: 1.2em;">Paßloch und Gewinde</td> </tr> <tr> <td colspan="3"></td> <td colspan="2" style="text-align: center; color: magenta; font-size: 1.2em;">XXX</td> </tr> <tr> <td colspan="3"></td> <td style="text-align: right;">Blatt</td> <td></td> </tr> <tr> <td colspan="3"></td> <td style="text-align: right;">Bl.</td> <td></td> </tr> <tr> <td>Zust</td> <td>Änderung</td> <td>Datum</td> <td>Name (Urspr.)</td> <td>(Ers. f.)</td> <td>(Ers. d.)</td> </tr> </table>		(Verwendungsbereich)	(Zul. Abw.)	(Oberfl.)	Maßstab 1:1	(Gewicht)				(Werkstoff, Halbzeug) (Rohteil-Nr) (Modell- oder Gesenk-Nr)				Datum	Name				Bearb. 24.09.06	vom Hagen				Gepr. 00.00.00	XXX				Norm						Paßloch und Gewinde					XXX					Blatt					Bl.		Zust	Änderung	Datum	Name (Urspr.)	(Ers. f.)	(Ers. d.)
(Verwendungsbereich)	(Zul. Abw.)	(Oberfl.)	Maßstab 1:1	(Gewicht)																																																						
			(Werkstoff, Halbzeug) (Rohteil-Nr) (Modell- oder Gesenk-Nr)																																																							
		Datum	Name																																																							
		Bearb. 24.09.06	vom Hagen																																																							
		Gepr. 00.00.00	XXX																																																							
		Norm																																																								
			Paßloch und Gewinde																																																							
			XXX																																																							
			Blatt																																																							
			Bl.																																																							
Zust	Änderung	Datum	Name (Urspr.)	(Ers. f.)	(Ers. d.)																																																					

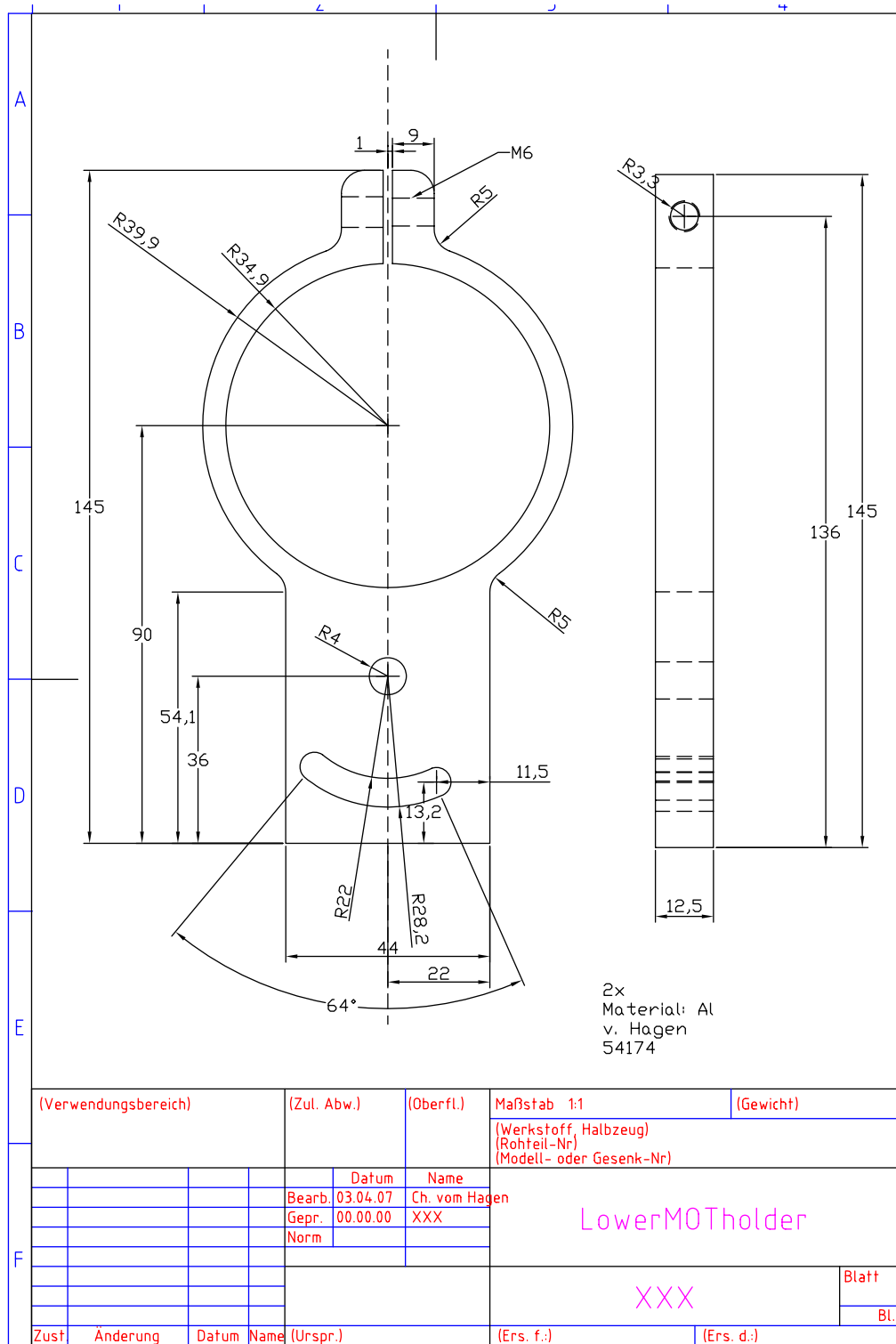


Figure A.13: Holder for lower-MOT precision mount. Angle and height is freely adjustable. The figure shows the clamp, which is attached to the CF-40 Ports of the lower-MOT.

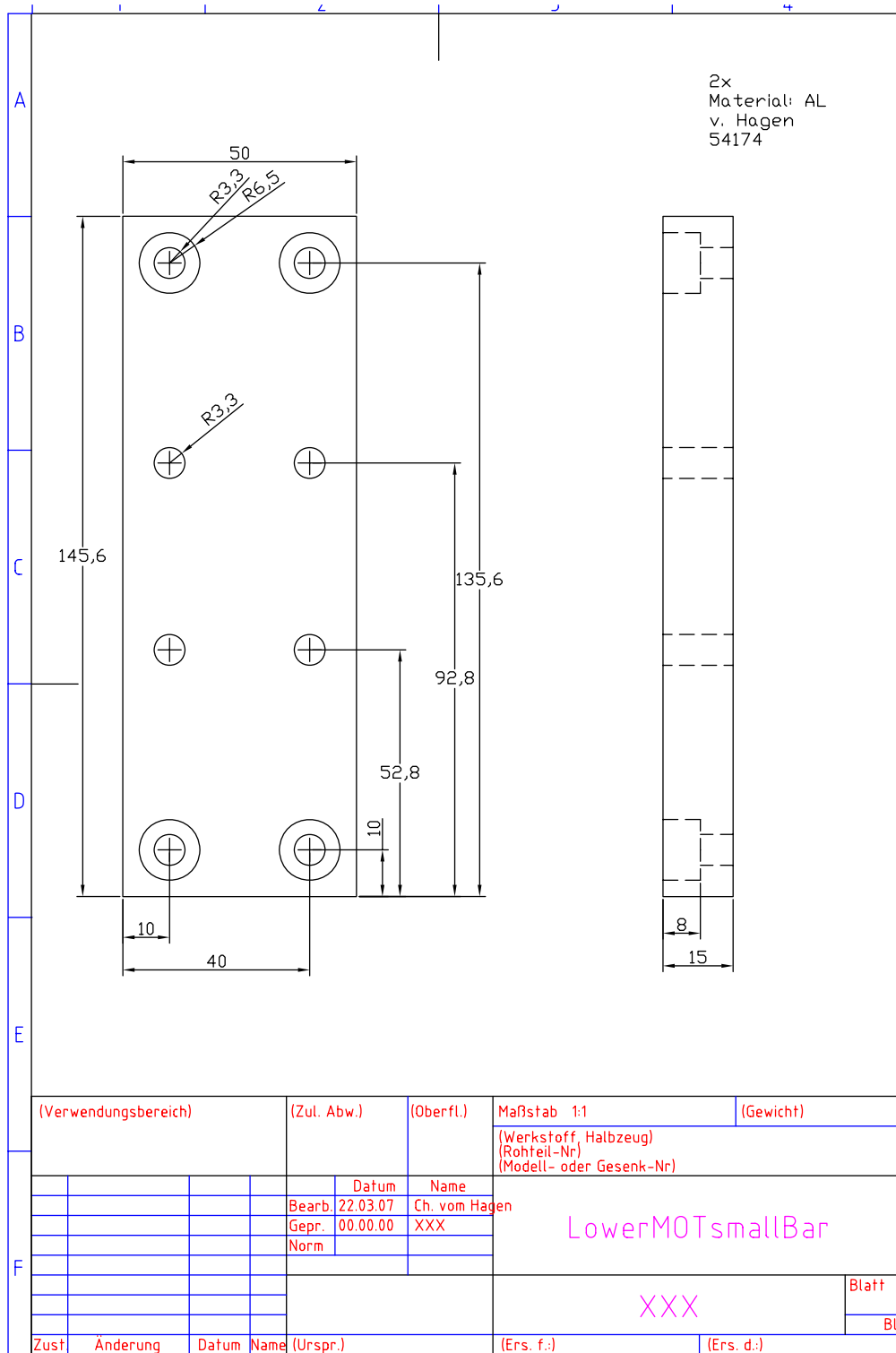


Figure A.14: Holder for lower-MOT precision mount. This Al-pice connects the two long bars, to which the two clamps are connected.

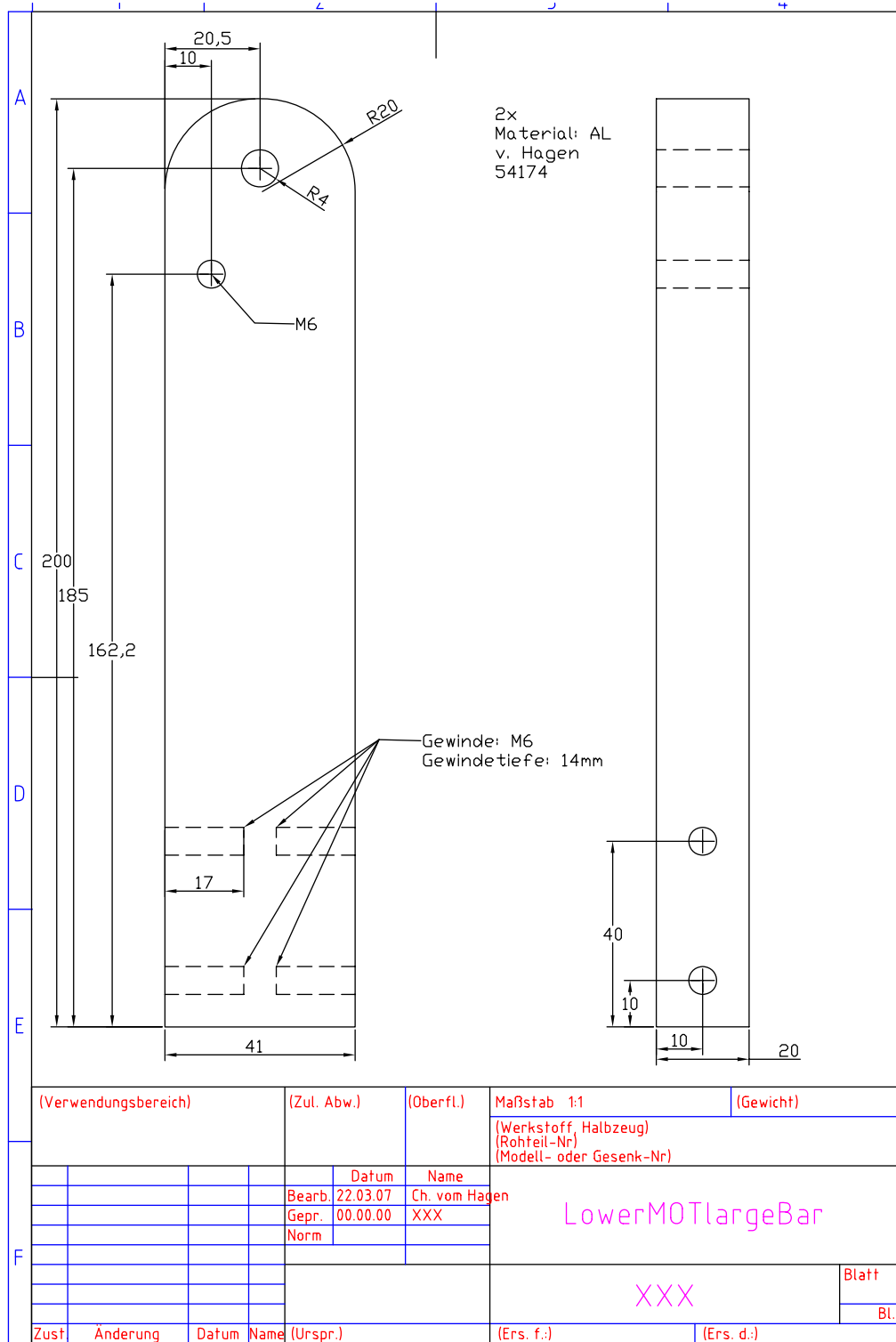


Figure A.15: Holder for lower-MOT precision mount. These bars are vertically upwards and hold the clamps in place. The angel of the clamp is adjustable due to the circular-elongated-holes.

## B Problems

The attempts to evacuate the science chamber with the two dedicated AR-coated 10mm-thick viewports were somewhat disappointing. At room temperature the sealing worked and the window survived for days at an inside vacuum of  $< 1 \times 10^{-8}$  mbar. However, during bakeout, one of the large windows reproducibly broke at a temperature of approximately 125 °C. After elaborate discussions with vacuum, glass and seal engineers the problem was accounted to two possible sources: the welding joint between the science chamber block and the DN 200 CF flange, where it is welded into, see figures A.10 and A.12, and the lacking of tempering during manufacturing. Due to heavy machining, steel can develop tensions in the steel matrix, which can cause deformations while heated. To avoid these kind of tensions, the material is usually tempered before the final fine machining is done. This science chamber did not get such a treatment. The welding causes a very local heating of the welding-steel which can also cause tensions in the material. Due to the asymmetric shape of the welding-seal, it is almost rectangular (figure A.10), such tensions are said to spread unevenly. Concluding it can only be stated that the exact reason of the problem remains still unknown. In the present setup a makeshift solution is used to seal the window; a 15mm-thick BK7 glass substrate (50% thicker than the previous window) without AR coating is used.

It should be noted, that the time involved in these changes is significant. The windows have a lead-time of 3-month, as they are non-standard. Each baking cycle takes a week to slowly heat the chamber, three weeks at the given temperature



Figure B.1: A broken window after a bake-out at 125 °C. The crack along the top-half of the window is clearly visible.

and finally one week to cool down.

# **C Other CAD files**

## **C.1 Optics Boards**





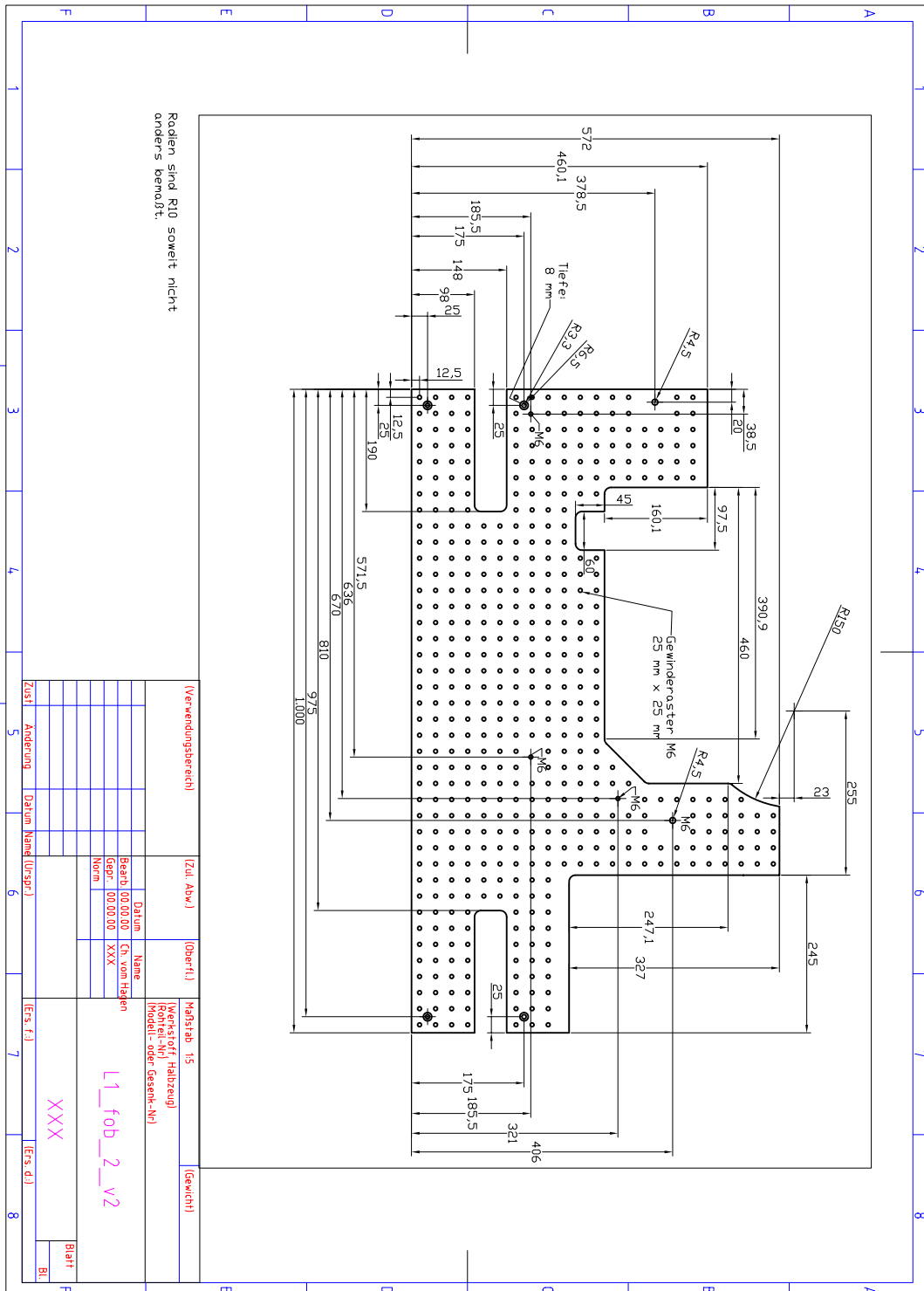


Figure C.2: optics board L1 no2

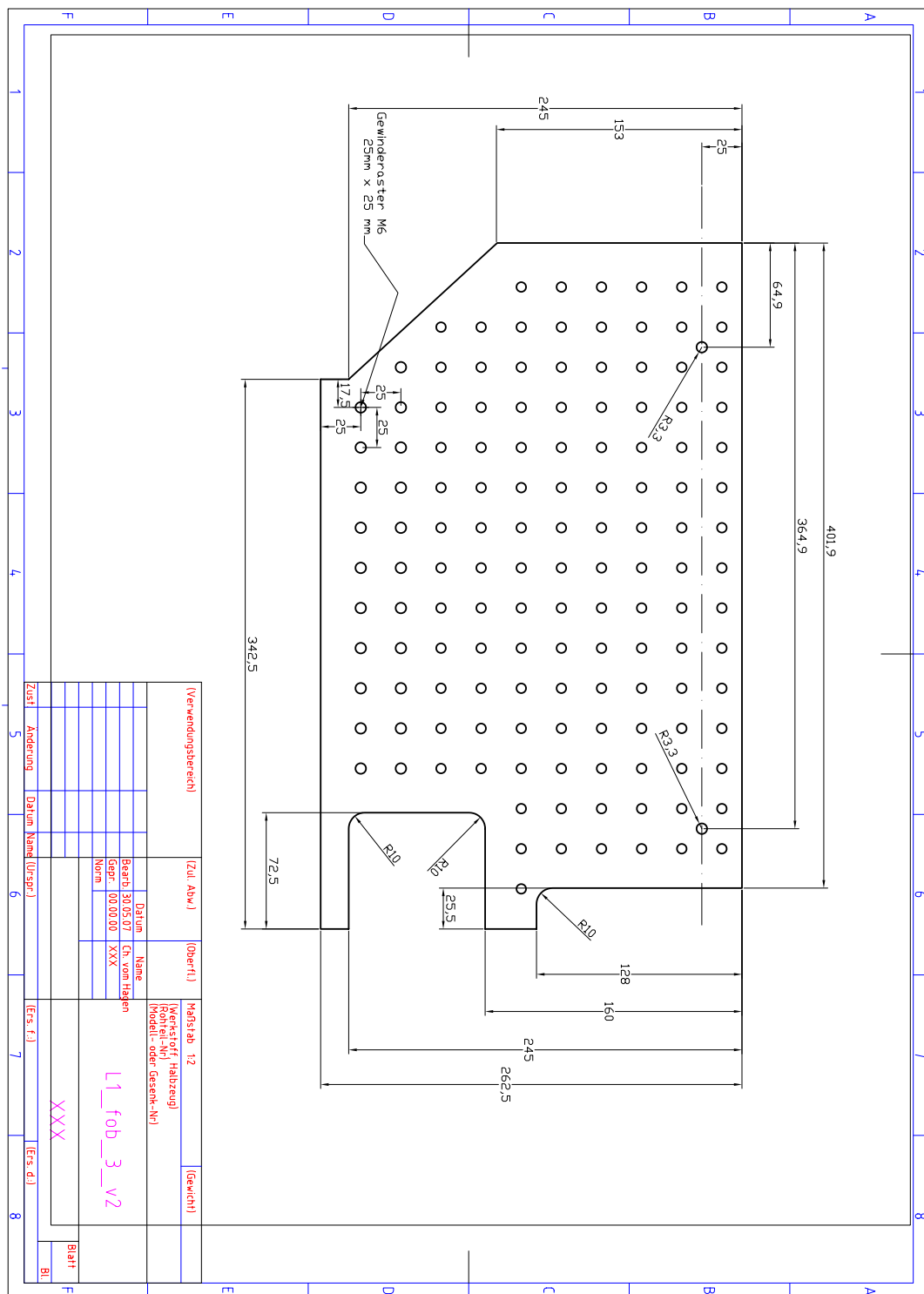


Figure C.3: optics board L1 no3

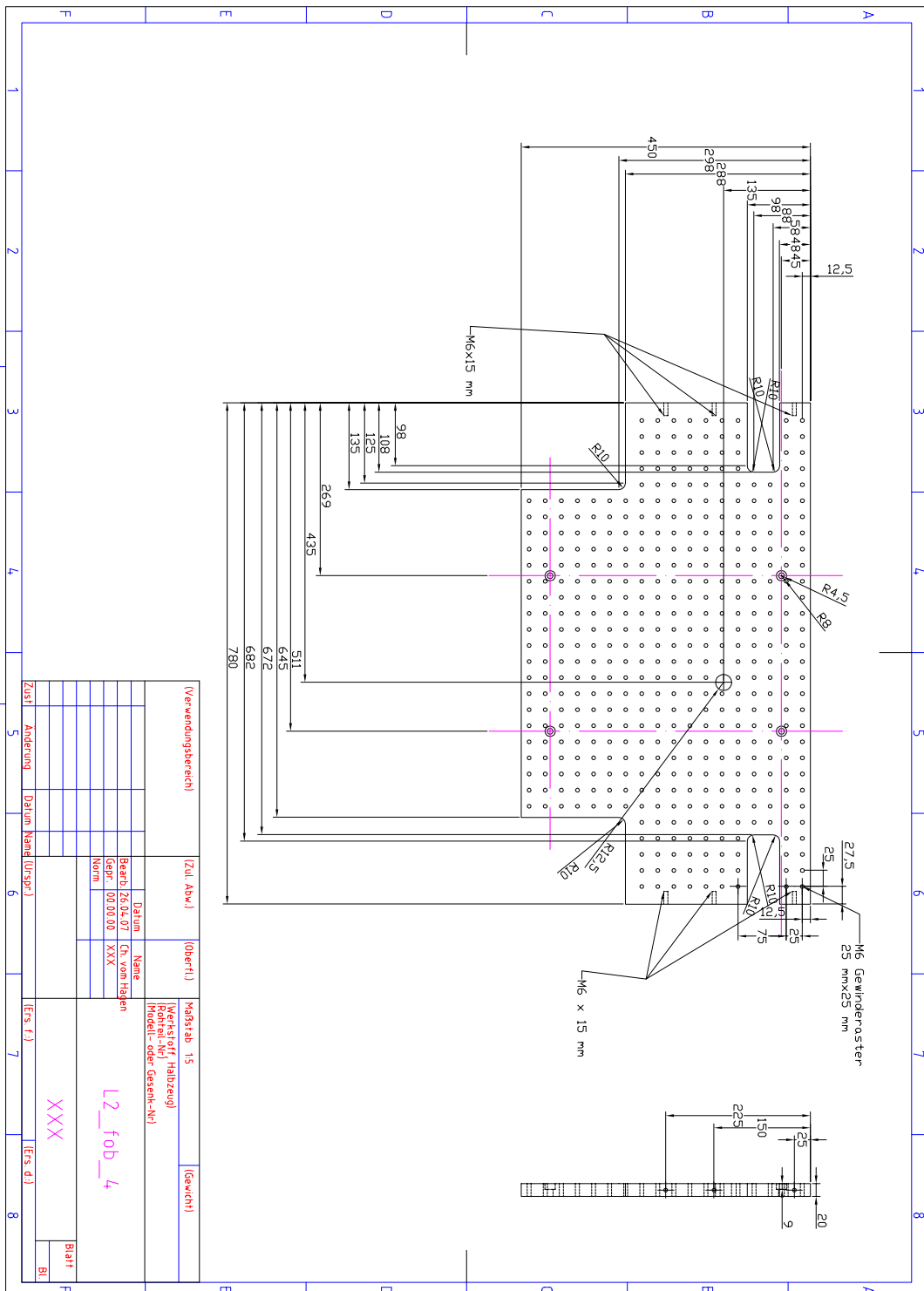


Figure C.4: optics board L2 no4



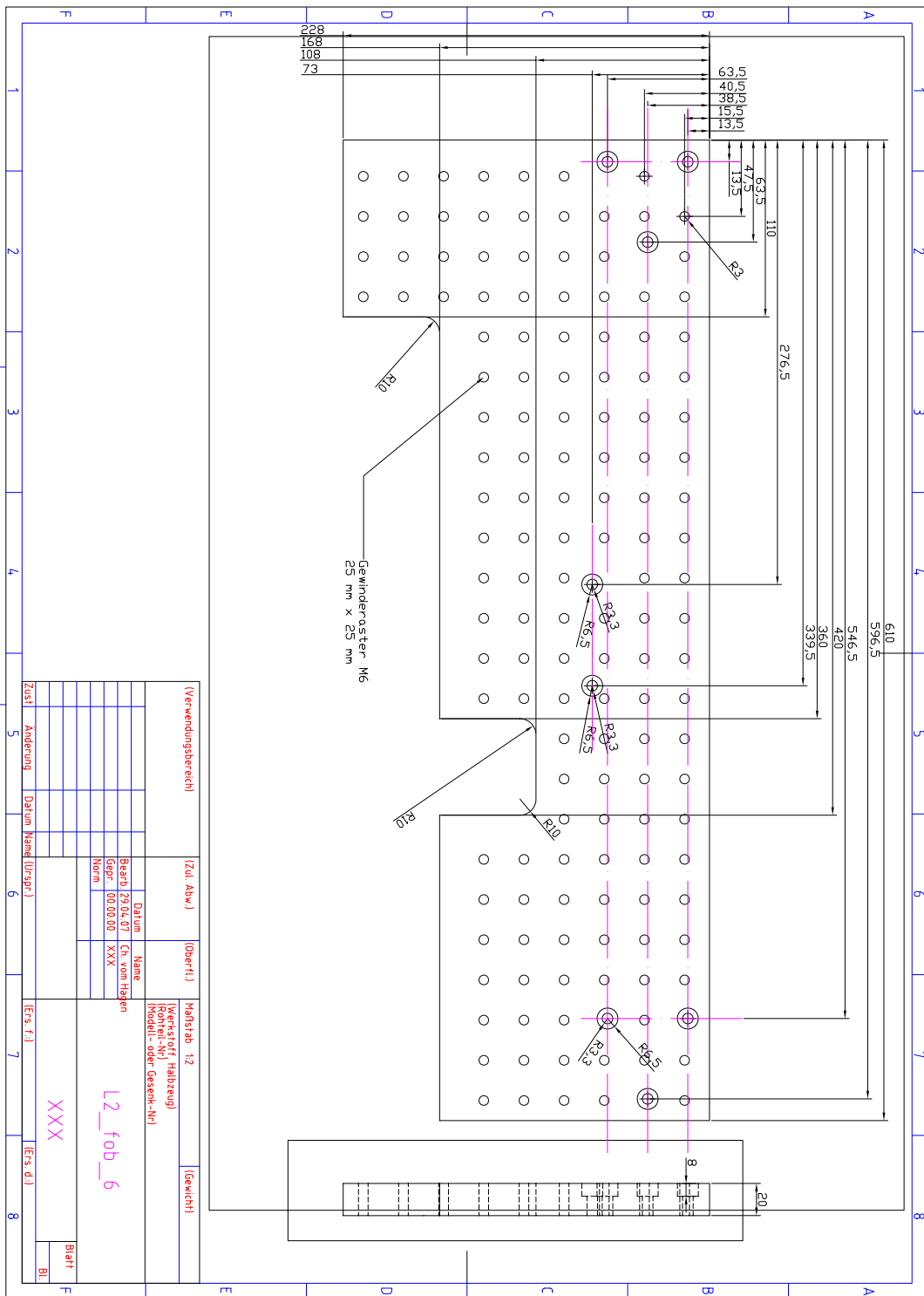


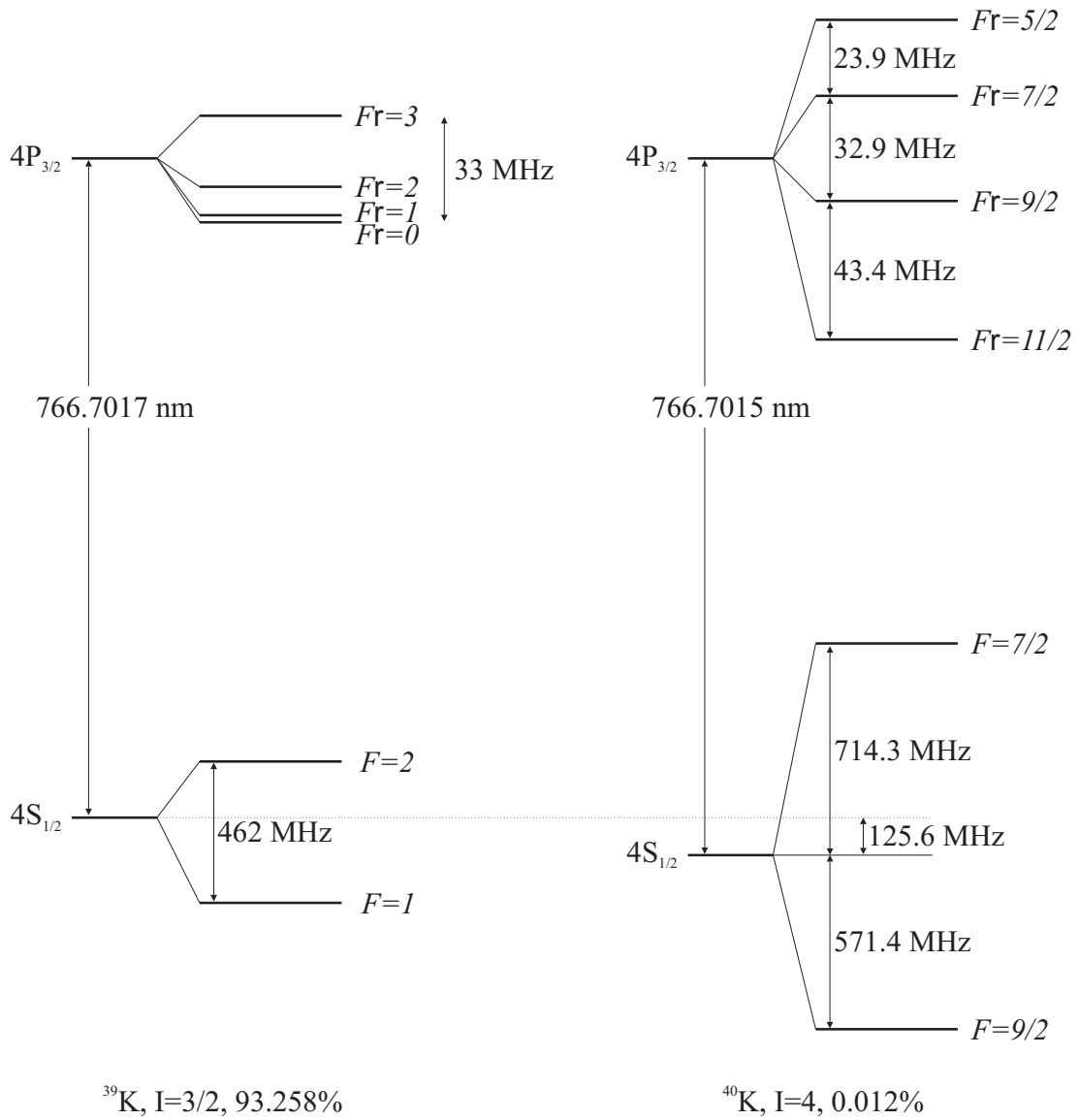
Figure C.6: optics board L2 no6



## **D Level Schemes**

**D.1 Potassium**

**D.2 Rubidium**

Figure D.1: Atomic Level Scheme for  $^{39}\text{K}$  and  $^{40}\text{K}$ .



# Rubidium ( $^{87}\text{Rb}$ )

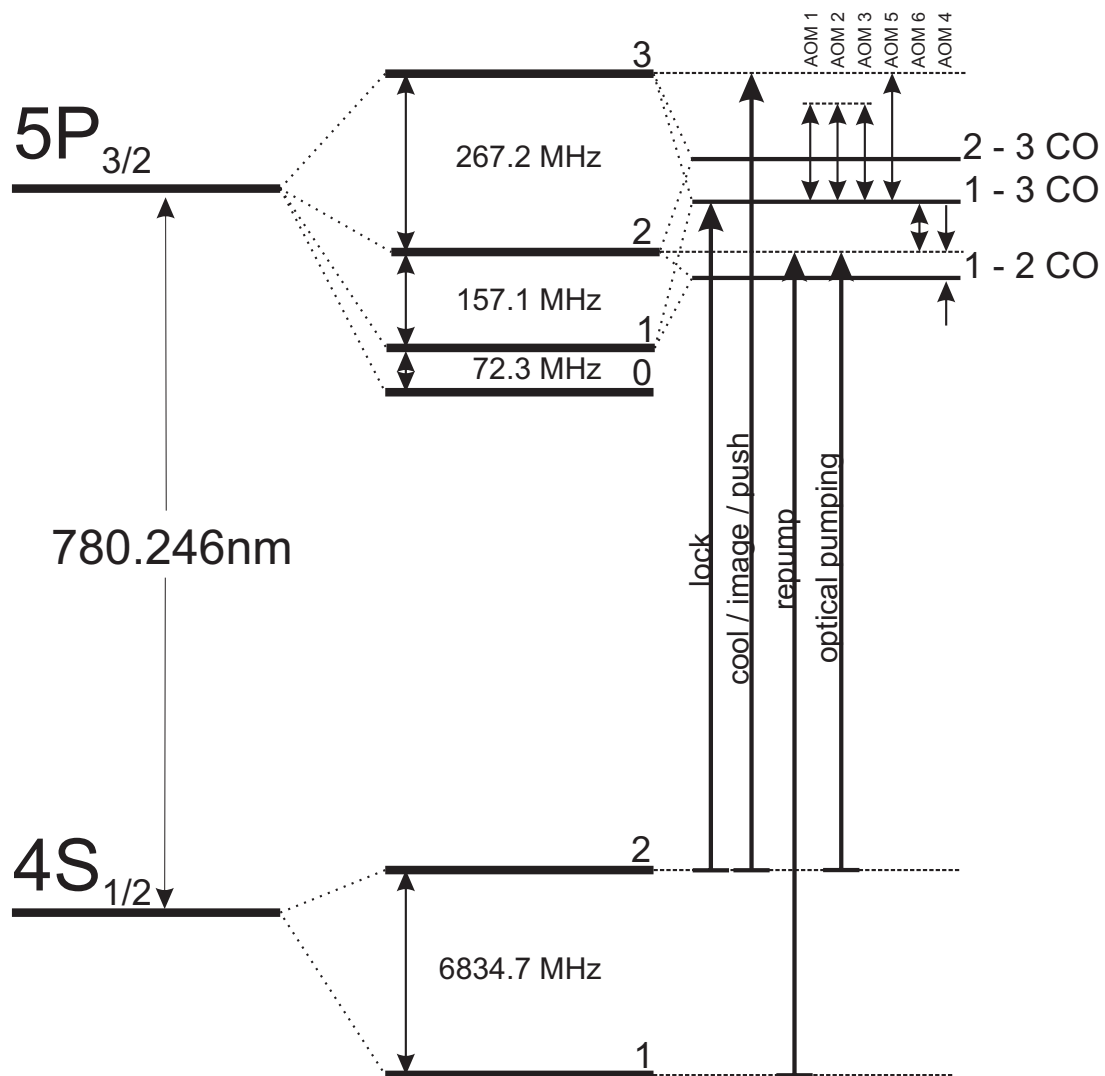


Figure D.2: Atomic level scheme for  $^{87}\text{Rb}$ . The transitions used are indicated.



# E Imaging

In this section, the ultimate limit of detection with the imaging optics discussed in [15] and section 9.5 will be investigated. All relevant details, starting with the photons arriving at the atoms, and the subsequent detection will be discussed.

The optical collection efficiency for a lens is given as:

$$\Omega = \frac{\pi r^2}{4\pi \times d^2} . \quad (\text{E.1})$$

For the current system,  $d = 51.15\text{mm}$  and the open diameter is  $r_1 = \frac{1}{2} \times 27\text{mm}$ , this results in a collection efficiency of  $\sim 5\%$  of all photons scattered into the  $4\pi$  solid angle. The resolution of this system is calculated to be  $2\mu\text{m}$  with the CCD camera in use (DV 435-BV958, pixelsize  $13 \times 13$  micron). On average, an atom scatters, at resonance with a saturation intensity  $I_{sat}$ ,  $N_a$  photons, where

$$N_a \approx \alpha \times \frac{\Gamma}{2} \times t , \quad (\text{E.2})$$

$\alpha$  is the relative fraction of the saturation intensity (usually 1/10 of the saturation intensity is assumed<sup>1</sup>) and  $\Gamma$  and  $t$  are the inverse lifetime and exposure time, respectively. The rms size  $r$  of the diffusive motion of the atom is [32]

$$r = \sqrt{\frac{N}{3}} v_{rec} t , \quad (\text{E.3})$$

from which the maximal exposure time until  $r$  reaches a certain limit ( $r_{limit}$ ) can be calculated to be

$$t_{limit} = \left( \frac{r_{limit}}{\sqrt{\frac{\alpha\Gamma}{6}} v_{rec}} \right)^{2/3} , \quad (\text{E.4})$$

where the recoil velocity  $v_{rec}$  was introduced.

---

<sup>1</sup>At this intensity, the cross section  $\sigma$  scales nearly linear with the intensity, see [32].

A plane wave front of intensity  $\alpha I_{sat}$  will provide a number of photons  $N_0$  in an area  $A$  and a time  $t$ , where  $E = hc/\lambda$  is the energy per photon.

$$N_0 = \frac{\alpha I_{sat} \times A \times t}{E} . \quad (\text{E.5})$$

$N_1$  is the average number of photons scattered by one atom:

$$N_1 \approx \alpha \times \frac{\Gamma}{2} \times t \quad (\text{E.6})$$

$N_2$  is the number of photons in the undisturbed wavefront transmitted through the optical system,

$$N_2 = \xi \times N_0 \quad (\text{E.7})$$

$N_2$  is the number of fluorescence photons transmitted through the optical system

$$N_3 = \xi \times \Omega \times N_1 \quad (\text{E.8})$$

$N_4$  is the difference between the photons from the incident wavefront and the absorption by the atom plus the amount of fluorescence light collected by the optical system,

$$N_4 = N_2 - N_1 + N_3 , \quad (\text{E.9})$$

where  $\xi$  is the transmission coefficient and includes losses at all optical surfaces, but no absorption by the atoms.  $N_1$  is the average number of photons scattered by one atom. Due to the collection efficiency of the optical system  $\Omega$ , a fraction  $N_3$  of the fluorescence photons will be collected.

The CCD camera will convert a photon into an electron with a probability of  $qe$ , which is called the quantum efficiency and is 0.75 for Rb and the camera used. Before readout, the photoelectrons are amplified by a factor *gain*. The absolute numbers of counts at the detector is therefore,

$$N_{2c} = qe \times gain \times N_2 \quad (\text{E.10})$$

$$N_{4c} = qe \times gain \times N_4 . \quad (\text{E.11})$$

Following [78], the column density of the atom is

$$d = -\sigma \log \left( \frac{N_{4c}}{N_{2c}} \right) \quad (\text{E.12})$$

$$\Delta = \frac{1}{\sigma \times \sqrt{N_{2c}}} \times (1 + \exp(\sigma \times d))^{1/2} \quad (\text{E.13})$$

where  $\Delta$  is the error from a Gaussian error propagation.

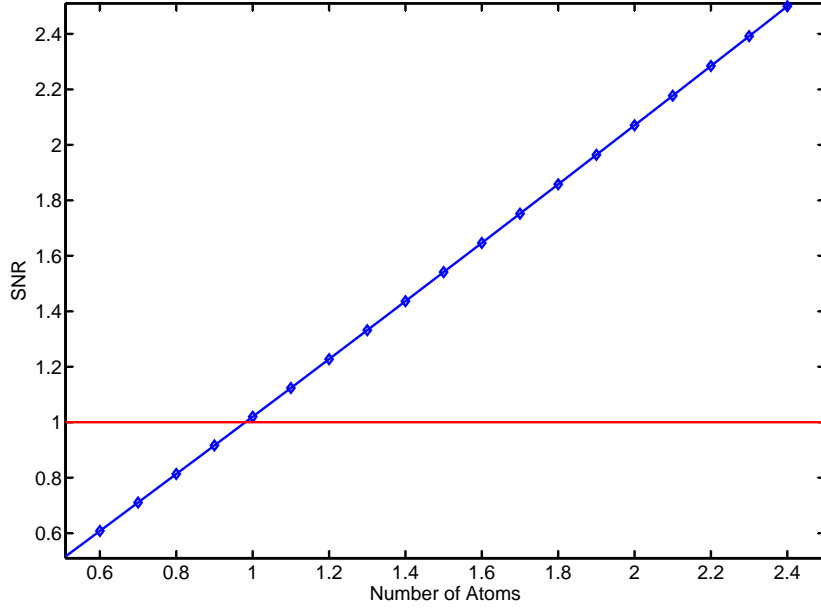


Figure E.1: The dependance of the signal-to-noise ratio on the number of atoms in the detection volume, for  $\alpha = 1/10$  and  $t = 35\mu s$ .

From these, the signal-to-noise ratio can be calculated to be

$$SNR = \frac{d}{\Delta}. \quad (\text{E.14})$$

The result of the  $SNR$  for a given number of atoms in the resolution area can be found in figure E.1. It shows the dependence of the  $SNR$  on the number of atoms (in the low-number range) in the detection area, which is  $A = \pi r^2$  in this calculation. The intensity was fixed at  $\alpha = 1/10$  of the saturation intensity and  $r = 1 \times 10^{-6}$ . The  $SNR$  becomes larger than 1 at approximately 1 atom in the area  $A = \pi \times 10^{-12} \text{m}^2$ .

In conclusion, this section shows, that the detection of 2 atoms in the resolution area  $A$  is possible with a signal to noise ratio of 2.



# F Electronics

## F.1 Laser Electronics

## F.2 Charge Pump

The first attempts to load the magnetic micro trap in the LiRb experiment suffered from the fact, that the bias field coil had a high inductance. To speed this switching time up, a charge pump was developed. The idea behind such a device is rather simple: a capacitor is charged to a high-voltage and rapidly discharged into the coil during switch on. To avoid any LC-circuit oscillations, the capacitor is disconnected from the circuit after the first quarter cycle of this possible oscillation. A thyristor is used for this purpose. A thyristor is in the isolating state until it receives a trigger pulse. This trigger pulse brings the thyristor into a conducting state, which is maintained until the current through the thyristor drops below a threshold value, typically some 100mA. In the current layout a capacitor is charged to 200V. The switch-on time for the coils in Heidelberg was decreased from  $12\pm 0.2\text{ms}$  to  $1.3\pm 0.2\text{ms}$ . The inductance of the coils was  $1286\mu\text{H}$ . Figure F.3 shows the switch-on behaviour for the new bias field coil in Vienna, see section 9. Figure F.4 shows the actual circuit diagram.

## F.3 H-Bridge High Current Switch

During experiments with the LiRb mixture it was needed to flip the direction of a field, hence the H-bridge circuit was developed. It can be used for inverting the direction of current flow, see figure F.5 for a diagram of the functional principle. This is useful for two situations, firstly, if a pair of coils is inserted at in the circuit, the direction of the field can be inverted, secondly, if one coil of a pair is inserted in the circuit, the configuration can be changed from a quadrupole configuration to a Helmholtz configuration. The current can be drawn through AB or CD, which reverses the current flow through the coil. In the current design, a fully integrated IGBT module is used. The switch was tested up to 150A. To allow for fast switching, a drain circuit is used to actively discharge the coil. Figures F.6 and F.7 show the actual circuit diagrams.

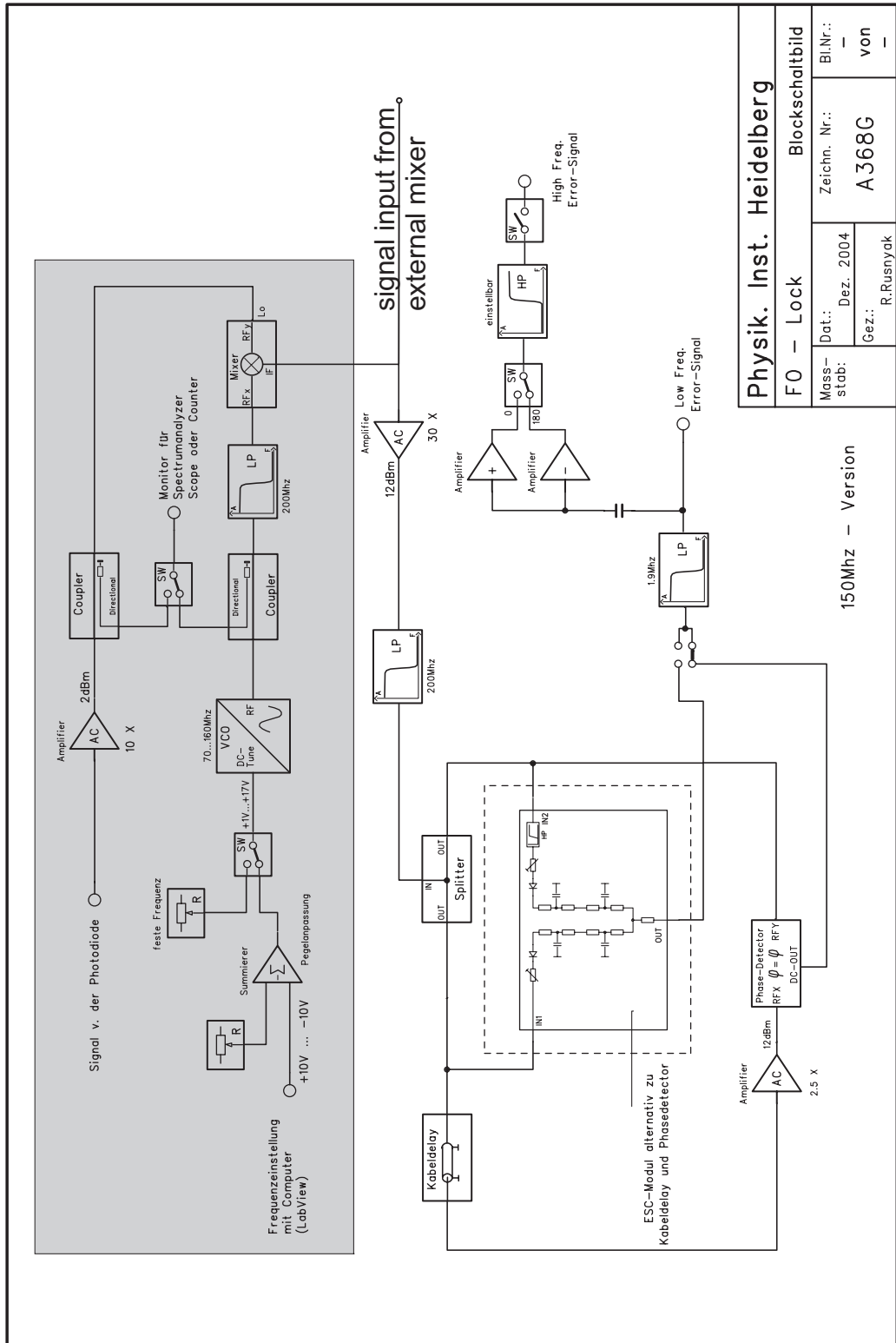


Figure F.1: Changes to the FO-lock card from Heidelberg. Parts within the grey area are removed. The input is connected to the front plane plug, which is labelled *Photo Diode*.



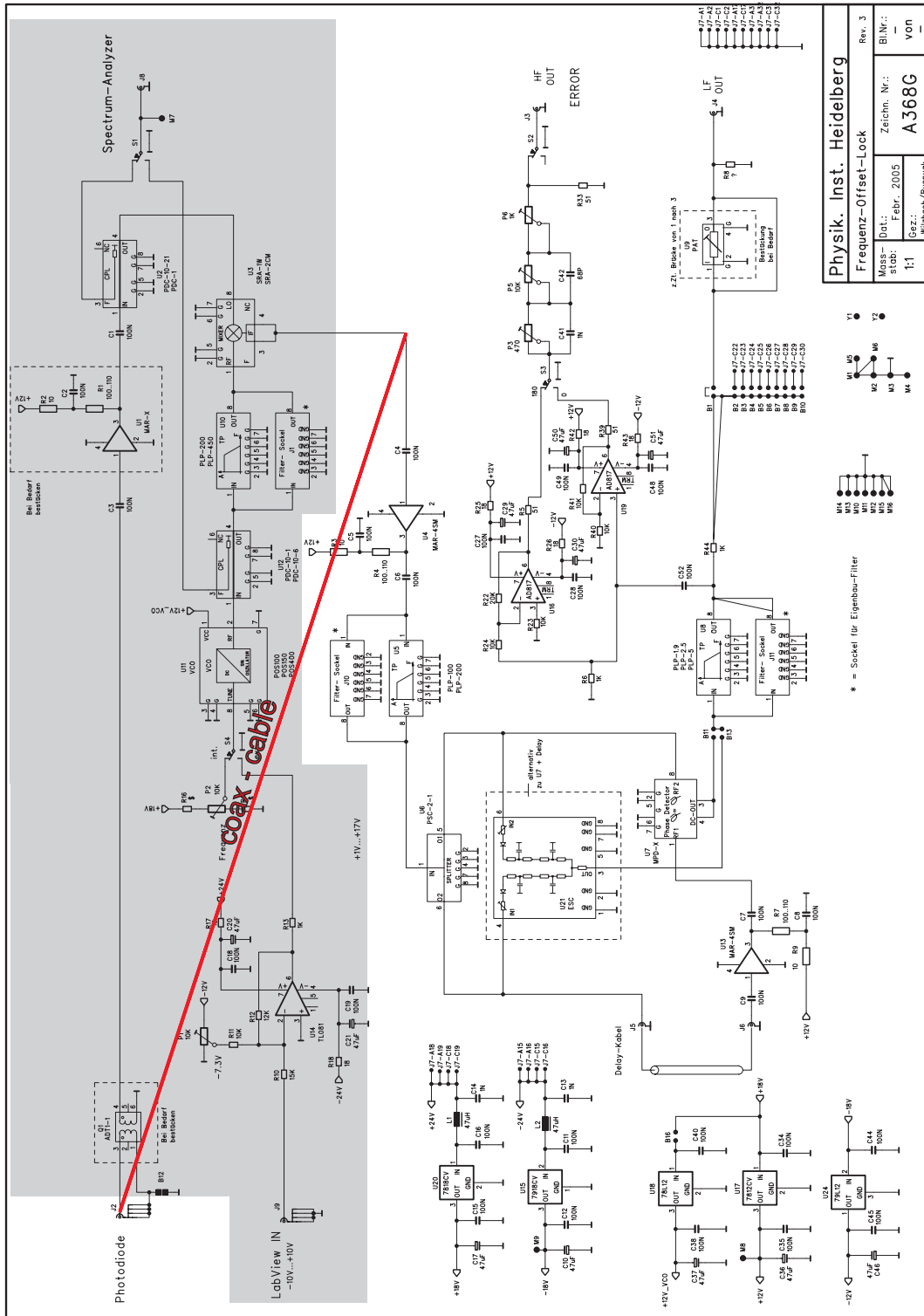


Figure F.2: Changes to the FO-lock board in detail.

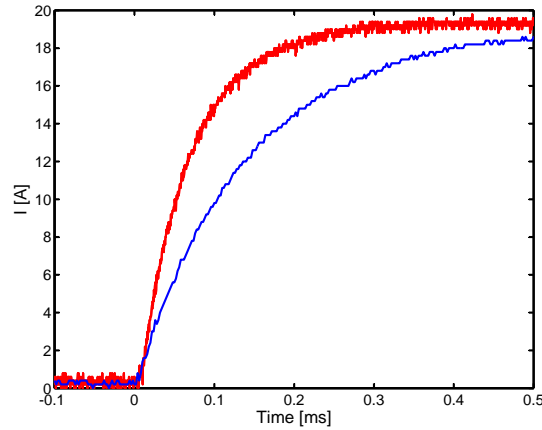
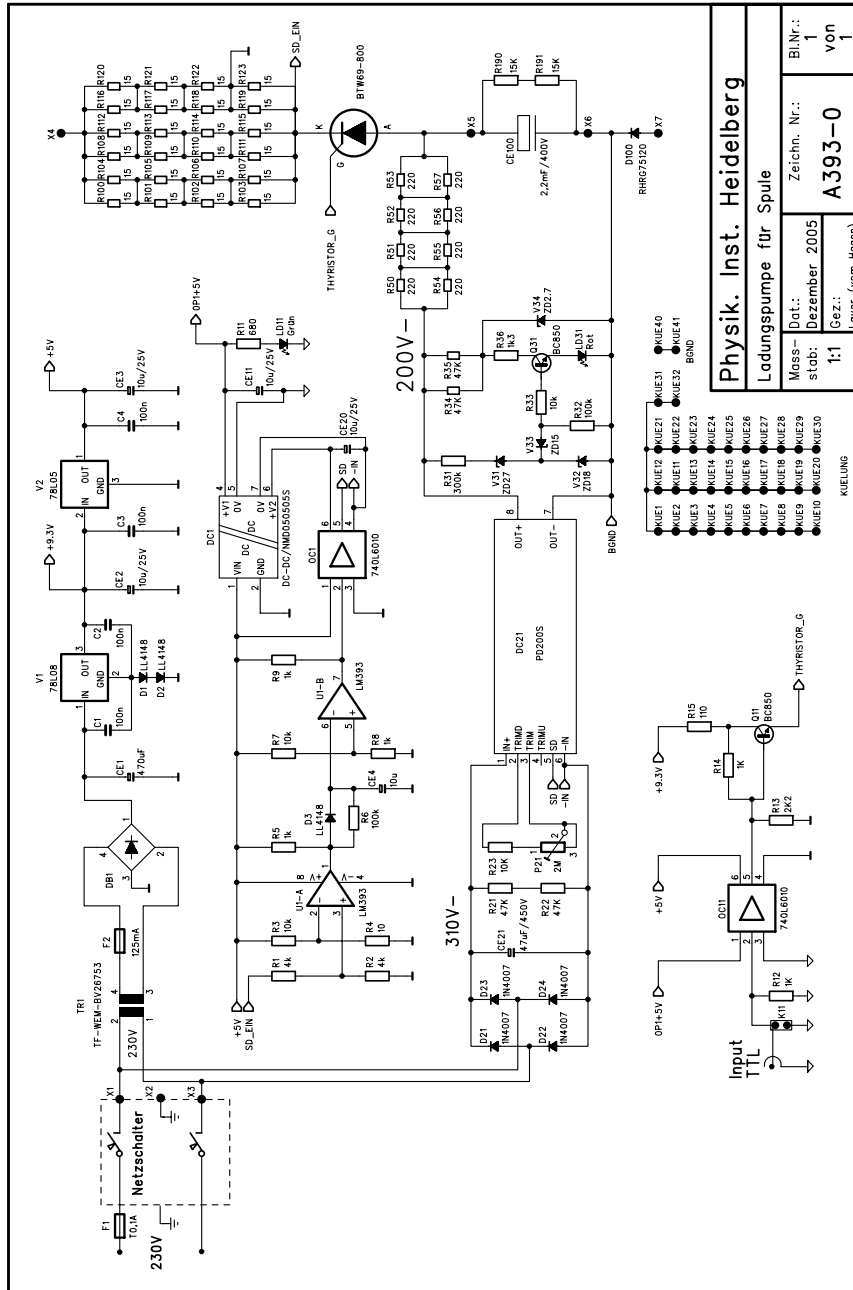


Figure F.3: The switch-on behaviour of the x-coils (red) and the z-coil (blue) with the charge pump. The difference in the switch on time for x and z is due to the difference in inductance.

## F.4 Current–Feedback

The circuit diagram of the feedback loop can be found in figure ???. The two INA114 amplifiers measure the signal from the sensing resistor and the control line from the ADWin system. The two signals are compared at the third INA114. With the PID stage the behaviour of the circuit can be adjusted to the specific coil configuration. The feedback will be used for all copper structures and bias field coils described in section 9. The layouts of the printed circuit boards are shown in figures F.8 and F.9. This layout was designed with the help of a summer student, Fabio Tonti.

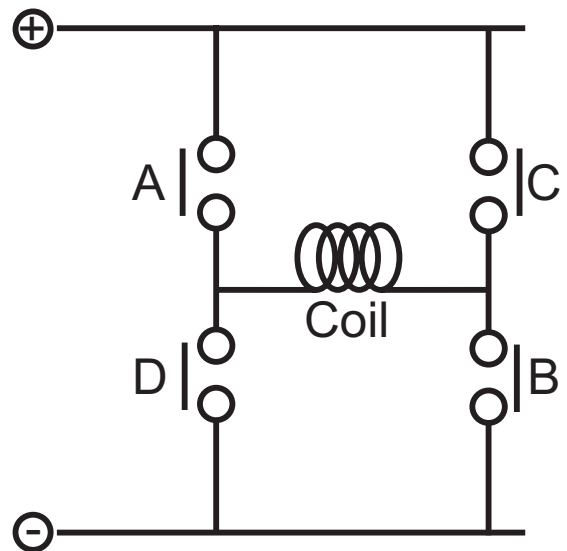


<b>Physik. Inst. Heidelberg</b>	
<b>Ladungspumpe für Spule</b>	
Mass- stab- 1:1	Zeichn. Nr.: <b>A393-0</b>
Bl.Nr.: 1	von 1
Layer: (vom Hohen)	

- KÜEHLUNG
- KUE10
  - KUE11
  - KUE12
  - KUE13
  - KUE14
  - KUE15
  - KUE16
  - KUE17
  - KUE18
  - KUE19
  - KUE20
  - KUE21
  - KUE22
  - KUE23
  - KUE24
  - KUE25
  - KUE26
  - KUE27
  - KUE28
  - KUE29
  - KUE30
  - KUE31
  - KUE32
  - KUE40
  - KUE41
  - KUE42
  - KUE43
  - KUE44

Figure F.4: The circuit diagram for the charge pump.

Figure F.5: Diagram of the functional principle of the H-bridge circuit. A,B,C,D denote independent addressable switches. Current path AB and CD are used to reverse the current flow in the coil.



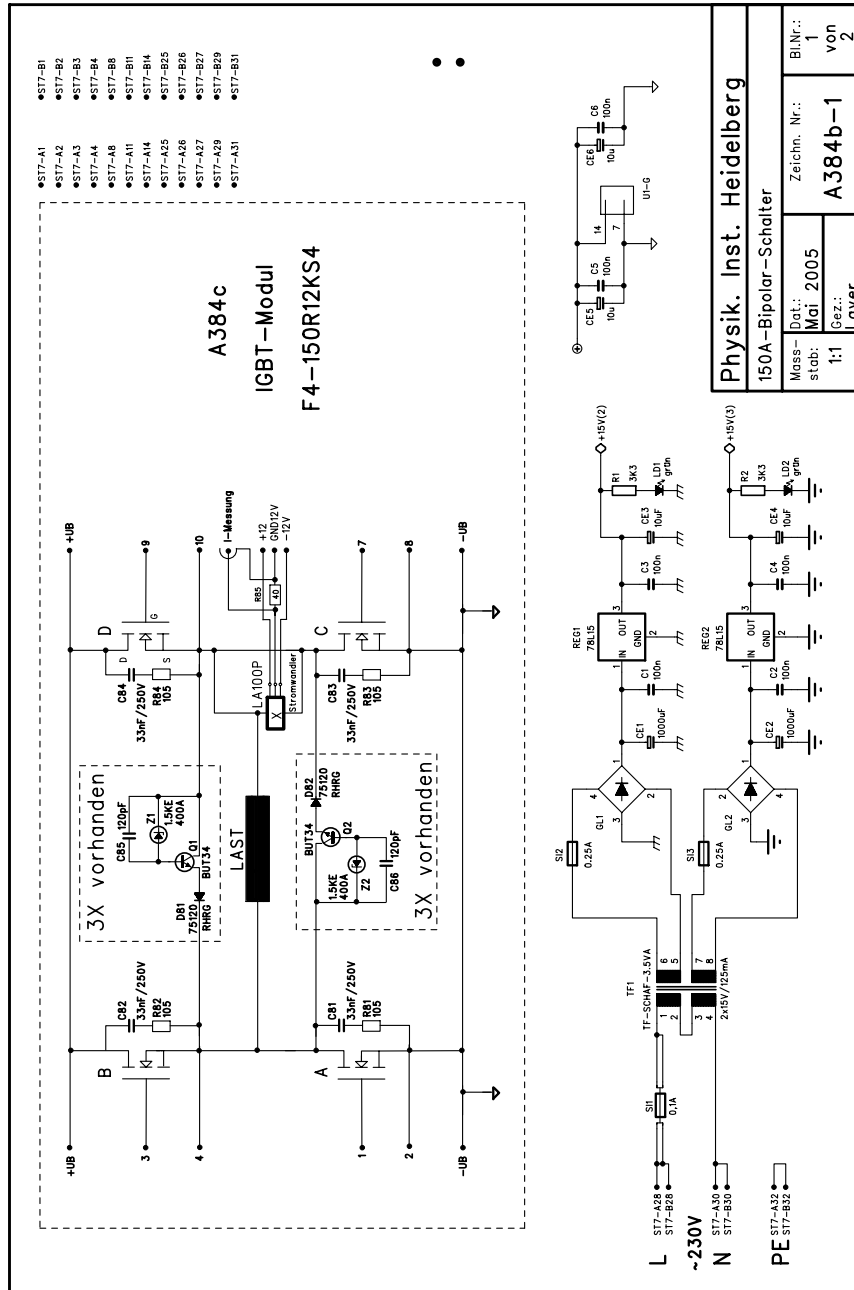


Figure F.6: The circuit diagram for the H-bridge switch is shown. The four IGBT switches and the emptying circuits are clearly visible.

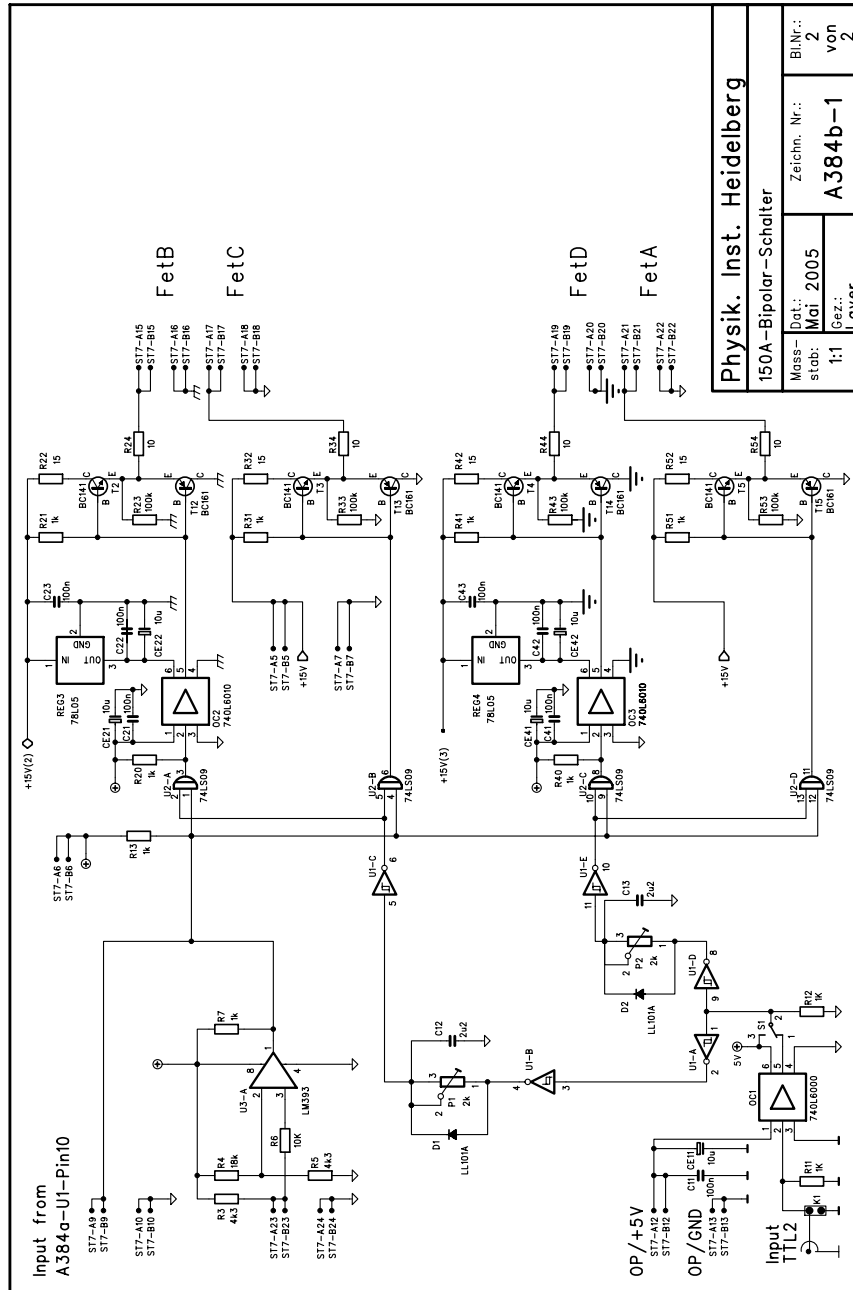


Figure F.7: The circuit diagram for the driving circuits for the four IGBT gates are shown.

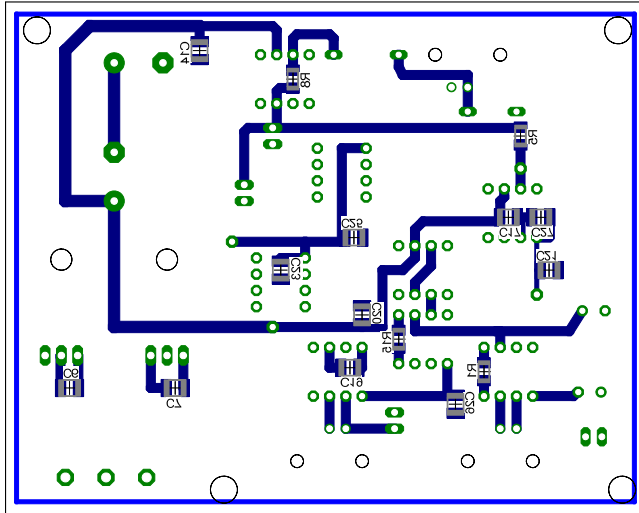


Figure F.8: Bottom layout of the printed circuit board for the feedback circuit.

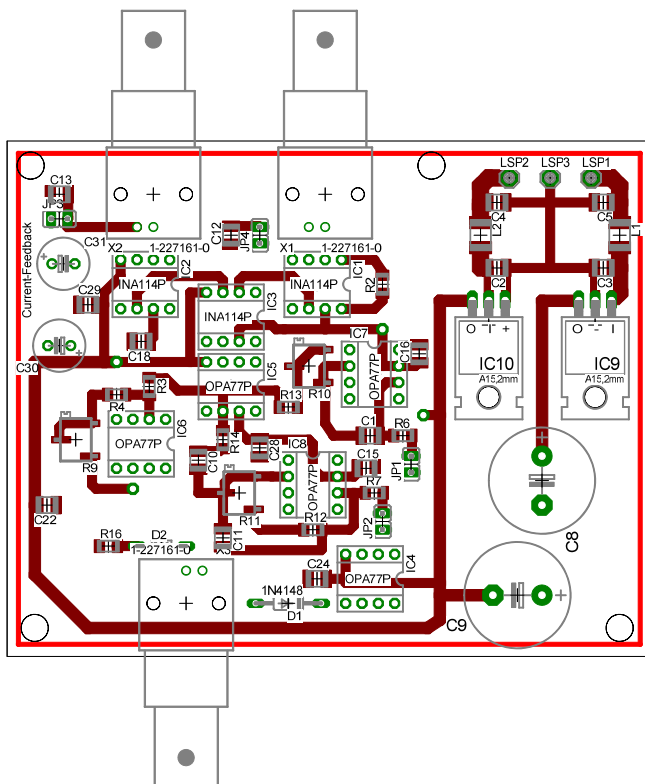


Figure F.9: Top layer of the printed circuit board for the feedback circuit.

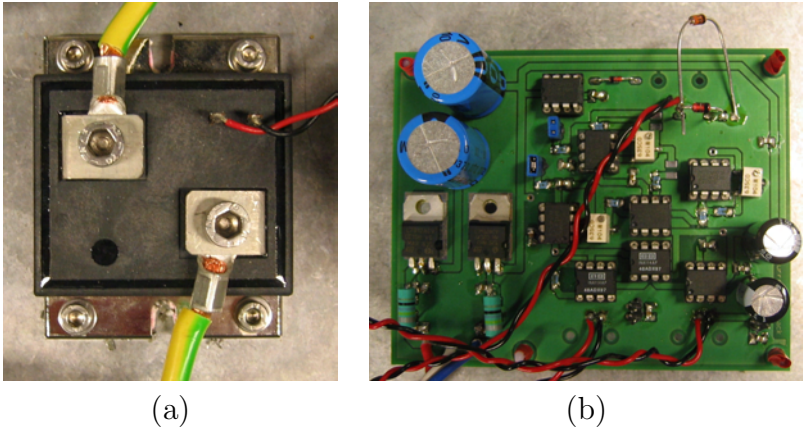


Figure F.10: (a) the sensing resistor and (b) the assembled board.



# Bibliography

- [1] M. H. Anderson, J. R. Ensher, M. R. Matthews, C. E. Wieman, and E. A. Cornell. Observation of Bose-Einstein Condensation in a Dilute Atomic Vapor. *Science*, 269(5221):198, 1995.
- [2] K. B. Davis, M. O. Mewes, M. R. Andrews, N. J. van Druten, D. S. Durfee, D. M. Kurn, and W. Ketterle. Bose-Einstein Condensation in a Gas of Sodium Atoms. *Phys. Rev. Lett.*, 75(22):3969, 1995.
- [3] B. DeMarco and D. S. Jin. Onset of Fermi Degeneracy in a Trapped Atomic Gas. *Science*, 285(5434):1703, 1999.
- [4] Jens Herbig, Tobias Kraemer, Michael Mark, Tino Weber, Cheng Chin, Hanns-Christoph Nägerl, and Rudolf Grimm. Preparation of a Pure Molecular Quantum Gas. *Science*, 301(5639):1510, 2003.
- [5] D. S. Petrov, C. Salomon, and G. V. Shlyapnikov. Weakly Bound Dimers of Fermionic Atoms. *Phys. Rev. Lett.*, 93(9):090404, 2004.
- [6] C. A. Regal, M. Greiner, and D. S. Jin. Lifetime of Molecule-Atom Mixtures near a Feshbach Resonance in  $^{40}\text{K}$ . *Phys. Rev. Lett.*, 92(8):083201, 2004.
- [7] K. Dieckmann, C. A. Stan, S. Gupta, Z. Hadzibabic, C. H. Schunck, and W. Ketterle. Decay of an Ultracold Fermionic Lithium Gas near a Feshbach Resonance. *Phys. Rev. Lett.*, 89(20):203201, 2002.
- [8] Roberto Casalbuoni and Giuseppe Nardulli. Inhomogeneous superconductivity in condensed matter and QCD. *Rev. Mod. Phys.*, 76(1):263, 2004.
- [9] Hui Hu, Xia-Ji Liu, and Peter D. Drummond. Phase Diagram of a Strongly Interacting Polarized Fermi Gas in One Dimension. *Phys. Rev. Lett.*, 98(7):070403, 2007.
- [10] D. S. Petrov, G. E. Astrakharchik, D. J. Papoular, C. Salomon, and G. V. Shlyapnikov. Crystalline Phase of Strongly Interacting Fermi Mixtures. *Phys. Rev. Lett.*, 99(13):130407, 2007.
- [11] D. A. Smith. private communication.
- [12] Christoph Hufnagel. *Cold Collisions between  $^6\text{Li}$  and  $^{87}\text{Rb}$  in a Two-Species Magneto-Optical Trap*. Master's thesis, Universität Heidelberg, 2005.

- [13] Karolina Brugger. *Experimente mit mikroskopischen atomoptischen Elementen*. Ph.D. thesis, Universität Heidelberg, 2004.
- [14] B. Bussery, Y. Achkar, and M. Aubert-Frécon. Long-Range molecular states dissociating to the three or four lowest asymptotes for the ten heteronuclear diatomic alkali molecules. *Chemical Physics*, 116:319, 1987.
- [15] B Stix. *N.N.* Master's thesis, Technische Universität Wien, 2008.
- [16] M. Kuhnert. *N.N.* Master's thesis, Technische Universität Wien, 2008.
- [17] H. J. Metcalf P. van der Straten. *Laser Cooling and Trapping*. Springer, 2002.
- [18] E. L. Raab, M. Prentiss, Alex Cable, Steven Chu, and D. E. Pritchard. Trapping of Neutral Sodium Atoms with Radiation Pressure. *Phys. Rev. Lett.*, 59(23):2631, 1987.
- [19] P. D. Lett, W. D. Phillips, S. L. Rolston, C. E. Tanner, R. N. Watts, and C. I. Westbrook. Optical molasses. *J. Opt. Soc. Am. B*, 6(11):2084, 1989.
- [20] C. Fertig and K. Gibble. Laser-cooled  $^{87}\text{Rb}$  clock. *Instrumentation and Measurement, IEEE Transactions on*, 48(2):520, Apr 1999.
- [21] Alan L. Migdall, John V. Prodan, William D. Phillips, Thomas H. Bergeman, and Harold J. Metcalf. First Observation of Magnetically Trapped Neutral Atoms. *Phys. Rev. Lett.*, 54(24):2596, 1985.
- [22] G. K. Woodgate. *Elementary Atomic Structure*. Oxford University Press, 2 edition, 1983.
- [23] William H. Wing. On neutral particle trapping in quasistatic electromagnetic fields. *Progress in Quantum Electronics*, 8(3-4):181, 1984.
- [24] W. Ketterle and D. E. Pritchard. Trapping and focusing ground state atoms with static fields. *Applied Physics B: Lasers and Optics*, 54(5):403, 1992.
- [25] E. Majorana. Atomi orientati in campo magnetico variabile. *Nuovo Cimento*, 9:43, 1932.
- [26] David E. Pritchard. Cooling Neutral Atoms in a Magnetic Trap for Precision Spectroscopy. *Phys. Rev. Lett.*, 51(15):1336, 1983.
- [27] Wolfgang Petrich, Michael H. Anderson, Jason R. Ensher, and Eric A. Cornell. Stable, Tightly Confining Magnetic Trap for Evaporative Cooling of Neutral Atoms. *Phys. Rev. Lett.*, 74(17):3352, 1995.

- [28] S. Wildermuth, P. Krüger, C. Becker, M. Brajdic, S. Haupt, A. Kasper, R. Folman, and J. Schmiedmayer. Optimized magneto-optical trap for experiments with ultracold atoms near surfaces. *Phys. Rev. A*, 69(3):030901, 2004.
- [29] A. Jaakkola, A. Shevchenko, K. Lindfors, M. Hautakorpi, E. Ilyashenko, T. H. Johansen, and M. Kaivola. Reconfigurable atom chip on a transparent ferrite-garnet film. *The European Physical Journal D - Atomic, Molecular, Optical and Plasma Physics*, 35(1):81, 2005.
- [30] J. Reichel, W. Hänsel, and T. W. Hänsch. Atomic Micromanipulation with Magnetic Surface Traps. *Phys. Rev. Lett.*, 83(17):3398, 1999.
- [31] Ron Folman, Peter Krüger, Donatella Cassettari, Björn Hessmo, Thomas Maier, and Jörg Schmiedmayer. Controlling Cold Atoms using Nanofabricated Surfaces: Atom Chips. *Phys. Rev. Lett.*, 84(20):4749, 2000.
- [32] W. Ketterle, D. S. Durfree, and D. M. Stamper-Kurn. Making, probing and understanding Bose-Einstein condensates. Contribution to the proceedings of the 1998 Enrico Fermi summer school on Bose-Einstein condensation in Varenna, Italy, page 1. Academic Press, 1998. And references therein.
- [33] Harald F. Hess. Evaporative cooling of magnetically trapped and compressed spin-polarized hydrogen. *Phys. Rev. B*, 34(5):3476, 1986.
- [34] O. J. Luiten, M. W. Reynolds, and J. T. M. Walraven. Kinetic theory of the evaporative cooling of a trapped gas. *Phys. Rev. A*, 53(1):381, 1996.
- [35] K. B. Davis, M. O. Mewes, and W. Ketterle. An analytical model for evaporative cooling of atoms. *Applied Physics B: Lasers and Optics*, 60(2):155, 1995.
- [36] C. R. Monroe, E. A. Cornell, C. A. Sackett, C. J. Myatt, and C. E. Wieman. Measurement of Cs-Cs elastic scattering at  $T=30 \mu\text{K}$ . *Phys. Rev. Lett.*, 70(4):414, 1993.
- [37] C. J. Pethnik and H. Smith. *Bose-Einstein Condensation*. Cambridge University Press, 2005.
- [38] D. J. Heinzen. *Bose Einstein Condensation in Atomic Gases*. IOS Press Inc., 1999.
- [39] E. G. M. van Kempen, S. J. J. M. F. Kokkelmans, D. J. Heinzen, and B. J. Verhaar. Interisotope Determination of Ultracold Rubidium Interactions from Three High-Precision Experiments. *Phys. Rev. Lett.*, 88(9):093201, 2002.

- [40] C. Silber, S. Günther, C. Marzok, B. Deh, Ph. W. Courteille, and C. Zimmermann. Quantum-Degenerate Mixture of Fermionic Lithium and Bosonic Rubidium Gases. *Phys. Rev. Lett.*, 95(17):170408, 2005.
- [41] Ferlaino and Modugno. K-Rb scattering. *PHYSICAL REVIEW A*, 74:039903, 2006.
- [42] C. J. Myatt, E. A. Burt, R. W. Ghrist, E. A. Cornell, and C. E. Wieman. Production of Two Overlapping Bose-Einstein Condensates by Sympathetic Cooling. *Phys. Rev. Lett.*, 78(4):586, 1997.
- [43] Immanuel Bloch, Markus Greiner, Olaf Mandel, Theodor W. Hänsch, and Tilman Esslinger. Sympathetic cooling of  $^{85}\text{Rb}$  and  $^{87}\text{Rb}$ . *Phys. Rev. A*, 64(2):021402, 2001.
- [44] L. Pricoupenko, H. Perrin, and ed. M. Olshanii. Quantum gases in low dimensions. *J. Phys. IV*, 116, 2004.
- [45] Kunal K. Das. Bose-Fermi Mixtures in One Dimension. *Phys. Rev. Lett.*, 90(17):170403, 2003.
- [46] Bing Ji, Chin-Chun Tsai, and William C. Stwalley. Proposed modification of the criterion for the region of validity of the inverse-power expansion in diatomic long-range potentials. *Chemical Physics Letters*, 236(3):242, 1995.
- [47] John Weiner. *Cold and Ultracold Collision in Quantum Microscopic and Mesoscopic Systems*. Cambridge University Press, 2003.
- [48] J. Vigué. Possibility of applying laser-cooling techniques to the observation of collective quantum effects. *Phys. Rev. A*, 34(5):4476, 1986.
- [49] Alan Gallagher and David E. Pritchard. Exoergic collisions of cold  $\text{Na}^*\text{-Na}$ . *Phys. Rev. Lett.*, 63(9):957, 1989.
- [50] A. M. Steane, M. Chowdhury, and C. J. Foot. Radiation force in the magneto-optical trap. *J. Opt. Soc. Am. B*, 9(12):2142, 1992.
- [51] Harold Metcalf. Magneto-optical trapping and its application to helium metastables. *J. Opt. Soc. Am. B*, 6(11):2206, 1989.
- [52] D. Hoffmann, P. Feng, and T. Walker. Measurements of Rb trap-loss collision spectra. *J. Opt. Soc. Am. B*, 11(5):712, 1994.
- [53] G. D. Telles, W. Garcia, L. G. Marcassa, V. S. Bagnato, D. Ciampini, M. Fazzi, J. H. Müller, D. Wilkowski, and E. Arimondo. Trap loss in a two-species Rb-Cs magneto-optical trap. *Phys. Rev. A*, 63(3):033406, 2001.

- [54] R. Grimm, M. Weidemüller, and Y. B. Ovchinnikov. Optical Dipole Traps for neutral Atoms. *Adv. At., Mol., Opt. Phys.*, 42:95, 2000.
- [55] U. Volz H. Schmoranzner. Precision Lifetime Measurements on Alkali Atoms and on Helium by Beam - Gas - Laser Spectroscopy. *Physics Scripta*, T65:48, 1996.
- [56] M. Wilzbach. *Single atom detection on an atom chip with integrated optics*. Ph.D. thesis, Universität Heidelberg, 2007.
- [57] M. Gehm. Properties of  ${}^6\text{Li}$ . *on the Web*, 2003.
- [58] D. Steck. Rubidium 87 D Line Data. 2001.
- [59] W. Demtröder. *Laser Spectroscopy*. Springer, 2003.
- [60] P. Horowitz and W. Hill. *The art of electronics*. Cambridge University Press, 1989.
- [61] Stanford Research Systems. About Lock-In Amplifiers, Application Note #3. Technical report, Stanford Research Systems, <http://www.thinksrs.com/downloads/PDFs/ApplicationNotes/AboutLIAs.pdf>, 2008.
- [62] Philip C.D. Hobbs. *Building Electro-Optical Systems: Making It All Work*. John Wiley, 2000.
- [63] James M. Supplee, Edward A. Whittaker, and Wilfried Lenth. Theoretical description of frequency modulation and wavelength modulation spectroscopy. *Appl. Opt.*, 33(27):6294, 1994.
- [64] Gary C. Bjorklund. Frequency-modulation spectroscopy: a new method for measuring weak absorptions and dispersions. *Opt. Lett.*, 5(1):15, 1980.
- [65] G. C. Bjorklund, M. D. Levenson, W. Lenth, and C. Ortiz. Frequency modulation (FM) spectroscopy. *Applied Physics B: Lasers and Optics*, 32(3):145, 1983.
- [66] M. Rückel. *Frequenzstabilisierung eines Diodenlasers über das "Frequency-offset-locking"*. Master's thesis, Universität Heidelberg, 2002.
- [67] M. Wilzbach. *Aufbau eines Experiments zur miniaturisierten und integrierten Detektion neutraler Atome*. Master's thesis, Universität Heidelberg, 2002.
- [68] K. Petermann. *Advances in Optoelectronics No.3: Laser Diode Modulation and Noise*. Springer, 1988.

- [69] U. Schünemann, H. Engler, R. Grimm, M. Weidemüller, and M. Zielonkowski. Simple scheme for tunable frequency offset locking of two lasers. *Rev. Sci. Instrum.*, 70(1):242, 1999.
- [70] Craig J. Sansonetti, Bruno Richou, Rolf Engleman, and Leon J. Radziemski. Measurements of the resonance lines of  $^6\text{Li}$  and  $^7\text{Li}$  by Doppler-free frequency-modulation spectroscopy. *Phys. Rev. A*, 52(4):2682, 1995.
- [71] A Kasper, S. Schneider, Ch. vom Hagen, M. Bartenstein, B. Engeser, T. Schumm, I. Bar-Joseph, R. Folman, L Feenstra, and J. Schmiedmayer. A Bose–Einstein condensate in a microtrap. *Journal of Optics B: Quantum and Semiclassical Optics*, 5:S143, 2003.
- [72] L. Della Pietra. *Coherent micromanipulation of 1-D BEC in designed potentials*. Ph.D. thesis, Universität Heidelberg, 2007.
- [73] E. A. Donley, T. P. Heavner, F. Levi, M. O. Tataw, and S. R. Jefferts. Double-pass acousto-optic modulator system. *Rev. Sci. Instrum.*, 76(6):063112, 2005.
- [74] Carl E. Wieman and Leo Hollberg. Using diode lasers for atomic physics. *Rev. Sci. Instrum.*, 62(1):1, 1991.
- [75] H. Ellmann. *DLX 110 High power Tunable Single-Mode Diode Laser*. Topica Photonics AG, 2005.
- [76] L. Ricci, M. Weidemüller, T. Esslinger, A. Hemmerich, C. Zimmermann, V. Vuletic, W. König, and T. W. Hänsch. A compact grating-stabilized diode laser system for atomic physics. *Optics Communications*, 117(5-6):541, 1995.
- [77] B. Shirinzadeh and Charles C. Wang. Accurate determination of the vapor pressure of potassium using optical absorption. *Appl. Opt.*, 22(20):3265, 1983.
- [78] S. Aigner. *Magnetfeld microscopy with ultracold atoms*. Ph.D. thesis, Universität Heidelberg, 2007.
- [79] H. Ellmann. *Diode Laser Supply Electronics Manual*. Toptica Photonics AG, m-007 version 01 edition, 2006.
- [80] Analog Devices. Integrated Synthesizer and VCO. Technical report, Analog Devices, Inc., 2004.
- [81] U. Tietze and C. Schenk. *Halbleiter-Schaltungstechnik*. Springer, 2002.

- [82] Z. Hadzibabic, S. Gupta, C. A. Stan, C. H. Schunck, M. W. Zwierlein, K. Dieckmann, and W. Ketterle. Fiftyfold Improvement in the Number of Quantum Degenerate Fermionic Atoms. *Phys. Rev. Lett.*, 91(16):160401, 2003.
- [83] S. Wildermuth. *Neue Experimente mit Atomchips*. Master's thesis, Universität Heidelberg, 2002.
- [84] John V. Prodan, William D. Phillips, and Harold Metcalf. Laser Production of a Very Slow Monoenergetic Atomic Beam. *Phys. Rev. Lett.*, 49(16):1149, 1982.
- [85] K. Brugger, P. Krüger, X. Luo, S. Wildermuth, H. Gimpel, M. W. Klein, S. Groth, R. Folman, I. Bar-Joseph, and J. Schmiedmayer. Two-wire guides and traps with vertical bias fields on atom chips. *Phys. Rev. A*, 72(2):023607, 2005.
- [86] M. Brajdic. *Entwicklung einer Computersteuerung und ihre Anwendung in einem Experiment zur vereinfachten Bose-Einstein Kondensation in einer Oberflächenfalle*. Master's thesis, Universität Heidelberg, 2003.
- [87] E. Haller. *Mikrofallen nahe der Oberfläche von Atomchips*. Master's thesis, Universität Heidelberg, 2004.
- [88] M. Taglieber, A.-C. Voigt, F. Henkel, S. Fray, T. W. Hänsch, and K. Dieckmann. Simultaneous magneto-optical trapping of three atomic species. *Phys. Rev. A*, 73(1):011402, 2006.
- [89] Michael Brown-Hayes and Roberto Onofrio. Optimal cooling strategies for magnetically trapped atomic Fermi-Bose mixtures. *Phys. Rev. A*, 70(6):063614, 2004.
- [90] S. Schneider, A. Kasper, Ch. vom Hagen, M. Bartenstein, B. Engeser, T. Schumm, I. Bar-Joseph, R. Folman, L. Feenstra, and J. Schmiedmayer. Bose-Einstein condensation in a simple microtrap. *Phys. Rev. A*, 67(2):023612, 2003.
- [91] G. Roati, F. Riboli, G. Modugno, and M. Inguscio. Fermi-Bose Quantum Degenerate  $^{40}\text{K}$ - $^{87}\text{Rb}$  Mixture with Attractive Interaction. *Phys. Rev. Lett.*, 89(15):150403, 2002.
- [92] Z. Hadzibabic, C. A. Stan, K. Dieckmann, S. Gupta, M. W. Zwierlein, A. Görlitz, and W. Ketterle. Two-Species Mixture of Quantum Degenerate Bose and Fermi Gases. *Phys. Rev. Lett.*, 88(16):160401, 2002.

- [93] F. Schreck, L. Khaykovich, K. L. Corwin, G. Ferrari, T. Bourdel, J. Cubizolles, and C. Salomon. Quasipure Bose-Einstein Condensate Immersed in a Fermi Sea. *Phys. Rev. Lett.*, 87(8):080403, 2001.
- [94] Andrew G. Truscott, Kevin E. Strecker, William I. McAlexander, Guthrie B. Partridge, and Randall G. Hulet. Observation of Fermi Pressure in a Gas of Trapped Atoms. *Science*, 291(5513):2570, 2001.
- [95] S. R. Granade, M. E. Gehm, K. M. O'Hara, and J. E. Thomas. All-Optical Production of a Degenerate Fermi Gas. *Phys. Rev. Lett.*, 88(12):120405, 2002.
- [96] S. Jochim, M. Bartenstein, A. Altmeyer, G. Hendl, C. Chin, J. Hecker Denschlag, and R. Grimm. Pure Gas of Optically Trapped Molecules Created from Fermionic Atoms. *Phys. Rev. Lett.*, 91(24):240402, 2003.
- [97] J. Cubizolles, T. Bourdel, S. J. J. M. F. Kokkelmans, G. V. Shlyapnikov, and C. Salomon. Production of Long-Lived Ultracold  $\text{Li}_2$  Molecules from a Fermi Gas. *Phys. Rev. Lett.*, 91(24):240401, 2003.
- [98] Cindy A. Regal, Christopher Ticknor, John L. Bohn, and Deborah S. Jin. Creation of ultracold molecules from a Fermi gas of atoms. *Nature*, 424(6944):47, 2003.
- [99] A. J. Leggett. Diatomic molecules and Cooper pairs. *Modern Trends in the Theory of Condensed Matter. Proceedings of the XVIth Karpacz Winter School of Theoretical Physics, Karpacz, Poland, (Springer-Verlag, Berlin)*, 1:13, 1980.
- [100] Wolfgang Ketterle and Martin W. Zwierlein. Making, probing and understanding ultracold Fermi gases. *arXiv:0801.2500v1*, 2008.
- [101] S. Aubin, S. Myrskog, M. H. T. Extavour, L. J. LeBlanc, D. McKay, A. Stummer, and J. H. Thywissen. Rapid sympathetic cooling to Fermi degeneracy on a chip. *Nat Phys*, 2(6):384, 2006.
- [102] R. Folman, P. Krüger, J. Schmiedmayer, J. Denschlag, and C. Henkel. Microscopic atom optics: from wires to an atom chip. *Adv. At. Mol. Opt. Phys.*, 48:263, 2002.
- [103] Henning Moritz, Thilo Stoferle, Kenneth Gunter, Michael Kohl, and Tilman Esslinger. Confinement Induced Molecules in a 1D Fermi Gas. *Phys. Rev. Lett.*, 94(21):210401, 2005.
- [104] Belen Paredes, Artur Widera, Valentin Murg, Olaf Mandel, Simon Fölling, Ignacio Cirac, Gora V. Shlyapnikov, Theodor W. Hänsch, and I. Bloch.



- Tonks-Girardeau gas of ultracold atoms in an optical lattice. *Nature*, 429(6989):277, 2004.
- [105] Shengwang Du, Matthew B. Squires, Yutaka Imai, Leslie Czaia, R. A. Saravanan, Victor Bright, Jakob Reichel, T. W. Hänsch, and Dana Z. Anderson. Atom-chip Bose-Einstein condensation in a portable vacuum cell. *Phys. Rev. A*, 70(5):053606, 2004.
- [106] M. Taglieber, A.-C. Voigt, T. Aoki, T. W. Hänsch, and K. Dieckmann. Quantum Degenerate Two-Species Fermi-Fermi Mixture Coexisting with a Bose-Einstein Condensate. *Phys. Rev. Lett.*, 100(1):010401, 2008.
- [107] Immanuel Bloch, Theodor W. Hänsch, and Tilman Esslinger. Atom Laser with a cw Output Coupler. *Phys. Rev. Lett.*, 82(15):3008, 1999.
- [108] A.D. Cronin, J Schmiedmayer, and D. E. Pritchard. Atom Interferometers. *arxiv:0712.3703v1*, 1:1, 2007.
- [109] C. Ospelkaus, S. Ospelkaus, K. Sengstock, and K. Bongs. Interaction-Driven Dynamics of  $^{40}\text{K}$ - $^{87}\text{Rb}$  Fermion-Boson Gas Mixtures in the Large-Particle-Number Limit. *Phys. Rev. Lett.*, 96(2):020401, 2006.
- [110] J. Fortágh, H. Ott, S. Kraft, A. Günther, and C. Zimmermann. Surface effects in magnetic microtraps. *Phys. Rev. A*, 66(4):041604, 2002.
- [111] A. E. Leanhardt, A. P. Chikkatur, D. Kielpinski, Y. Shin, T. L. Gustavson, W. Ketterle, and D. E. Pritchard. Propagation of Bose-Einstein Condensates in a Magnetic Waveguide. *Phys. Rev. Lett.*, 89(4):040401, 2002.
- [112] J. Estève, C. Aussibal, T. Schumm, C. Figl, D. Maily, I. Bouchoule, C. I. Westbrook, and A. Aspect. Role of wire imperfections in micromagnetic traps for atoms. *Phys. Rev. A*, 70(4):043629, 2004.
- [113] M. P. A. Jones, C. J. Vale, D. Sahagun, B. V. Hall, and E. A. Hinds. Spin Coupling between Cold Atoms and the Thermal Fluctuations of a Metal Surface. *Phys. Rev. Lett.*, 91(8):080401, 2003.
- [114] S. Wildermuth, S. Hofferberth, I. Lesanovsky, E. Haller, L.M. Andersson, S. Groth, I. Bar-Joseph, P. Krüger, and J. Schmiedmayer. Microscopic magnetic-field imaging. *Nature*, 435:440, 2005.
- [115] S. Aigner, L. Della Pietra, Y. Japha, O. Entin-Wohlman, T. David, R. Salem, R. Folman, and J. Schmiedmayer. Long-Range Order in Electronic Transport through Disordered Metal Films. *arXiv:0802.0386*, *Science in print*, 1:1, 2008.

- [116] S. Groth, P. Krüger, S. Wildermuth, R. Folman, T. Fernholz, J. Schmiedmayer, D. Mahalu, and I. Bar-Joseph. Atom chips: Fabrication and thermal properties. *Appl. Phys. Lett.*, 85:2980, 2004.
- [117] J.-B. Trebbia, C. L. Garrido Alzar, R. Cornelussen, C. I. Westbrook, and I. Bouchoule. Roughness Suppression via Rapid Current Modulation on an Atom Chip. *Phys. Rev. Lett.*, 98(26):263201, 2007.
- [118] L. Della Pietra, S. Aigner, Ch. vom Hagen, S. Groth, I. Bar-Joseph, H. Lezec, and J. Schmiedmayer. Designing potentials by sculpturing wires. *Phys. Rev. A*, 75(6):063604, 2007.
- [119] T. Schumm, S. Hofferberth, L. M. Andersson, S. Wildermuth, S. Groth, I. Bar-Joseph, J. Schmiedmayer, and P. Krüger. Matter-wave interferometry in a double well on an atom chip. *Nat Phys*, 1(1):57, 2005.
- [120] S. Hofferberth, I. Lesanovsky, B. Fischer, J. Verdu, and J. Schmiedmayer. Radiofrequency-dressed-state potentials for neutral atoms. *Nat Phys*, 2(10):710, 2006.
- [121] T. Calarco, E. A. Hinds, D. Jaksch, J. Schmiedmayer, J. I. Cirac, and P. Zoller. Quantum gates with neutral atoms: Controlling collisional interactions in time-dependent traps. *Phys. Rev. A*, 61(2):022304, 2000.
- [122] B. Engeser. *Optische Abbildung einer atomaren Dichteverteilung*. Master's thesis, Universität Heidelberg, 2002.
- [123] W. Alt. An objective lens for efficient fluorescence detection of single atoms. *Optik*, 113:142, 2002.
- [124] J. R. Abo-Shaeer, C. Raman, J. M. Vogels, and W. Ketterle. Observation of Vortex Lattices in Bose-Einstein Condensates. *Science*, 292(5516):476, 2001.
- [125] T. Tsurumi and M. Wadati. Dynamics of Magnetically Trapped Boson-Fermion Mixtures. *Journal of the Physical Society of Japan*, 1:97, 2000.
- [126] K. Xu, T. Mukaiyama, J. R. Abo-Shaeer, J. K. Chin, D. E. Miller, and W. Ketterle. Formation of Quantum-Degenerate Sodium Molecules. *Phys. Rev. Lett.*, 91(21):210402, 2003.
- [127] B Lev. *Magnetic Microtraps for Cavity QED, Bose-Einstein Condensates, and Atom Optics*. Ph.D. thesis, Stanford University, 2005.
- [128] Dana Z. Anderson and Jakob Reichel. Cold atom system with atom chip wall. Technical Report 7126112, FreePatentsOnline, <http://www.freepatentsonline.com/7126112.html>, 2006.

- [129] A. Kasper. *Bose – Einstein condensation in a robust microtrap – the combination of wire traps and atom chips*. Ph.D. thesis, Universität Heidelberg, 2003.
- [130] S. Wildermuth. *One-dimensional Bose-Einstein condensates in microtraps*. Ph.D. thesis, Universität Heidelberg, 2005.
- [131] S. N. Atutov, V. Biancalana, P. Bicchi, C. Marinelli, E. Mariotti, M. Meucci, A. Nagel, K. A. Nasyrov, S. Rachini, and L. Moi. Light-induced diffusion and desorption of alkali metals in a siloxane film: Theory and experiment. *Phys. Rev. A*, 60(6):4693, 1999.
- [132] J. Fortágh, A. Grossmann, T. W. Hänsch, and C. Zimmermann. Fast loading of a magneto-optical trap from a pulsed thermal source. *J. Appl. Phys.*, 84(12):6499, 1998.
- [133] C. Klempt, T. van Zoest, T. Henninger, O. Topic, E. Rasel, W. Ertmer, and J. Arlt. Ultraviolet light-induced atom desorption for large rubidium and potassium magneto-optical traps. *Phys. Rev. A*, 73(1):013410, 2006.
- [134] S. Schneider. *Bose-Einstein Kondensation in einer magnetischen Z-Falle*. Ph.D. thesis, Universität Heidelberg, 2003.
- [135] T. Mukai, C. Hufnagel, A. Kasper, T. Meno, A. Tsukada, K. Semba, and F. Shimizu. Persistent Supercurrent Atom Chip. *Physical Review Letters*, 98(26):260407, 2007.
- [136] S. Kadlecěk, J. Sebby, R. Newell, and T. G. Walker. Nondestructive spatial heterodyne imaging of cold atoms. *Opt. Lett.*, 26(3):137, 2001.
- [137] D. Gallego Garcia. *Dipolfallen in Atomchip-Experimenten*. Master’s thesis, Universität Heidelberg, 2005.
- [138] Robert Bücken. *Fluorescence Imaging of Ultracold Atoms*. Master’s thesis, Universität Heidelberg, 2008.
- [139] M. Göbel. *N.N.* Ph.D. thesis, Universität Heidelberg, 2008.
- [140] E. Hartungen. *Aufbau einer Apparatur zum Einfang kalter Atome*. Master’s thesis, Universität Innsbruck, 2001.
- [141] B. DeMarco, H. Rohner, and D. S. Jin. An enriched  $^{40}\text{K}$  source for fermionic atom studies. *Review of Scientific Instruments*, 70(4):1967, 1999.
- [142] S. Hofferberth, I. Lesanovsky, B. Fischer, T. Schumm, and J. Schmiedmayer. Non-equilibrium coherence dynamics in one-dimensional Bose gases. *Nature*, 449:324, 2007.

- [143] I. Lesanovsky, S. Hofferberth, J. Schmiedmayer, and P. Schmelcher. Manipulation of ultracold atoms in dressed adiabatic RF-potentials. *Phys. Rev. A.*, 74:033619, 2006.
- [144] S. Ospelkaus, C. Ospelkaus, O. Wille, M. Succo, P. Ernst, K. Sengstock, and K. Bongs. Localization of Bosonic Atoms by Fermionic Impurities in a Three-Dimensional Optical Lattice. *Physical Review Letters*, 96(18):180403, 2006.
- [145] Scott A. Bender, Kevin D. Erker, and Brian E. Granger. Exponentially Decaying Correlations in a Gas of Strongly Interacting Spin-Polarized 1D Fermions with Zero-Range Interactions. *Physical Review Letters*, 95(23):230404, 2005.

# Acknowledgements

I am grateful to my parents and my sister for providing me with the greatest support thinkable.

Jörg Schmiedmayer gave me, with this project, the great opportunity to develop my own ideas and to learn. He gave us all freedom during the design and trusted Martin and me to get this experiment off the ground. I am grateful to Martin Göbel for sharing all the ups and downs of this story (and there are a few more than have been told) and finally making it all work. I feel strongly encouraged by David Smith, who bought the "pig in a poke" and adopted it so quickly – thank you for your excellent support and friendship.

**I would like to thank:** Simon Aigner, who became a good friend and who had a challenging question no matter where or when. Alexander Kasper, who actually talked me into all this before I started my diploma thesis and from whom I learned the fine art of knowing what could be the bug. Mauritz Andersson for many good discussions. Christian Koller for giving hands on instruction to Vienna and its inhabitants. Christoph Hufnagel for the nice work in the LiRb lab and email support. Stephan Schneider for his contributions to this work and for organising the construction of the new labs in Vienna and the move. Barbara Stix and Max Kuhnert for their fast learning curve and nice work in the lab. The whole group here in Vienna for the "competitive fun" and the people from the ATI for a warm welcome to us Piefkes.

I would like to express my thanks to Jörg, Jian-Wei Pan, Thomas Gasenzer and Christoph Cremer for being my referees.

I am in great debt to the workshops in Heidelberg. The electronics workshop did not only delivered outstanding quality, but were very open for discussions and the realisation of specific needs. Furthermore, due to their willingness to share knowledge, I learned a lot. Two people contributed most to the electronics used in this work, Mr. Rusnyak on the analog electronics for the lasers and Mr. Layer on the the "dangerous" high-voltage / high-current electronics. The mechanical workshop, under the careful supervision of Mr. Stahl, supported us even after the move to Vienna with their excellent work. Particular, the construction of our atom chip mounting would have been impossible without their support. I would like to extend this "thank you" to the whole crew at the Physikalisches Institut in Heidelberg. The mechanical workshop in Vienna did a very good job

with the manufacturing of the new coils and countless small and not-so-small parts we needed during the building phase in Vienna.

There is a long list of people outside of the lab, who made the last years special (in random order): Frank Würker for countless hours of discussions in the old town of Heidelberg; Flo, Malte and Hilka, the Brunnengasse crew and a number of people at the upper end of the Hauptstrasse; Julie; Antonia, Ann-Kathrin, Katharina, Helena, Nora and Wolf for sharing flat in Vienna; Lutz, THE guide to the Vienna night life.

Finally, David, Martin and Simon contributed with careful proofreading of the manuscript and supplied helpful questions – thank you!